2.33 p53 Transcription Activity and Possible Bystander Effects in Mouse Fibroblast Cells Irradiated by Heavy Ion-microbeam

M. Saitou*, T. Sugihara*, K. Tanaka*, Y. Oghiso*, T. Funayama**, S. Wada**, T. Sakashita** and Y. Kobayashi**
Department of Radiobiology, Institute for Environmental Sciences*
Department of Ion-beam-applied Biology, JAERI**

1. Introduction

The experiment with microbeam irradiation targeting individual cells will be necessary to verify biological effects induced by low dose rate radiation. Last year, we established irradiation procedures of the microbeam and detection system for p53 gene transcription activity in mouse-cultured cells. This year, the confluent cells were irradiated by either ion microbeam or broad ion beam, and the transcription levels of p53 in irradiated cells were observed by the luciferase detection system.

2. Experimental procedure

2.1 Cell line

A mouse fibroblast cell line, NIH3T3/pG13 Luc, was used for present study. The transformant NIH3T3 cell has luciferase gene-introduced plasmid DNA (pG13 Luc), which is incorporated upstream sequence for p53-binding region. The plasmid DNA can emit chemiluminescent light after treatment of cell-lysis as luciferase gene is expressed by transcription activity of p53 protein.

2.2 Microbeam irradiation of heavy ion

Microbeam or "broad-field" irradiation was performed by using 260-MeV $^{20}Ne^{7+}$ ion beam from TIARA AVF cyclotron. Cells (0.24 ml, 1.2 x 10^5 cells/ml) were seeded onto a narrow sample area (8 mm ϕ in diameter in a center of specially made 35mm dish covered with a 7.5 μm-thick replaceable Kapton polyimide film at the bottom side, where a density of cells (2.3 x 10^3 cells/mm^2) for 2 or 3 days with D-MEM medium including 5% FBS until becoming confluent cells before irradiation. Then, cells were cultured and the D-MEM medium solution was removed between confluent cells and Kapton film just before start of irradiation. In each of broad ion beam irradiation, three samples were used. The particle fluence was about one ion/(10 μm)^2, which is correspondent to the average number for one ion per cell. In microbeam irradiation, the exact number of one ion was irradiated at each cross point of orthogonal lattice in area of 3 x 3 mm square. Cells (1.2 x 10^5 cells/ml in 0.24 ml) were seeded in the same conditions as above mentioned. The numbers of irradiation cross points were set up as 1 x 1 = 1, 1 x 4 = 4, 2 x 4 = 8, 3 x 4 = 12, and 4 x 4 = 16 in an area of 3 mm square with an interval of 1 mm. To measure p53 transcription activity depending on the density of irradiation cross point (i.e. the number density of ion per area), 1 x 1 = 1, 4 x 4 = 16, 8 x 8 = 64, 11 x 11 = 121 and 16 x 16 = 256 on the same area, where there was an interval of 1, 1, 0.429, 0.300 and 0.200 mm, respectively, were set up. After irradiation, cells were

incubated for 4h in D-MEM at 37°C. All of the present experiment was performed under the moisture condition become we have confirmed that the humidity condition did not related to the cell viability and p53 transcription activity.

2.3 Measurement of p53 transcription activity

After 4h-incubation, cells were treated by Passive Lysis buffer and the cell lysate was poured into each well in a 96-well white plate for fluorescent measurement and then, pure water and luciferase assay reagent were added into each well. Chemiluminescence light from the sample was measured by plate-reader. An aliquot of identical sample was used for quantification of total protein. The cell lysate was poured into each well in a 96-well transparent plate and then, diluted protein assay dye reagent was serially added into each well. The absorbance of the sample was analyzed at 595 nm by another plate-reader. The p53 transcription activity was calculated by the ratio of chemiluminescence intensity to the protein absorbance, A595, of the cell lysate.

3. Results and Discussion

The p53 transcription activities in cells irradiated by broad beam of 260-MeV Ne ion (about 0.7 Gy) showed about 2-fold increase of control (Fig. 1). The p53 transcription activities in the cells irradiated by microbeam of 260-MeV Ne ion had a tendency of decrease with the increase of irradiation points from 1 to 16 (Fig. 2). In the similar way, the p53 transcription activities also decreased with the number of irradiation point per sample lattice area (Fig. 3). The increase of irradiation point per area showed an inverse

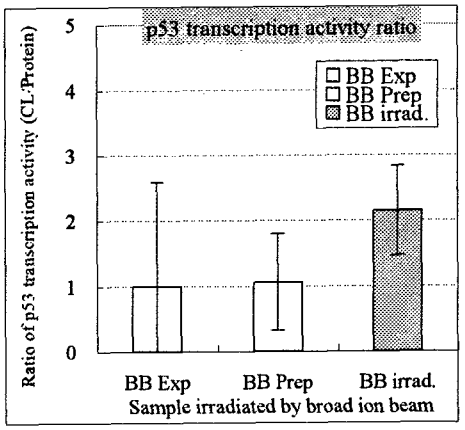

Fig. 1 p53 protein transcription activities of cells irradiated by broad beam of Ne ion under the moisture condition. BBExp.: sham-irradiated control, BBPrep.: unirradiated control, BBirrad.: broad beam irradiation. Each ordinate shows chemi-luminescence intensity normalized by amount of protein.

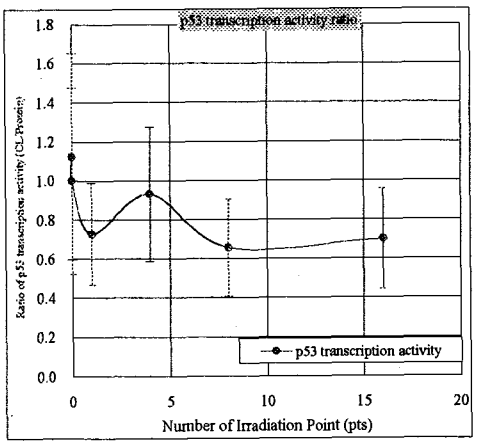

Fig. 2 p53 protein transcription activities of cells irradiated by microbeam of Ne ion under the moisture condition. An each abscissa shows the number of irradiation point.

to p53 transcription activities (Fig. 3). These results suggest that microbeam irradiation induced a reduction of the p53 transcription activities in irradiated cell population, where different mechanism

seem to have in the case from those obtained by irradiation with broad beam. Irradiation of one ion seems to be 30–40% reduction of p53 transcription activities (Fig. 2). When the number of cells hit by ions reaches to the level of about 1/10,000 in the total number of cells, the range of secondary electrons in the penumbra around one ion track becomes 3-16 μm[1]. Therefore, the reduction can not be explained by the effect of secondary electrons and it may be induced by other mechanism, like bystander effects, although the why p53 transcription activity showed a reduction is not known. In the opposite, broad beam irradiation caused the increase of p53 transcription activity. There results also indicate that a fluence giving a minimum level of p53 transcription activity may exist somewhere between the fluence of 256 points (i.e. 256 ions) per area in microbeam irradiation and that of one ion per cell in broad beam irradiation.

This study was financially supported by Aomori Prefecture, Japan.

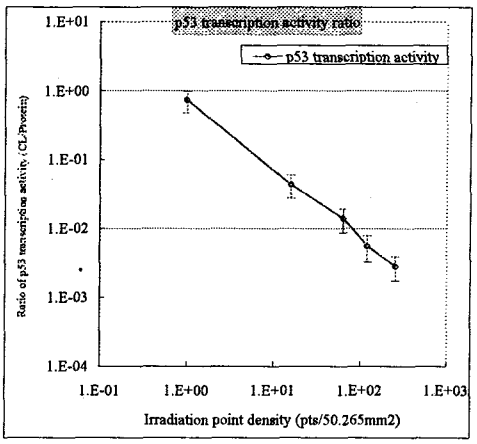

Fig. 3 p53 protein transcription activities of cells irradiated by microbeam of Ne ion under the moisture condition. An each abscissa shows the number of irradiation point per sample lattice area of 3 x 3 mm square (i.e. the point density).

References

1) J. Kiefer, in Biological Radiation Effects (1993), pp.91.

2.34 Bystander Effects on Chromosomal Aberrations Induced by Heavy Ion Beam Irradiation

Y. Kanasugi*, T. Funayama**, S. Wada**, T. Sakashita**, Y. Kobayashi** and K. Takakura*
Graduate School of Natural Science, International Christian University*
Department of Ion-beam-applied Biology, JAERI**

1. Introduction

Genomic instability, mutation, cell death, carcinogenesis, and DNA double strand breaks have been considered as a result of radiation exposure. However these responses were observed in unirradiated cells located near by irradiated cells or co-cultured in the same medium[1), 2), 3)]. These studies showed that direct exposure of ionizing radiation is not necessarily required to induce a cellular response. Although the mechanisms of induction of these bystander effects are not clearly understood, recent studies indicate that bystander effects are transmitted by gap-junction intercellular communication or by releasing of soluble factors into culture medium.

DNA double strand break is one of the most lethal damage to cells in several kind of cellular responses caused by radiation exposure and bystander effects[4), 5)]. If DNA double strand breaks remain unrepaired or are misrepaired, further cellular aberrations such as, genomic instability, carcinogenesis, mutation, and cell death could be occurred. The bystander effect has not been considered to play a role in an induction of DNA double strand breaks, though earlier study clearly indicated that exposure of radiation induces DNA double strand breaks on the cells. In this study, bystander effects on chromosomal aberration induced by exposure to heavy ion beams are studied. Chromosome aberrations of human lymphoblast cells were observed after irradiation of heavy ion beams on whole part or limited part of cells in order to measure the bystander effect quantitatively.

2. Experimental procedure

2.1 Cell Culture and Treatment

GM14511, normal human lymphoblast cells were purchased from CORIELL institute. Cells were cultured in RPMI medium 1640 supplemented with 10% FBS and 100 unit/ml penicillin and 100 μg/ml streptomycin. Cultures were maintained at 37℃ in an atmosphere with 5% of CO_2. 6 hours before heavy ion irradiation, cells were attached onto the bottom of cell culture dishes by using Cell-tak adhesive (BD, UK).

2.2 Heavy Ion Irradiation

Just before heavy ion irradiation, medium in dishes were removed and covered by kapton sheet for keep moisture in dishes. 80% of cells on the culture dishes were masked in order to distinguish irradiated and unirradiated part of cells. Using heavy ion accelerator at TIARA of JAERI-Takasaki, the whole or 80% masked cells were exposed to 5 Gy of Ne^{7+} (LET = 430 keV/μm) heavy ion beam. In this irradiation, it was calculated that about 5-7 ions passed through each single cell.

2.3 Premature Chromosome Condensation Method

In order to observe the chromosomal aberrations in irradiated cells, premature

chromosome condensation method with Calyculin A was used. After heavy ion irradiation, cells were cultured in fresh culture medium for 0, 2, 4, and12 hours. Then each cultures were treated with 0.5μg/ml of Calyculin A for 30min at 37℃. Cells were harvested, treated with 2ml of 75mM KCl for 20 min at 37℃, and fixed with methanol-acetic acid (3:1). Cell suspensions were dropped onto slide glass and stained by Giemsa. 50 Cells on each slide glass were microscopically observed and chromosomal aberrations were counted.

3. Result and Discussion

Observation of chromosomes demonstrated that number of cells with chromosomal aberrations were larger than the number of cells received radiation exposure in the case of 80% masking and those numbers increased (Fig. 1). This result suggested that further chromosomal aberrations among cells received no direct exposure of heavy ion caused by other than direct exposure of heavy ion causes.

The number of chromosomal aberrations per single cells was widely distributed. Those distributions of chromosomal aberrations contain both caused by direct exposure and bystander effect. Therefore, we divided cells into two categories according to the distribution. The percentage of cells with more than 5 chromosomal aberrations did not change even 12 hours after the irradiation (Fig. 2). On the other hand, the percentage of cells with 5 or less chromosomal aberrations increased (Fig. 3). Generally, initial chromosomal damage of irradiated cells should be decreased because of DNA repair depending on incubation time after irradiation. However, the result in this study indicates that bystander effect might be a cause of DNA double strand breaks increasing time dependently.

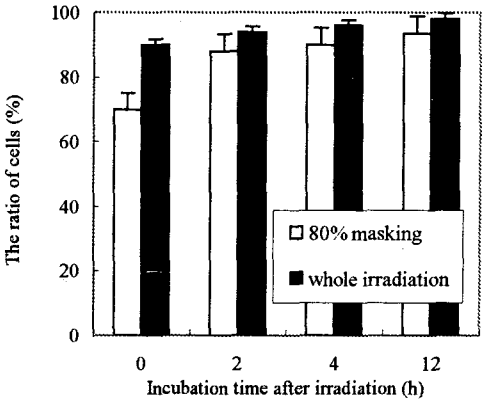

Fig. 1 The ratio of cells with chromosomal aberrations in the whole cells (The ratio of cells).

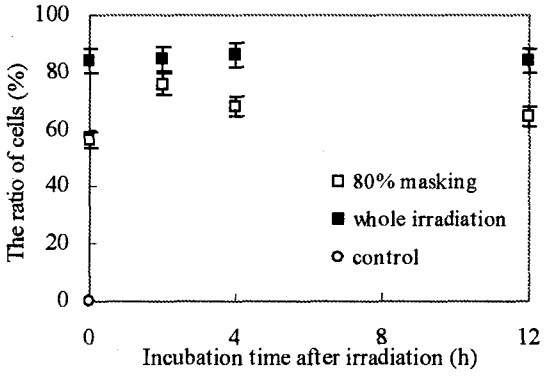

Fig. 2 The ratio of cells with more than 5 chromosomal aberrations per single cell in the whole cells (The ratio of cells).

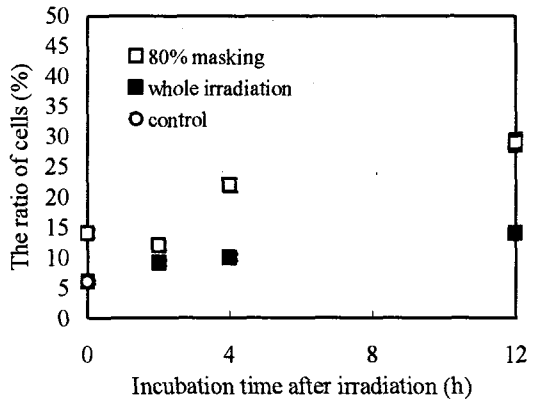

Fig. 3 The percentage of damaged cells with 5 or less chromosomal aberrations per single cell to the whole cells (The ratio of cells).

References

1) Nagasawa H, Little JB. Cancer Res. 1992 Nov 15;52(22):6394-6.
2) Azzam EI, de Toledo SM, Gooding T, Little JB. Radiat Res. 1998 Nov;150(5):497-504.
3) Azzam EI, de Toledo SM, Little JB. Proc Natl Acad Sci U S A. 2001 Jan 16;98(2):473-8.
4) Kadhim MA, Lorimore SA, Townsend KM, Goodhead DT, Buckle VJ, Wright EG. Int J Radiat Biol. 1995 Mar;67(3):287-93.
5) Suzuki M, Zhou H, Hei TK, Tsuruoka C, Fujitaka K. Biol Sci Space. 2003 Oct;17(3):251-2.

2.35 Induction of Tumor Suppressor p53 by Heavy-ion Beam Irradiation

H. Aotani*, T. Funayama**, S. Wada**, T. Sakashita**, Y. Kobayashi**, S. Kaul*** and K. Takakura*
Graduate School of Natural Science, International Christian University*
Department of Ion-beam-applied Biology, JAERI**
Gene Function Research Center, National Institute of Advanced Industrial Science & Technology (AIST)***

1. Introduction

The cancer therapy using heavy-ion beams is getting to be active from recent ten years ago. Some successful results are reported in cancer therapy using heavy-ion beams in HIMAC or GSI. The reasons why heavy-ion beams are useful at cancer therapy are as follows. The Bragg peak by heavy-ion radiations has beneficial applications to cancer therapy, because they focus and selectively attack tumor cells located in deep positions within the body. The other advantage of the heavy-ion radiations for cancer therapy is high RBE value on the irradiated materials comparing to the X rays or γ rays irradiation therapy. The further researches of basic and fundamental radiation effect on biological systems are necessary to develop the heavy ion beam radiation therapy further more.

It is well known that tumor suppressor protein p53 is activated when the cells are irradiated with some kind of radiations, such as X rays or γ rays. P53 is important protein at cell-cycle control, apoptosis and maintenance of gene stability. It promotes transcription of genes that induces cell cycle arrest or apoptosis in response to DNA damage or other stress.[1] p53 protein acts as a check point in the G1-phase of the cell cycle.[2] It is said that p53 gene is one of the most frequently mutated gene in human cancer in some literature.[3] In this study the observation of p53 induction by irradiation with heavy ion beams is aimed using U2OS cells.

Though U2OS cells, human osteosarcoma cells, are cancer cells, they carry p53 protein normally. Furthermore, U2OS has 20-30 % of p53 in the nucleus while 70-80 % of p53 can be found in the cytoplasm. Therefore, when U2OS cells are irradiated, the increase of p53 concentration in nucleus should be able to be observed as well as the transfer of cytoplasmic p53 to the nucleus.

Recently protein CARF is identified as a protein having relation to p53.[4] It is suggested that the binding of CARF to p53 is necessary in order to activate p53, thus the binding and colocalization between CARF and p53 in nucleus might be expected. In this study, the interaction of p53 and CARF was also investigated when the cells are irradiated with heavy-ion beams.

2. Experimental procedure

2.1 Cell culture & Irradiation

U2OS cells, bone cancer cells of human cultured cells, were used as irradiated samples throughout this study. One day before the irradiation with heavy-ion beams cells were trypsinized and plated into 3.5 cm dishes. Just before the irradiation, the medium was removed from the dishes and poly-imide sheets were covered to protect the cells from drying up. The cells were irradiated with 220 MeV $^{20}Ne^{7+}$ beams at the beam line of TIARA AVF-cyclotron accelerator (Takasaki). The value of LET of the beam was 430 keV/μm. As

a reference experiment, the UV irradiation experiment was done with a germicidal lamp having wavelength of 253 nm. Irradiated samples were kept in incubator for various hours after irradiation and analyzed by some methods, such as immunostainig, Western blotiing and immunoprecipitation methods.

2.2 Immunostaining

For the analyses of immunostaining cells were grown in glass coverslips placed in 3.5 cm dishes. After various incubation times irradiated cells on the coverslip were washed with cold PBS and fixed with 4% formaldehyde for 10 min. at room temperature. Fixed cells were washed with PBS and permeabilized with 0.2% bovine serum albumin in PBS for 20 min. Cells were then incubated in blocking buffer containing the primary p53 antibody (Santa Cruz, DO-1) and CARF antibody for 1 h and washed extensively in PBS before incubation with the appropriate fluorochrome conjugated secondary antibody for a further 30 min. Alexa-488 conjugated goat anti-rabbit and Alexa-594 conjugated goat anti-mouse (Molecular Probes) were used as secondary antibody. After six washes in PBS with 0.1% Triton X-100, cells were overlaid with a coverslip with Fluoromount (Difco). The cells were examined on a Zeiss microscope with epifluorescence optics. The co-localization of two proteins, p53 and CARF, was assessed by combining two images using Fluoview software.

2.3 Western Blotting

The protein sample separated on a SDS-polyacrylamide gel was electroblotted onto a nylon membrane (Millipore) using a semidry transfer blotter (Biometra). Immunoassays were performed with anti-p53 (Santa Cruz, DO-1) and anti-CARF. The immunocomplexes formed were visualized with horseradish peroxidase-conjugated rabbit anti-mouse IgG antibody (ECL kit, Amersham Biosciences).

2.4 Immunoprecipitation

Cell lysates were incubated at 4 °C for 1–2 h with an antibody. Immunocomplexes were separated by rotation with Protein-A/G–Sepharose, and Western blotting. The amount of p53 protein remaining in the supernatant was visualized by Western blotting with anti-p53 antibody.

3. Results and Discussion

As shown in Fig.1 the induction of p53 was clearly observed in both cases of irradiation with Ne-ion beams and ultra-violet light. The amount of p53 induction was maximum at 24 hours after irradiation. On the other hand, the induction of protein CARF was not clear in the case of irradiation with Ne-ion beams, while it was clearly shown with ultra-violet light irradiation. Furthermore, the agreement of the localization of p53 and CARF was observed undoubtedly in the case of irradiation with ultraviolet, though the co-localization of these proteins was not seen in the case of irradiation with Ne-ion beams (Fig. 2). The analyses of p53 and CARF by the method of Western blotting were performed as shown in Fig. 3 and the results showed the same tendency as the results from immunostaining assay. From these results it is suggested that some differences in the interaction of p53 to CARF exist between the case of irradiation with Ne-ion beams and ultra-violet light.

In this study, only the effects of 4 Gy irradiation were examined. In future study, dose dependence of p53 and CARF induction should be examined further. The reference study using X rays or γ–rays should be tried also for these analyses in order to know the characteristics of irradiation effects by Ne-ion beams.

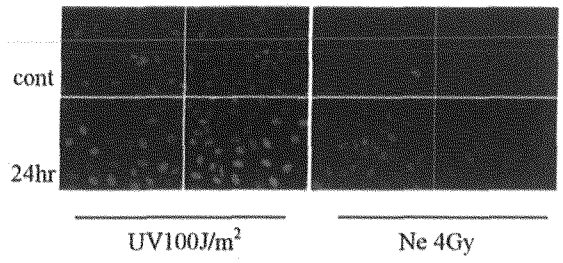

The observations of immunostaining assay by fluorescence microscope with 594 nm light source. Red signal is fluorescence from p53 and green signal is fluorescence from CARF.

Fig.1

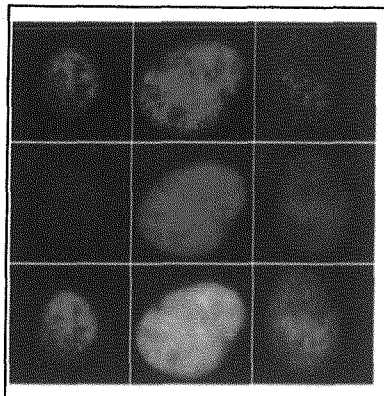

Immunostained cells with p53 antibody and CARF antibody at 24 hours after the irradiations with UV and Ne-ion beams. Merging of the images from p53 and CARF shows the co-localization of these proteins in the case of UV irradiation, but does not show in the case of irradiation with Ne-ion beams.

Fig.2

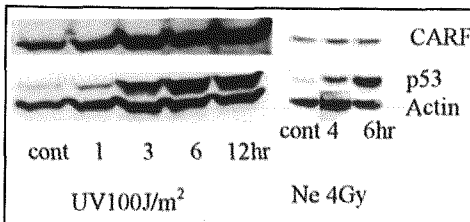

P53 and CARF in Western blotting assay at various times after irradiation with UV and Ne-ion beams. The induction of CARF increases as increasing incubation time when the cells are irradiated with UV light, but the induction of CARF is little when the cells are irradiated with Ne-ion beams.

Fig.3

References

1)Alberts B., A. Johnson, J. Lewis, M. Raff, K. Roberts, and P. Walter (2002). *Molecular Biology of the Cell.* Forth Edition. Garland Science. New York. p.997-1010

2)Farmer G., J. Bargonetti, H. Zhu, P. Friedman, R. Prywes, and C. Prives (1992). "Wild-type p53 activates transcription in vitro." *Nature* 358. p.83-86

3)Hollstein,M., D.Sidransky, B.Vogelstein, and C.C. Harris (1991). "p53 Mutations in Human Cancer." Science253. p49-53

4)Hasan MK, Yaguchi T, Minoda Y, Hirano T, Taira K, Wadhwa R, Kaul SC.
Alternative reading frame protein (ARF)-independent function of CARF (collaborator of ARF) involves its interactions with p53: evidence for a novel p53-activation pathway and its negative feedback control.
Biochem J. 2004 Jun 15;380(Pt 3):605-10.

2.36 Effects of Microbeam Irradiation on G1 Arrest and Apoptosis in Germ Cells of *Caenorhabditis elegans*

A. Higashitani*, T. Sugimoto*, K. Dazai*, T. Sakashita**, T. Funayama**
S. Wada**, N. Hamada**,***, T. Kakizaki** and Y. Kobayashi**,***
Graduate School of Life Sciences, Tohoku University*
Department of Ion-beam-applied Biology, JAERI**
Graduate School of Medicine, Gunma University***

1. Introduction

DNA double-strand breaks (DSBs) caused by ionizing radiation and some chemical agents can induce great damage to genetic material. All cells maintain repair systems for such breaks and apoptosis to eliminate cells that have failed to repair DNA lesions, however, these activities are fluctuated in a tissue specific and/or age dependent manners. We have studied the effects of radiation on meiosis and reproductive development using and experimental model organism, the nematode *Caenorhabditis elegans*. In the adult hermaphrodite, germ cells in tip of gonad arm divide mitotically and thereafter enter meiotic prophase I, progressing from zygotene to diakinesis stage in maturing oocyte. DNA damage induced G1 arrest can be monitored in the tip germ cells[1),2)]. In addition, DNA damage induced apoptosis can occur in the germ cells at meiotic pachytene stage[1)]. The linear array of developmental phases of oogenesis makes the hermaphrodite a convenient model system to study these radiation effects.

Recently, considerable evidences of the existence of a "bystander effect", in which cells having received no irradiation show biological consequences from their neighboring irradiated cells, have been accumulated in mammalian cultured cells[3),4),5)]. However, in other eukaryotic cells and/or individuals a "bystander effect" is little understood. We therefore study whether or not a "bystander effect" exists in germ cells of *C. elegans* using micro beam irradiation system.

2. Experimental procedure

2.1 *C. elegans* strains

In this study, we used *C. elegans* N2 wild-type hermaphrodites and XR1 mutant strain carrying an *abl-1* (*ok171*) deletion allele. The XR1 mutant hermaphrodites become specifically hypersensitive to radiation-induced apoptosis in the germ line cells[6)].

2.2 Irradiation of $^{12}C^{5+}$ ion particles

N2 wild-type L4 larvae were irradiated with $^{12}C^{5+}$ ion particles (220MeV) by HY1 broad beam port at TIARA of JAERI. Thirty-six hours after irradiation, the germ-cell proliferation was visualized with 4', 6-diamidino-2-phenylindole (DAPI) nuclear staining, and each dimension of anterior and posterior gonad was measured with Image J system (NIH imaging software). For micro beam irradiation, $^{12}C^{5+}$ ion particles by HZ1 micro beam port were used with ϕ20μm aperture. Young gravid hermaphrodites were anesthetized with 5 to 10mM sodium azide in M9 buffer and were held between Slide Seal for *in situ* PCR (TaKaRa Co.) and slide grass (Thickness

No. 1: 0.12 – 0.17mm, Matsunami Co.). After the irradiation, the hermaphrodites were washed with M9 buffer and awakened on NGM agar plate for 5 hr. Apoptosis in germ cells were monitored with DIC microscopy[1), 6)].

3. Results and Discussion

Irradiation of more than 60 Gy of $^{12}C^{5+}$ ion broad beams at L4 larvae stage arrested germ cell proliferation (Fig. 1A a, b and 1B). The dimension of each gonad decreased by 60% of that of non-irradiated control (Fig. 1B). When the tip of the gonad arm was hit by 1500 particles of $^{12}C^{5+}$ ion with ϕ20μm aperture, whose levels was nearly identical to 100 Gy irradiation, the arrest of the germ cell proliferation was caused in the irradiated side (Fig. 1A d and 1B). On the other hand, the significantly arrest was not detected in the gonad of non-irradiated side. In addition, when either middle region (pachytene nuclei) of the gonad arm or the worm tail was hit by 1500 particles with ϕ20μm aperture, the arrest was not observed (Fig. 1A c and 1B).

We further studied the effect of micro beam irradiation on DNA damage induced apoptosis in the meiotic pachytene nuclei (Fig. 2A). When the pachytene region of adult posterior gonad was hit by 1500 particles of $^{12}C^{5+}$ ion with ϕ20μm aperture, germ-cell apoptosis in wild-type worms increased from 0.6±0.7 to 3.4±1.5 (mean ±s.d.) 5 hr after irradiation (Fig. 2B). In *abl-1* deletion mutants, germ-cell apoptosis increased from 2 ± 1.7 to 5.8 ± 2.1. Increments in wild-type and *abl-1* adult hermaphrodites were only observed in irradiated side (posterior gonad), but not in non irradiated side (anterior gonad) (Fig. 2B).

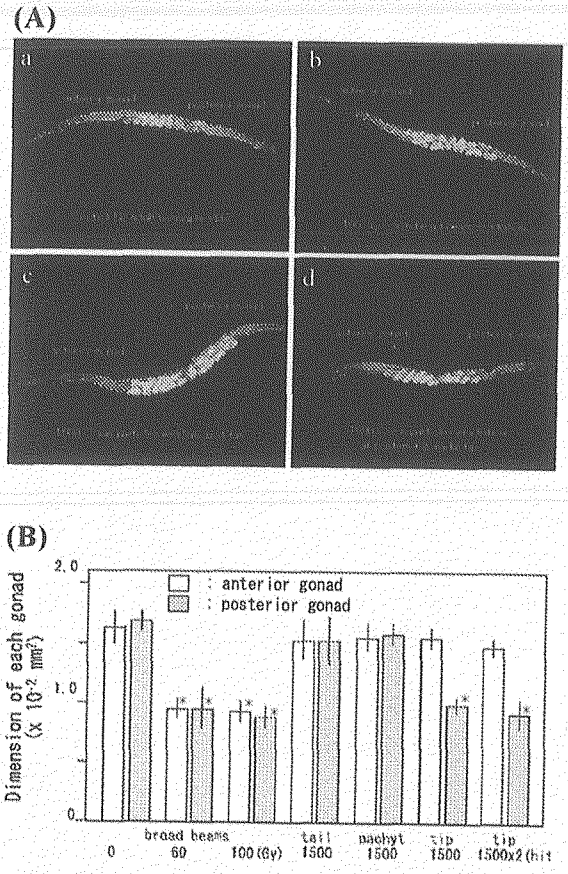

Fig. 1 Arrest of germ cell proliferation caused by irradiation of $^{12}C^{5+}$ ion particles. Thirty-six hr after irradiation, the germ cell proliferation was visualized with DAPI (A), and each dimension of anterior and posterior gonad was measured (B). Micro beams were irradiated onto worm tail (:tail), middle gonad (:pachyt), and tip of posterior gonad arm (:tip), respectively.

When the worm tail was hit by 1500 particles, the germ-cell apoptosis did not increase in either posterior or anterior gonad (Fig. 2B). By 100 Gy broad-beams irradiation of $^{12}C^{5+}$ ion particles, the erm-cell apoptosis increased equally in either posterior or anterior gonad.

These results indicate that DNA damage induced G1 arrest and apoptosis specifically caused in the micro-beam irradiated region,

(A)

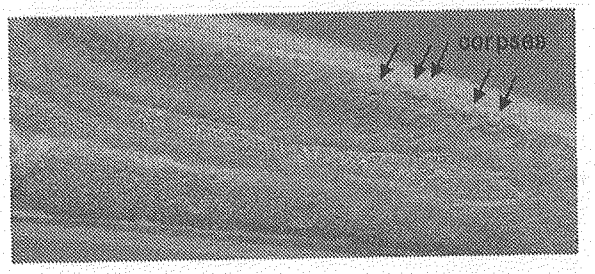

(B)

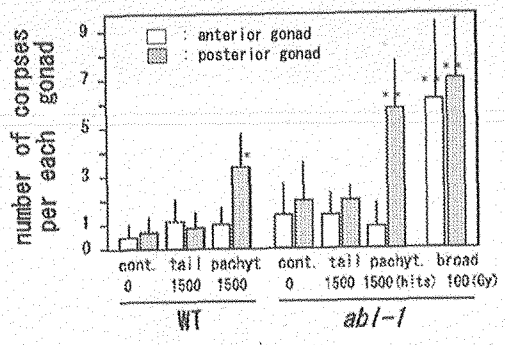

Fig. 2 Germ-cell apoptosis caused by irradiation of $^{12}C^{5+}$ ion particles. The cell corpses were observed with DIC microscopy 5 hr after irradiation (A). The number of cell corpses per distal gonad arm was plotted (B).

but "bystander effects on these phenomena" were not observed in the non-irradiated neighboring region of individuals of the nematode *C. elegans*. It has been reported that both nitric oxide (NO) signal transduction pathway with inducible NO synthase is one of the radiation-induced bystander responses[7), 8)]. A possibility of no "bystander effects" in *C. elegans* may be due to absence of the NO signal transduction system, since any orthologs of iNOS gene could not be found in the nematode genome. As other possibility, in general, germ line cells may be isolated and protected from radiation-induced bystander responses.

References

1) A. Gartner, S. Milstein, S. Ahmed, J. Hodgkin, M. O. Hengartner, Molecular Cell 5 (2000) 435-443.
2) T. Takanami, Y. Zhang, H. Aoki, T. Abe, S. Yoshida, H. Takahashi, S. Horiuchi, A. Higashitani, Journal of Radiation Research 44 (2003) 271-276.
3) C. Shao, Y. Furusawa, Y. Kobayashi, T. Funayama, S. Wada, The FASEB Journal 17 (2003) 1422-1427.
4) R. Iyer, B. E. Lehnert, Archives of Biochemistry and Biophysics 376 (2000) 14-25.
5) C. Mothersill, C. Seymour, Radiation Research 155 (2001) 759-767.
6) X. Deng, E. R. Hofmann, A. Villanueva, O. Hobert, P. Capodieci, D. R. Veach, X. Yin, L. Campodonica, A. Glekas, C. Cordon-Cardo, B. Clarkson, W. G. Bornmann, Z. Fuks, M. O. Hengartner, R. Kolesnick, Nature Genetics 36 (2004) 906-912.
7) H. Matsumoto, S. Hayashi, M. Hatashita, K. Ohnishi, H. Shioura, T. Ohtsubo, R. Kitai, T. Ohnishi, E. Kano, Radiation Research 155 (2001) 387-396.
8) C. Shao, Y. Furusawa, M. Aoki, H. Matsumoto, K. Ando, International Journal of Radiation Biology 78 (2002) 837-844.

2.37 Study on the Photoassimilates Transportation and Partitioning under the CO_2 Enrichment

S. Matsuhashi, S. Fujimaki, N. Kawachi, S. Ishii, N. Suzui and K. Sakamoto
Department of Ion-beam-applied Biology, JAERI

1. Introduction

The Positron Emitting Tracer Imaging System (PETIS) is one of few tools today that can present moving images of long-distance transportation in an intact plant body. It collects serial images of two-dimensional distribution of positron-emitting radiotracer in a test plant without contact[1-3]. However, advantage of PETIS is more than just capturing a movie for qualitative understanding. Numerical data of temporal and spatial distribution of the tracer are sequentially obtained with PETIS.

In this study, we employed a new PETIS apparatus with a larger field of view, 14 cm in width and 21 cm in height. We focused on the quantification of dynamics of photoassimilate transportation through a stem from a leaf, and on the demonstration of the change of the dynamics when only the leaf was exposed to an elevated concentration of carbon dioxide (CO_2). At the present time, such change of transportation dynamics in a single plant can be pursued only when a non-invasive imaging method and a short-life tracer are applied together. Our method passes this criterion because the half-life of the positron-emitting radionuclide ^{11}C is only 20 minutes, which is short enough for repetitive experiments in a single plant.

2. Experimental procedure

Plant material

Broad bean (*Vicia faba* L.) seeds were germinated in water and sown on vermiculite. They were grown for 25 days under atmospheric air in an incubator with a cycle of 15 hours light at 25 °C and 9 hours dark at 20 °C.

Production of $^{11}CO_2$ tracer

$^{11}CO_2$ was produced by bombarding pure nitrogen gas with an energetic proton beam delivered from a cyclotron[2].

Settings of PETIS imaging

A test plant was placed on the middle of opposing PETIS detectors in a chamber. The largest expanded, fourth bifoliate leaf of the plant was inserted into a "gas-cell", a clear acrylic box. The light was conditioned to approximately 500 μmol photon m^{-2} s^{-1} at the surface of the gas-cell.

Procedures of PETIS experiment

Room air was fed to the gas-cell. Soon after the PETIS imaging was started, $^{11}CO_2$ was introduced with room air to the gas-cell for five minutes. Then the $^{11}CO_2$ was drained off and substituted again with room air without the radiotracer.

After the imaging finished, the air fed to the gas-cell was changed to air containing 1000 Pa of non-radioactive CO_2 gas. The enriched CO_2 gas was fed only to the leaf in the gas-cell. This condition was kept for five hours. The second turn of imaging was conducted in the same manner except that all the air fed to the gas-cell contained 1000 Pa of non-radioactive CO_2 gas.

Preparation of time-series data

Regions of interests (ROIs) were set on the obtained movie data and the time course of radioactivity within each ROI was extracted from the data.

Transfer function analysis

The following model was employed for describing the transportation dynamics of photoassimilates in this study:

$$C_d(n) = a\,C_d(n-1) + b\,C_u(n-d),$$

where $C_u(n)$ and $C_d(n)$ mean the amounts of photoassimilates, which had started out from the fed leaf, in an upstream ROI and a downstream ROI at the n-th frame of PETIS imaging, and a, b and d are parameters ($0 < a < 1$, $0 < b < 1$, d is positive integer).

We performed multiple regression analysis with the least-squares method to estimate the best fitting model for each experiment.

Two physical parameters, average transit time t and leakage k, can be estimated from the model. The average transit times and leakages in this study were calculated as follows from the obtained parameters:

$$t = T\,(d + (a / (1-a))$$

and

$$k = 1 - b / (1-a).$$

We defined the errors of the respective calculated parameters as the shifts when the values of corresponding parameter d vary within a range of ± 1.

3. Results and Discussion

Figure 1 shows an test plants and its PETIS image under the condition with ambient CO_2 concentration. It demonstrates that $^{11}CO_2$ was assimilated in the fed leaf and the ^{11}C –photoassimilates were transported via the petiole and stem toward the roots. Similar images were obtained with the other individual and when the enriched CO_2 was fed (not shown).

The transfer function analysis was applied to the time-activity curves extracted from all the ROIs of the plants[4]. Average flow speeds of tracer between neighboring ROIs were estimated from calculated average transit times. Figure 2 shows the distribution of the transit speeds with ambient and enriched CO_2. It indicates that the phloem flow got faster in farther internodes from the fed leaf, and the flow speeds were higher with enriched CO_2.

The leakage, k, would be interpreted as "net phloem leakage" which represents unloading rate from the phloem minus reloading rate into the phloem, in terms of physiology[5]. Distribution ratios, defined as portions deposited into respective internodes or intervals when a unit (100 %) of tracer has been loaded into the first upstream node ROI 1, were calculated from the leakages and are shown in Fig. 3. The respective distribution ratios of the upstream three internodes (ROI 1-3, 3-5 and 5-7) and the distribution ratios separately estimated for the total interval (ROI 1-7) are displayed together. They show good consistency and confirm reliability of our estimation. In the both individuals, slight decrease of distribution ratios

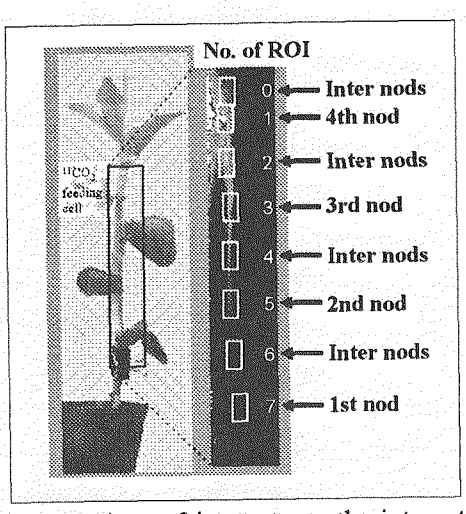

Fig. 1 Regions of interests on the integrated image of the flow of 11C-photoassimilates monitored by PETIS under the ambient CO_2 condition.

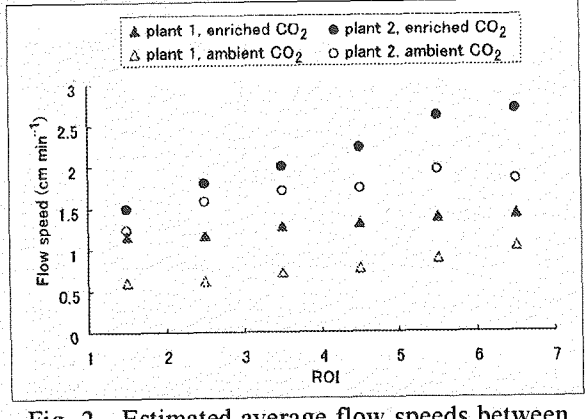

Fig. 2 Estimated average flow speeds between neighboring ROIs.

to the three internodes was induced when enriched CO_2 was fed. In other words, the relative share of the internodes was decreased and that of the lower part of the plant was increased.

We deduce the physiological mechanism of the results as follows. Enriched CO_2 increased the speed and amount of photoassimilate export from the fed leaf. In the other hand, limited sink capacity of the internodes resulted in decrease of the relative share, that is, the distribution ratios.

Grimmer et. al. studied thoroughly about effects of elevated CO_2 concentration on the balance sheet of carbon import and export in leaves of castor bean (*Ricinus communis* L.) plants[6]. They reported that amount of carbon exported from a leaf to phloem per unit time per unit area of the leaf was the same during daytime for plants grown at 350 μL L^{-1} and 700 μL L^{-1} of CO_2. It indicates the phloem-loading capacity of the leaves was saturated under both conditions. We do not think their results argue against ours because the plant species were different and their light condition was stronger (700-750 μmol photon m^{-2} s^{-1}). In other words, it is suggested that the phloem-loading capacity of the fed leaf was not saturated yet under the ambient CO_2 condition in our experiment.

The positron imaging method is based on detecting of collinear gamma rays caused by a positron-electron annihilation. However, an emitted positron from radioisotope travels a certain distance in / out of tissue before it undergoes annihilation. This phenomenon depends on the thickness of the tissue and biases the quantification of the tracer amount. In this study, ROI 1, 3, 5 and 7 were set onto nodes with almost the same thickness. Therefore, we think the bias was uniform and quantification of the leakage was sufficiently reliable. On the other hand, the result of mathematical estimation of average transit time is not affected by the

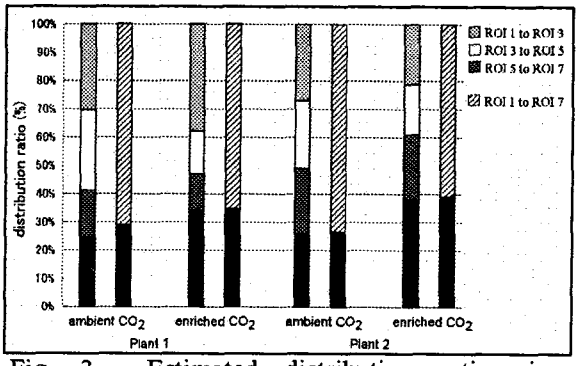

Fig. 3 Estimated distribution ratios in internodes expressed as percentages. Left columns: Distribution ratios estimated for the three respective internodes (ROIs 1-3, 3-5 and 5-7). Right columns: distribution ratios estimated for the total interval (ROI 1-7). The black filled portions show the residuals.

unequal tracer sensitivity[7]. This feature is one of the best merits of the transfer function analysis, and it ensures validity of our estimation of the average transit times and the average flow speeds between ROIs on nodes and internodes.

Here we demonstrated that the combination of PETIS and quantitative modeling has great advantages. The same region of the same individual can be observed with PETIS again and again after decay, and differences of concentrations of fed RI or unequal tracer sensitivity can be cancelled by the modeling analysis. These features enable quantitative discussion of physiological changes in each individual.

References

1) Kume T, et. al., 1997: *Appl. Radiat. Isot.*, **48**, 1035-1043
2) Ishioka NS, et. al., 1999: *J. Radioanal. Nucl. Chem.*, **239**, 417-421
3) Uchida H, et. al., 2004: *Nucl. Instrum. Meth. A*, **516**, 564-574
4) Keutgen N, et. al., 2002: *Appl. Radiat. Isotopes*, **57**, 225-233
5) Minchin PEH, et. al., 1987: *J. Exp. Bot.*, **38**, 211-220
6) Grimmer C, et. al., 1999: *Planta*, **209**, 275-281
7) Minchin PEH, et. al., 1980: *Ann. Rev. Plant Physiol.*, **31**, 191-215

2.38 Estimation of nitrate absorption and translocation in NADH-NR deficient mutant Az12

N. Ohtake*, S. Ito*, A. Yamazaki*, R. Salwa*, T. Ohyama*, K. Sueyoshi*,
K. Sakamoto**, S. Fujimaki**, N. S. Ishioka**, S. Watanabe**,
Y. Kawachi**, N. Suzui**, S. Ishii**, S. Matsuhashi**
Faculty of Agriculture, Niigata University*
Department of Ion-Beam-Applied Biology, JAERI**

1. Introduction

The biochemical, genetic and molecular characterization of higher plant NRs has advanced a great deal in the past decade, however barley is the only crop species where all of these aspects of NR have been characterized in detail. Barley has two NR isozymes; one is the NADH-specific NR (NADH-NR) and the other is the NAD(P)H-bispecific NR (NAD(P)H-NR). Both enzymes are nitrate-inducible and expressed in the roots, but only NADH-NR reaction in the pathway of N assimilation. In whole plants, NADH-NR is responsible for 80 to 90% of the overall *in vitro* NR activity, while the activity of NAD(P)H-NR accounts for the remaining 10 to 20% (Warner and Huffaker 1989).

NADH-NR deficient mutant Az12 was selected from Steptoe by EMS treatment. In the absence of nitrate, neither NADH nor NADPH-dependent NR activities were detected in root and leaf extracts of either the wild type, Steptoe, or the mutant, Az12. In NADH-NR deficient mutant Az12, NAD(P)H-NR activity is detected in leaves as well as in roots, while only the NADH-NR is detected in Steptoe leaves. It is deficient in NADH-NR in leaves as well as roots.

However, Az12 appears to be sufficient to permit essentially normal growth, same as Steptoe, under field conditions and accumulation of the same amount of biomass as in the case of the wild type. This may be result from the remaining NAD(P)H-NR permits normal growth (Savidov et al., 1997; Oh et al., 1980).

To determine the effect of NADH-specific NR deficiency on *in vivo* nitrate absorption, transport from root to shoot and accumulation, ^{13}N-labeled nitrate that able to high-precision and highly time-resolved measurements was supplied to the root of Az12 and Steptoe then monitoring by PETIS.

2. Experiments

Radiotracer synthesis

The radiotracer ^{13}N (half-life = 9.96 min) was produced in AVF cyclotron TIARA (Takasaki Ion accelerators for Advanced radiation Application) at the Takasaki Radiation Chemistry Research Establishment, Japan Atomic Energy Research Institute by proton irradiation of water. This procedure produces mostly $^{13}NO_3^-$ with high radiochemical purity. The irradiated solutions were supplied in sealed 20 mL glass vials.

Feeding procedure

The seedlings were incubated with 2.3 mM KNO_3^-, one seedling was selected and transferred to a feeding container that

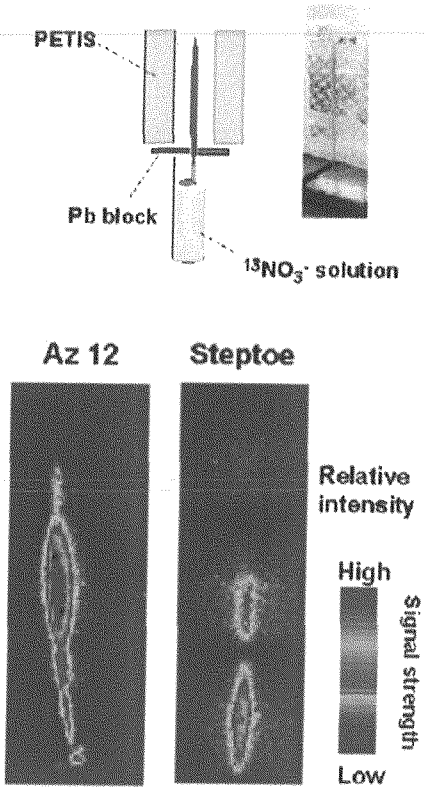

Fig.1 Imaging of radioactivity in barley shoot supplied with $^{13}NO_3^-$ for 40 minutes

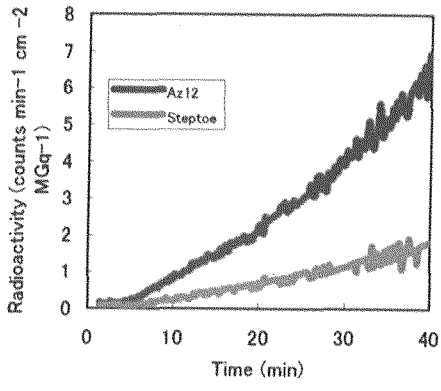

Fig. 2 The count of radioactivity in barley shoot supplied with $^{13}NO_3^-$ after 40 minutes.

contained 8 mL of pretreatment solution. Subsequently, 100 μL of 2.3 mM KNO_3^- and 2 mL of $^{13}NO_3^-$ solution (113 MBq) were immediately added.

Nitrate labeled with ^{13}N (a positron emitter with a half-life of 10 min) was produced from $^{16}O(p, \alpha)^{13}N$ reaction, bombarding 6 ml of target water with 1 μA of 20 MeV H^+ particles from the AVF cyclotron of Takasaki Ion Accelerators for Advanced Radiation Application.

The solution of $^{13}NO_3^-$ was purified by passing it through a cation exchange column and a basic alumina column as described previously. The ^{13}N accumulation in shoots was monitored using PETIS every minute after the addition of $^{13}NO_3^-$ to the medium for 30 min .

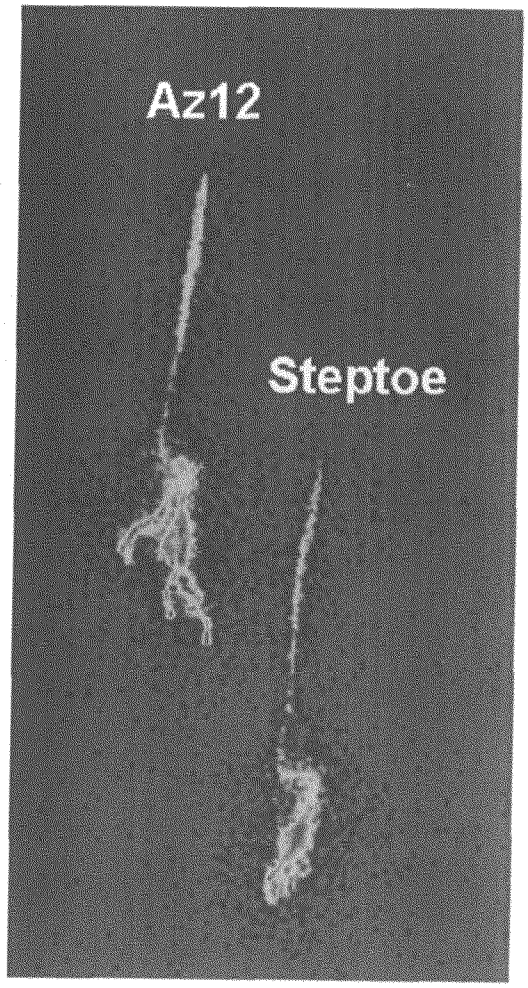

Fig.3 Imaging of radioactivity in whole plants two barley genotupes using Bioimaging Analyzer System (BAS).

After the measurements by PETIS, barley roots were rinsed three times, for 1 min in three successive 100 mL of de-ionized water. Then, plant roots were wiped with paper towels to remove excess water. The accumulation of ^{13}N in the whole plant was visualized using Bioimaging Analyzer System (BAS; BAS1500, FujiFilm, Tokyo, Japan).

3. Results and Discussion

The imaging pictures of ^{13}N radioactivity were monitored after $^{13}NO_3^-$ was supplied to barley seedlings in the medium in the presence of 2.3 mM KNO_3^-(Fig. 1). PETIS images show high ^{13}N absorption in Az12 than in Steptoe. Also the radioactivity count for 40 min after the addition of $^{13}NO_3^-$ in the Az12 and Steptoe was increased over time after a lag of several minutes (Fig. 2).

The count of radioactivity of Az12 shoots was higher than that of Steptoe and BAS images showed that ^{13}N-labeled was stronger in the whole seedling of the Az12 than in Steptoe (Fig. 3). In conclusion, roots are important and responsible for nitrate uptake, reduction and accumulation particularly in Az12 to sustain growth in a similar pattern as Steptoe.

2.39 ^{11}C Translocation under Salinity Condition

R. Suwa*, S. Fujimaki**, N. Kawachi**, K. Sakamoto**, S. Ishii**, N. Suzui**, S. Matuhashi** and K. Fujita*.
Guladuate School of Biosphere Science Hiroshima University*
Department of Ion-beam-applied Biology, JAERI**

Introduction

Salinity stress affects assimilate partitioning between source and sink organs, however its effect on the supply of assimilates of source organs and demand of sink organs are less understood. Relationship between source and sink organs being closely knitted, adverse effect of sub-optimal condition on one organ is misinterpreted for the other. Lack of knowledge on the regulation of carbon partitioning negates efforts for improvement of stress resistance. The objective of this study was to reveal the effect of salinity to translocation of photoassimilates by monitoring the translocation of the radioisotope in the stem segments adjacent to the basal and apical sides of the petiole of the fed leaf. We examined alteration of carbon partitioning in tomato plant (*Lycopersicon esculentum* L. cv. Momotarou) under saline (NaCl) environment using PETIS and $^{11}CO_2$.

MATERIALS AND METHODS

Experimental plants were exposed to the control (0 mM NaCl) or salinity (150 mM NaCl) treatment. The experiment was repeated twice. Both the control and saline treated plants were fed with $^{11}CO_2$ according to time schedule given in Fig. 1.

$^{11}CO^2$ was produced in the $^{14}N(p,\alpha)^{11}C$ reaction by bombarding N_2 gas with a 20 MeV proton beam from TIARA-AVF cyclotron using a beam current of 2 pμA for 2 min. Approximately 50 MBq of $^{11}CO_2$ was produced. Each plant was fixed in the middle between a pair of PETIS detectors. They were kept in dark for 2 h before feeding. $^{11}CO_2$ was fed to the 5th matured leaf for 2 min under a light source of 150 μmol m^{-2} s^{-1}. γ-Ray emitted from ^{11}C-labeled photoassimilates was continuously monitored by the PETIS for 2 h beginning at the start of feeding. The same plant was subjected to $^{11}CO_2$ feeding and monitoring for three times in a sequence. During the experiment using $^{11}CO_2$, a series of two-dimensional distribution of the ^{11}C-labeled photoassimilates (360 frames at twenty-second intervals) was monitored by PETIS.

RESULTS AND DISCUSSION

The translocation of the ^{11}C-labeled photoassimilates at the 4 regions of interests (ROI) were analyzed, two each in the upper and lower stem parts from the fed leaf petiole) in both control and salinity treatment conditions (Fig.2). Translocation of ^{11}C into the apical and basal sides of the fed leaf could be compared between control and saline-treated plants in a time course study. The time activity curves at the ROIs in control and NaCl plants were made. Fed ^{11}C pass through a ROI as a pulse shape and thereafter maintained. The equation mentioned below was adopted for measuring relative translocation rates (RSR) in the

upper (RSR_{up}) and lower parts (RSR_{low}) of the stem in both control and saline treated plants.

$$RSR_{upX} = \frac{A2_X / A1_X}{A2_1 / A1_1};$$

$$RSR_{lowX} = \frac{A4_X / A3_X}{A4_1 / A3_1}$$

(A is relative activity of γ -Ray recorded at ROI)

A1, A2, A3 and A4 are relative activity of γ -ray monitored at ROI 1, 2, 3 and 4, respectively. Each A value was mean of 20 frames, frame No. 321-340. This is because, after the pulse phase, relative activity of γ -ray was stable during this time period. The subscripts (x and 1) indicate feeding time.

The equation was adopted by the assumption described below.

(1) ^{11}C-labeled photoassimilates transfer through the phloem in the ROI depict as a pulse form.

(2) Because high flow rate shortens the time to pass the ROI, the ratio of ^{11}C- photoassimilates unloading from phloem will decrease compared with that of low flow rate.

(3) Because of unloading occurred at phloem, relative γ -ray activity at ROI in the lower part stem decreases compared with upper part. This together with (2) indicate that high flow late maintain a higher ratio of A_{low}/A_{up} compared with that of low flow rate.

Stable relative activity after pass the pulse from the fed leaf indicate maintained unloaded ^{11}C. The measurement of translocation rates indicated no significant discrimination in ^{11}C movement to the upper part of the stem during the imposition of salinity, but the rate was significantly reduced in the lower part of the stem (Fig 3). Therefore salinity stress affect assimilate partitioning between source and sink organs in spite of less source affection by salinity. Because these ^{11}C tracer experiments were conducted under dark condition except for feeding to separate transpiration factor. In addition, salinity did not affect photosynthetic activity during 7h from the initiation of salinity treatment (data not shown). The reduction in translocation towards the basal side of the plant occurred before any significant decrease of photosynthesis could be noticed in the saline treated plants. A stimulus from the saline treated root might be responsible for reduction of carbon assimilates translocation from the leaf. In concert with the reduction, stem shrinking occurred under dark condition (data not shown). Phloem shrinking was also expected under salinity condition. These results suggest that direct effects of salinity toxicity initially occur on impairment of phloem transport and consequential reduction of photosynthesis is induced.

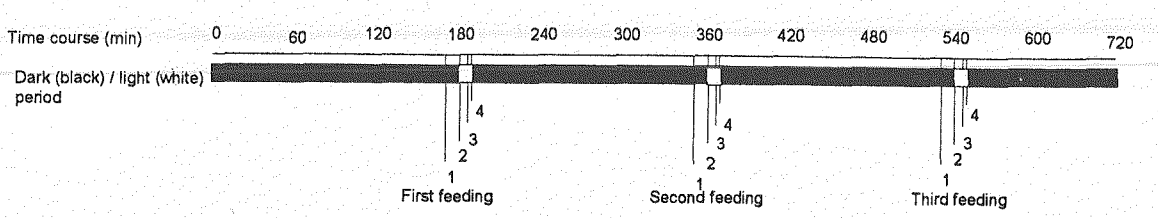

1: Treatment solutions were applied 15 min before each feeding. At the first feeding, the control treatment solution (0 mM NaCl) was applied to both control and salt-treated plants. At the second and third feeding 150 mM NaCl was applied to salt-treated plants

2: Switch on the light (150 μmol m^{-2} s^{-1}) 5 min before each feeding

3: Start ^{11}C feeding and PETIS monitoring. The ^{11}C feeding and mornitoring lasted 2 min and 2 hours, respectively

4: Stop ^{11}C feeding and and witch off the light

Fig. 1 Time schedule of experiment.
Sixty days old tomato plants were exposed to 0 or 150 mM NaCl mainly under dark condition. ^{11}C was fed to 5th leaf and its tranlocation was mornitor by PETIS

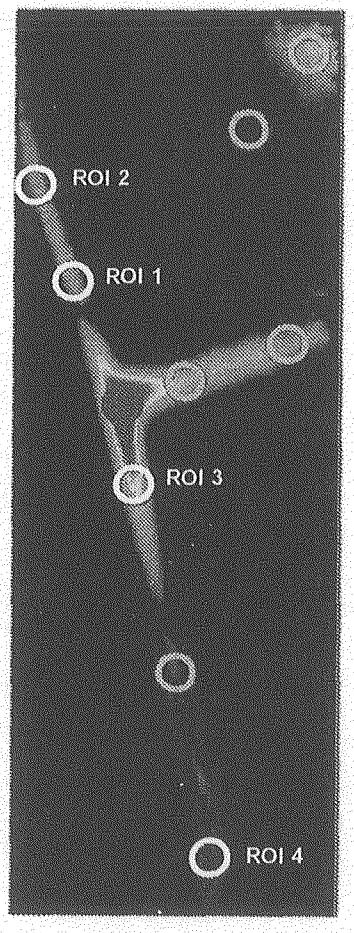

Fig. 2 The images made by integrated γ-Ray signal during translocation of ^{11}C in the phloem. ^{11}C was fed to the 5th leaf of 60 days old tomato plants treated with 0 or 150 mM NaCl. γ-Ray signal was monitored by PETIS system. The circles define the regions of interest (ROI), in which the data from four region (ROI 1-4) have been use to calculate translocation rates

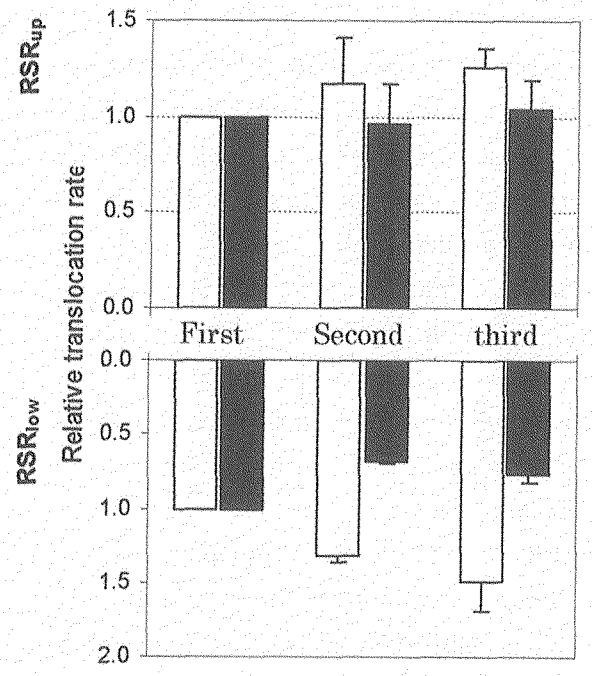

Fig. 3 Effects of salinity treatment on the relative translocation rate of ^{11}C in upper and lower stems in tomato. ^{11}C feedings were carried out sequentially three times in the same plant (Fig. 2). At the first feeding, both control and salt-treated plants were irrigated with soultion without NaCl. At the second and third feeding the salt-treated plants were irrigated with solution containing 150 mM NaCl. ^{11}C was fed to the 5th leaf for 2 min under light, and then plants was kept in dark. Three feedings were carried out sequentially in the same plant (Fig. 2). γ-Ray emitted from ^{11}C was continually monitored by PETIS for 2 hours (360 frames) at each feeding. The calculation of relative translocation rate (RSRup and RSRlow) for each feeding was describe in Materials and Methods. Values in the figure are mean and standard deviation of two replicates.

JP0650207

2.40 ^{62}Zn Absorption and Translocation in Rice using a Positron Emitting Tracer Imaging System (PETIS)

T. Tsukamoto*, H. Nakanishi**, M. Suzuki*, S. Watanabe***, S. Matsuhashi***, N. K. Nishizawa*, **** and S. Mori**
Department of Global Agricultural Sciences, The University of Tokyo*
Department of Applied Biological Chemistry, The University of Tokyo**
Department of Ion-beam-applied Biology, JAERI***
Core Research for Evolutional Science and Technology (CREST)****

1. Introduction

Zinc (Zn) is an essential element for living organisms, including higher plants. However, in many regions of the world, particularly those with calcareous soils, little Zn is present in the soil solution, which results in reduced plant growth. In plants, Zn deficiency causes extensive oxidative damage to membranes, lipids, proteins, chlorophyll, and nucleic acids. Many higher plants take up Zn from the rhizosphere *via* transporters. There are two hypotheses about Zn absorption. One is that Zn is absorbed as free Zn^{2+} ions from rhizosphere. Several Zn^{2+} transporter genes have been isolated from rice[1]. Another is that Zn is absorbed as a Zn(II)-mugineic acid family (MAs) complex. It is reported that the maize YS1, which is the Fe(III)-MAs transporter, also transports Zn(II)-MAs in yeast and *Xenopus* oocytes[2]. It is not clear which form, Zn^{2+} or Zn(II)-MAs, is effective for graminaceous plants to absorb Zn from rhizosphere.

We have already reported [^{11}C]Met, $^{13}NH_4^+$ and $H_2{}^{15}O$ translocation in plants[3)-8)]. In this study, we compared the real time ^{62}Zn translocation in intact rice plants under various conditions by a positron emitting tracer imaging system (PETIS).

2. Experimental procedure

2.1 Plant material

Rice (*Oriza sativa* L. cv. Nipponbare) seeds were germinated at room temperature (ca. 24°C) on paper towels soaked with distilled water. After germination, the plantlets were transferred to a plastic net floating on water in a growth chamber under a mixture of incandescent and fluorescent lamps with a 14 h light (30 °C)/10 h dark (25 °C) regime and a photon flux density of 320 μmol m^{-2} s^{-1}. After two days, the plants were transferred to modified Kasugai's medium: 1 mM $(NH_4)_2SO_4$, 0.3 mM KH_2PO_4, 0.7 mM K_2SO_4, 2.0 mM $CaCl_2$, 0.5 mM $MgSO_4$, 10 μM H_3BO_3, 0.5 μM $MnSO_4$, 0.2 μM $CuSO_4$, 0.5 μM $ZnSO_4$, 0.01 μM Na_2MoO_4, 0.1 mM Fe-EDTA. The pH was adjusted daily to 5.5 with 1 N HCl or 1 N NaOH, and the nutrient solution was renewed once a week. For Zn deficiency, the plants were transferred to the culture solution without Zn 12 days before the beginning of the experiments. The absorption experiments were performed about 4 weeks after germination.

2.2 Production of ^{62}Zn

^{62}Zn (half life: 9.186 h) was produced by the ^{63}Cu(p, 2n)^{62}Zn reaction by bombarding a 1 mm thick Cu foil (natural isotopic

composition, 99.9% purity, Nirako Ltd., Japan) with a 30 MeV proton beam from the TIARA (Takasaki Ion Accelerators for Advanced Radiation Application) AVF cyclotron[9]. Using a beam current of 1 μA for 30 min, about 50 MBq of ^{62}Zn was produced. The radiochemical separation of the ^{62}Zn from the target was carried out with a method described earlier[9]. After the pH of the $^{62}Zn^{2+}$ solution without cold carrier Zn was adjusted to about pH 4 with 1 M KOH, the $^{62}Zn^{2+}$ was chelated with 3.36 μmol of deoxymugineic acid (DMA) in the dark over 3 h.

2.3 Experimental setting up

Experiment 1: ^{62}Zn Translocation in Zn-deficient and Zn-sufficient rice

Zn-deficient and Zn-sufficient rice plants were supplied with 15 mL of culture solution without Zn in polyethylene bags. The plants and the bags were fixed between two acrylic boards and placed between a pair of PETIS detectors in a chamber at 30°C under 65% humidity and a light density of 320 μmol m^{-2} s^{-1}. $^{62}Zn^{2+}$ (20 MBq, 1.6 pmol) was added to each culture solution. Shoots were monitored by PETIS for 6 h.

Experiment 2: ^{62}Zn(II)-DMA or $^{62}Zn^{2+}$ Absorption in Zn-deficient rice

Two Zn-deficient rice plants were supplied with 15 mL of culture solution without Zn in different polyethylene bags. 1 mL solution with ^{62}Zn(II)-DMA (10.0 MBq, 0.8 pmol) and $^{62}Zn^{2+}$ (10.0 MBq, 0.8 pmol) was added to each culture solution. Shoots were monitored by PETIS for 6 h.

3. Results and discussion

Experiment 1:

In order to clarify the effect of nutritional Zn status on Zn absorption and translocation in intact plants, $^{62}Zn^{2+}$ was fed to roots of Zn-deficient and Zn-sufficient rice plants, and translocation of ^{62}Zn was monitored using PETIS method. After 6 h of absorption, ^{62}Zn translocation to shoots of Zn-deficient rice was higher than that of Zn-sufficient rice (Fig. 1). Especially, the leaf sheaths of both plants were strongly labeled. Zn-deficient rice accumulated approximately 2 times higher ^{62}Zn in the discrimination center (DC), the basal part of the shoots, compared to Zn-sufficient rice after 6 h of absorption (Fig. 2A). In shoots of Zn-deficient rice, the ^{62}Zn accumulation rate was gradually increased until about 4 h after supplying $^{62}Zn^{2+}$ and, rapidly increased after 4 h (Fig. 2B). On the other hand, ^{62}Zn was gradually increased during measuring time in Zn-sufficient rice. It was reported that *OsZIP1* and *OsZIP2*, which are Zn^{2+} transporter genes in rice, are expressed and induced in roots by Zn deficiency[1]. It is assumed that these transporter genes play an important role in Zn uptake in Zn-deficient rice.

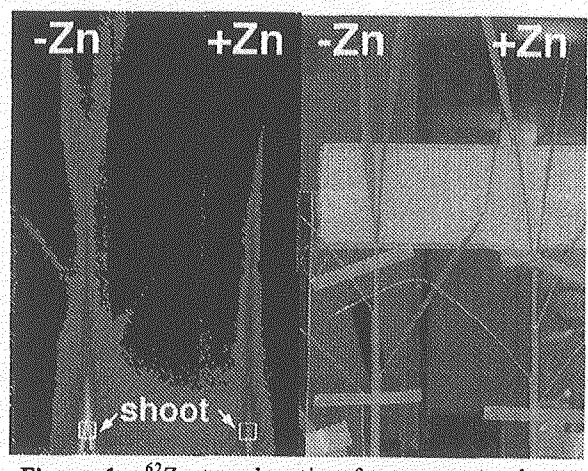

Figure 1 ^{62}Zn translocation from roots to shoots of Zn-deficient (-Zn) and Zn-sufficient (+Zn) rice. (Left) PETIS image. (Right) Gross image of plants.

Experiment 2:

In order to clarify the effect of DMA on Zn absorption and translocation, ^{62}Zn(II)-DMA or $^{62}Zn^{2+}$ was fed to roots of Zn-deficient rice. In shoots, about 0.7 times ^{62}Zn was accumulated to shoot when ^{62}Zn(II)-DMA was supplied to rice than when $^{62}Zn^{2+}$ ion was supplied (Fig. 3 and 4A). This suggests that Zn(II)-DMA is less effective to absorb Zn in rice than Zn^{2+} ion. In rice, *OsZIP* genes may play a more important role in Zn uptake than *YS1*-like genes. However, the time course of ^{62}Zn translocation in the youngest leaf showed distinct pattern from shoot (Fig. 4B). The radioactivity in the youngest leaf of ^{62}Zn(II)-DMA fed plant was equal to that of $^{62}Zn^{2+}$ fed plant till about 1 h, whereas it became higher after 1 h. This suggests that ^{62}Zn translocation in the youngest leaf was enhanced by supplying the form of ^{62}Zn(II)-DMA. In rice, endogenous MAs were found in leaves[10]. It is possible that DMA enhances Zn translocation in rice leaves.

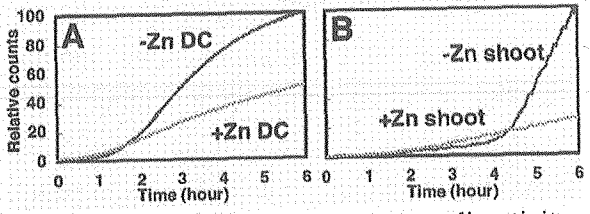

Figure 2 Time course for radioactivity accumulation in the DC (A) and the shoot (B; indicated as 'shoot' in Fig. 1) of Zn-deficient and Zn-sufficient rice.

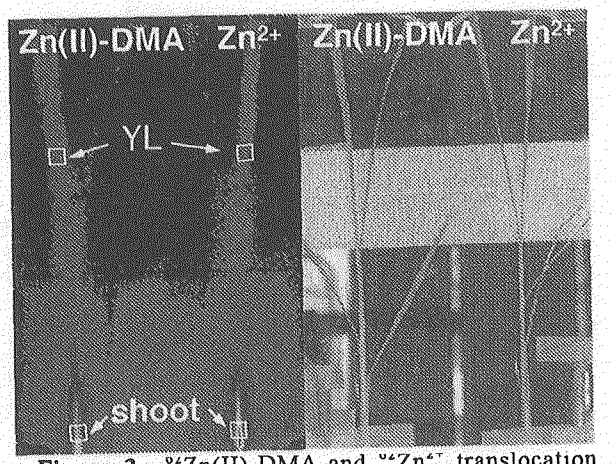

Figure 3 ^{62}Zn(II)-DMA and $^{62}Zn^{2+}$ translocation from roots to shoots of Zn-deficient rice. (Left) Accumulative PETIS image of ^{62}Zn after 6 h analysis. YL indicates youngest leaf. (Right) Gross image of plants.

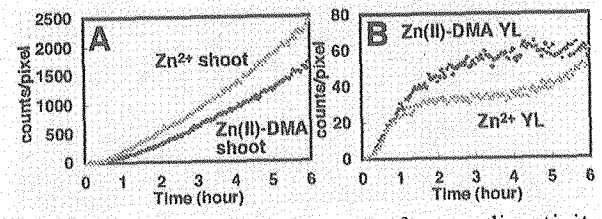

Figure 4 Time course for radioactivity accumulation in the shoot (A; indicated as 'shoot' in Fig. 3) and the youngest leaf (B; indicated as 'YL' in Fig. 3) of Zn-deficient rice.

References

1) SA. Ramesh et al., *Plant Physiol.* 133: 126-134 (2003)
2) G. Schaaf et al., *J. Biol. Chem.* 279: 9091-9096 (2004)
3) S. Kiyomiya et al., *Physiol. Plant.* 13: 359-367 (2001)
4) H. Nakanishi et al., *J. Exp. Bot.* 50: 637-643 (1999)
5) S. Kiyomiya et al., *Plant Physiol.* 125: 1743-1753 (2001)
6) S. Mori et al., *Soil Sci. Plant Nutr.* 46: 975-979 (2000)
7) H. Nakanishi et al., *Soil Sci. Plant Nutr.* 48: 759-762 (2002)
8) T. Tsukamoto et al., *Soil Sci. Plant Nutr.* 50: 1085-1088 (2004)
9) S. Watanabe et al., *Radiochim. Acta* 89: 853-858 (2001)
10) K. Higuchi et al., *Plant J.* 25: 159-167 (2001)

JP0650208

2.41 Visualization and Quantitative Analysis of Interception of the Translocating Nitrogen in the Host Plant by a Root Parasite

H. Sekimoto*, R. Matsuki*, K. Yoneyama*, Y. Ochiai*, K. Yoneyama**, Y. Takeuchi**, S. Matsuhashi***, S.Fujimaki***, K. Sakamoto***, N. Suzui***,S. Ishii***, N.S.Ishioka***, S. Watanabe***, N. Kawachi ***, K. Arakawa*** and T. Kume***

Faculty of Agriculture, Utsunomiya University *

Center for Research on Wild Plants, Utsunomiya University**

Department of Ion-beam-applied Biology, JAERI***

1. Introduction

Broomrapes (*Orobanche* spp), root holoparasites, can cause enormous damage before their scapes appear above ground, because their infestation occurs underground. As a consequence, efficient control is extremely difficult and infestation frequently results in a severe reduction of crop yields.

As known that nitrogen fertilizer application reduced the crop damage caused by these root parasites[1,2]. Ammonium has the toxicity or inhibitory effect. On the contrary, it is known that nitrate markedly promoted production and excretion of germination stimulants for root parasitic plants in the host roots[3].

To share the absorbed nitrogen with host plant would be one of strategy for survival of root parasites. Then, translocation of ^{13}N-nitrate or ^{13}N-ammonium in the root systems of red clover (*Trifolium pratense* L.) infected by broomrapes (*Orobanche minor* Sm.) was examined by a positron emitting tracer imaging system (PETIS).

2. Materials and methods

2.1 Plant material

To make root systems of red clover infected by broomrapes, broomrape seeds were sown in the soil mixed with vermiculite diagonally under from red clover seeds. Also they are put in red clover roots grown in water culture mediated by glass fiber. After 2 or 3 months, when broomrapes have infected enough and formed tubers, red clover plants with broomrapes were transplanted to the culture solution[4]. They were grown in a growth chamber (continuous light 350 μmol $m^{-2}s^{-1}$ at 23℃) for 5 days.

2.2 Experimental set up for $^{13}NO_3^-$ and $^{13}NH_4^+$ translocation in the plant root system

Red clover roots were used with or without a tuber of broomrape, and also divided into two bundles with or without a tuber of broomrape, and fixed between two acrylic boards and placed midway between a pair of PETIS detectors. The end of the roots which hanged out of the boards was soaked with 10 mL of the culture solution. About 150 MBq of ^{13}N-nitrate or ^{13}N-ammonium were added to the culture solution to feed them, and ^{13}N translocation in the root and shoot of host plant (red clover) and a broomrape tuber was monitored using PETIS for 90 min.

3. Results and discussions

It was observed that distribution ratio of ^{13}N originated from $^{13}NH_4^+$ in *Orobanche* to basal stem of host plant was higher than that from $^{13}NO_3^-$, implying that $^{13}NH_4^+$ would stagnate more than $^{13}NO_3^-$ in *Orobanche* (Fig. 1).

As shown in Table 2, stagnation rate of

$^{13}NO_3^-$ in *Orobanche* was estimated 73.6 % from the difference of radio activity between in input and output area of the root stuck by *Orobanche*, correcting the root volume by $^{18}F^-$ image(Fig. 2 and Table 1). For quantitative analysis of stagnation rate of absorbed nitrogen by host plant root in broomrapes, the correction of root volume by $^{18}F^-$ image analysis.

References

1) B.E. Abu-Irmaileh, Weed Sci. 42 (1994) 57-60
2) G.N. Dhanapal, P.C. Struik, M. Udayakumar and P.C.J.M. Timmermans, Agron. Crop. Sci. 176 (1996) 335-359.
3) K. Yoneyama, Y. Takeuchi amd T. Yokota, Physiol.Plant.112 (2001) 25-30.
4) T. Tadano and A. Tanaka, Jpn. J. Soil Sci. Plant Nutr. 51 (1980) 399-404

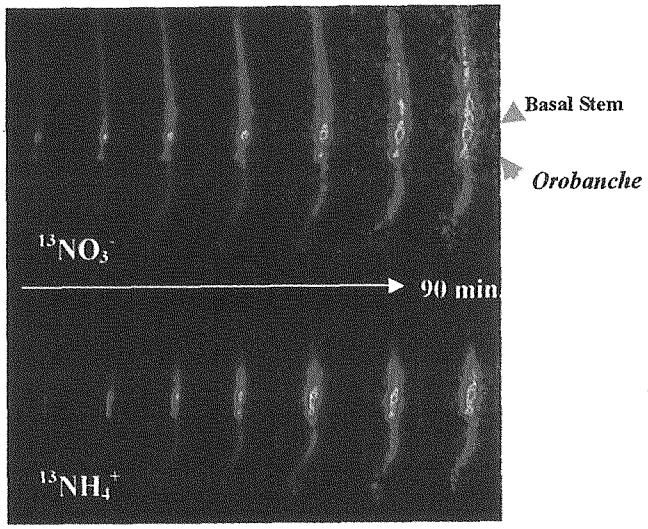

Fig. 1 Monitored points in the plant and the pattern of translocation of ^{13}N

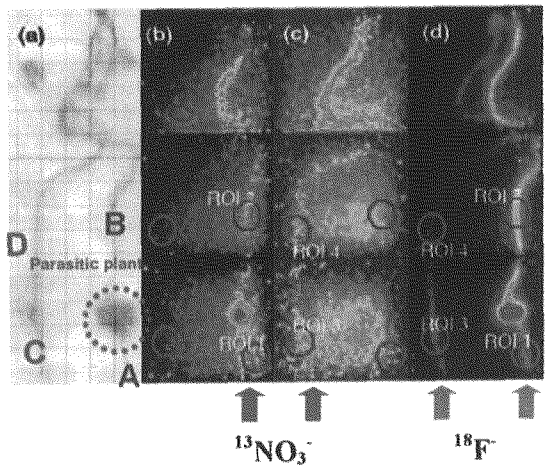

Fig. 2 Images of $^{13}NO_3^-$ and $^{18}F^-$

Table 1 Correction of root volume by $^{18}F^-$ images

	A	B	C	D
Counts	31182	88354	26285	15853
Rate	1	2.83	0.84	0.51

Table 2 Stagnation rate of $^{13}NO_3^-$ in *Orobanche* (%)

	Wituout *Orobanche*	With *Orobanche*
Before correction of root volume	38.6 ± 5.1	25.2 ± 11.0
After correction	-1.2 ± 8.5	73.6 ± 3.9

2.42 Transportation and Distribution of Photosynthetic Products in Hemp Visualized using the Positron-emitting Tracer Imaging System

K. Sakamoto*, S. Fujimaki*,**, N. Kawachi*, S. Ishii*, N. Suzui* and S. Matsuhashi*

Department of Ion-beam-applied Biology, JAERI*

Theoretical Analysis Group for Radiation Application, JAERI**

1. Introduction

Plants perform photosynthesis to produce organic matter in the form of sugar from carbon dioxide and water. The photosynthetic products produced in leaves (source) accumulate in various plant organs (sink) following transport through sieve tubes. The relationship between source and sink is influenced by the environment and growth stage of the plant. The photosynthetic products required for vegetative growth are transported mainly to the roots and stem, whereas those required for reproductive growth are transported to the fruits and seeds. It is thought that a drastic change in the transportation of carbon occurs during the transition from vegetative growth to reproductive growth. However, no studies have analyzed the translocation and distribution of photosynthetic products captured between vegetative and reproductive growth.

To analyze in real time the behavior of photosynthetic products in leaves at different growth stages, we used the positron-emitting tracer imaging system (PETIS). Hemp (*Cannabis sativa* L.) was used as the plant material because it grows very rapidly and can be induced to transition from vegetative growth to reproductive growth by short-day conditions. We report here the relationships between sink and source in several leaves at different growth stages during hemp vegetative growth.

2. Experimental procedures

2. 1 Plant material

Seeds of *C. sativa* L. var. *sativa* (CBDA) obtained from random crossbreeding of males and females of various strains were used for plant cultivation. Plants were grown at 25°C with 16 h of light and 8 h of darkness daily. Plants of about 30-50 cm in height were used in experiments.

2. 2 Production of $^{11}CO_2$ tracer

The gas-target system was used, as described by Ishioka *et al.* (1999) [1], to produce $^{11}CO_2$ by the $^{14}N(p,\alpha)^{11}C$ reaction of nitrogen (99.9999% purity, pressure under 5 kg/cm^2). Following irradiation, approximately 50-100 MBq of $^{11}CO_2$ were collected in a stainless-steel trap immersed in liquid nitrogen. The collected $^{11}CO_2$ was used in experiments on the translocation of photosynthetic products.

2. 3 PETIS measurements

The PETIS consists of two planar detectors, each of which is a $Bi_4Ge_3O_{12}$ scintillator array coupled to a position-sensitive photomultiplier tube. The two detectors, placed facing each other and flanking a plant, detect annihilation γ-rays that are emitted from the plant (Fig. 1). Although the detection area is limited to 19 x 21 cm, and the resolution in space to 2 mm, the great advantage of the system is that the plant being

analyzed is alive, since it can be fed, watered, and irradiated with light. Two-dimensional counting data are accumulated in real time and the data collected in computer memory.

2. 4 PETIS experimental procedures

Ambient air was conditioned in the chamber to 25°C and to a humidity level of 50 to 60%. The target hemp leaf was inserted into a "gas cell," a clear acrylic box with inside dimensions of 12 cm in length, 8 cm in width, and 1 cm in depth, to allow the feeding of gases. The light intensity was measured with a light meter and conditioned to approximately 250 μmol photons m^{-2} s^{-1} at the top of the stem. $^{11}CO_2$ was supplied to the second to fifth leaves of the same plant for 5 min, and then the $^{11}CO_2$ was drained off and substituted with ambient air lacking the radiotracer. The image frame was updated every 30 seconds, and 360 frames were collected over 3 hrs. Figure 1 shows a hemp plant being subjected to PETIS analysis, with the photo taken during $^{11}CO_2$ feeding.

3. Results and Discussion

PETIS measurements were taken from several hemp leaves at different growth stages during the vegetative growth stage. After the second expanded leaf was supplied with $^{11}CO_2$, the ^{11}C tracer was transported *via* the stem to the roots that supply the lower leaf (Fig. 2, bottom right). Supply of $^{11}CO_2$ to the third expanded leaf resulted in the ^{11}C tracer being distributed *via* the stem to the roots that supply the lower leaf, and *via* the stem to the shoot apex leaf (Fig. 2, bottom left). When $^{11}CO_2$ was supplied to the fourth (and largest) expanded leaf, the ^{11}C tracer accumulated rapidly in most parts of the growing stem below the leaf and at the shoot apex (Fig. 2, right). However, when $^{11}CO_2$ was supplied to the fifth expanded leaf, which was immature, no photosynthetic products were transported to the stem; they stopped, instead, at the end of the petiole (Fig. 2, left). It appears that the photosynthetic products that are produced in an immature leaf remain in the leaf for use in its own growth, and other organs do not receive photosynthate from this leaf. Similar results were obtained when two other sets of hemp plants with either four or six expanding leaves were used. These results suggest that the sink/source patterns are decided in each leaf during vegetative growth. We propose that hemp plants in the vegetative growth stage maintain the four sink/source patterns during growth.

This study revealed, for the first time, the transportation and distribution of photosynthetic products captured in real-time during vegetative growth in hemp. This study and further investigations into the behavior of photosynthetic products should contribute to the elucidation of the drastic transition from vegetative growth to reproductive growth.

Reference

1) N. S. Ishioka, H. Matsuoka, S. Watanabe, A. Osa, M. Koizumi, T. Kume, S. Matsuhasi, T. Fujimura, A. Tsuji, H. Uchida and T. Sekine, J. Radioanal. Nucl. Chem. 239(2): 417-421 (1999)

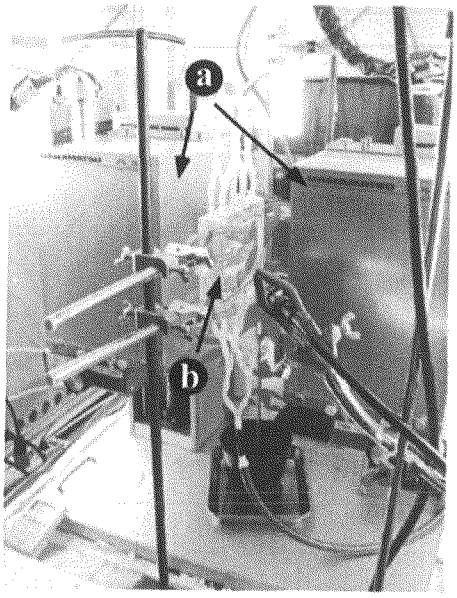

Fig. 1 PETIS experimental setup.
a: Pair of planar detectors.
b: $^{11}CO_2$ feeding cell.

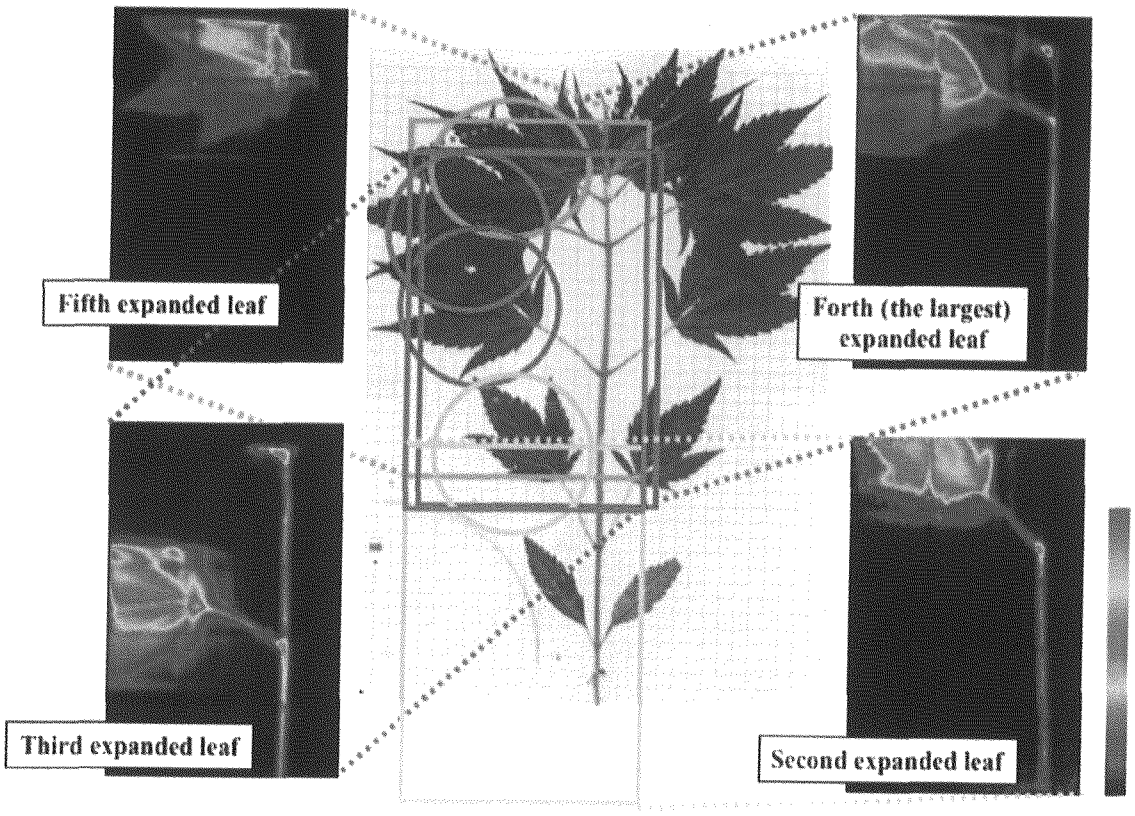

Fig. 2 A multiplication image and morphological features of a hemp plant during the supply of $^{11}CO_2$ to four expanded leaves. The yellow, orange, blue, and light blue circles indicate the fifth, fourth, third, and second expanded leaves supplied with $^{11}CO_2$, respectively. The yellow, orange, blue, and light blue boxes indicate the detection area (19 cm x 21 cm) used for each of the leaves, respectively. The gradient color bar indicates the RI strength, with red the strongest.

2.43 Real-time Imaging of Cadmium Transport in Intact Plant Bodies

S. Fujimaki*, S. Nakamura**, N. Suzui*, N. S. Ishioka*, M. Chino** and S. Matsuhashi*
Department of Ion-beam-applied Biology, JAERI*
Faculty of Bioresource Sciences, Akita Prefectural University**

1. Introduction

Presently, cadmium (Cd) pollution of soil and foods is serious problem in the world. In particular, it is an urgent need to reduce the pollution of rice in Japan. Repression of Cd transport in rice plants and decontamination of soil can be major measures against the problem. Recently, phytoremediation is drawing attention as a method for decontamination of soil. This method is to make plants to uptake Cd from the contaminated soil and to accumulate it in their aerial portion, and harvest the plants. Therefore, comprehension of dynamics of Cd transport in plant bodies will be a pivotal step to realize the two measures above described: the repression of Cd transport in rice plants and the phytoremediation.

In this study, we employed the Positron Emitting Tracer Imaging System (PETIS), and tried to visualize Cd transport in intact plants.

2. Experimental procedure

2.1 Plant materials

Rice (*Oryza sativa* L. cv. Nihonbare) and oilseed rape (*Brassica napus* L. cv. Nourin No. 16) were used. The oilseed rape is a model plant for phytoremediation. Rice plants had been grown in an incubator with a cycle of 14 h light at 30°C and 10 h dark at 25°C with modified Kimura B hydroponic solution. Oilseed rape plants had been grown in an incubator with a cycle of 18 h light at 25°C and 6 h dark at 20°C with modified Hoagland hydroponic solution. A 32 day-old rice plant and a 26 day-old oilseed rape plant were subjected to the imaging experiments reported here.

2.2 Production of tracer

^{107}Cd was produced in the ^{nat}Ag(p, n)^{107}Cd reaction by bombarding silver with a 20 MeV proton beam from the TIARA AVF cyclotron. ^{107}Cd was recovered as water solution through chemical purification. See "Production of positron-emitting cadmium tracer for plant study" by Ishioka *et al*[1] in this issue for more detailed procedures. Approximately 100 MBq of ^{107}Cd was applied to the hydroponic solution of the test plant without non-radioactive carrier Cd, to make total concentration of Cd Approximately 100 pmol L^{-1}.

2.3 PETIS experiments

Each test plant was carefully set in the PETIS apparatus to make its shoot and the base of root placed within the view-field. The surface of the hydroponic solution was below the bottom-end of the view.

The PETIS measurement was carried out by refreshing frames of image by every four minutes (rice) or 10 seconds to two minutes (oilseed rape), and continued for 24 (rice) or 37 (oilseed rape) hours. The atmospheric temperature around the plants was kept 30°C (rice) or 25°C (oilseed rape), and the light was kept on during the measurement.

3. Results and Discussion

We successfully captured movie images of Cd transport in the rice plant and the oilseed rape plant.

In the rice plant, ^{107}Cd signal was dominantly accumulated in the base of the leaf sheaths (Fig. 1). It is known that the emerging shoot bud and the very short stem are localized in this region referred as to "discrimination center (D.C.)". There was also notable signal on a newly emerged root and the old dry coleoptile. It possibly shows phloem transport of Cd from the D.C. in the former case. The latter case would show the capillary phenomenon and simple evaporation. In contrast, the upper shoot, *i.e.* leaf sheath and leaf blade, had little signal of ^{107}Cd. Similar images have been obtained from six individuals in total. These results suggest that D.C. repress Cd transport in xylem toward the upper shoot.

In the oilseed rape plant, intense signal appeared on the root first, and then remarkable signal was accumulated in the thick-grown hypocotyl (Fig. 2). Subsequently, a little signal was shown to move to the shoot bud, petioles, and leaf blades.

We extracted time-activity curves, *i.e.* time courses of radioactivity, from regions of plant organs on the image data. We analyzed these time-activity curves to estimate models describing the dynamics of Cd transport between the organs in the plant bodies. Figure 3 shows time-activity curves of the root and hypocotyl of the oilseed rape plant. In general, it should be noted that when some activity is detected on a plant organ, the activity consists of two components, one is derived from fixed tracer in the tissue, and the other is from mobile tracer in the vascular bundles. If the unloading rate of Cd from a vascular bundle to the surrounding tissue is proportional to the Cd concentration in the vascular bundle, the rate of change of the fixed component is proportional to the mobile component. The bars in Fig. 3 show the rate of change of the time-activity curve of the hypocotyl. The shape was very similar to that of the time-activity curve of the root. This result suggests that the activity of the hypocotyl mainly consisted of the fixed component, and contrary, that of the root mainly consisted of the mobile one. This leads a model that the unloading of Cd from xylem vessel to the surrounding tissue is weak in root and strong in thick-grown hypocotyl in an oilseed rape plant.

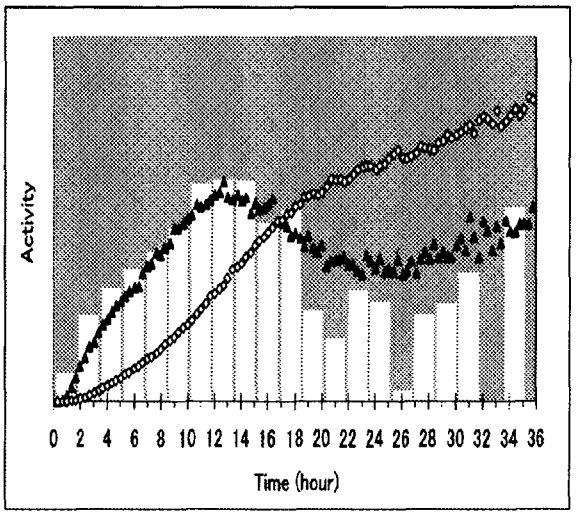

Fig. 3 Shapes of time-activity curves extracted from PETIS data. ▲: root, ◇: hypocotyl. The white bars indicate the rate of change of the time-activity curve of hypocotyl.

Reference

1) N. S. Ishioka, S. Fujimaki, N. Suzui, S. Watanabe and S. Matsuhashi, TIARA Annual Report (2005), this issue.

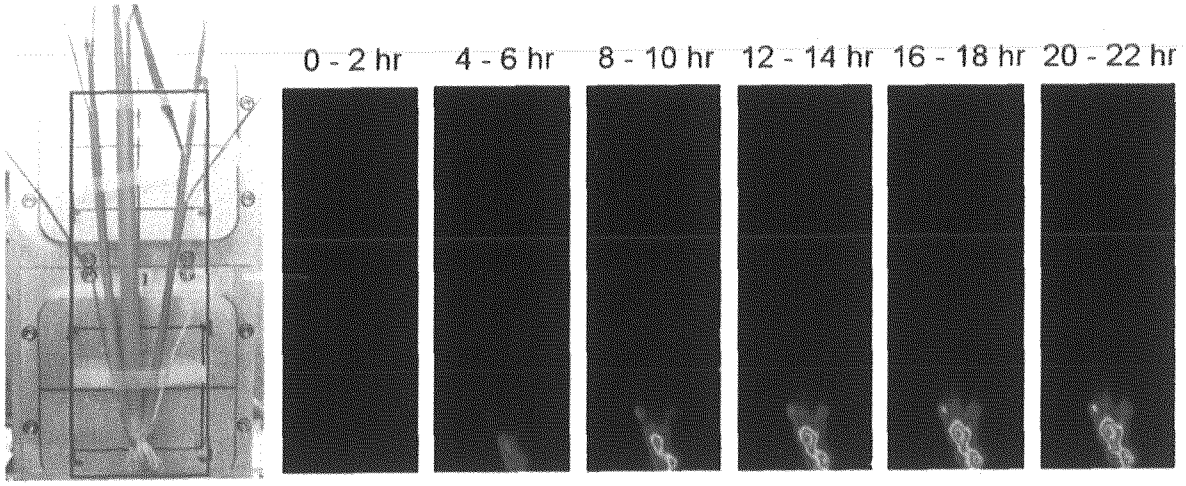

Fig. 1 The test rice plant (left). Red square indicates the view-field of PETIS. Serial images of ^{107}Cd transport (right). Each image was integration of 60 serial images obtained every two minutes by PETIS.

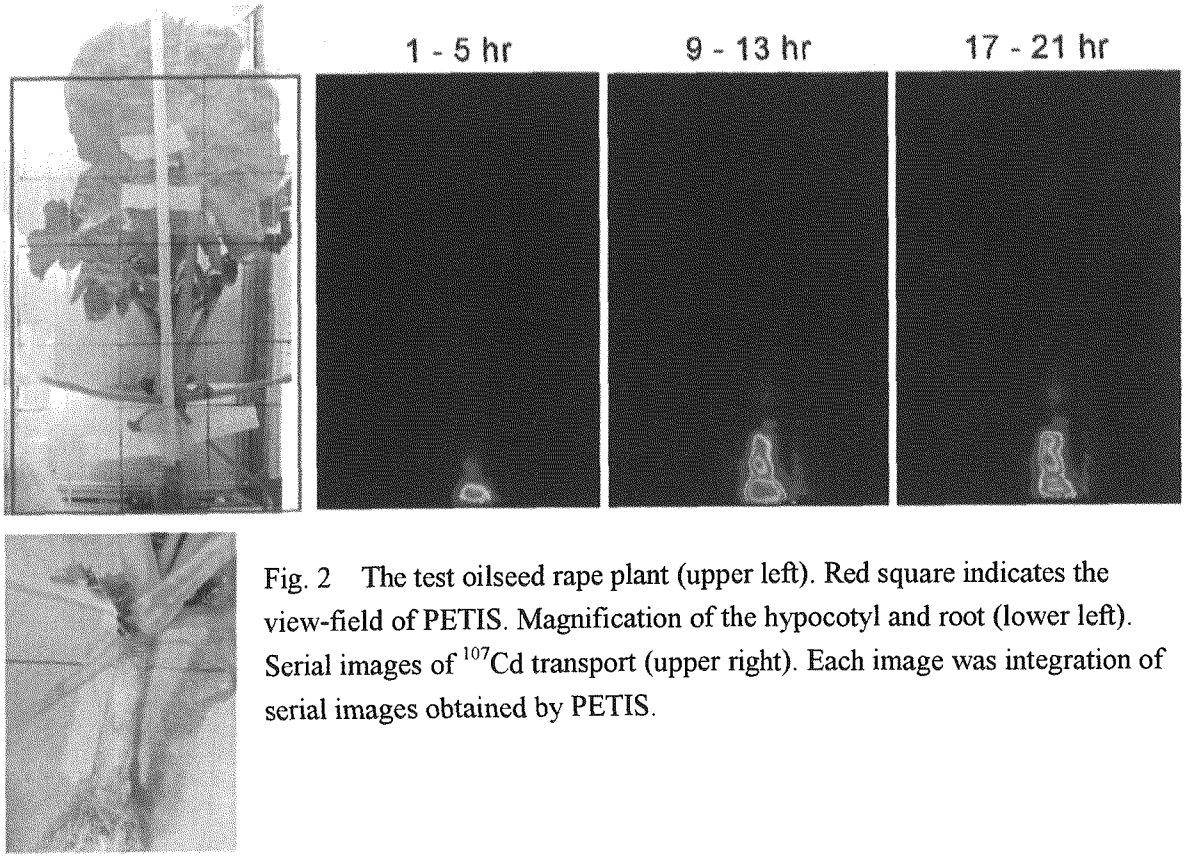

Fig. 2 The test oilseed rape plant (upper left). Red square indicates the view-field of PETIS. Magnification of the hypocotyl and root (lower left). Serial images of ^{107}Cd transport (upper right). Each image was integration of serial images obtained by PETIS.

2.44 PETIS Analysis of ^{13}N-nitrate in Transgenic Rice Plant Over-expressing Nitrate Transporter

D. Sato*, M. Mori*, H. Kitamura*, N. Suzui**, S. Fujimaki**, S. Matsuhashi**, T. Tanaka***, T. Tsukamoto****, N. K. Nishizawa**** and M. Mori*****
Advanced Technology Development Division, Shiga Prefecture Agricultural Technology and Promotion Center*
Department of Ion-beam-applied Biology, JAERI**
Nagasaki Agricultural and Forest Experiment Station***
Department of Applied Biological Chemistry, The University of Tokyo****
Research Institute of Agricultural Resources, Ishikawa Agricultural College*****

1. Introduction

Nitrogen is the most important nutrient for growth in higher plants[1]. Therefore, the uptake and assimilation of nitrogen is a major limiting factor in crop production. However, the excessive fertilizers applied to the farming fields cause water pollution. An improvement in the nitrogen utilization ability of crops reduces the pollution in the crop production. Nitrate uptake is a highly regulated multi-component process[2] and classified into low- and high-affinity transport systems[3] in term of affinity.

Our aim is to improve the rice plants that maintain high productivity under a low input of nitrogen fertilizers. In our previous study, we constructed a transgenic rice plant over-expressing the *OsNRT2* gene (NRT2 rice plant), coding a high-affinity nitrate ion transporter involved in the uptake of nitrate by the rice plant root. The molecular-based analysis of the gene function is in progress.

PETIS (Positron-Emitting Tracer Imaging System) of the JAERI is capable of real time visualization of ^{13}N-translocation in intact plants[4].

In this study, we aim to clarify the functions of the *OsNRT2* gene and visualize the translocation of $^{13}NO_3^-$ in the NRT2 rice plant by using PETIS.

2. Materials and Methods

Seeds of wild type (WT) rice (cv. Yumeoumi) and transgenic rice were germinated on a paper towel. The seedlings of rice were grown hydroponically (1/2 Kimura B medium) in an incubator (light/dark, 16 h/8 h, 30°C/25°C, 250 μmol m^{-2} s^{-1}) for 10 days. The culture medium was replaced by the tracer media containing $^{13}NO_3^-$ (1.5–3.0 MBq mL^{-1}), which is produced by using the TIARA AVF cyclotron. The $^{13}NO_3^-$ absorbed by the third leaf stage rice plants was measured using PETIS for 1 h. In addition, the rice plants were set in BAS 1500 imaging system, and the autoradiographs were obtained. The total amount of $^{13}NO_3^-$ absorbed by the NRT2 rice plant and the WT rice plant was compared.

3. Results and Discussion

The region of interest, that is, the aerial part of each rice plant of the PETIS data was collected for, and the relative count (count/pixel/root) of WT and NRT2 rice plants over 60 min was plotted (Fig. 1). Figure 1 shows that $^{13}NO_3^-$ uptake of NRT was more than that of WT in all detection time. To confirm this, the velocity of the $^{13}NO_3^-$ uptake of 5–15 min by NRT2 rice

plants was compared with WT rice plants (increment of count/min). The velocity of $^{13}NO_3^-$ absorption of the NRT2 rice plant (count/10 min/ root) was more than that of WT rice plant in the three independent experiments (Fig. 2).

The plant bodies after PETIS analysis were set in BAS 1500 imaging system, and the autoradiographs were obtained. The threshold was set to 20% of the highest count of the autoradiographs (Fig. 3). The count value of the autoradiograph standardized by dry weight of root was integrated and compared between the WT rice plant and NRT2 rice plant. The NRT2 rice plant had absorbed larger amount of $^{13}NO_3^-$ than the WT rice plant. Similar results were obtained with both the three-leaf stage and five-leaf stage rice plants. These data suggest that the NRT2 rice plants have an improved nitrate uptake ability.

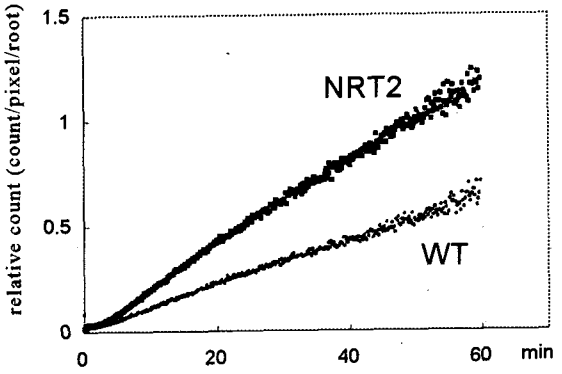

Fig. 1 PETIS analysis of $^{13}NO_3^-$ uptake into NRT2 and WT rice plants.
The region of interest, that is, the aerial part of each rice plant of the PETIS data was set, and the relative count (count/pixel/root) of 60 min was plotted.

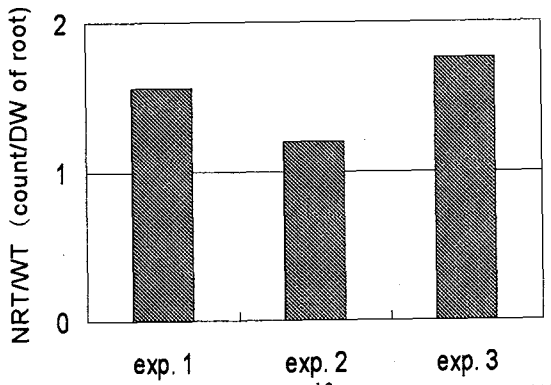

Fig. 2 Comparison of $^{13}NO_3^-$ uptake ability between NRT2 and WT rice plants.
The bar indicates a value that is dividing the increment of NRT by the increment of WT in 5-15 min.

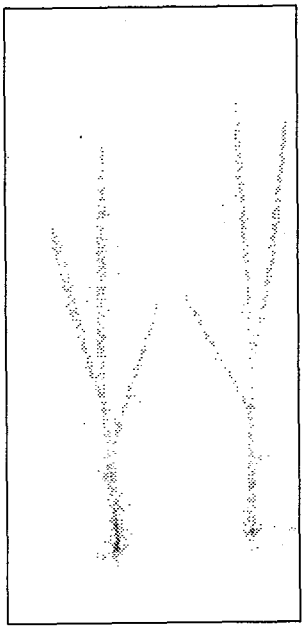

Fig. 3 Autoradiograph of NRT2 and WT rice plants.
The threshold was set to 20% of the highest count of the autoradiographs and a value less than this was considered to be noise. The count of each plant was integrated and compared.

References

1) B. G. Forde, Biochimica et Biophysica Acta 1465 (2000) 219–236.
2) A. Krapp, V. Fraisier, W-R. Scheible, A. Quesada, A. Gojon, M. Stitt, M. Caboche, F. Daniel-Vedele, The Plant Journal 13 (1998) 723–732.
3) M. Orsel, S. Filleur, V. Fraisier, F. Daniel-Vedele, Journal of Experimental Botany 53 (2002) 825–833.
4) S. Kiyomiya, H. Nakanishi, H. Uchida, A. Tsuji, S. Nishiyama, M. Futatsubashi, H. Tsukada, N. S. Ishioka, S. Watanabe, T. Ito, C. Mizuniwa, A. Osa, S. Matsuhashi, S. Hashimoto, T. Sekine, S. Mori, Plant Physiology 125 (2001) 1743–1753.

JP0650212

2.45 Imaging Analysis of the Mechanisms of Low Dose Radiation-induced DNA Double-strand Break Repair

M. Tomita*, T. Funayama**, S. Wada**, Y. Kobayashi** and T. Sakashita**
Cyclotron Center, The Institute of Physical and Chemical Research (RIKEN)*
Department of Ion-beam-applied Biology, JAERI**

1. Introduction

DNA double-strand breaks (DSBs) are the most serious form of DNA damage induced by ionizing radiation. If not repaired efficiently, DSBs cause cell death, chromosome translocation and genomic instability.

In mammalian cells, there are two major DSB repair pathways, namely, homologous recombination (HR) and non homologous end-joining (NHEJ). NBS1, ATM and histone H2AX are essential for DSB repair by HR and for cell cycle checkpoints. These proteins are phosphorylated after irradiation and forms nuclear foci in the vicinity of DSBs. We previously reported that NBS1 and γ-H2AX (phosphorylated histone H2AX at Ser139) form highly localized large foci after high LET iron-ion exposure, which cannot be observed after 5 Gy of X-irradiation[1]. Large foci of these proteins are remained even 16 h after irradiation. These results may suggest that a single heavy particle can induce even complex clustered DNA damages[2]. Thus, it is very important to estimate not only the radiation dose but the distribution of DNA damages in the irradiated cells.

To elucidate the DSBs induced by low dose of high LET heavy ions, we examined the foci formation of HR-related proteins induced by high LET heavy ion microbeam irradiation using immunofluorescence.

2. Experimental procedure

2.1 Cells

Human cervical carcinoma HeLa cells were cultured in a DMEM and Ham's nutrient mixture F12 medium (DME-F12 medium, Sigma) supplemented with 10% FBS. The exponentially growing cells (3000 cells) were cultured on CR-39 plate in 50 μl of medium 8 h before irradiation as previously reported[3].

2.2 Heavy ion irradiation

Just before irradiation, medium was removed, and the cells were covered with a polyimide (Kapton) film[3]. Irradiation of 11.5 MeV/u $^{40}Ar^{13+}$ microbeam was performed at TIARA JAERI-Takasaki[4]. Irradiation was performed at room temperature. Just after irradiation, 200 μl of fresh medium was added and cells were incubated for the times indicated.

2.3 Antibodies

Mouse monoclonal anti-phospho-ATM (Ser1981) antibody was purchased from Cell Signaling Technology. The rabbit polyclonal anti-NBS1 antibody was purchased from Oncogene Research Products. The mouse monoclonal anti-phospho-SMC1 (Ser957) and anti-phospho-histone H2AX (Ser139) antibodies were purchased from Upstate Biotechnology.

2.4 Immunofluorescence

Cells were washed with PBS(-) three

times, fixed with 4% paraformaldehyde-PBS(-) for 30 min and permeabilized with 0.1% Triton X-100 in PBS(-) for 10 min. Cells were blocked with 10% bovine serum albumin and were incubated in primary antibodies overnight at 4°C. Alexa 488 or 546 conjugated anti-rabbit or anti-mouse IgG (Molecular Probes) were used as secondary antibodies. The CR-39 was mounted with 90% glycerol and its backside was etched with an alkaline-ethanol solution[3]. The image of fluorescence and etched pits were obtained using fluorescence microscope.

3. Results and Discussion

Figure 1 (A) shows the Ar-ion-induced focus formation of γ-H2AX assessed by immunofluorescence in HeLa cells and an etched pit on CR-39. Cells were fixed 30 min after irradiation. Single γ-H2AX focus almost coincided with single etched pit, suggesting that single Ar ion can induce single damaged DNA region. We also detected the foci formation of NBS1, phosphorylated ATM (Ser1981) and phosphorylated SMC1 (Ser957) after exposure to Ar-ion microbeam (data not shown).

We next observed the kinetics of γ-H2AX foci after exposure to Ar-ion microbeam (Fig. 1B). At 5 min after exposure to Ar ions, γ-H2AX formed nuclear foci and the size of foci was larger at 3-8 h. The number of foci per cell was not decreased even 8 h after irradiation. On the other hand, X-ray-induced γ-H2AX foci were almost disappeared within 8 h (data not shown).

A series of results obtained suggests that single accelerated heavy ion can induce complex clustered DNA damage, which were difficult to repair efficiently, along the track.

Acknowledgement

The present study is supported by the REIMEI Research Resources of JAERI.

References

1) M. Tomita, T. Tsukada, N. Fukunishi, F. Yatagai, RIKEN Accel. Prog. Rep. 36 (2003) 133.
2) D.T. Goodhead, J. Radiat. Res. 40 (1999) 1-13.
3) T. Funayama, S. Wada, T. Sakashita, Y. Kobayashi, JAERI Review 2004-025, TIARA Annual Report 2003 (2004) 82-84.
4) Y. Kobayashi, T. Funayama, S. Wada, M. Taguchi, H. Watanabe, Nucl. Instr. and Meth. in Phys. Res. B 210 (2003) 308-311.

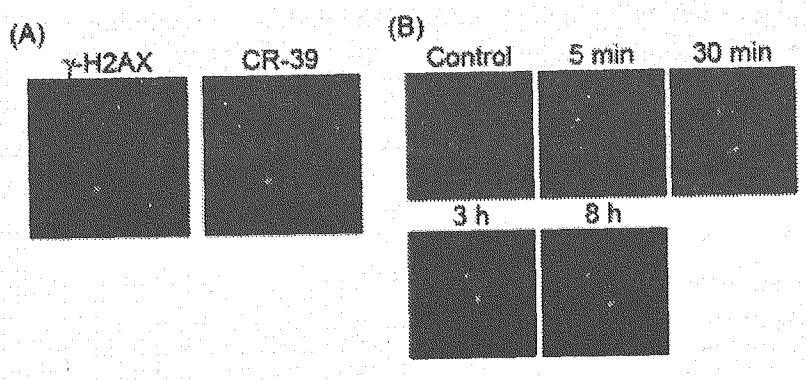

Fig. 1 Formation of γ-H2AX foci induced by Ar-ion microbeam. (A) γ-H2AX foci and an etched pit 30 min after irradiation. (B) Kinetics of γ-H2AX foci.

2.46 Analyses on Effects of Irradiation with Heavy Ions on Cellular and Viral Genes

H. Hoshino*, A. Tanaka*, M. Shinagawa*, N. Shimizu*, Saha M. Narayan*, T. Ohtsuki*, A. Oue*, Hoque Sk. Ariful*, A. Shimizu**, O. Ishikawa**, S. Wada***, T. Funayama*** and Y. Kobayashi***

Department of Virology and Preventive Medicine*, and Department of Dermatology**, Gunma University Graduate School of Medicine

Department of Ion-beam-applied Biology, JAERI***

1. Introduction

Human T-cell leukemia virus type I (HTLV-I) is the causative agent of adult T-cell leukemia (ATL) and HTLV-I-associated myelopathy (HAM). Human immunodeficiency virus (HIV) causes acquired immunodeficiency syndrome (AIDS). The purposes of this study, which will especially use the heavy-ion beam irradiation facility of JAERI-Takasaki, are to clarify the entry mechanisms of human retroviruses such as HTLV-I or HIV into cells and to clarify effects of heavy-ion beam irradiation on retrovirus-related genes such as long-interspersed repetive element 1(LINE1).

2. Experimental procedures

As heavy ions, He, C, or Ne ion was used, while ultraviolet (UV), X-ray or γ -ray, or physicochemical environmental factors (stress) as controls. We analyzed HIV-1 and HTLV-I as viruses, and LINE1 as a gene related to retrovirus. As target cells of vurus infection, human cell lines, K562, C8166 and NP-2/CD4/CCR5, were used. K562 cells are derived from chronic myelogenous leukemia and C8166 cells are from cord blood T-cells latently infected with and transformed by HTLV-I. NP-2/CD4/CCR5 is a glioma cell line transuded with human CD4 and CCR5. The susceptibilities of irradiated target cells to HTLV-I was determined by infecting vesicular stomatitis virus (VSV) pseudotype bearing HTLV-I envelope. As VSV, a chimeric VSV strain, VSV△G*, bearing the green-fluorescent protein (GFP) gene instead of VSV G envelope protein was used. As for HIV-1 infection, HIV-1 antigen-positive cells were detected by indirect immunofluorescene (IFA).

As for LINE1, LINE1 gene was cloned from genomic human DNA. GFP gene was introduced into sites downstream to the ORF2 of this LINE1 gene in the normal orientation, and reverse orientation. The former construct of LINE1 vector (LIGFP) was used to quantitative detection of LINE1 expression while the latter (LIrGFP) was used to detect the LINE1 gene retro-transposed in the genomes of the target cells.

3. Results and Discussion

3.1 Effects of heavy-ion beam irradiation on HTLV-I infection

C8166 and K562 cells are highly sensitive and relatively resistant to HTLV-I, respectively. C8166 and K562 cells were irradiated with Ne ion at doses

indicated in Fig.1 and infected with VSV △G* (HTLV-I) pseudotype one day later. GFP-positive cells were detected on the following day. GFP-positive cells slighty decreased in the irradiated C8166, suggesting that an amount of a molecule(s) necessary for HTLV-I infection was decreased upon irradiation. In contrast, irradiated K562 cells became two- to threefold more susceptible to HTLV-I. Irradiation with heavy ions might have induced transcription of a cellular factor necessary for HTLV-I infection. K562 cells are known to differeciate upon various stimuli, e.g., treatment with many chemicals and irradiation with heavy ions may induce differentiation of K562 cells. So far we tested, expression of major proteins were inhibited in cells irradiated with heavy ions. We shall examine effects of Ne ion irradiation as well as He, C, or Ar ion irradiation on HTLV-I infection and hope to identify a gene that is involved in HTLV-I infection.

3.2 Effects of heavy ion beam irradiation on HTV-1 injection

C8166 and NP2/CD4/CCR5/ cells were irradiated with C or Ne ion beam and infected with HIV-1 two days later. As HIV-1 strains, R5X4 dual tropic GUN-1wt, R5Ba-L and R5 mSTD104, were used. Two days later, expression of HIV-1 antigens was detected (Fig.2), HIV-1 antigen-positive cells markedly increased and numerous syncytia were formed, indicating that heavy ion beam irradiation will enhance HIV-1 infection. IFA for CD4 and CCR5 showed that irradiated cells seemed to express smaller amounts of CD4 and CCR5 than non-irradiated NP-2/CD4/CCR5 cells. Therefore, there is a possibility that heavy ion irradiation may not enhance the entry of HIV-I into the cells. If so, the irradiation may have enhanced HIV-1 infection process after virus entry. In irradiated C8166 cells, the accumulation and transfer of NF-KB in the cell nucleus from the cytoplasm was detected, suggesting that this effect on NF-KB may be one of reasons for the enhancement of HIV-1 infection by heavy ion irradiation. It remains to be analysed further how heavy ion irradiation enhances HIV-1 infection.

3.3 Establishment of a system to analyze effects of heavy ion beam irradiation on the retroposon LINE1

We tried to produce two cell lines designated NP2/CD4/L1GFP and NP-2/CD4/L1rGFP for detection of expression and transposition of a human retrotransposon (retroposon), LINE1. In both cell lines, GFP-positive NP-2/CD4 cells were detected after transfection of the expression plasmids. Even when NP-2/CD4/L1GFP cells were irradiated with Ne ion, a number of GFP-positive cell did not increase apparently. NP-2/CD4/L1rGFP cells were irradiated with Ne ion beam, and their cellular DNA was extracted and analyzed using the inverse PCR methed for transposition of the vector. There seems to be difference in localization of the LIrGFP plasmid between non-irradiated and irradiated NP2/CD4/L1rGFP cells.

We did not have enough chances to repeat experiments to confirm the findings described above. Further analyses will be needed to reach solid conclusions.

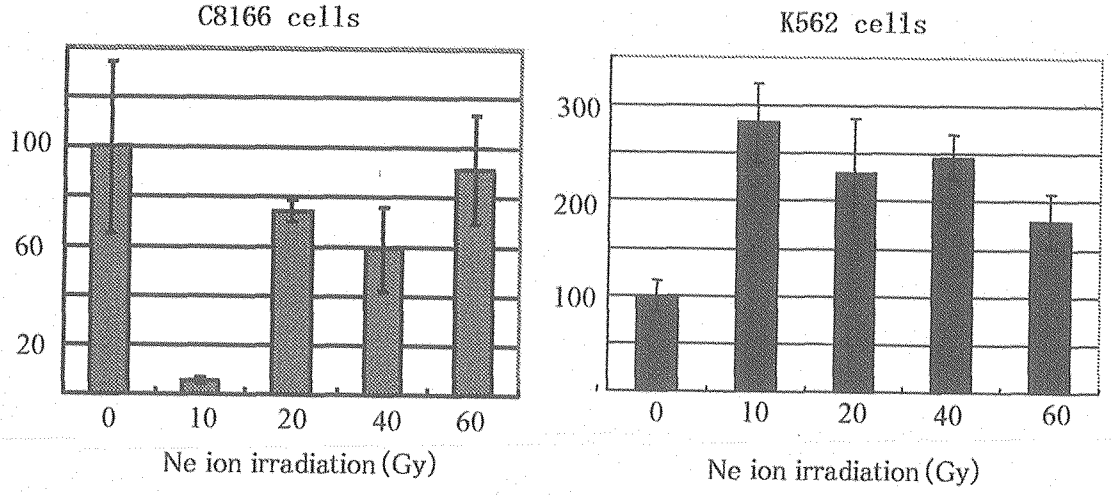

Fig. 1 Relative susceptibilities of human hemtopoietic cell lines to HTLV-I pseudotype

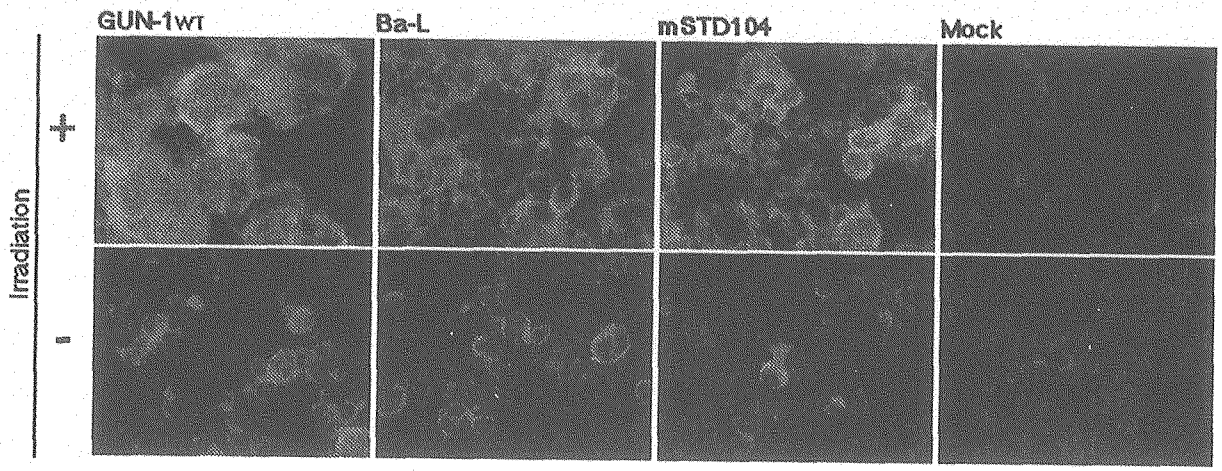

Cells were infected with HIV-1 48 hr after irradiation and examined another 48 hr after infection.

Fig. 2 Susceptibilities of heavy-ion-irradiated NP-2/CD4/CCR5 cells to HIV-1

2.47 Effects of Heavy-ion Irradiation on the Early Embryo of *Drosophila melanogaster*

K. Tatei[*], H. Kawamura[*,**], T. Funayama[***], N. Hamada[***,****], T. Sakashita[***], S. Wada[***], T. Nonaka[**], H. Obinata[*], T. Nakano[**], Y. Kobayashi[***,****] and T. Izumi[*]

Department of Molecular Biochemistry[*], Department of Radiation Oncology[**], Gunma University Graduate School of Medicine

Department of Ion-beam-applied Biology, JAERI[***]

Subdivision of Quantum Biology, Gunma University Graduate School of Medicine[****]

1. Introduction

Radiotherapy using high linear energy transfer (LET) charged particle has been thought to be highly effective alternative for conventional X-ray treatment, since it has higher relative biologic effectiveness (RBE) and can be delivered to limited structure such as lesional tissue or site.

Apoptosis is a fundamental process required to form the organ structure, to terminate a certain cell type from the lineage, and eliminate damaged cell exposed to radiation. Extensive studies about programmed cell death in mammals and invertebrate such as *Drosophila* and *C. elegans* have shown that the basic machinery for apoptosis is conserved throughout evolution.

Accumulating evidences indicated that the *p53* gene plays major roles for the apoptosis in response to DNA-damaging stimuli, such as X-rays and UV lights as well as heavy ions. Previous studies have shown that high-LET particle can induce apoptosis in certain cell type lacking *p53* gene, indicating the existence of the *p53*-independent apoptotic pathway[1]. Several groups reported that ionizing radiation including heavy-ion particle causes DNA double-strand breaks and also membrane and/or cytoplasmic damage, which lead to apoptosis.

The fertilized nucleus of a *Drosophila* embryo undergoes first 13 divisions synchronously, then the divided nuclei move to the cell surface where the membrane forms and separate them into individual cells. Recent development of a heavy ion microbeam technology enabled us to analyze effects of heavy ion delivered to restricted compartment within a single cell with high accuracy[2]. We carried out the heavy ion irradiation to the 1- or 2-nuclei stage embryos and examined the expression of *Ark* (*Apaf-1 related killer*) that is a *Drosophila* ortholog of the mammalian *Apaf-1*.

2. Materials and Methods

Embryos from yw^{67c23} as wild type were collected for 10 minutes and dechorionated. Embryos were washed and then exposed to carbon ion microbeam with 20-μmϕ aperture provided by the AVF cyclotron at TIARA JAERI-Takasaki[2].

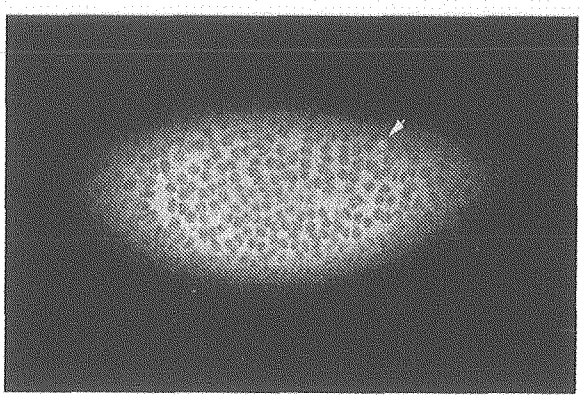

Fig 1 Heavy ion irradiation induced cell death in the early *Drosophila* embryo.
Irradiated embryos were subjected to acridine orange staining and viewed by confocal laser scanning microscope. Arrow indicates the nucleus stained with acridine orange.

Embryos were aged at 25°C for 1-2 hours and then fixed with 4% formaldehyde. *In situ* hybridization using digoxigenin- labeled RNA probe of *Ark* was carried out as described previously[3].

To detect cell death, acridine orange staining was done. Irradiated embryos were collected and placed in equal volumes of heptane and 5 μg/ml of acridine orange in PBS with vigorous shaking for 5 minutes. Samples were viewed with either fluorescence microscope or confocal laser microscope (Zeiss).

3. Results and discussion

The size of *Drosophila* embryos is about 500 μm long and 200 μm wide. The fertilized nucleus is located in central region slightly closer to the anterior end of the embryo during the first 2 rounds of the nuclear division. We irradiated around the position of 1/3 to the posterior end of the embryo with heavy ion beam using 20 μmϕ aperture so that the particle is likely to hit the structure other than nucleus. Followed by about 2-hour incubation at 25°C, we have detected few dying cells with the vital dye acridine orange (Fig. 1). It was reported that the acridine orange staining could detect only apoptotic cells in the *Drosophila* embryos[4]. In *Drosophila*, there is no detectable developmental cell death during the first 7 hours after the egg laying corresponding to the fully extended germ band stage. Therefore, it is likely that the heavy ion irradiation at the part of the fertilized egg where the nucleus is absent induced the apoptosis within the very restricted area at the late syncytial blastderm stage.

We further investigate the *Ark* expression in embryos exposed to heavy ions. UV-B irradiation of fertilized eggs can induce *Ark* transcription in the later stage of embryos as previously reported by others[5] (Fig. 2B). We detected high levels of its expression in the restricted area in the heavy-ion-irradiated embryos (Fig. 2C), whereas wild type embryos show low-level expression of *Ark* (Fig. 2A).

These data suggest that heavy-ion irradiation induce *Ark* transcription and lead the cells to apoptosis. The experiments to examine *p53* dependency of the *Ark* expression in irradiated embryos are ongoing.

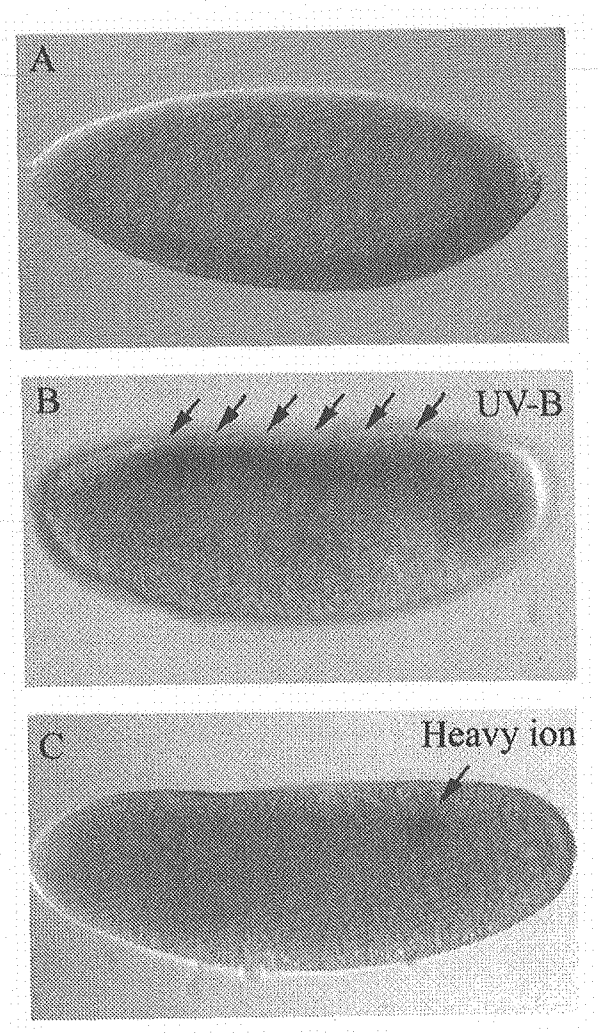

Fig 2 Heavy ion and UV-B induced *Ark* expression.

When fertilized eggs were irradiated with heavy ion or UV-B, *Ark* expression was observed at the later stage of embryos. Low-level and ubiquitous expression was seen in the wild type embryo (A), whereas higher expression was detected in the one side of the UV-B irradiated embryo (B, Arrows). The heavy ion irradiated embryo showed *Ark* expression in the restricted area (C, Arrow).

4. References

1) Y. Iwadate, J. Mizoe, Y. Osaka, A. Yamaura, H. Tsuji: Int. J. Radiat. Oncol. Biol. Phys. **50**, 803-808 (2001)

2) T. Funayama, S. Wada, T. Sakashita, Y. Kobayashi: JAERI-Review 2004-25, TIARA Annual Report 2003, 82-84 (2004).

3) K. Tatei, H. Cai, Y. T. Ip, M. Levine: Mech. Dev. **51**, 157-168 (1995)

4) J. M. Abrams, K. White, L. I. Fessler, H. Steller: Development, 117, 29-43 (1993)

5) L. Zhou, H. Steller: Dev. Cell **4**, 599-605 (2003)

2.48 Cytotoxic Effect of High Linear Energy Transfer Charged Particle Radiation on Human Glioblastoma Cells

S. Ishiuchi[*], M. Hasegawa[**], N. Hamada[***, ****], T. Funayama[****], S. Wada[****], T. Sakashita[****], Y. Kobayashi[***, ****] and T. Nakano[**]
Department of Neurosurgery[*], Department of Radiology and Radiation Oncology[**], Subdivision of Quantum Biology[***], Gunma University Graduate School of Medicine
Department of Ion-beam-applied Biology, JAERI[****]

1. Introduction

High linear energy transfer (LET) charged particle radiation, such as carbon and argon ion beam, have a higher relative biological effectiveness (RBE), compared with low-LET X-rays. The new radiation therapy may give a promising modality to the therapy for one of the most undifferentiated and invasive human cancer such as a glioblastoma usually resistant to conventional X-ray therapy. Moreover, the high-LET charged-particle radiation has the precise spatial distribution by Bragg peak that makes sharp and well-defined localization of irradiation, thereby it enables to treat the lesion with minimizing any harmful effect on the surrounding vital structure. At present, however, information on the biological effect of heavy particle radiation on glioblastoma cells remains elusive. Thus we investigated cytotoxic effects of high- and low-LET radiations on human glioblastoma cells by conventional broad-field beam radiation.

2. Material and method

2.1 Cell line

A human glioblastoma cell line, CGNH-89[1], was used in the present study. Cells were cultivated in DMEM (Life Technologies, Gaithersburg, Mayryland) supplemented with 10% FBS and 2 mM glutamine.

2.2 Irradiation

The AVF cyclotron installed at Takasaki Ion Accelerators for Advanced Radiation Application (TIARA) facilities of Japan Atomic Energy Research Institute (JAERI) was used as an ion-beam source[2]. The ion beams used were $^{12}C^{5+}$ (18.3 MeV/nucleon, LET 108 keV/μm), and $^{40}Ar^{13+}$ (11.5 MeV/nucleon, LET 1260keV/μm). Just before irradiation, the medium was removed to allow the ions penetrate the cells. During the irradiation, the cells were covered with an 8-μm thick polyimide film (Kapton, Dupont-Toray Co.Ltd) to keep the cells wet during irradiation. For comparison, cells seeded onto 35-mm-diameter Petri dished with 2mL medium were irradiated with a X-ray machine (MBR-1505R, Hitachi) that was operated at 140 kV, 4.5 mA with 0.5-mm Al filter and focus-source distance of 30 cm at a dose rate of 1.11 Gy/min[3]. Irradiation was performed in air at room temperature.

2.3 Clonogenic assay

Surviving fractions were determined by clonogenic assay. Colonies were fixed by 4% paraformaldehyde and stained with

hematoxylin-eosin (H & E) at least 14 days after subculture for counting.

3. Results and Discussion

We examined the cytotoxic effects of high-LET carbon and argon beam radiations on a human glioblastoma cell line, compared with those of X-ray treatment. The survival rates subjected to X-rays, carbon ion beams, and argon ion beams treatment by broad-field radiation are shown in fig. 1. Equivalent doses of the carbon beams were more effective at reducing the survival rates than X-rays. The RBE values for carbon- and argon-ion beams (compared with X-rays), calculated for surviving fraction of clonogenic cells after 1 Gy irradiation, were 4.4 and 7.5, respectively. Argon-ion beam was the more effective than carbon beams or X-rays. We found high-LET charged-particle radiations such as carbon or argon beam showed higher cytotoxic effect than X-rays as revealed by their RBE and cell morphology. The cytotoxic effect including flattening and widening of cell soma appearance of bizarre multinuclear cells, and cytoplasmic vacuolation were detected in cells exposed to 0.5-1Gy of argon and 3Gy of carbon ions. To note, at least 5-7 Gy of X-rays is required to cause similar effect. We found high-LET charged-particle radiation, such as carbon beam or argon beam showed higher cytotoxic effect than X-rays, as revealed by their RBE. The cytotoxic effect as revealed by the morphological changes as described were gradually prominent until 4 days post-irradiation (4 DPI) and were prominent at 8-10 DPI.

Fig. 1

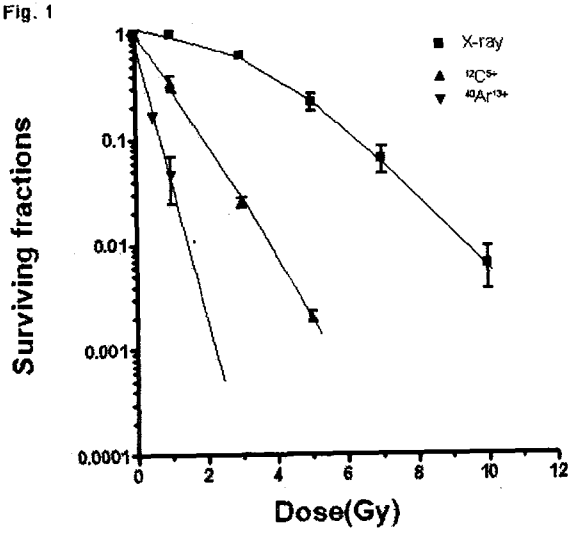

In conclusion, high LET radiation displayed marked cytotoxic effect on a human glioblastoma cell line, CGNH-89. Thus, high-LET radiation therapy may be a promising modality for human glioblastomas.

References

1) S. Ishiuchi, K.Tsuzuki K, Y.Yoshida, N. Yamada, N. Hagimura, H. Okado, A. Miwa, H. Kurihara, Y. Nakazato, M. Tamura, T. Sasaki, A. Ozawa.
Nature Medicine 8 (2002) 971-978.

2) T. Funayama, S. Wada, Y. Kobayashi, H. Watanabe.
Radiation Research 163 (2005) 89-94.

3) T. Akimoto, T. Nonaka, H. Ishikawa, H. Sakurai, J. Saito, T. Takahashi, N. Mituhashi.
International Journal of Radiation Oncology, Biology, Physics 50 (2001) 195-201.

2.49 Analysis of the Distribution the Dynamics of Trace Elements Associated with Radiation- and Drug-induced Apoptosis

T. Nakano*, M. Hasegawa*, H. Sakurai*, M. Shioya*, T. Sakai**,
M. Oikawa**, M. Fukuda**, T. Satoh** and K. Arakawa**
Department of Radiation Oncology, Gunma University Graduate School of Medicine*
Advanced Radiation Technology Center, JAERI**

1. Introduction

To evaluate the modes of cell death and the signal transduction following irradiation is essential for radiation biology. We have already investigated apoptosis induced by X-rays, heavy ion beams, and anticancer agents, and indicated that p53-dependent apoptosis was induced at a higher rate in radiosensitive tumor cells and normal cells having wild-type p53, while the apoptosis at a lower rate in cells having mutant-type p53[1-4]. Although the signal transduction during the p53-dependent apoptosis induced by radiation has been studied in detail, the p53-independent apoptosis is yet to be understood. Thus it is necessary to study the signal transduction and the dynamics of the relevant elements in radiation-induced cell death in detail. An in-air micro-particle-induced X-ray emission (micro-PIXE) has been used for biological research recently, and expected to be a useful technique for evaluating radiation biology. In the present study, we investigated the distribution and the dynamics of elements associated with radiation-induced apoptosis and necrosis by using a micro-PIXE.

2. Experimental procedure

A human ependymoblastoma having wild-type p53 and a human small cell lung cancer having mutant-type p53 were transplanted into nude mice subcutaneously, and they were irradiated with 200 kV X-rays. These tumors were excised 3, 4.5, or 6 hours after 10 Gy irradiation, and in vivo samples were prepared for evaluating the distribution and the dynamics of elements associated with apoptosis or necrosis induction by using a micro-particle-induced X-ray emission (micro-PIXE). In particular, the localization of these elements in vivo was studied in comparison with that by conventional light microscopic morphological studies (hematoxylin or TUNEL staining).

3. Results and Discussion

In the non-irradiated control groups of the both tumors, wide distributions of phosphorus (P), potassium (K), chlorine (Cl), and sulfur (S) were demonstrated in the nucleus and the cytoplasm of tumor cells. These distributions were well correlated with the morphologic features shown by hematoxylin staining, and the elements were extremely decreased in the necrotic areas that were often found in the small cell lung cancer. A small amount of calcium (Ca), silicon (Si), and iron (Fe) was also found in these samples, however, their distributions were not correlated with the morphologic features.

In the treated groups of the ependymoblastoma, the morphologic

studies showed that apoptosis was frequently induced 3-6 hours after irradiation, but no significant change of the elements was observed. P, K, Cl, and S were widely demonstrated in the nucleus and the cytoplasm of tumor cells as shown in the control group. No significant change of distribution of P, K, Cl, S, Ca, Si, and Fe was observed regardless of the prominent morphologic changes.

In the treated groups of the small cell lung cancer, necrosis was often found, but the morphologic features were not different from those of the control group. P, K, Cl, and S were decreased in the areas of necrosis, however, no significant change of elements was found compared with the control group.

The present study has suggested that the micro-PIXE is useful for radiobiological research, but these data are preliminary and further investigations are required.

References

1) M. Hasegawa, G. Wilson, L.D. Russell, M.L. Meistrich. Radiat Res 147 (1997) 457-467.
2) M. Hasegawa, N. Mitsuhashi, M. Yamakawa, M. Furuta, K. Maebayashi, R. Imai, K. Hayakawa, H. Niibe. Radiat Med 15 (1997) 171-176.
3) M. Hasegawa, Y. Zhang, H. Niibe, N.H. Terry, M.L. Meistrich. Radiat Res 149 (1998) 263-270.
4) M. Kawashima, M. Hasegawa, K. Hayakawa, S. Nasu, H. Toda, Y. Suzuki, N. Mitsuhashi, H. Niibe. Anticancer Res 19(1B) (1999) 5101-5110.

3. Radiation Chemistry / Organic Materials

This is a blank page.

JP0650217

3.1 First Preparation of Ion-track Membranes of Poly(*p*-phenylene terephthalamide)

–Control of Pore Shape and Size under Various Irradiation Conditions–

Y. Suzuki*, A. Hiroki*, T. Yamaki*, M. Asano*, K. –O. Voss**, R. Neumann** and M. Yoshida*

Department of Material Development, JAERI*,

Materials Research, Gesellschaft für Schwerionenforschung (GSI)**

1. Introduction

When polymer films are irradiated with ion beams, the materials along the incident axis are damaged enough to be etched out in alkaline solutions because of scission of the polymer main chains. Ion-track membranes, which possess cylindrical through-holes with diameters ranging from 10 nm to 1 μm, are easily prepared by ion beam irradiation followed by chemical etching of the damaged part[1]. There have been a number of reports on the ion-track membranes of poly(ethylene terephthalate) (PET), polycarbonate (PC) and polyimide (PI). The PI ion-track membranes were obtained by the etching with an oxidative solution[2] and precursor method[3]. However, the ion-track membrane of chemically and thermally stable polyamide has not yet been prepared by the chemical etching. This is because sensitivity of the track etching is inversely related to polymer stability.

In the present study, therefore, the ion-track etching of various polyamide films was investigated based on our screening experiments. We report herein, for the first time, the preparation of ion-track membranes of poly(*p*-phenylene terephthalamide) (PPTA), which is one of polyamides with the highest strength, chemical and thermal stability. The variation of irradiation parameters, such as ion species and energy, and etching conditions made it possible to control the pore shape and size.

2. Experimental procedures

2.1 Ion beam irradiation of PPTA films

A PPTA film with 16 μm in thickness was obtained from Teijin Advanced Films Co., Ltd. The PPTA films were irradiated with ^{84}Kr, ^{102}Ru and ^{129}Xe ions at energies of 6.2, 3.6 and 3.5 MeV/n, respectively, from the Azimuthally Varying Field (AVF) cyclotron at the Takasaki Ion Accelerators for Advanced of Radiation Application (TIARA) of the Japan Atomic Energy Research Institute (JAERI). Irradiations with ^{152}Sm, ^{197}Au and ^{238}U ions at energies of 11.1, 11.4 and 11.1 MeV/n, respectively, at the linear acceletator called UNILAC of the GSI (Darmstadt), Germany. The ion fluence was 3 x 10^7 ions/cm^2.

2.2 Conductometric measurement during the chemical etching process

Based on the findings from our extensive screening experiments, the irradiated PPTA films were etched in a sodium hypochlorite (NaClO) solution at 40°C without stirring, whose pH value was adjusted at pH 9±0.5 by adding a 2 M hydrochloric acid (HCl) solution. The etched sample was washed with a large amount of water and dried at 40°C for 2 hours *in vacuo*. The surface and cross-section of the membranes were coated with gold using a Giko IB-3 ion coater and then observed with a JEOL JXA-733 scanning electron microscope (SEM).

To measure a track etching rate (V_t), the etching was performed in an electrolytic

conductivity cell[4]. The irradiated film was inserted as a dividing wall in the cell containing the NaClO solution at pH 9. The conductance through the film was monitored as a function of etching time. As soon as the track-etched cones approaching from both sides of the film surface had contact to each other, electrical current suddenly increased. V_t was calculated by dividing the half thickness of the films by the breakthrough time. A bulk etching rate (V_b) was estimated at 0.05 μm/h by taking the decrease in film thickness during one-hour etching. Using the ratio of the two etching rates, we obtained the track formation sensitivity, Q, according to the following simple equation:

$$Q = (V_t / V_b) - 1.$$

3. Results and Discussion

The PPTA ion-track membranes were prepared by ^{238}U and ^{129}Xe ion beam irradiation followed by the chemical etching with the pH 9 NaClO solution at 40°C. Figure 1 (a) shows the SEM photographs of the surface and cross-section of the membranes, which were obtained by the irradiation with ^{238}U ions and the 12-hour etching. This clearly confirms the perfectly cylindrical pores with a 0.3-μm diameter. The cylindrical shapes were also observed for the ^{197}Au ion irradiated films. In contrast, as shown in Fig. 1 (b), the tracks of ^{129}Xe ions were etched for 18 hours, leading to the observable tracks with a surface diameter of 0.8 μm. The cross section appeared to be not cylindrical all over the thickness of the membrane. The films irradiated with ^{84}Kr, ^{102}Ru and ^{152}Sm ions provided such a funnel-shaped pores, too.

The conductometric measurement was applied to determine the Q value. Figure 2 shows current across the film as a function of etching time in the pH 9 NaClO solution at 40°C

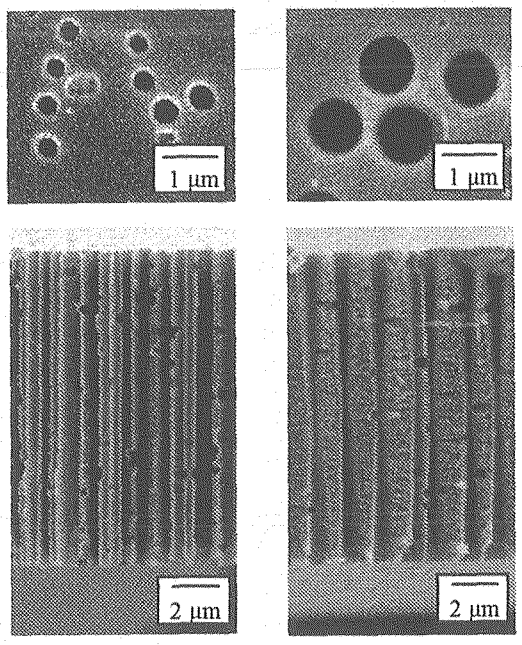

Fig. 1 SEM photographs of the surface and cross section of PPTA ion-track membranes obtained by the irradiation with (a) ^{238}U and (b) ^{129}Xe ions.

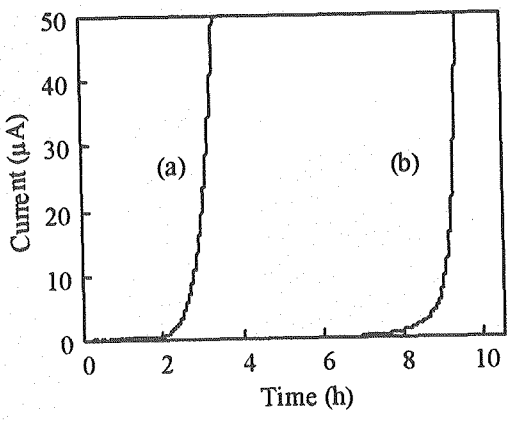

Fig. 2 Representative conductometry results: current vs. etching time curves for the PPTA films irradiated with (a) ^{238}U and (b) ^{129}Xe ions.

for the PPTA films irradiated with ^{238}U and ^{129}Xe ions.

The breakthrough times were estimated to be about 2.2 and 8.5 hours, respectively. These times correspond to V_t values of 3.2 and 0.76

μm/h, respectively. Accordingly, Q values of 63.4 and 14.2 were obtained for the ^{238}U and ^{129}Xe ion irradiated films, respectively. Q for other ion species, ion beam energy and the geometry of the etched pore are summarized in Table 1.

Table 1 Ion irradiation parameters, Q and the etched pore geometry.

Ion species	Energy (MeV/n)	Q	Pore geometry
^{84}Kr	6.2	2.4	funnel
^{102}Ru	3.6	6.8	funnel
^{129}Xe	3.5	14.2	funnel
^{152}Sm	11.4	17.1	funnel
^{197}Au	11.1	62.4	cylindrical
^{238}U	11.4	63.4	cylindrical

Etching conditions : pH 9 NaClO solution at 40℃

Probably because the latent tracks of lighter ^{84}Kr, ^{102}Ru, ^{129}Xe and ^{152}Sm ions had lower sensitivity, these funnel-shaped pores appeared in the membranes, where the pore diameter at the film surface became large before the formation of through-holes. On the other hand, the track sensitivity of heavier ^{197}Au and ^{238}U ions were found to be more than 4 times larger under the same etching conditions. Interestingly, the tracks of ^{152}Sm ions had low sensitivity in spite of as high velocity as ^{197}Au and ^{238}U. These indicate that Q depends on the mass of the ions rather than the incident velocity. There should be the threshold of the ion mass between ^{152}Sm and ^{197}Au, at which the etched track transformed from the funnel to cylindrical pore. Consequently, the geometry of the etched tracks in PPTA will be controlled by varying the irradiation parameters.

4. Future remarks

PPTA possesses high glass transition temperature reaching 350°C, and so exhibits thermal stability as much as PI. We have been developing polymer electrolyte membranes for high-temperature fuel-cell applications by incorporating proton-conductive ion exchange groups within the pores of the PPTA ion-track membranes.

References

1) P. Apel, V. Kuznetsov, V. Luppov, A. Levkovich, V. Altynov, O. Orelovich, *Nucl. Tracks Radiat. Meas.*, 22 (1993) 97-100.

2) Z. Tian-cheng, R. Brandt, P. Vater and J. Vetter. *Nucl. Tracks Radiat. Meas.*, 15 (1988) 771-774.

3) Y. Suzuki, Y. Maekawa. M. Yoshida, K. Maeyama and N. Yonezawa, *Chem. Mater.*, 14 (2002) 4186-4191.

4) P. Apel, A. Schulz, R. Spohr, C. Trautmann, V. Vutsadakis et al., *Nucl. Instr. and Meth. B*, 131 (1997) 55-63.

3.2 Creation of Nano-Gel Channels by Ion Beam Irradiation

S. Hasegawa, H. Koshikawa, T. Yamaki, Y. Maekawa, Y. Suzuki, A. Hiroki and M. Yoshida
Department of Material Development, JAERI

1. Introduction

Energy deposition area along an incident axis in ion-beam-irradiated polymer films, namely a latent track, is commonly divided into a core and a penumbra. The core is a narrow cylindrical region near the incident axis, and the penumbra is the outer region surrounding the core.

The latent track as localized damage is preferentially dissolved by alkaline etching, resulting in the formation of track-etched membrane with uniform pores [1-3]. For example, the track-etched membrane of the most popular poly(ethylene terephthalate) (PET) was obtained by hot NaOH aqueous solutions. The alkaline etching of PET also produces functional groups such as carboxyl (-COOH) and hydroxyl (-OH) terminals through hydrolysis of the main chain (Fig. 1). It is considered, therefore, that an internal surface of the track-etched pore is covered with hydrophilic thin layers, which are swollen by etchant penetration just before etching out.

Our target is the creation of this so-called nano-gel channel based on ion-track technology. The channel has wide applications to development of functional nano-tech membranes because the terminal end groups of PET are easily functionalized by well-known organic-chemical methodologies. Here we report recent results regarding chemical modification and thickness control of the gel layer within the track-etched pores. These techniques were then applied to the preparation of membrane materials for the optical resolution of amino acid isomers.

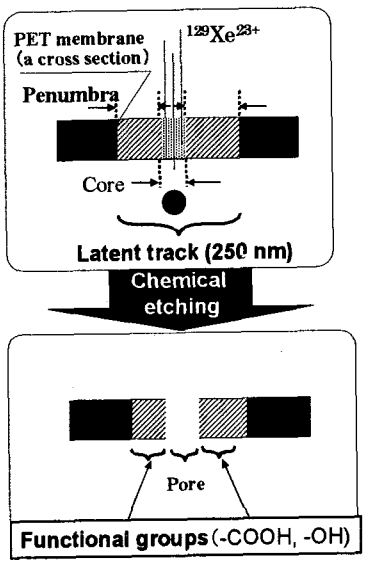

Fig. 1 Schematic illustration for the preparation of ion track membranes.

2. Chemical Modification of Internal Surfaces of Track-Etched Pores

Chemical modification of pore internal surfaces in the track-etched PET membranes was carried out using the alkylation reaction with the -COOH end groups, in which pyrene derivatives were incorporated as a fluorescent probe

The track-etched membrane with the pores of 540 nm in diameter was prepared by the etching of the PET film bombarded with $^{129}Xe^{23+}$ ions of 3.5 MeV/n in a 0.5 M NaOH aqueous solution at 40°C. The internal surface of track-etched pores was treated with a DMF solution of 0.02 M 1-(bromoacetyl) pyrene (BrPy) and 0.05 M KF at room temperature. The DMF solution was loaded into a glass syringe connected to a

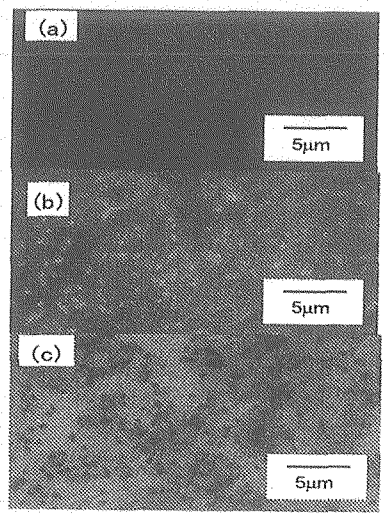

Fig. 2 Fluorescence micrographs of the ion track membranes (a) before and (b) after the reaction with BrPy. (c) optical image at the same area of the membrane.

membrane filter holder. The solution was introduced into the pore of the track-etched membrane with a constant pressure (5.3 kPa) to make sure the contact of the reaction solution to the pore internal surface.

The fluorescent images were taken using a microscope with a standard CCD digital camera. No fluorescence image was observed on the membrane before the alkylation treatment (Fig. 2(a)). The fluorescent spots of about 500 nm in diameter were observed clearly in the image of the Py-modified membrane (Fig. 2(b)). Compared to the optical image at the same area of the membrane (Fig. 2(c)), the positions of the fluorescent spots were almost the same as those of the etched pores. This indicates that the pores were modified by the reaction of the surface -COOH groups with the alkylation reagent bearing the pyrene fluorophore.

3. γ-irradiation Effect on Latent Tracks of PET Film

Many researchers have reported that ultraviolet irradiation as well as soaking of organic solvents is a useful technique for high sensitization of ion tracks [3]. Instead of such pre-treatments, we investigated the effect of γ-irradiation on the latent tracks of PET films bombarded with $^{129}Xe^{23+}$ ions of 3.5 MeV/n.

The irradiated PET films were etched for 6 hours in a 0.2 M NaOH aqueous solution at 70°C. The evolution of the tracks during the etching has been generally examined by the conductometric method [4] and scanning electron microscopy (SEM). Strikingly, a discrepancy was found to appear between pore sizes estimated by these two methods. This became large with increasing γ-irradiation doses up to 160 kGy (Fig. 3). The decrease in pore diameter observed by SEM should be caused by the formation of the insoluble crosslinked polymer region in the latent track. Thus this gel layer was probably swollen by absorbing the etchant to form the ion-transportable nano-gel channel. Consequently, the pore diameter from the conductometric method is considered equal to the sum of pore size observed by SEM and gel-layer thickness.

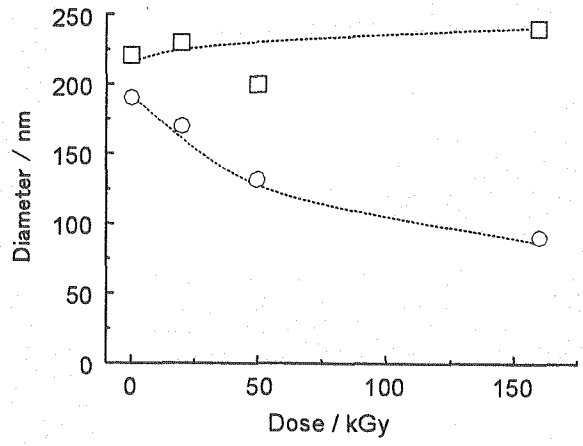

Fig. 3 Surface pore diameter obtained from SEM (○) and electric conductometry (□) as a function of γ-irradiation dose for PET films.

4. Development of Membrane Materials for Optical Resolution of Amino Acid Isomers

The nano-gel channels in the PET membrane

were modified with optically active amino acid moieties to develop novel membranes for chiral separation.

The track-etched PET membranes with a cylindrical pore of 120-nm diameter were used for their chemical modification according to a similar method. The COOH groups existing on the wall of the pores were selectively modified by the alkylation of N-bromoacetyl-L-phenyl alanine methyl ester (N- BrAc-L-PheOMe). The optical resolution of racemic phenyl alanine (D, L-Phe) mixtures through the functionalized nano-gel channels was performed by a one-hour batch reaction at 25°C (Fig. 4). As a result, a separation factor as the ratio of L to D-Phe was constant at 1.4 through five batch reactions. This undoubtedly suggests the preferential separation of L-amino acids.

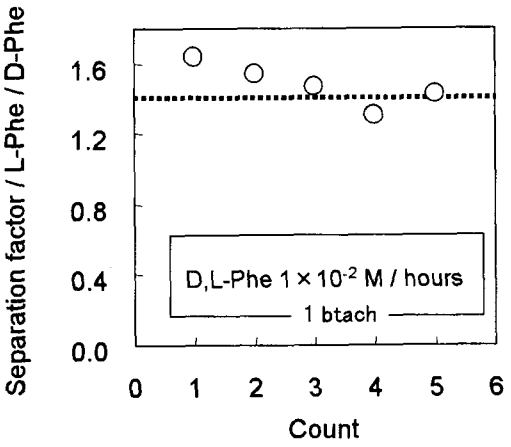

Fig. 4. Separation factor through the N-Ac-L-PheOMe modified etched-track membrane by the one-hour batch reaction at 25°C.

Acknowledgement

The present work was supported by the REIMEI Research Resource of Japan Atomic Energy Research Institute in 2004.

References

1) P. Apel, Radiat. Meas. 34 (2001) 559-566.
2) R. L. Fleisher, P. B. Price, and R. M. Walker, in "Nuclear Tracks in Solids: Principles and Applications," ed. by R. L. Fleisher, University of California Press, Berkley.
3) Z. Zhu, Y. Maekawa, H. Koshikawa, Y. Suzuki, N. Yonezawa, M. Yoshida, Nucl. Instr. and Meth., B217, (2004) 449-456.
4) P. Apel, A. Schulz, R. Spohr, C. Trautmann, V. Vutsadakis, Nucl. Instr. and Meth., B131, (1997) 55-63.

3.3 Time-dependence of Differential G-values of OH Radicals in Water under Ne Ion Radiolysis

M. Taguchi and T. Kojima
Department of Material Development, JAERI

1. Introduction

The oxidations of solutes in aqueous solutions are mainly induced by OH (hydroxyl) radicals formed from water molecules upon heavy ion irradiation. Characteristics of the oxidations of solutes are strongly dependent on initial concentrations and spatial distributions of OH radicals in water at irradiation. Clarification of reaction mechanisms of OH radicals is a critical point for interpretation of the radiation effects both in radiation chemistry and also radiation biology. The heavy ion deposits its kinetic energy densely along and around its trajectory. The initial spatial distribution of OH radicals is the same as that of the energy deposition. OH radicals, however, disperse as time passed within their life, and this makes the interpretation of relevant chemical reactions very complicate. Therefore, neither 'average LET' nor 'average yield' is suitable parameter for detailed investigation on radiation effects. Investigations based on three parameters, which are incident ion species, their kinetic energy in interested materials, and elapse time for subsequent energy transfer in vicinity are indispensable to understand chemical reactions in the track.

The yields of OH radicals have been investigated for several ten MeV/n Ne ions as a function of reaction time by means of changing the solute concentration.

2. Experimental

Phenol as a solute was dissolved in water at 10-100 mM as a sample solution. The solution was saturated with oxygen by 30-minute bubbling, and put into an aluminum irradiation cell with a magnetic stirrer chip. The cell has an aluminum window of 15-μm thickness and 40-mm diameter, which makes Ne ion pass through to the sample solution.

The procedure of the ion beam irradiation and the product analyses were performed as described in the previous papers.[1,2] Heavy ion used in this study was 350-MeV Ne^{8+} ion provided from an AVF cyclotron in TIARA facility. Fluence rate was about 3×10^{8} ions/cm^2/s at the surface of the sample solution. Thin aluminum foils for reducing the incident energy of the ion were placed on the irradiation cell. The dose in the sample solution was controlled by changing the irradiation time up to 200 seconds.

The sample solutions were analyzed after irradiation by High Performance Liquid Chromatography (HPLC) with a reversed phase column (Shodex, Rspak DE-613) at 40 ℃. Acetonitrile mixed with 70%(v/v) aqueous H_3PO_4 solution (0.01 M) was used as an eluent at a flow rate of 1.0 mL/minute.

3. Results and discussion

The specific peaks of hydroquinone, resorcinol and catechol were recorded on the HPLC chromatogram as Ne-ion irradiation products formed through the reaction, in which one OH radical attached to phenyl ring at *p*-, *m*- and *o*- positions,

$$OH + C_6H_5OH \longrightarrow \text{hydroquinone, resorcinol, catechol} + H \quad (1).$$

The number (N) of oxidized products per a single Ne ion, which was integration of differential G-value (G'-value) over entire trajectory, increased super-linearly with an incident energy of Ne ion,

$$N = \int_0^{E_0} G' \mathrm{d}E \times 100. \qquad (2).$$

The G'-values are estimated by differentiating N with a third order function of energy. The G'-values of the oxidized products were in the range of 1/10 to 4/5 of the G-values obtained for ^{60}Co γ-ray irradiation. In the case of γ-ray irradiation, total G-value of the whole oxidized products is larger than 90 % of the G-value of OH radical. The G'-values of OH radicals were estimated by regarding that the mechanisms of oxidations under Ne ion irradiation are the same as that by γ-ray irradiation. The estimated G'-values of OH radicals for three different concentrations of the aqueous phenol solution were plotted against specific energy (energy per nucleon) of Ne ion as shown in Fig. 1. The mean value of the reaction time of the OH radical with phenol is regarded as $(k_{OH}[\text{phenol}])^{-1}$, where k_{OH} and [phenol] are the rate constant of OH radicals with phenol and the concentration of phenol, respectively. The G'-values, accordingly, obtained for the phenol concentrations of 10, 60 and 100 mM are correspondent to the mean value of the reaction time of about 1.5, 2.5 and 15 ns, respectively. The G'-values of OH radicals increase monotonously with the specific energy. The G'-values will become closer to the constant value (2.7) obtained for ^{60}Co γ-rays. The G'-values are relatively larger at the primary stage and decrease with reaction time after irradiation. Such decreases of the G-values are generally observed for γ-ray and electron beam irradiation. OH radicals are consumed in consequence of the reactions with hydrogen, hydrated electron, and other transient species produced by irradiation.

The result suggests that consideration of transient process of radicals, e.g. diffusion and reaction of transient species in track, is critical to give better understanding of radiation effects for heavy ions. The further discussion will be done by considering such particularity of chemical reactions occurred just in the vicinity of physical track.

References

1) M. Taguchi, et al., *Radiat. Phys. Chem.*, **60**, 263 (2001).

2) M. Taguchi, T.Kojima, *Radiat. Res.*, **165,** 455 (2005).

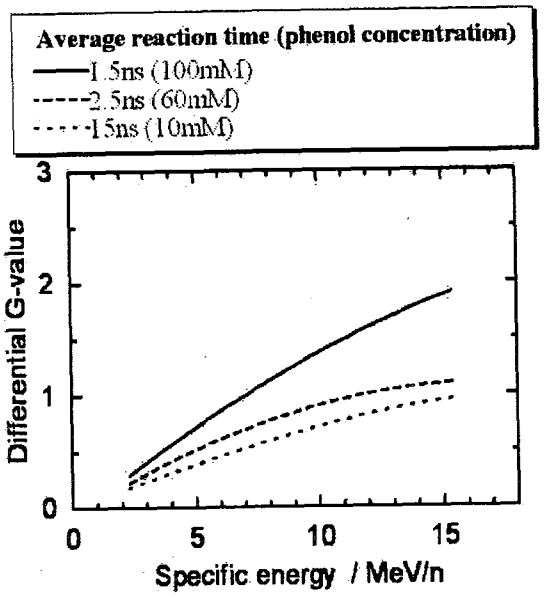

Fig. 1. Differential G-value of hydroxyl radicals in phenol solution depending on the reaction time after 350-MeV Ne^{8+} ion irradiation.

JP0650220

3.4 Study of Radiation-induced Primary Process by Ion Pulse Radiolysis

Y. Yoshida*, J. Yang*, T. Kondoh*, S. Seki*, T. Kozawa, S. Tagawa*,
H. Shibata**, M. Taguchi***, T. Kojima*** and H. Nanba****
ISIR, Osaka University*
Faculty of Engineering, Kyoto University**
Department of Radiation Research for Environment and Resources, JAERI***
Department of Material Development, JAERI****

1. Introduction

Radiation effects of high-energy and high-LET ion beams on the material produce the highly-densed damage which is different from that by low-LET radiation, such as electrons and γ rays. The effects were investigated by many researchers, and used for many industrial applications. The study of the primary process of the ion beam-induced radiation chemistry is also very important for opening the wide application field of the ion radiation.

The LET effect on the time-dependent emission is easy to be investigated by emission spectroscopy [1-3]. However, the information on the other important short-lived species, such as electron and cation radical, can not be obtained by the emission spectroscopy.

To study the behavior of the short-lived species, an ion beam pulse radiolysis based on absorption spectroscopy is a useful tool. The first ion beam pulse radiolysis was developed by using a proton beam, and used to study the primary process of radiation chemistry[4]. For a heavy-ion beam, there are many difficulties to the absorption spectroscopy, such as the fluctuation of the ion beam intensity, the penetration of the ion beam into material, the light source, and so on. To overcome the difficulties, we developed at first a heavy-ion-pulse radiolysis by using a single-photon-counting technique. In the system, the ion beam was passed through a thin scintillator before irradiating the sample. The light emitted from the scintillator by the ion irradiation was used as analyzing source to detect the absorption. The time-dependent absorption of hydrated electrons in water has been measured.

2. Experimental Setup

Figure 1 shows the system for the developed ion-beam pulse radiolysis for absorption spectroscopy. A 25mm-diameter sample cell was used and located into a vacuum chamber. The ion beam produced from the AVF cyclotron in the TIARA accelerator was passed through a 20-μm-thick Ti foil and guided into the sample cell. A thin scintillator was located upstream of the sample. The ion beam was passed through the scintillator and then irradiated the sample. The light emitted from the scintillator by the ion irradiation was used as analyzing source. The transient absorption was detected by a single photon counting technique, as shown in Fig. 1.

In the experiment, a 220MeV C^{5+} pulsed ion beam from the AVF cyclotron was used as an irradiation source. A BGO

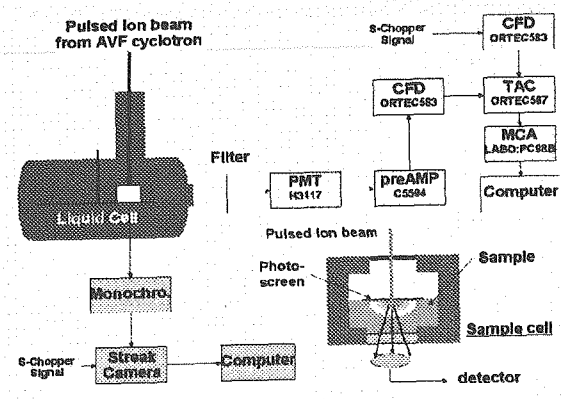

Fig. 1 Experimental setup of ion beam pulse radiolysis

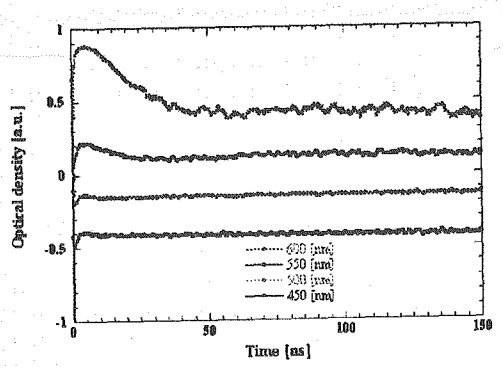

Fig. 2 Transient absorption kinetics of hydrated electron obtained in 220 MeV C^{5+} pulse radiolysis

(Bismuth Germanate; $Bi_4Ge_3O_{12}$) scintillator was used as an emitter to produce an analyzing light. The lifetime and the peak wavelength of the emission are 300 ns and 480 nm, respectively. The slow reactions with the decay of <300 ns thus can not be measured because of the BGO lifetime.

3. Results and Discussion

In the experiment, the analyzing light intensity after passing through the sample (I), and the intensity without the sample (I_0) have been measured to obtain the optical density (OD). In this system, it is difficult to measure I_0 because the analyzing light is produced by the ion beam. To avoid the problem, I_0 was measured by using empty cell. Therefore, the value of OD can be calculated as

$$OD = \log(I_0 \times A / I) = \log(I_0 / I) + \log(A) \quad ,$$

where A is a factor which is caused by the disagreement of the analyzing light intensity at time = 0. The value of the factor A could not be determined in the experiment. This means that the zero position of the optical density can not be decided. Figure 2 shows the time-dependent optical absorption of the hydrated electron obtained in the 220MeV C^{5+} ion beam pulse radiolysis of water monitored at the wavelength of 450-600 nm scale.

To measure the zero position of the optical density, a 30 μm-thick screen which was made of sintered Al_2O_3 doped with Cr was used for the next experiment. The emission spectrum was measured with 220MeV C^{5+} pulsed ion beam. Figure 3 shows the spectrum and the decay of the scintillator. A long lifetime was shown. A flattop light emission within 450 ns was observed by using the new scintillator. The peak wavelength of 700 nm was observed. It may be suitable for the study of the time-dependent optical absorption kinetic of the

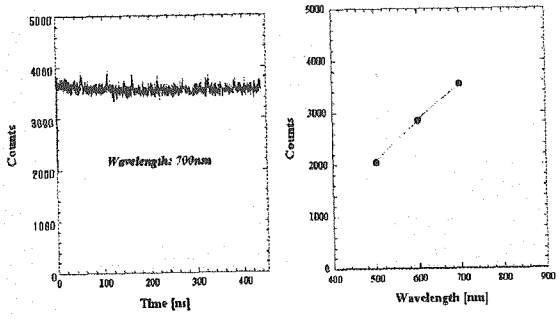

Fig. 3 spectrum and the decay of the scintillator made of sintered Al_2O_3 doped with Cr

hydrated electron in matter.

4. Summary

An ion beam pulse radiolysis based on absorption spectroscopy was developed to study the primary process of the ion beam-induced radiation chemistry. The transient absorption kinetics of the hydrated electrons in water was observed in the 220MeV C^{5+} ion beam irradiation. A long-lifetime scintillator is proposed to produce a flattop analyzing light source for the next ion-beam pulse radiolysis.

References

1) H. Shibata et al., Nucl. Instrum. Meth., A327, 53, 1993
2) Y. Yoshida et al., Nucl. Instrum. Meth, A327, 41, 1993
3) H. Shibata et al., Nucl. Instrum. Meth., B105, 42, 1995
4) W. G. Burns et al., Faraday Diss. Chem. Soc. 63 (1977) 47.

3.5 Size Dependence of Nanowires Formed by Single Ion Hitting on Molecular Configuration of Target Polymers

S. Seki*, S. Tsukuda*, S. Tagawa* and M. Sugimoto**
The Institute of Scientific and Industrial Research, Osaka University*
Department of Material Development, JAERI**

Introduction

In recent years, high-energy charged particles have been examined in terms of the effects of deposited energy density on chemical products in solid polymer materials,[1-5] and the difference in the types of radiation-induced reactions has been ascribed to a variation in the density of reactive intermediates. The spatial distribution of energy deposited by charged particles plays a significant role in promoting chemical reactions in target materials.[6-10]

From the viewpoint of nano-fabrication, the small volume of chemical reactions in the target material is realized by a single incident ion. The small reaction volume, which is known as the "chemical core", has been studied vigorously, because of the narrow pores produced by chemical etching procedures after the ion irradiation.[11] The pore sizes are controlled precisely by adjusting the chemical etching conditions. Membranes with pores of etched ion tracks as the template for metallic replicas was also used successfully to prepare copper whiskers and organic tubes on a substrate.[12-15] For the preparation of nano-structured devices with precisely controlled sizes, it will be very important to suppress the surface roughness of the structures. The material origin of the roughness has been investigated vigorously, however still incomplete to date. Configuration of the polymer chain in the base resin, as well as the molecular weight and its distribution of polymers, is one of the most crucial primary factors to determine the roughness, and not only experimental analysis[16] but also simulations based on the statistical theory of polymer backbone configuration[17] have been demonstrated. In the present paper the roughness is discussed quantitatively in the side-walls of the nanostructures which have been prepared by single particle negative-tone imaging.[9] The single particle imaging is the powerful tool to give 1-D nanostructures with sub-nm spatial resolutions.[10] Intrinsic cylinder-like shapes of the nanostructures realize to observe the side walls directly by scanning probe microscopes, reflecting the shape of "polymer molecules".

Experimental

Polystyrenes derivatives and poly(3-hexylthiophene) (P3HT) were purchased from Aldrich Chemical Co. LTD., or synthesized by anion polymerization technique from doubly distilled corresponding monomers using *n*-butyllithium as an initiator, giving the polymers with monomodal molecular weight distributions with their polydipersity less than 1.2.[18] Polyaniline (PANi) was synthesized by the oxidation of aniline with ammonium persulfate as the oxidizing agent. The thin films of the polymers on Si substrates were irradiated by several kinds of ion beams from cyclotron accelerator at Japan Atomic Energy Research Institute, Takasaki Research Establishment, and developed by adequate solvents. The sizes and shapes of the nanostructure formed along particle trajectories were observed using a Seiko Instruments Inc. atomic force microscope (AFM).

Results and Discussion

1. Roughness of Nanostructures

A heavy ion particle impinging on target polymers can release high-density intermediates within a limited area of the ion projectile. Irradiation of the polymers results in a cross-linking reaction along an ion track, forming a cylinder-like structure (nano-wire) for each ion projectile. The non-cross-linked area can then be eliminated by development with an adequate solvent for each

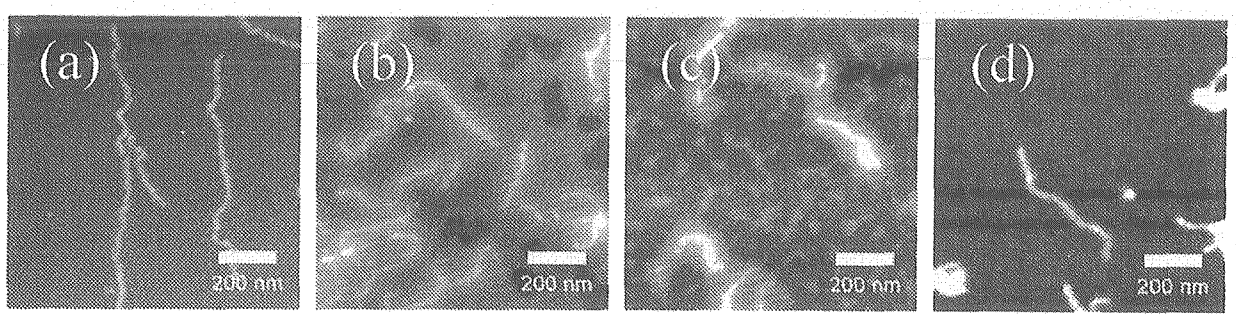

Fig. 1 AFM micrographs of nanostructures based on polystyrene derivatives produced by single particle negative tone imaging. The 1-D nanostructures were collapsed by the development, and observed as "lying" wires on the substrate. Images (a) – (d) were observed in the thin films of **PHS**, **PBrS**, **PClS**, and **PS**, respectively after irradiation of 560 MeV $^{129}Xe^{26+}$ ion beams at the fluence of $1 - 10 \times 10^9$ ions cm^{-2}.

polymer, utilizing the change in solubility induced by gelation of the polymers. The nano-wires become completely isolated on Si substrates. Figure 1 shows a series of AFM images of nano-wires on a Si substrate formed in polystyrene (**PS**), poly(vinyl-phenol) (**PHS**), poly(*p*-bromostyrene) (**PBrS**), and poly(*p*-chlorostyrene) (**PClS**), respectively. The correlation between the size (radii of the cross section of the nano-wires) and the molecular weight has been investigated precisely, showing clear increase in the radii with an increase in the molecular weight of target polymers.[9,10)]

The values of surface roughness were defined as the standard deviation (σ) of radii of the cross section in the AFM traces. Figure 2 shows the dependence of the values of σ on the degree of polymerization (N) of **PS**. According to the statistical theory on configuration of polymer chains, gyration radius (R_g) of polymer molecules is determined by following formula considering the impermeable rigid-body approximation;[10,19)]

$$R_g = aM^{\nu} = a\left(\frac{N}{M_m}\right)^{\nu} \qquad (1)$$

where M_m denotes the mass of a unit in a polymer chain. The correlation represented in Fig. 2 is well interpreted by eq. 1, giving the value of index ν as 0.758. The observed value of ν is close to the upper limit of ν: 0.8 which should be observed in case of complete-expanded chains. This is due to the surface approaching to a rich solvent (toluene for **PS**) of the polymers during development procedures, and drying without enough shrinking of the molecules. AFM traces of nano-wires based on the other polymers also estimates the values of σ, giving 2.5, 4.1, 4.3, and 5.3 nm for **PS**, **PClS**, **PHS**, and **PBrS**, respectively after the calibration of their molecular weight at 5.0×10^4 according to eq. 1. Backbone configurations of polystyrene derivatives have been investigated precisely in both solution and solid phases. On the basis of the good approximation of expanded-chain model in solution for the roughness estimates, the values of characteristic ratio (C_∞) of the polymer chain in each respective solvent used for the development procedure are given as 10.8, 11.1, 12.0, and 12.5 for **PS**, **PClS**, **PHS**, and **PBrS**, respectively.[20)] The C_∞ values show a striking contrast to the values of σ, thus this is the case giving the experimental evidence of the clear quantitative correlation between the surface roughness of the nanostructures and backbone configuration of the polymers.

2. Properties of Nanostructures

The nanowires based on **PANi** and **P3HT** can

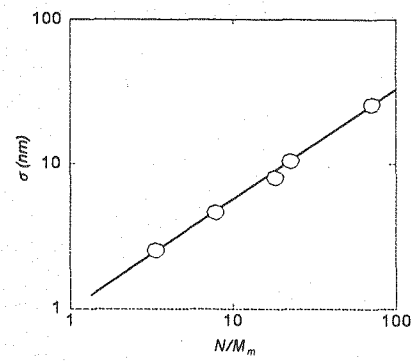

Fig. 2 Correlation between estimated values of edge roughness (s) and polymerization degree of **PS**s. Molecular weights of **PS**s were ranging from 5.2×10^4 – 1.1×10^6.

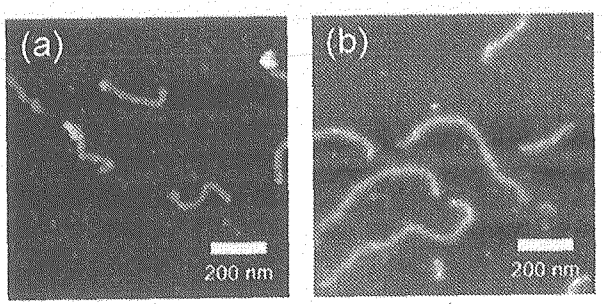

Fug. 3 AFM images of the nanowires based on **PANi** (a) and **P3HT** (b). The nanowires were formed by 450 MeV $^{129}Xe^{23+}$ and 500 MeV $^{197}Au^{31+}$ irradiation to the thin films at 1.0×10^9 ions/cm^2.

be also formed and observed clearly by the ion beam irradiation as shown in Fig. 3. The structure and the sizes would play a critical role in determining the physical properties of conducting polymers. Steady-state UV-Vis absorption maxima (λ_{max}) have been attributed to the π-π^* transition of the conjugated polymer backbone in poly-3-n-alkylthiophenes. [21, 22] The λ_{max} depended strongly on the conditions, showing remarkable shift as thermochromic or solvatochromic behaviors. The photoluminescence intensity of conjugated polymers and oligomers is strongly influenced by interchain interactions. In fact, in most cases, strong interactions among the chains, both in solid state and in aggregates in solution, have dramatic effects on the PL quantum yield of conjugated systems. [23]

The absorption bands attributed to the molecular aggregates were observed for the spectra of nanowires. However an intense peak of the spectrum of nanowires appears at 603 nm. The sharp fluorescence peak was observed at 700 nm for the nanowires based on **P3HT**, which was in contrast with the broad spectral features observed for the thin film. It should be noted that the relative quantum yield of the photoluminescence also increased drastically in case of the nanowires. This might be rationalized by considering that the conjugated electronic structures of the **P3HT** molecular aggregates were converted from indirect-gap to direct-gap semiconductors. The clear correlation was not observed in the optical properties of **PANi** based nanowires, because of the lower extinction coefficient and emission quantum yield relative to those of **P3HT**.

Conclusion

The formation of polymer nanowires by ion beam irradiation of carbon backborn polymers has been observed. The sizes (length and radius of cross-section of nanowires) and number density can be completely controlled by changing film thickness, molecular weight, LET, and fluenece. Characteristic opto-electronic properties observed for the various size of nanowires are different than those from the solid state, suggesting that the nanowires are not just the finely patterned analogs of the conjugated polymer materials.

References

1) S. Tsukuda, et al. J. Phys. Chem. B 108 (2004) 3407.
2) L. Calcagno, et al. Appl. Phys. Lett. 51 (1987) 907.
3) M. B. Lewis and E. H. Lee Nucl. Instrum. Methods, B69 (1992) 341.
4) Z. Chang and J. A. LaVerne, J.Phys Chem. B104 (2000) 10557.
5) S. Seki, et al. J. Phys. Chem. B 103 (1999) 3043.
6) J. L. Magee and A. Chattarjee: Kinetics of Nonhomogenious Processes, G. R. Freeman Ed., Chapter 4, p.171 (1987) (John Wiley & Sons, New York).
7) J. A. LaVerne and R. H. Schuler J. Phys. Chem. 98 (1994) 4043.
8) E. J. Kobetich and R. Katz: Phys. Rev. 170 (1968) 391.
9) Seki, S. et al. Adv. Mater. 13 (2001) 1663.
10) Seki, S. et al. Phys. Rev. B70 (2004) 144203.
11) N. Reber, et al. J. Membrane Sci. 193 (2001) 49.
12) J. Vetter and R. Spohr Nucl. Instr. Methods B 79 (1993) 691.
13) M. E. T. Molares, et al. Adv. Mater. 13 (2001) 62.
14) E. Ferain and R. Legras Nucl. Instr. Methods B 174 (2001) 116.
15) M. Delvaux, et al. Synthetic Metals 113 (2000) 275.
16) G.P. Patsis, et al. Microelectro. Eng. 75 (2004) 297.
17) E.W. Scheckler, et al., Jpn. J. Appl. Phys. 32 (1993) 327.
18) S. Seki, et al., J. Am. Chem. Soc. 126 (2004) 3521.
19) Flory, P.J., "Statistical Mechanics of Chain Molecules", Wiley Interscience, NewYork 1969.
20) Brandrup, J., et al., eds., "Polymer Handbook", Wiley Interscience, NewYork 1999, and references are therein.
21) R. D. McCullough, et al. J. Org. Chem. 58 (1993) 904.
22) A. Bolognesi, et al. Synthetic Metals 139 (2003) 303.
23) L. Magnani, et al. Synthetic Metals 84 (1997) 899.

JP0650222

3.6 Highly-sensitive Contaminant Analysis of Semiconductor Surface using Pulsed Cluster Ion Beams

K. Hirata*, Y. Saitoh**, A. Chiba**, K. Narumi***, Y. Kobayashi* and M. Fukuda**
National Institute of Advanced Industrial Science and Technology (AIST)*
Advanced Radiation Technology Center, JAERI**
Advanced Science Research Center, JAERI***

1. Introduction

Organic and metallic contaminants on the surface of a semiconductor wafer cause serious degradation on electrical performance of integrated circuit devices fabricated on the wafer. In order to optimize the manufacturing processes for high performance devices, analytical tools are required for the surface contaminations. Time-of-flight (TOF) secondary ion mass spectrometry is one of the most powerful tools to characterize the surface contaminants with high sensitivity. Mass analysis of secondary-ions is based on the phenomenon that secondary ions are ejected from the surface when the primary ions bombard the target. To TOF secondary ion mass spectroscopy, we have applied pulsed cluster ion beams, which give different secondary ion emission yields from those for monoatomic ions because of their peculiar irradiation effect [1),2)]. In this paper, we show that the emission yields of secondary ions originating from organic and metallic contaminants on silicon wafers are enhanced by cluster ion bombardments, which will be applicable to highly sensitive characterization of the contaminants by secondary ion mass analysis.

2. Experimental

Two samples with organic and metallic (Cr) 'contaminants' were prepared. A fresh point of the samples was bombarded for each measurement.

Positive Secondary ion (p-SI) TOF measurements for the samples were performed with a linear type TOF mass analyzer using pulsed monoatomic and cluster ion beams produced by a 3 MV tandem accelerator at the Japan Atomic Energy Research Institute (JAERI)/Takasaki[1-7]. Several improvements were made in the TOF system detailed in our previous paper to improve the mass resolution by shortening a half-width of the pulsed incident ion beam and extending a length of the TOF drift tube and to enhance the SI transmission efficiency by inserting an electrostatic lens with transmission grids between an extractor grid and a microchannel plate.

3. Results and discussion

Figure 1 shows the p-SI TOF spectra of organically contaminated Si for (a) 0.5MeV-C_1^+ (0.5MeV/atom-C_1^+), and (b) 4.0MeV-C_8^+ (0.5MeV/atom-C_8^+),

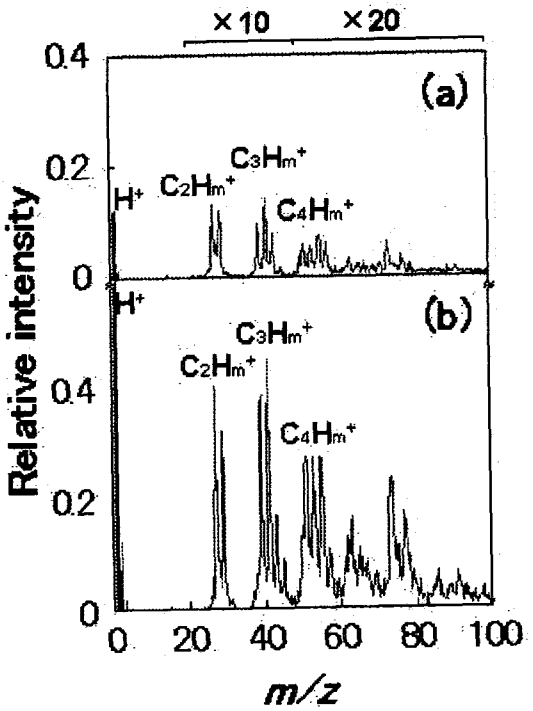

Fig.1 Positive secondary ion TOF spectra of organically contaminated Si wafer for (a) 0.5MeV-C_1^+ (0.5MeV/atom-C_1^+), and (b) 4.0MeV-C_8^+ (0.5MeV/atom-C_8^+). The relative intensity on the vertical axis is proportional to the SI emission yield per incident atom. The total area of the spectrum for 0.5MeV/atom-C_1^+ is equal to unity.

bombardments, respectively. The relative intensity on the vertical axis is proportional to the SI emission yield per incident atom. The major peaks observed in Fig.1 can be attributed to ions of singly charged atomic and molecular hydrogen, hydrocarbon, and organosilicon from the surface-contaminants. The peaks at m/z=1, and 2 correspond to H^+, and H_2^+, respectively. The peaks observed at 27-29, 39-43, and 51-57 are mainly due to hydrocarbon fragments $C_2H_m^+$, $C_3H_m^+$, and $C_4H_m^+$, respectively. The peak at m/z=73 can be assigned to $Si(CH_3)_3^+$.

For easy comparison of the yields of H^+, H_2^+, $C_2H_m^+$, $C_3H_m^+$, $C_4H_m^+$, and

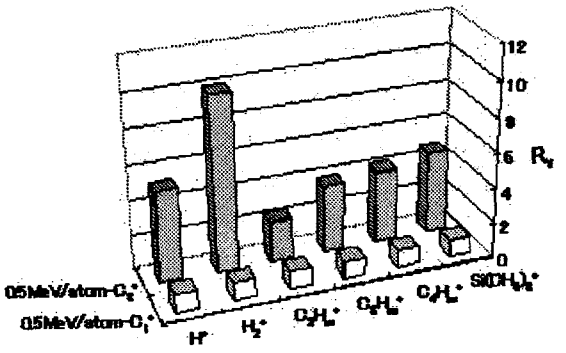

Fig. 2 Comparison of the yields for the major ions [H^+, H_2^+, $C_2H_m^+$, $C_3H_m^+$, $C_4H_m^+$, and $Si(CH_3)_3^+$] among the three spectra shown in Fig.1. For easy comparison, the scale of the vertical axis is defined as the ratio R_Y of the yield for the each ion to that for the corresponding ion upon the C_1^+ bombardment.

$Si(CH_3)_3^+$ between the spectra in Fig. 1, the ratio R_Y of the emission yield of each secondary ion for the C_8^+ bombardment to that of the C_1^+ bombardment is shown in Fig. 2. The figure reveals that the 0.5MeV/atom-C_8^+ impact provides higher R_Y values than the 0.5MeV/atom-C_1^+ impact although the primary ions of the same element bombard the same sample with the same velocity.

The considerably different R_Y among different peaks for 0.5MeV/atom-C_8^+ in Fig. 2 indicate that the enhancement effect of the cluster impact on the relative SI emission yield per incident atom depends strongly on ion-species. SI emission occurs via sputtering and ionization processes as a result of the energy deposition from the incident ion to the target. The SI emission processes are affected by the local density of deposited energy by a ion bombardment. The C_8^+ impact gives a deposited energy density distribution around the impact-point different from the C_1^+ impact because constituent atoms originating from the same cluster

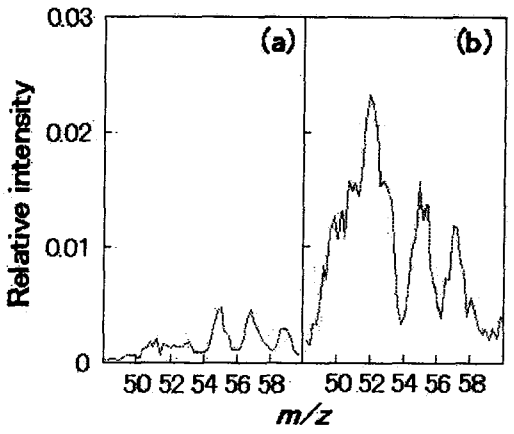

Fig.3 Positive secondary ion TOF spectra of metallically (Cr) contaminated Si for (a) 0.5MeV-C_1^+ (0.5MeV/atom-C_1^+), and (b) 4.0MeV-C_8^+ (0.5MeV/atom-C_8^+). The relative intensity on the vertical axis is proportional to the SI emission yield per incident atom. The total area of the spectrum for 0.5MeV/atom-C_1^+ is equal to unity.

simultaneously transfer their kinetic energy to a small area of the target surface. The difference in the deposited energy density around the point makes the sputtering and ionization processes for C_8^+ different from those for C_1^+, which probably provides the ion-specific R_Y values.

The cluster impacts also provide high emission yields of metallic SI from the metallically contaminated Si wafer. Figure 3 shows the p-SI TOF spectra of the Si contaminated by Cr for (a) 0.5MeV/atom-C_1^+, and (b) 0.5MeV/atom-C_8^+, bombardments, respectively. The relative intensity on the vertical axis is proportional to the SI emission yield per incident atom. The C_1^+ bombardment gives no clear peak at m/z=52 (Cr^+). In contrast, the C_8^+ bombardment results in intense peak at m/z=52, which indicate that the cluster impact is useful for highly sensitive detection of not only organic but also metallic contaminants on Si wafers.

In conclusion, the use of a cluster ion instead of a monoatomic ion as a primary ion provides higher emission yields of secondary ions originating from organic and metallic contaminants on Si wafers in the SI TOF measurements.

References

1) K. Hirata, Y. Saitoh, A. Chiba, K. Narumi, Y. Kobayashi, and K. Arakawa, Appl. Phys. Lett., **83**, 4872 (2003).
2) K. Hirata, Y. Saitoh, A. Chiba, K. Narumi, Y. Kobayashi, and Y. Ohara, Appl. Phys. Lett., **86**, 044105 (2005).
3) Y. Saitoh, S. Tajima, I. Takada, K. Mizuhashi, S. Uno, K. Ohkoshi, Y. Ishii, T. Kamiya, K. Yotsumoto, R. Tanaka, E. Iwamoto, Nucl. Instrum. Methods Phys. Res. B **89**, 23 (1994).
4) K. Narumi, K. Nakajima, K. Kimura, M. Mannami, Y. Saitoh, S. Yamamoto, Y. Aoki, and H, Naramoto, Nucl. Instrum. Methods Phys. Res. B **135**, 77 (1998).
5) Y. Saitoh, K. Mizuhashi, and S. Tajima, Nucl. Instrum. Methods Phys. Res. A **245**, 61 (2000).
6) K. Hirata, Y. Saitoh, K. Narumi, Y. Nakajima, and Y. Kobayashi, Nucl. Instrum. Methods. Phys. Res. B **193**, 816 (2002).
7) K. Hirata, S. Saitoh, K. Narumi, and Y. Kobayashi, Appl. Phys. Lett., **81**, 3669 (2002).

This is a blank page.

4. Inorganic Materials

JP0650223

4.1 Swelling Behavior and Microstructural Change of SiC/SiC Composites under Simultaneous Irradiation of Hydrogen, Helium and Silicon Ions

T. Taguchi*, N. Igawa*, S. Miwa**, T. Imada,** E. Wakai***,
S. Jitsukawa*** and A. Hasegawa**
Neutron Science Research Center, JAERI/Tokai*
Department of Quantum Science and Energy Engineering, Tohoku University**
Department of Materials Science, JAERI/Tokai***

1. Introduction

Continuous silcon carbide (SiC) fiber reinforced SiC matrix (SiC/SiC) composites are known to be attractive candidate materials for fusion power reactors in part due to their high temperature strength and low residual radioactivity following neutron irradiation. However, the effect of transmutation gasses on SiC, which are not produced in the current fission-neutron damage studies, is largely unknown. Of particular concern are the high levels of helium (He) and hydrogen (H) transmutation atoms produced by the 14.1-MeV fusion neutrons. The production rates of He and H in SiC in first wall region are approximately gas/dpa ratios of 130 appm He/dpa and 40 appm H/dpa[1]. Irradiation-induced microstructural changes may be accelerated in SiC/SiC composites under the fusion condition since He is insoluble in virtually all materials and is captured easily within vacancy clusters produced during cascade formation.

In this study, the swelling behavior and microstructural change of SiC/SiC composites under simultaneous irradiation of H, He and Si ions were investigated.

2. Experimental procedure

2.1 Materials

The 2D plane weave of Hi-Nicalon Type S and Tyranno SA SiC fiber fabrics as reinforcement were used in this study. The SiC/SiC composites were fabricated using the forced thermal gradient chemical vapor infiltration (F-CVI) process at Oak Ridge National Laboratory. The details of fabrication procedure are described elsewhere[2].

2.2 Irradiation

Simultaneous ion irradiation was carried out at TIARA (Takasaki Ion Accelerators for Advanced Radiation Application) facility of JAERI. The specimens were irradiated at 800, 1000 and 1300 °C by 6.0 MeV Si^{2+} ions, 1.0 MeV He^{+} ions and/or 340 keV H^{+} ions. Various combinations of ions were examined in this study as summarized in Table 1. The implantation of He^{+} and H^{+} ions was conducted using an aluminum foil energy degrader in order to control He and H distribution in the depth range of about 1.0-1.8 μm from the specimen surface. The displacement damage, He, H and Si concentration as a function of depth from the surface in SiC calculated by TRIM code[3] is shown in Fig. 1.

3. Results and discussion

Cross-sectional TEM microphotographs of the

Table 1 Irradiation condition of simultaneous ion-beams in this study

Condition ID	Kinds of ions	Displacement damage (DPA)	He concentration (appm)	H concentration (appm)
Single (Si)	Si^{2+}	10	0	0
Dual	Si^{2+}+He^{+}	10	1300	0
Triple	Si^{2+}+He^{+}+H^{+}	10	1300	400
Triple (Hx10)	Si^{2+}+He^{+}+H^{+}	10	1300	4000

irradiated SiC matrices at about 1.4 μm depth from the surface are shown in Fig. 2. For implantation at 800, 1000 °C, He bubbles were not observed in the matrix irradiated by single Si ions. However, He bubbles were observed in the matrix irradiated under dual (Si+He) or triple (Si+He+H) ion-beams. These results revealed that the simultaneous ion-beams irradiation enhanced the formation of stable He clusters. It was thought that this was caused by the simultaneous formation of vacancies by the silicon ion damage and these vacancies were stabilized in the presence of helium. Once stable vacancy clusters are formed they continue to add helium leading the helium bubbles observed. These He bubbles were preferentially formed at the grain boundaries.

The average size of He bubbles in the composites irradiated at 800 °C increased with increasing the amount of implanted H ions. On the other hand, the average size of He bubbles in the composites irradiated at 1000 °C decreased with increasing the amount of implanted H ions. The number density of He bubbles slightly increased with increasing the amount of implanted H ions. These results indicated that the simultaneously implanted H might prevent the migration of He and the growth of He bubbles might be inhibited. Hojou has reported that H atoms implanted simultaneously with He atoms would contribute to forming a large number of nuclei for bubbles formation at room temperature by in-situ TEM observation technique[4]. The result in this study is corresponding to this previous work.

At irradiation temperature of 1300 °C, He bubbles were observed in the matrix irradiated by single He ions, dual and triple ion-beams. Hasegawa has reported that He bubbles were formed in He pre-implanted matrix of SiC/SiC composite annealed at 1400 °C for 1 hour[5]. Such voids (average size: 5.8 nm) were also observed in the matrix irradiated by single Si

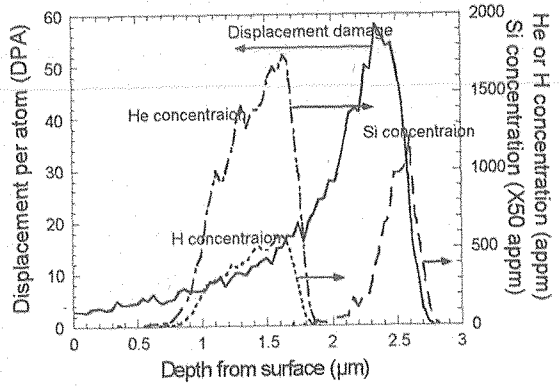

Fig. 1. Displacement damage, He, H and Si concentration as a function of depth from the surface in SiC calculated by TRIM code

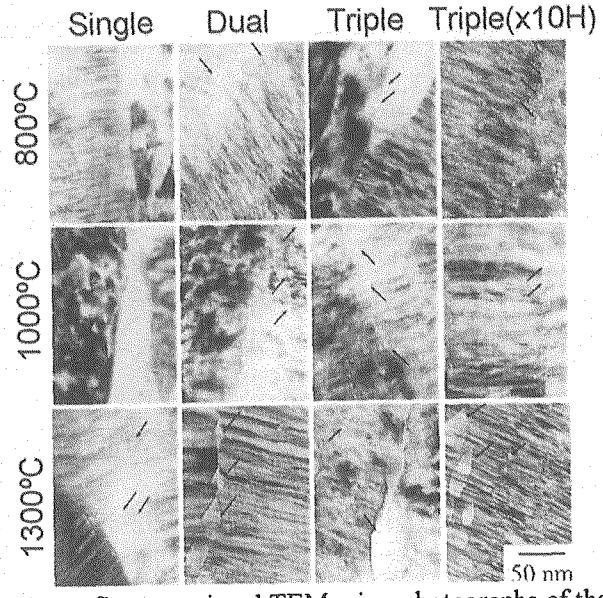

Fig. 2. Cross-sectional TEM microphotographs of the irradiated SiC matrices at about 1.4 μm depth from the surface.

ions although gas atoms such as He and H were not implanted. Price reported that neutron irradiation at 1250 °C produced voids in β-SiC and the average size of voids was 4.2 nm[6]. The results in this study are in good agreement with the previous studies. Helium bubbles in the matrix irradiated by single He ions and the voids were mainly formed at grain boundary. Helium bubbles in the matrix irradiated by dual and triple ion-beams were formed both at grain boundary and within the grain.

The average size of He bubbles at the grain boundary was much larger than that in the grain. The reason is that the recombination of He clusters was accelerated since the mobility of He

interstitial and vacancy at grain boundary is larger than that in the grain.

Both average size and number density of He bubbles increased with increasing irradiation temperature. He bubbles formed at irradiation temperature of 1000 and 800 °C were observed only in the He implanted region (0.7-1.8 μm from the surface). On the other hand, He bubbles at 1300 °C were also observed outside of He implanted region; the formation depth-range of He bubbles was from 0-3.0 μm. The mobility of He interstitial and induced vacancy increased with increasing the irradiation temperature. Therefore, He bubbles grew easily and the number of visible He bubbles increased at higher temperature.

The estimated swelling amount of SiC matrix by the average size and number density of He bubbles were shown in Fig. 3. At the irradiation temperature of 800 °C, swelling amount increased with increasing the amount of implanted H. On the other hand, at irradiation temperature higher than 1000 °C, swelling amount was maximized by triple ion irradiation, which is the same environment as that in fusion reactors.

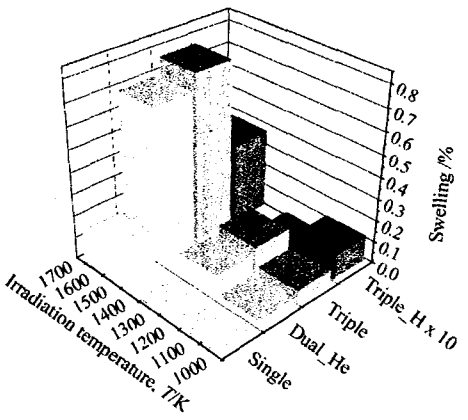

Fig. 3 Estimated swelling of SiC matrix by average size and number density of He bubbles.

4. Conclusions

(1) At the irradiation temperature of 1000 °C, He bubbles were not observed in the matrix irradiated by single Si ions or single He ions while He bubbles were observed in the matrix irradiated by dual or triple ion-beams. Simultaneous existence of the induced vacancies by Si ion beam and implanted He ions contributed to the formation of He bubbles.

(2) The average size of He bubbles in the matrix decreased with increasing the density of implanted H ions. The number density of He bubbles increased when the implantation temperature was increased from 1000 to 1300°C and the amount of implanted H was increased.

(3) At the irradiation temperature of 1000 °C, He bubbles in the matrix were mainly formed near the grain boundary. At the irradiation temperature of 1300 °C, He bubbles in the matrix were formed both at grain boundary and within the grains. The average size of He bubbles at grain boundary was much larger than that near the grain.

(4) The swelling of SiC matrix at irradiation temperature of 800 °C increased with increasing the amount of implanted H. On the other hand, the swelling of SiC matrix at irradiation temperature higher than 1000 °C was maximized by triple ion irradiation.

References:

1) L.L. Snead, R.H. Jones, A. Kohyama, P. Fenici, J. Nucl. Mater. 233-237 (1996) 26.

2) T. Taguchi, N. Igawa, S. Jitsukawa, T. Nozawa, Y. Katoh, A. Kohyama, L. L. Snead, J. C. McLaughlin, Ceram. Trans. 144 (2002) 69.

3) J. F. Ziegler, J. P. Biersack, U. Littmark, The Stopping and Ranges of Ions in Matter, vol. 1, Pergamon Press, New York, 1985.

4) K. Hojou, S. Furuno, K. N. Kushita, H. Otsu, K. Izui, Nucl. Instr. and Meth. in Phys. Res. B 91 (1994) 534.

5) A. Hasegawa, M. Saito, S. Nogami, K. Abe, R. H. Jones, H. Takahashi, J. Nucl. Mater. 264 (1999) 355.

6) R. J. Price, J. Nucl. Mater. 48 (1973) 47

4.2 Dose Dependence of Radiation Hardening of Ion-irradiated F82H Measured by Nano-indentation

T. Sawai*, M. Ando**, N. Okubo*, K. Matsuhiro**, E. Wakai*, S. Jitsukawa*, K. Oka***, M. Murata***, S. Ohnuki*** and I. S. Kim****
Department of Materials Science, JAERI*
Department of Fusion Engineering Research, JAERI**
Graduate School of Engineering, Hokkaido University***
Faculty of Textile Science and Technology, Shinshu University****

1. Introduction

Reduced Activation Ferritic Steels (RAFS) are the most promising structural materials for the blanket of fusion reactors. An 8Cr-2W-TaV steel, F82H is the present candidate RAFS in JAERI[1]. Different types of degradation and deformation depending on the service temperatures will limit the service life of RAF. Several types of coolants and breeder materials systems are being discussed and JAERI plans to build a water-cooled ceramic breeder system[2]. Temperature of blanket structural materials in such systems is lower than about 550 C, which varies depending on the design. Radiation embrittlement is the largest concern to use RAFS in this temperature range. Generally materials are more brittle at lower temperatures and more ductile at higher temperatures. The temperature at which the transition takes place is known as the ductile to brittle transition temperature (DBTT). Irradiation raises the DBTT of RAFS. DBTT should never exceed a reasonable temperature, for example 100 C, for the structural safety of the blanket during the maintenance time.

To measure loss of toughness and DBTT shift due to irradiation is very difficult using ion-irradiated specimens, because the thickness of damaged region in an ion-irradiated specimen is very small and toughness tests usually require a large specimen volume. Radiation hardening has some relationship with the DBTT shift[3, 4] and it has been measured by nano-indentation.

In this study, radiation hardening of F82H was measured up to 100 dpa and the dose dependence is analyzed.

2. Experimental

Chemical composition of F82H is Fe-8Cr-2W-0.2V-0.04Ta-0.1C. Plates were normalized at 1313 K for 0.5 hr, followed by air-cooling. Tempering was performed at three different temperatures, 973, 1023, 1073 K for 1hr. Specimens were irradiated in MT chamber at 543 and 633 K up to 105 dpa (measured at 0.6 μm) with 10.5 MeV Fe^{3+} ions at TIARA facility. Further details of irradiation are given elsewhere[5]. Nano-indentation tests were performed at loads to penetrate about 400 nm in irradiated specimens using a UMIS-2000 (CSIRO, Australia). Hardness values were obtained at 35 points on the irradiated surface and averaged. With this indentation condition, plastic deformation up to about 1000 nm[6] is reflected to the measured hardness. Figure 1 shows the depth

distribution of displacement damage and indentation depth.

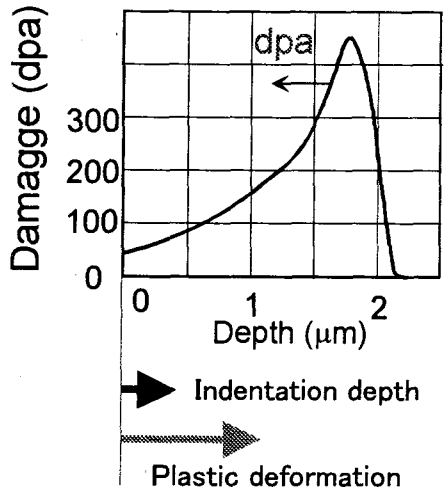

Fig. 1 Damage profile of 10.5 MeV Fe^{3+} ion irradiation to F82H. Indentation depth and plastic deformation depth in hardness test are also given.

3. Results and Discussion

Change of hardness of F82H with different tempering conditions irradiated at 543 K up to 43 dpa is shown in Fig. 2. The higher the tempering temperature is, the lower the initial hardness of the specimen. The hardness increases with irradiation dose in all specimens and the specimen tempered at 1073 K shows the lowest hardness even after 43 dpa. This result suggests that F82H tempered at higher temperature, which has a higher toughness before irradiation, would have a higher toughness after irradiation.

Dose-dependent hardening behavior in 633 K irradiation up to 105 dpa is shown in Fig. 3. Note that Fig. 3 represents the increment of hardness due to irradiation while Fig. 2 represents measured hardness. As shown in Fig. 2, radiation hardening is largest in 1073 K-tempered

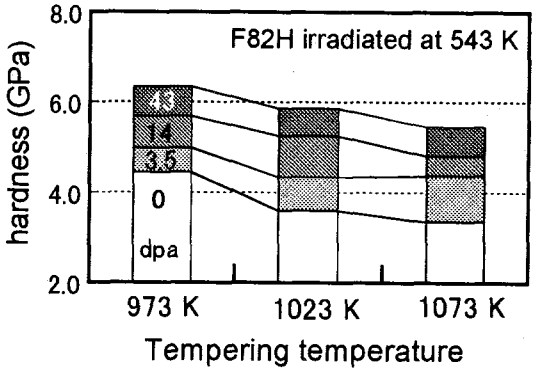

Fig. 2 Radiation hardening of F82H tempered at different temperatures irradiated at 543 K.

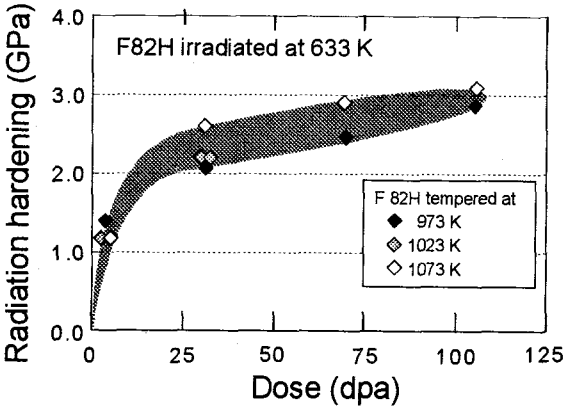

Fig. 3 Dose-dependent hardening of F82H irradiated at 633 K.

specimen, which has the lowest initial hardness. It is also show that almost one third (1/3) of hardening up to 105 dpa is achieved in initial 5dpa. Radiation hardening rate decreases rapidly with irradiation dose and such hardening behavior is often fitted by $(\phi t)^{1/n}$. Fitting present data with $(\phi t)^{1/n}$ suggests n=4.

It should be noted, however, that present dose-dependent hardness data are obtained with ion-irradiated specimens, which have a depth-dependent damage profile. Measured hardness data reflect the different hardness at different depth

with different weight of contribution.

Local hardness $h(\phi t,x)$ at depth x with irradiation dose ϕt is experessed as follows assuming hardening proportional to $(\phi t)^{1/n}$;

$h(\phi t, x) = k \{ \phi t \times D(x)\}^{1/n}$,

where D(x) is the damage distribution and k is a constant.

Depth-dependent sensitivity profile of nano-indentation is $\mu(x)$, where $\int \mu(x)dx = 1$. Measured hardness H is given by the product of above two profiles;

$$H = \int \mu(x)\, h(\phi t, x)\, dx$$
$$= k \int \mu(x) \{ \phi t \cdot D(x) \}^{1/n} dx$$
$$= k (\phi t)^{1/n} \cdot \int \mu(x) \{D(x)\}^{1/n} dx .$$

Because $\int \mu(x)\{D(x)\}^{1/n} dx$ is independent on ϕt, $H \propto k (\phi t)^{1/n}$. Assuming a hardening behavior of the material proportional to $(\phi t)^{1/n}$, radiation hardening measured by nano-indentation which has a depth-dependent sensitivity profile on an ion-irradiated specimen which has depth-dependent damage profile would be also proportional to $(\phi t)^{1/n}$. Therefore hardening behavior derived from Fig. 3, $H=(\phi t)^{1/n}$ and n=4, can be regarded as the hardening behavior of the material.

References

1) M. Tamura et. al., J. Nucl. Mater. 141-143(1986)1067-1073.
2) S. Konishi et. al., Fus. Eng. Des. 63-64(2002)11-17.
3) S. Jitsukawa et. al., J. Nucl. Mater, 329-333(2004)39-46.
4) T. Sawai et. al., Fus. Sci. and Technolo., 44 (2003) 201-205.
5) E. Wakai et. al., JAERI-Review 2001-039 "TIARA Annual Report 2000" p.141.
6) M. Ando et. al., J. Nucl. Mater., 307-311(2002)260-265.

4.3 Microstructures of Ion-irradiated Zirconium

S. Yamada*, M. Kinoshita** and T. Sawai***
Materials Science Research Laboratory, Central Research Institute of Electric Power Industry (CRIEPI)*
Nuclear Technology Research Laboratory, CRIEPI**
Department of Materials Science, JAERI***

1. Introduction

In order to reduce costs of electric power generation using boiling water reactors (BWRs), it is useful to develop fuel cladding tubes tolerant of high burnup conditions. The cladding used in the current BWRs is made from Zircaloy-2 which is the Zr base alloy with predominant addition of Sn (~1.5wt. %). The cladding shows excellent performance of corrosion resistance, however it has been reported that an axial crack in the cladding was observed at the power rump test[1]. The principal cause of the crack is not understood yet, and hence it is important to elucidate the mechanism of ductility loss for the improvement of the cladding properties. We think that a characterization of microstructures is useful to overcome the problem because the ductility loss should be influenced by irradiation damages. It is generally known that <a> and <c> component dislocations are formed in Zircaloy-2 by neutron irradiation[2]. The former dislocation is formed on the prismatic plane $(11\bar{2}0)$ and the latter one is on the basal plane (0001).

We have reported that microstructures of Zircaloy-2 cladding irradiated up to 60 MWd/kgU in the commercial reactor (Ringhals-1, Sweden) showed a dose-dependence and also the damage structure of <c> component dislocations could be simulated in Zircaloy-2 using ion irradiation[3].

The purpose of this study is to characterize microstructures of Zr irradiated by ions to study the effects of alloy components and irradiation temperatures on the formation of damage structures.

2. Experimental

The bulk specimens of Zr were irradiated by 12 MeV Zr^{4+} ions up to 20 dpa at 573 and 673 K using 3 MV tandem accelerator at TIARA facilities of JAERI. Thin foils for transmission electron microscopy (TEM) were prepared using the focused ion beam (FIB) method and were characterized using 300kV field emission TEM at CRIEPI.

3. Results and discussion

Figure 1 shows a bright-field (BF) TEM image of unirradiated Zr. Dislocations were not clearly observed. Precipitates seen in the figure are hydrides.

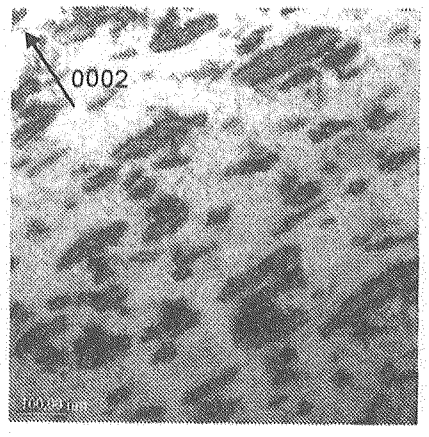

Fig. 1 BFTEM image of unirradiated Zr.

Figure 2 shows a BFTEM image of Zr irradiated by the ions at 573 K. The specimen was extracted at the depth of 3μm from the front surface. Monte-Carlo simulation code predicts that a damage peak is at the depth of ~2.5μm. Line dislocations roughly parallel to the trace of the basal plane and loops with a large diameter ~100 nm were observed. A dark-field (DF) TEM image obtained using the reflection g=0004 showed that the line dislocations and the loops are visible and this implies that the defects have the Burgers vectors of the <c> component dislocations.

Figure 3 shows a BFTEM image of Zr irradiated by the ions at 673 K. The specimen was extracted at the depth of 3μm from the front surface. Straight lines with a ~30 nm spacing parallel to the basal plane were formed. The damage structure agrees well with that of Zircaloy-2 irradiated by neutron. A DFTEM image obtained using the reflection g=0004 showed that the dislocations are visible and this implies that the defects are the <c> component dislocations.

From the results, we can infer the reason why the <c> component dislocations were formed at high irradiation temperature of 673 K and not formed at 573 K. At low temperature it is easy for vacancy to recombine with interstitial and thus the <c> component dislocation loops with vacancy are not formed. On the other hand, at high temperature a mobility of vacancy is larger than that of interstitial, therefore the accumulation of the vacancy to the growing vacancy structure preferentially occurs and thus the <c> component dislocations are formed.

The results are summarized as follows;

(1) The damage structure of <c> component dislocations formed in Zircaloy-2 by neutron irradiation can be simulated in Zr by using Zr ion irradiation.

(2) The line dislocations and large loops (diameter~100 nm) were formed in Zr after the irradiation of 20 dpa with Zr^{4+} ions at 573 K, on the other hand, aligned <c> component dislocations were formed at 673 K.

References

1) Report on High Burnup Fuel Safety Experiments, Nuclear Power Engineering Corporation, March 2002 (in Japanese).

2) M. Griffiths, R. W. Gilbert, V. Fidleris, R. P. Tucker and R. B. Adamson, J. Nucl. Mater. 150 (1987) 159.

3) S. Yamada, M. Kinoshita and T. Sawai, JAERI-Review 2002-035(2002)158.

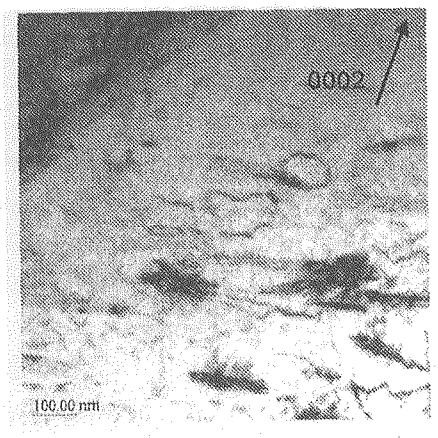

Fig. 2 BFTEM image of Zr irradiated at 20 dpa with 12 MeV Zr^{4+} ions at 573 K.

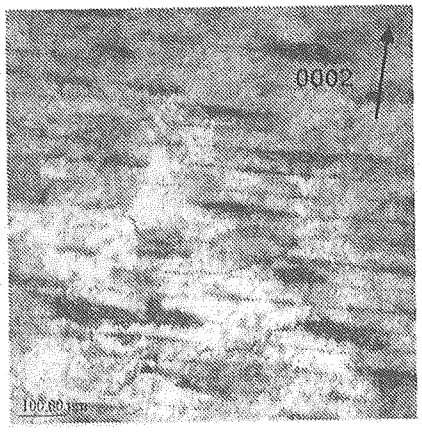

Fig. 3 BFTEM image of Zr irradiated at 20 dpa with 12 MeV Zr^{4+} ions at 673 K.

4.4 Mechanical Properties of Austenitic Stainless Steel Ion-irradiated under External Stress

I.Ioka*, M.Futakawa**, T.Suzuki*, K.Kiuchi* and T.Naoe***
Department of Nuclear Energy System, JAERI*
Center for Proton Accelerator Facilities, JAERI**
Graduate School of Ibaraki University***

1. Introduction

Irradiation creep has been studied extensively to provide data that can be used for component analysis of fusion, fast breeder and light water reactors. It is now generally recognized that the irradiation creep data were in agreement with an empirical equation[1]. Moreover, there have been many irradiation experiments done under applied stress to investigate stress effects on microstructural evolution. It is reported that the total nucleation rate of Frank loops was increased with increasing external stress[2]. However, there are few studies on the effect of external stress on mechanical properties of the material under irradiation.

A triple ion irradiation can simulate the irradiation environment by producing displacement damage in the material while simultaneously implanting H and He. However, the ion-irradiated area is limited to the very shallow surface layer (<2μm depth) of the specimen so that the irradiation damage is distributed in a thin layer. Hence, a nanoindentation technique combined with inverse analysis using a finite element method (FEM) was applied to examine the influence of ion irradiation on the mechanical properties of the thin layer and derive the constitutive equation of the damaged layer[3]. The purpose of this study is to evaluate the mechanical properties of the irradiated material under external stress.

2. Experimental procedure

The material tested is type 304 stainless steel in the solution-annealed condition. The chemical composition is given in Table 1. The configuration of the specimen and the ion irradiation holder for applying the required stress are shown in Fig. 1. The thickness of specimen is about 0.5mm. It has three different cross-sections (1.5mm, 1.75mm, 2.0mm in width) in order to be irradiated at different stress at the same time. The surface of specimen was polished with #2400 paper. The spring was used in order to apply the required stress in the specimen during irradiation. The strain gauge was attached at M division (1.75mm in width) of the specimen to measure the tensile strain before ion-irradiation. The spring was adjusted so that the tensile strain at M division might become about 0.2%. The applied stress, about 228MPa, at M division was estimated from the stress-strain curve of type 304SS. In this time, the applied stresses of L division (2.0mm in width) and S division (1.5mm in width) were about 200MPa and 266MPa, which were calculated from each cross section. The strain of L and S divisions were estimated from strain-stress curve about 0.1% and 0.5%, respectively. The strain gauge was removed before irradiation.

The specimens were irradiated in triple (12MeV Ni^{3+}, 1.1MeV He^{+} and 380keV H^{+}) ion beam mode at a temperature of 300°C using the triple ion beam facility (TIARA) at JAERI. The temperature of the specimen was measured by an infrared thermometer (THERMAL VISION, Nikon Co.). The

temperature of the spring was lower than 50°C during irradiation at 300°C. It was believed that the stress applied to the specimen was maintained during irradiation. The displacement damage in the specimen was mainly attributed to Ni^{3+} ion irradiation. The peak dose was about 10dpa around 2μm. The He^+ and H^+ ions were implanted in depth ranges from 1.0 to 1.5μm using aluminum foil energy degraders. The concentrations of He^+ and H^+ ions in the implanted range were 11 appmHe and 91 appmH, respectively, which correspond to LWR condition. The dose was about 5dpa in the implanted range of He^+ and H^+ ions.

The nanoindentation test was carried out on the surfaces of the irradiated and unirradiated specimens at room temperature. A conical indenter that had a hemispherical apex with radius of 1.2μm was used. A DUH-200 (Shimadzu Co.) testing machine was used for the nanoindentation test. The load was applied with a loading speed of 2.6×10^{-3} N/s, held 1 second and then removed. During loading and unloading, the load was continuously monitored along with the displacement with a resolution of 19.6mN and 0.01μm, respectively.

The interaction between the irradiated thin layer and substrate (unirradiated region) complicates the deformation under the indenter and makes it difficult to characterize the irradiated thin layer. An inverse analysis was carried out using an explicit FEM code which enables us to roughly analyze a large deformation that accompanys contacting behavior. In the analysis, the indenter and specimen were treated as axisymmetric two-dimensional bodies to improve the efficiency of the calculation. The indenters were modeled as a perfectly rigid. The fineness of the mesh size was determined by the required accuracy. The minimum element size of 0.05μm was near the apex contacting zone.

The constitutive equation of the material employed in the model was assumed to be a simple power-law which is generally believed to be applicable to normal metallic materials as follows:

$$\sigma = E\varepsilon \qquad \sigma \le \sigma_y \tag{1}$$

$$\sigma = A(\varepsilon_0 + \varepsilon)^n \tag{2}$$

$$\varepsilon_0 = (\sigma_y / A)^{1/n} - (\sigma_y / E) \qquad \sigma > \sigma_y \tag{3}$$

where σ is true stress, ε true strain, E Young's modulus, σ_y yield stress, A work hardening coefficient and n work hardening exponent. Therefore, we have to identify the following material constants; σ_y, A and n through the inverse analysis on the L-D curve. The inverse analysis method is described in detail elsewhere[3].

3. Results and discussion

Figure 2 shows the ratio of hardness in the irradiated region to that of the unirradiated region in the S, M and L divisions. The result for a stress-free specimen is added to Fig.2. The irradiated layer of all specimens was hardened by irradiation. The ratio of the stress-free specimen was higher than those of the stressed specimens. It is well known that the increase in hardening of solution-annealed material is higher than that of cold-worked material in the same irradiated condition. The degree of hardening did not depend on the external stress level in this test condition. It was considered that little difference in hardening was attributed to the applied stress levels.

The constitutive equations identified for the irradiated layer with or without applied stress were used for the FEM analysis to obtain the

stress-strain relationship. A two dimensional axisymmetric model as shown in Fig.3 was used for the analysis. The model has a high mesh density around the center of the specimen. The deformation of the specimen was calculated by the FEM code. Figure 3 shows the calculated nominal stress-strain curves of the irradiated specimen with or without applied stress. The analytical results indicated irradiation hardening and ductility loss from the very shallow irradiated layer. It was considered that there was little influence of applied stress on yield stress and nominal stress-strain curve of the irradiated specimen in this test condition.

4. Summary

The mechanical properties of type 304 austenitic stainless steel irradiated under external stress were examined using a nanoindentation technique combined with inverse analysis using a finite element method. The degree of hardening did not depend on the external stress level in this test condition. From the analytical results, there was little influence of applied stress on yield stress and nominal stress-strain curve of the irradiated specimen in this test condition.

References

1) F.A.Garner, M.B.Toloczko, J. Nucl. Mater. 251(1997)252.

2) H.Tanigawa. Y.Katoh, A.Kohyama, Nucl. Instru. and Methods in Phy. Resea. B 102(1995)151.

3)I.Ioka,M.Futakawa,Y.Nanjyo,T.Suzuki, K.Kiuchi,JAERI-Review2002-35(2002)149.

Table 1 Chemical composition of the material in wt%

Materials	Fe	C	Si	Mn	Cr	Ni
Type 304SS	bal.	0.063	0.49	1.45	18.72	10.27

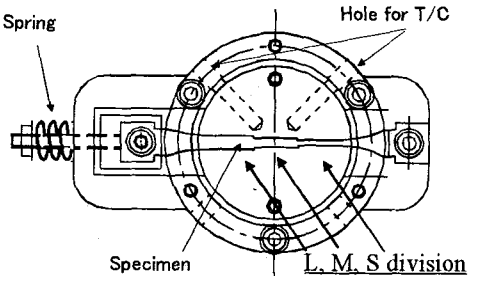

Fig. 1 Configuration of the specimen and the ion irradiation holder

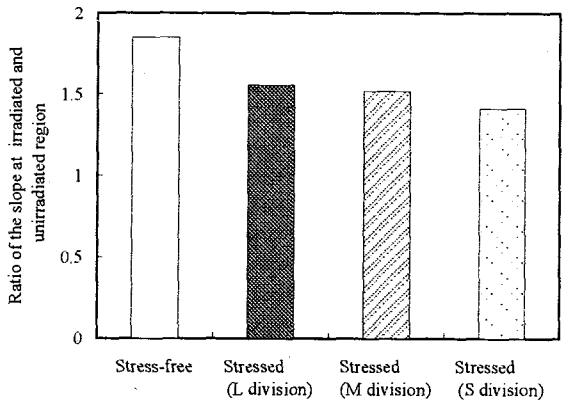

Fig.2 Ratio of hardness in irradiated region to that of the unirradiated region in the S, M and L divisions

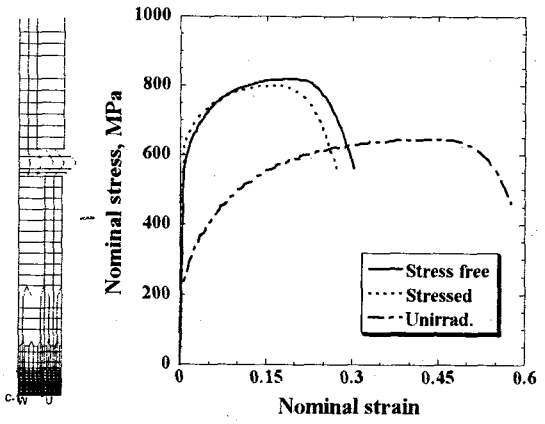

Fig.3 Calculated nominal stress-strain curves of the stressed and stress-free irradiated specimens

4.5 Triple Ion Beam Irradiation Effect on Structural Material of Mercury Target for the Spallation Neutron Source

H. Kogawa*, M. Futakawa*, T. Naoe** and S. Zherebtsov***
Center for Proton Accelerator Facilities, JAERI*
Graduate School of Ibaraki University**
Satellite Venture Business Laboratory, Ibaraki University***

1. Introduction

The pulsed spallation neutron source of the MW class is being developed in the world. The Japan Atomic Energy Research Institute (JAERI) develops and constructs the pulsed spallation neutron source under the J-PARC (Japan Proton Accelerator Research Complex) project in corporation with the High Energy Accelerator Research Organization (KEK). The neutron produced in mercury target will be used in innovative researches associated with the material and life sciences.

Material of mercury target container will be degraded by proton and neutron irradiation. Moreover, a cavitation will occur and cavitation bubbles will collapse in the mercury to make pitting damage on the container contacting with liquid mercury[1]. Since the degradation by the pitting damage has a correlation with hardness of the material[2], it is supposed as one of methods to extend a lifetime of the target container by hardening the surface of the container material. We conducted the triple-ion irradiation test on nitriding or curburizing hardening-treated surfaces of the type 316 austenitic stainless steel to simulate the irradiation damage[3]. These materials hardly showed the change of the hardness after the irradiation and we consider these hardening treatments are useful to suppress the pitting damage.

Surface treatment by laser alloying was carried out on the type 316 SS which can realize hard layer thicker than that of the nitriding and curburzing treatment and the triple-ion irradiation test on this material was carried out at the TIARA facility.

In this report, the change of the mechanical property is described based on the results of the hardness test and the observation by the scanning electron microscope (SEM).

2. Experimental

The laser alloying surface treatment was applied on the surface of a substrate of type 316 SS, which is the candidate material for the mercury target container. In this laser alloying, mixed powder of aluminum and silicon (Al:Si = 3:2) was used for an alloy on the surface of the substrate by using the laser under the optimized condition for this alloying. The size of the test piece was 3 x 2 x 6 mm^3.

The triple-ion irradiation test was carried out at the TIARA facility in consideration of the spallation condition. The cross-section of the specimen including the laser alloying layer was irradiated at 200°C by 12 MeV Ni^{3+}, 380 keV H^+ and 1.1 MeV He^+. The amount of radiation damage was 10 dpa, and the amount of injected H^+ and He^+ was about 2000 appm/dpa and about 200 appm/dpa, respectively, taking into account of the spallation condition. The

hardness of the irradiated surface was measured by the micro-indenter. The SEM observation and a height distribution measurement on the irradiated surface were carried out by using the SEM and the laser microscope, respectively.

3. Result

Figure 1 shows the hardness distribution of the laser alloying surface layer. The thickness of the hardening layer is 150 μm from the surface as shown in Fig.1. The hardness of the laser alloying layer decreased to about 1000 Hv from 1200 Hv due to the irradiation. Figure 2 shows the change in hardness of the laser alloying material due to the irradiation of the triple ion beam comparing with the case of the nitriding material and the carburizing material which were irradiated under the same condition as that of the laser alloying case. Hardness of the laser alloying layer was the highest in the non-irradiation case. However, the hardness of the laser alloying layer decreased after the irradiation while those of the nitriding and carburizing layers hardly decreased.

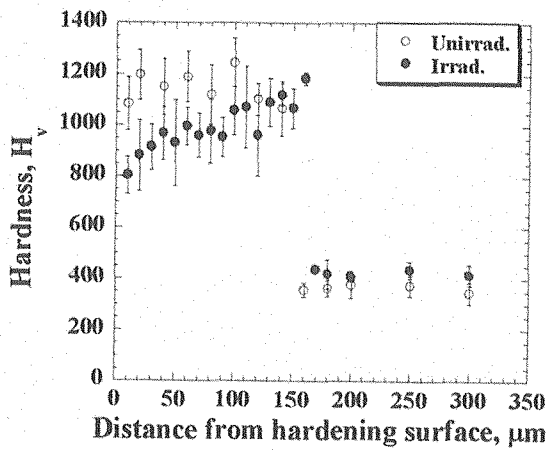

Fig.1 Hardness distribution along the distance from surface.

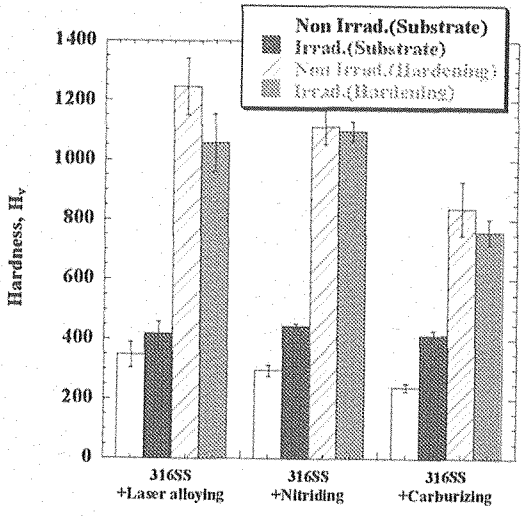

Fig.2 Effect of irradiation on hardness

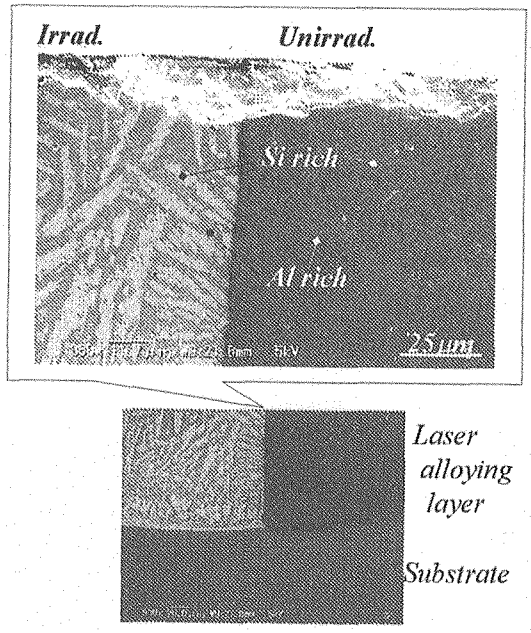

Fig.3 SEM micrograph of the laser alloying surface layer

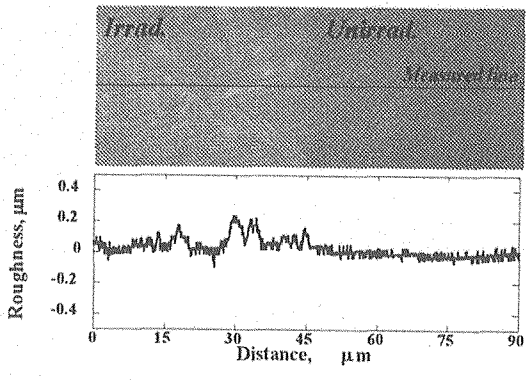

Fig.4 Irradiated surface of the laser alloying surface layer and depth profile

Figure 3 shows the SEM image of the laser alloying layer. Change of color in the irradiation part was observed in the laser alloying layer. And, a needle-shaped pattern which separated in two colors was observed in both the irradiation part and the non-irradiation part. The white colored part was richer in the silicon than the gray part from a result of the elemental analysis by the EDAX setting on the SEM; Al:Si = 1:5 in the white part and Al:Si = 4:1 in the gray part.

Figure 4 shows the height distribution image and the height distribution of the laser alloying layer measured by the laser microscope. In the height image, the needle-shaped pattern was observed as well as the pattern observed by SEM as shown in Fig.3. And the white colored part (Si rich part) in the irradiation area obtained by SEM observation corresponded with the higher part observed by the laser microscope. Though the non-irradiation part was flat, a swell was observed in the irradiation part from the result of the height distribution measurement.

Figure 5 shows the harnesses of the gray and white parts shown in Fig.3 before and after the irradiation. The hardness of the white part decreased after the irradiation, which was Si rich and swelled after the irradiation. The decrease of the hardness of the laser alloying layer, as shown in Fig.1 and Fig.2, seems to be caused by the decrease of the hardness of the white part, which was Si rich part and swelled after the irradiation.

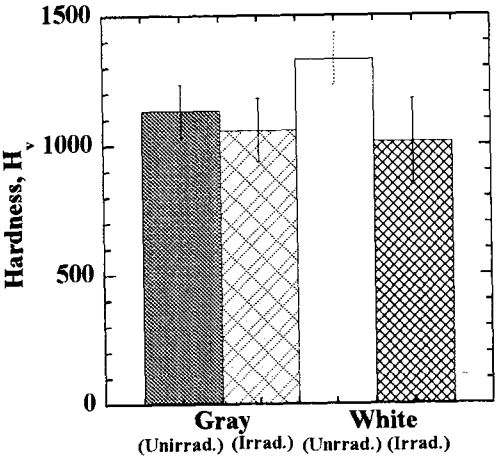

Fig.5 Comparison of the harnesses of the gray and white parts shown in Fig.3 before and after irradiation.

4. Summary

The effect of the irradiation on the mechanical property of the Al-Si laser alloying surface layer was investigated by hardness test and SEM observation. The hardness of the laser alloying layer decreased after the irradiation of 10 dpa at 200℃ though it showed the high hardness before the irradiation.

References

1) M.Futakawa, T.Naoe, H.Kogawa, C.C.Tsai and Y.Ikeda, Journal of Nuclear Science and Technology 40 (2003) 895-904.
2) M.Futakawa, T.Naoe, H.Kogawa, S.Ishikura and H.Date, Journal of the Society of Materials Science Japan 53 (2004) 283-288.
3) M.Futakawa, A.Naito, I.Ioka, and H.Kogawa, JAERI-review 2004-025 (2004) 165-167.

4.6 Evaluation of Material Property Change on Advanced Fuel Cladding Material by Triple Ion Irradiation

Y. Ishijima*, I. Ioka*, Y. Nanjyo*, K. Kiuchi* and K. Fujimura**

Department of Nuclear Energy System, JAERI*

Japan Atomic Power Company**

1. Introduction

The advanced fuel cladding material, adapted to the 100GWd/t of ultra high burn-up extension with Mixed Oxide (MOX) fuel, is developed on the view points of the radioactive waste reduction, Pu effectual utilization and improvement of economical efficiency. A stabilized austenitic stainless steel with high Cr concentration and high gamma phase stabilization, Fe-25Cr-35Ni-0.2Ti, has been adopted for the candidate fuel cladding material. In addition, niobium alloy, Nb-5Mo, has been adopted to improve pellet-clad interaction (PCI) resistance for the candidate liner material. The purpose of this study is to clarify the reliability of the joint composed of austenitic stainless steels cladding (Fe-25Cr-35Ni-0.2Ti) and niobium alloy liner(Nb-5Mo) under the ultra high burn-up condition.

For evaluating a change in material characteristics, the joint, Fe-25Cr-35Ni-0.2Ti and comparisons (SUS304L, SUS316L) were irradiated with triple ion beams of Ni^{3+}, He^{+} and H^{+} that simulate ultra high burn-up condition. Then, microstructure changes around the joint interface between Fe-25Cr-35Ni-0.2Ti and Nb-5Mo were investigated. In addition, corrosion resistance for Fe-25Cr-35Ni-0.2Ti and comparisons were investigated.

2. Experimental

2.1 Alloys

Compositions of candidate alloys and comparisons are shown in Table 1.

Fe-25Cr-35Ni-0.2Ti was made through vacuum induction melting (VIM) and electron beam melting (EB) methods. Nb-5Mo was made through EB method. The joints were made by hot rolling (rolling ratio: 0.7, rolling temperature: 973-1773 K) after Fe-25Cr-35Ni-0.2Ti and Nb-5Mo were enclosed in a steel capsule in vacuum.

2.2 Irradiation specimen

The block specimen was rectangular parallelepiped block of 6x2x3mm^3 cut from the joint and the joint interface was allocated at the center of specimen. The disk of ϕ. 3x0.2 mm was cut from Fe-25Cr-35Ni-0.2Ti and comparisons. The

Table 1 Chemical compositions of candidate and conparison materials.

		Composition (wt%)													
	Material	Fe	Nb	Cr	Ni	Ti	C	N	O	S	Si	Mn	P	Mo	Ta
Candidate	Fe-25Cr-35Ni-0.2Ti	bal.	-	24.90	36.49	0.22	0.0003	0.0007	0.0002	0.001	<0.005	<0.01	0.001	-	-
	Nb-5Mo	0.03	Bal.	-	-	-	<0.001	0.0034	0.0025	-	-	-	-	5.01	0.15
Comparison	316LSS	bal.	-	17.54	12.55	-	0.008	-	-	0.001	0.43	0.83	0.023	2.11	-
	304LSS	bal.	-	18.43	9.78	-	0.009	-	-	0.001	0.490	0.85	0.020	-	-

block specimen was polished by water abrasive paper to #2400 on the irradiation side. The disk specimen was buff-polished on the irradiation side and then it was electro-chemically polished prior to irradiation.

2.3 Irradiation

For simulating the neutron irradiation under 100GWd/t of ultra high burn-up extension, the specimens were irradiated by triple ion beams, 12MeV Ni^{3+}, 380KeV H^{+} and 1.1MeV He^{+}, at TIARA facility in JAERI Takasaki. In irradiation, temperature of the specimen was kept at 573 K. He^{+} and H^{+} were irradiated through the energy degraders to be spread at the implanting range. Distributions of displacement damage and each implanted ion in the specimen were calculated with SRIM 2003 code. He^{+} and H^{+} were assumed to be located at 1.0-1.5 μm from the bombarded surface based on the calculation. Displacement damage was adjusted up to 15 dpa at the depth and H and He concentrations were adjusted to 20 appm/dpa and 2 appm/dpa, respectively. The displacement damage was smaller than a value (50dpa) under the condition of 100GWd/t.

2.4 Micro hardness measurement

The nanoindentation test was carried out on the surface of irradiated and unirradiated specimen around the joint interface at room temperature. The applied load was 5g with 0.45g/sec. A DUH-601 (Shimadzu Co.) testing machine with a triangular pyramid indenter was used for the test.

2.5 Microstructure and microchemistry observation

Microstructure observation was carried out by transmission electron microscopy (TEM). TEM specimen was cut out with 10x10x0.1 μm by focused ion beam method (FIB) at right angle to the joint interface.

Microchemistry measurement was carried out by Auger electron spectroscopy (AES).

2.6 Corrosion resistance evaluation

Corrosion test was carried out by Straus corrosion test with the corrosion time of 1sec to prevent loss of test specimen. After corrosion test, microstructure observation was carried out by scanning electron microscopy (SEM) to evaluate grain boundary corrosion.

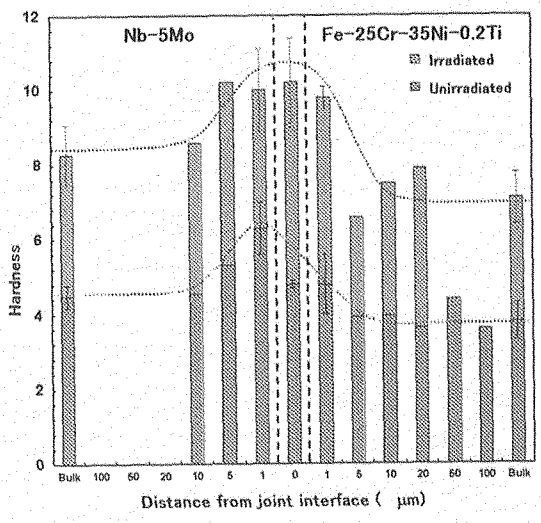

Fig. 1 Nanoindentation results of irradiated and unirradiated joint interface.

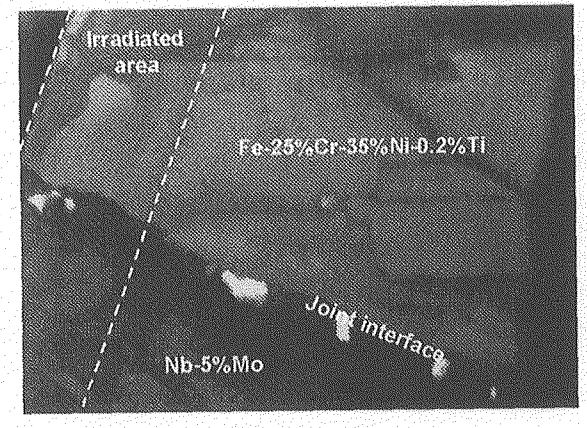

Fig. 2 TEM micrograph of irradiated joint interface.

3. Results and Discussion

The results of micro hardness measurement are shown in Fig. 1. After irradiation, the hardness of the joint interface was uniformly increased in 4gf/μm^2 but it was no remarkable. The results of TEM observation are shown in Fig. 2. Irradiation defect was observed as darker contrast uniformly but no growth of defect was observed at the irradiation condition. White spots were observed at the joint interface, but no diffraction pattern and no element were observed. Thus, it was suggested that these white spots were considered to joining defects. The results of AES observation are shown in Fig. 3. This result shows that no radiation induced segregation and precipitation has occurred.

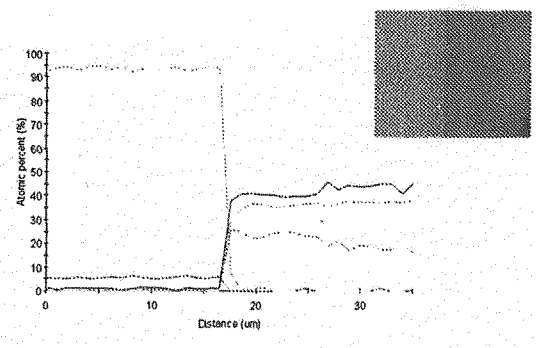

Fig. 3 AES result of joint interface.

Above results suggests that the remarkable degradation could not occur in joint interface under the ultra high burn-up condition. The results of SEM observation are shown in Fig. 4. After corrosion test, Fe-25Cr-35Ni-0.2Ti and SUS316L showed good corrosion resistance. However, SUS304L showed white line parallel to grain boundary. It was considered that the white line appeared due to radiation induced segregation. This result suggests that Fe-25Cr-35Ni-0.2Ti has good corrosion resistance after irradiation.

4. Conclusion

The joint interface showed no remarkable radiation hardening, good microstructure stabilization and no radiation induced segregation. In addition, Fe-25Cr-35Ni-0.2Ti showed good corrosion resistance. As a result, the candidates have good reliability under the ultra high burn-up condition.

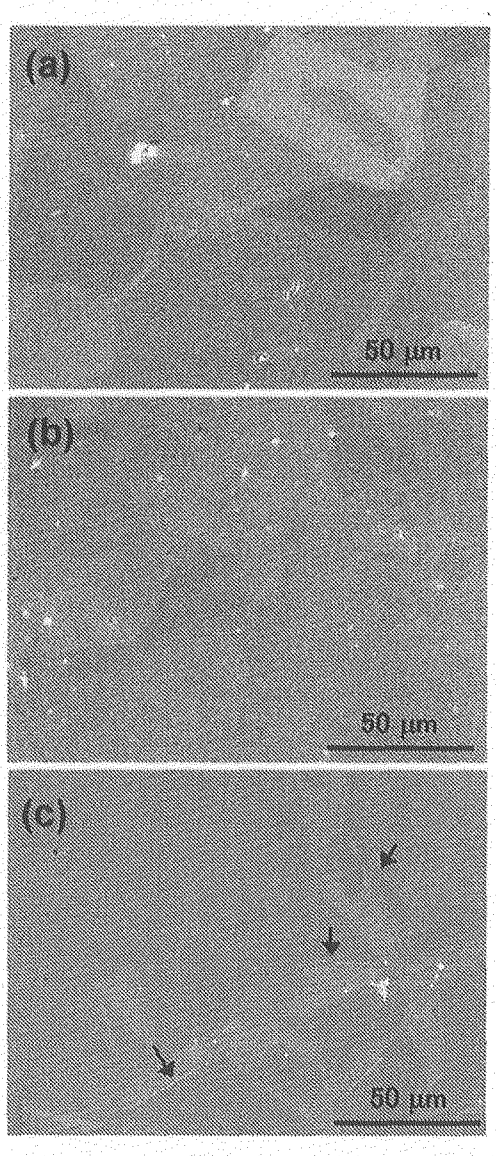

Fig. 4 SEM micrographs after corrosion test, (a) candidate stainless steel, (b) SUS316L, (c) SUS304L

4.7 Observation of Microstructural Changes in Li_2TiO_3 Caused by Multi-ion Beam Irradiation

D. Yamaki, T. Nakazawa, T. Tanifuji, T. Aruga and S. Jitsukawa
Department of Materials Science, JAERI

1. Introduction

Li_2TiO_3 is regarded as one of the most suitable candidates for the solid tritium breeder material of D-T fusion reactors[1]. It is known that, in an operating fusion reactor, the radiation damage in Li_2TiO_3 will be caused by fast neutrons, energetic tritons and helium ions generated in $^6Li(n,\alpha)^3H$ reaction. The irradiation damage caused by such radiation may result in the microstructural changes, and the changes may affect the characteristics of Li_2TiO_3 such as tritium release behavior. Thus the study of irradiation defects and microstructural change caused by irradiation in Li_2TiO_3 is essential to evaluate its irradiation performance.

Simulation of the fusion reactor environment and hence the study of a synergistic effect of atomic displacement damage in Li_2TiO_3 are presumed to be approached by a simultaneous irradiation with "triple" ion beams which consist of O^{2+}, He^+ and H^+ ion beams. In the previous study, the formation of the anatase (TiO_2) layer on the surface of Li_2TiO_3 by irradiation with triple ions has been found. It was also clarified that the formation was mainly caused by the effect of knock on with O^{2+} ion beam irradiation[2-6], and the amount of the formed anatase was strongly affected by the radiation dose in displacement per atom (dpa). In addition, the defects generated by irradiation would trap hydrogen near the surface. In the present study, the results of the FT-IR photoacoustic spectroscopy (PAS) with Li_2TiO_3 samples irradiated with the single beams, with the triple ion beams simultaneously and with the triple ion beams sequentially were analyzed to study the relation between the irradiation effects and the microstructural change.

2. Experimental

The characteristics of the Li_2TiO_3 samples used in this experiment were described in ref.3. The Li_2TiO_3 samples were irradiated at 573K with the single and the triple ion beams of 0.25 MeV H^+, 0.6 MeV He^+ and 2.4 MeV O^{2+}. The fluence of the respective ions was about $3x10^{20}$ - $1x10^{21}$ ions/m^2 .The ion energies were so chosen that the projected ranges of the irradiated ions in Li_2TiO_3 were around 2 μm[2]. For estimating the effects of simultaneous multi-ion beams irradiation, simultaneous and sequential irradiation of the three kinds of ion beams were performed.

Using the FT-IR photoacoustic spectroscopy (PAS) technique, the non-irradiated sample, the samples irradiated with the triple ion beam and the samples irradiated by the single ion beams were examined in order to obtain information near the end of the ion range. The photoacoustic signal was generated from the surface layers of the sample with a thickness of some micrometers, which is a function of the mirror velocity of the FT-IR interferometer and wave number. In this

case, the mirror velocity was 2 cm/s that corresponds to the thickness of about 15-5 μm for 400-4000 cm^{-1}, so that the spectra of irradiated samples are a superposition of spectra of irradiated and non-irradiated zones of the sample.

3. Results and discussion

The FT-IR PAS spectrum of the non-irradiated sample is shown in Fig. 1. The characteristic peaks in FT-IR PAS spectra were observed around 680, 780, 880, 1090, 1430, 1480, 1570, 3150 and 3450 cm^{-1}. In comparison to the reported spectra of TiO_2 and Li_2TiO_3, 680 and 780 cm^{-1} peaks are identified from Ti-O bond, and 1570, 3150 and 3450 cm^{-1} peaks are from the O-H bond in hydroxyls adsorbed on or near the surface[3].

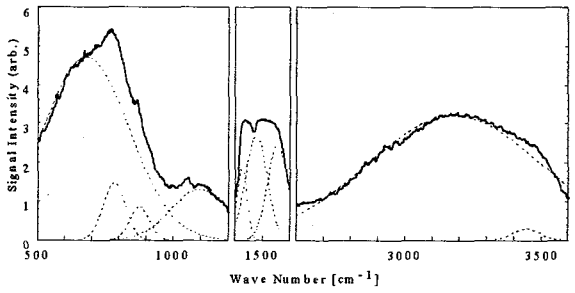

Fig. 1 FT-IR PAS spectrum of non-irradiated Li_2TiO_3 sample. Dashed lines are the results of peak analysis.

Among the observed peaks, irradiation effect is clearly found for 780 and 3450 cm^{-1} peaks. Figure 2 shows the relation between dpa and the 780 cm^{-1} peak area from the Ti-O bond, for each irradiation. The dpa was estimated with the TRIM code. It is shown that the peak area increases in proportional to the dpa, and any difference is not observed in the dependence of the peak area on dpa among the single, the simultaneous triple and the sequential triple ion beams irradiation, as shown in Fig.2.

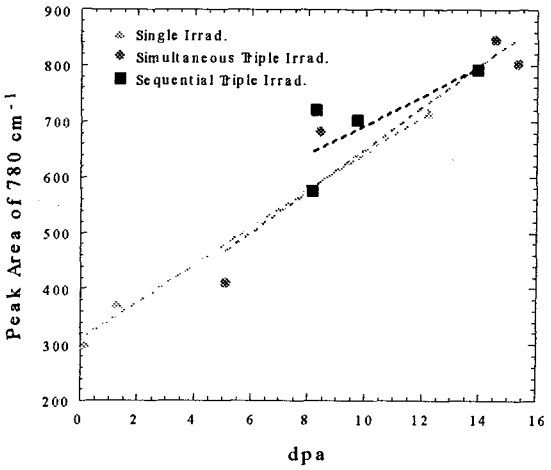

Fig. 2 Dependence of the 780 cm^{-1} peak area on dpa.

Figure 3 shows the relation between dpa and the increase of 3450 cm^{-1} peak area, which is due to the O-H bond. For the single and the simultaneous triple irradiation, the peak area increases proportionally to the dpa, respectively. However, the increase of the peak area for the simultaneous triple irradiation seems to be smaller than that for the single irradiation. For the sequential triple irradiation, the peak area for the samples which irradiated with O^{2+} after simultaneous dual irradiation of He^+ and H^+, and with He^+ after simultaneous dual irradiation of O^{2+} and H^+ seems to have similar dependence on dpa to that for the case of simultaneous triple ion beams. On the other hand, increase of the peak area in the samples irradiated with H^+ after simultaneous dual irradiation of He^+ and O^{2+}, and with He^+ and H^+ simultaneously after O^{2+} irradiation seems to be smaller than that for the simultaneous triple irradiation samples. This result may suggest that H^+ implantation affects the generation of hydroxyl near the surface by trapping hydrogen in the irradiation defects and the effect of implantation is larger in the case

where the implantation is performed after introducing the defects than that performed simultaneously.

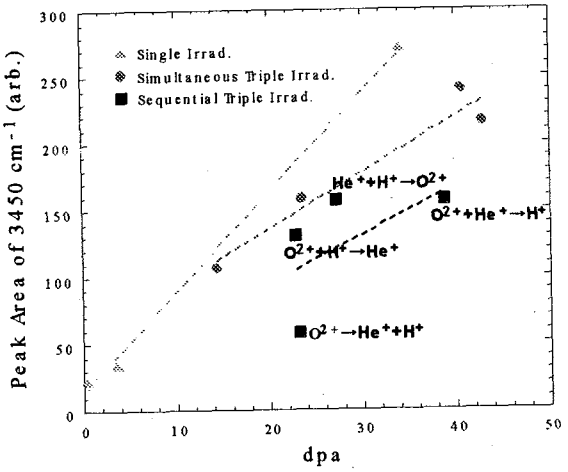

Fig. 3. Dependence of the 3450 cm^{-1} peak area on dpa. Notation for the sequential irradiation as "A → B" means that irradiation of beam B was performed after closing of irradiation of beam A.

4. Conclusion

The microstructural changes in Li_2TiO_3 irradiated with the H^+, He^+ and O^{2+} beams were observed by FT-IR PAS. The results suggest that the amount of TiO_2 formed is proportional to the dpa and that the method of irradiation, that is, single, simultaneous triple or sequential triple, does not affect the dependence of formation of TiO_2. On the other hand, the amount of defects generated by irradiation, which is considered to trap hydrogen near the surface, is found to be affected by the method of irradiation. The results suggest that the H^+ irradiation after introducing the defects may degrade the amount of hydroxyl generated near the surface. Further study of the effects of H^+ irradiation is needed.

References

1) P.Gierszewski, Report no CFFTP G-9561, 1995.
2) T. Nakazawa, V.Grishmanovs, D.Yamaki, Y.Katano, T.Aruga and A.Iwamoto, in: Proceedings of the 2000 International conference on Ion Implantation Technology, 2000, p.753-756.
3) D.Yamaki, T.Nakazawa, T.Tanifuji, T.Aruga, S.Jitsukawa and K.Hojou, J.Nucl.Mater. 329-333 (2004)1279-1282.
4) D.Yamaki, T.Nakazawa, T.Aruga, T.Tanifuji, S.Jitsukawa and A.Iwase, JAERI-Review 2002-035 (2002)133-135.
5) D.Yamaki, T.Nakazawa, T.Aruga, T.Tanifuji, and S.Jitsukawa, JAERI-Review 2003-033 (2003)162-164.
6) D.Yamaki, T.Nakazawa, T.Aruga, T.Tanifuji, and S.Jitsukawa, JAERI-Review 2004-025 (2004)173-175.

4.8 In-situ TEM Observations of Mobility of Interstitial-type Defect Clusters in Cu and Au under Irradiations with Heavy Ions

H. Abe*, N. Sekimura** and H. Itoh ***
Nuclear Professional School, University of Tokyo*
Department of Quantum Engineering and Systems Science, University of Tokyo**
Department of Materials Development, JAERI***

1. Introduction

Irradiation with ions and neutrons introduces lattice defects in materials. When kinetic energy of more than a few keV is transferred to a primary knock-on atom, dense displacements, so-called a displacement cascade is generated. It is characterized as a local volume of the order of 10^3 to 10^4 atoms spontaneously melted and rapidly cooled to leave vacancies and interstitial atoms. Defect clusters may therefore be formed after the cooling phase and can be simultaneously observed with transmission electron microscopes (TEM) interfaced with ion accelerators. The recent molecular dynamics simulations and experimental investigations [1-3] claimed that the formation of tiny crowdion-related interstitial-type dislocation loops associated with displacement cascades in pure metals. By in-situ TEM work [1,2] were successful to observe interstitial-type defect clusters were detected at the temperature of vacancy-mobile regime. Due to their size and short lifetime, such the defects have not been detected by the conventional TEM. Development of modified weak-beam dark-field (WBDF) method, which allows highest resolution detecting weak strain field around defects, was required. The purpose of this study is to summarize experimental evidences of highly-mobile and crowdion-related interstitial clusters by in-situ TEM observations under ion irradiations.

2. Experimental procedure

Well-annealed copper and gold disks were electrochemically perforated to achieve electron-transparent thin foils. Irradiation was performed with 240 keV Cu^+ ions or 900 keV Xe^{3+} ions and 5 x 10^{11} ions/cm^{2}s at temperatures ranging from 573 K to 823 K. Taking the irradiation geometry into account, projected ranges from the sample surface were estimated as 57 and 110 nm for the Cu and Xe ions, respectively, by TRIM calculations. Thickness of the observed regions was fixed at 50 nm, so as to achieve the identical implantation rate and to allow quantitative analysis such as areal density measurements of defect clusters. Microstructural evolution was observed mainly with the WBDF technique (**n** = [001], **g** = 200, **g** (4-6**g**)). The sample geometry and the g vector were carefully chosen to minimize sample vending effect on the microstructure. The image was videotaped with time resolution of 1/30 s and analyzed without image processors to achieve the maximal time resolution.

3. Results and discussion

Majority of defect clusters formed under ion irradiation was vacancy-type clusters (V-clusters) and stacking fault tetrahedra (SFTs); their lifetime ranges below tens of seconds. In addition to the V-clusters, the interstitial-type ones (I-clusters) were observed to have lifetime of several thirtieth seconds at temperatures from 673 to 823 K.

Some of them became mobile, indicating sessile-to-glissile transition of I-clusters. The Burger's vectors of sessile and glissile defects are presumed to be b= 1/3 {111} (111) and b=1/2 {110} (110), respectively, according to molecular dynamics simulations. The glissile defects were typically several nm in diameter and short lifetime less than several thirtieths of a second.

The typical features of the mobile defects were (1) one-dimensional back-and-forth migration with an amplitude of approximately 5 nm and a frequency of 1 s^{-1} or more, and (2) one-directional motion with velocities ranging from 50 to $>10^3$ nm/s. The mobility of the defects appeared to be significant in <110> directions. Further, the defect motion was retarded by an increase in the irradiation fluence, indicating the motion was influenced by accumulation of point defects in matrix.

The formation rate of the mobile defects was investigated as a function of irradiation temperature, ion species and ion flux. The higher formation rate for irradiations with heavier ions and a monotonous decrease in the formation within the investigated temperature were observed. The ratio of the formation probability of glissile clusters for Xe against Ar was estimated to be 2.5 to 4 depending on the temperature. On the contrary, estimation of cascade formation by an application of TRIM code gives the ratio of 6. The result suggests elimination of the glissile clusters among densely distributed subcascades. The result is consistent with the MD simulation results wherein the bundled crowdions are formed at the periphery of the displacement cascades.

The probability of sessile-to-glissile transition per ion (p) was observed to be nonlinear against the ion flux (ϕ):

$$p \propto \phi^{1.4}$$ (for 240 keV Cu).

The deviation from linearity indicates reactions among individual objects and impacts, whereas the linearity is generally interpreted that an object transforms into the other form by an impact. The pre-existing sessile clusters transform into glissile ones presumably through intercascade reactions. Another expected factor on the nonlinearity is the change in stability of the interstitial-type defect clusters influenced by evolution of point defects.

A model for the observed phenomena is, therefore, proposed as follows: glissile defects, presumed to be identical to a bundle of crowdions, are formed during the displacement cascade process. Due to the low activation energy for the crowdion bundle motion, a large diffusion length in micrometers is achieved even at low temperatures. The motion of crowdion bundles is retarded by lattice defects introduced under irradiation because they work as diffusion obstacles.

4. Conclusions

Simultaneous microscopic observations under ion irradiations were performed in Cu and Au in a TEM interfaced with an ion accelerator. The interstitial-type glissile defects, which have high mobility and short lifetime under ion irradiation at temperatures of vacancy-mobile regime, were successfully observed. A proposed mechanism has partly been confirmed with molecular dynamics simulations.

References

1) H. Abe, N. Sekimura and T. Tadokoro; Materials Transactions, 46 (2005) 433-439
2) H. Abe, N. Sekimura, Y. Yang; J. Nucl. Mater. 323 (2003) 220–228.
3) H. Abe, N. Sekimura, R.E. Stoller, S.J. Zinkle; 3rd JUPITER –II Workshop on Interaction of Modeling and Design of Materials Systems for Fusion Blankets (CD-ROM).

JP0650231

4.9 Growth Mechanism of Cubic Titanium Nitrides Thin Films by Nitrogen-Implantation

Y. Kasukabe*, J. J. Wang**, T. Yamamura**, S. Yamamoto*** and M. Yoshikawa***
International Student Center, Tohoku University*
Department of Metallurgy, Tohoku University**
Department of Material Development, JAERI***

1.Introduction

Cubic titanium nitride (TiN_y) of NaCl-type has widely been used for many purposes such as a hard wear-resistant coating in cutting tools, a diffusion barrier in microcircuits, etc.[1),2)] Recently, it was reported that NaCl-type (110)- and (001)-oriented TiN_y crystallites were "epitaxially" grown by nitrogen (N-) implantation into CaF_2-type (110)-oriented TiH_x and (03•5)-oriented hcp-Ti in deposited Ti films held at room temperature (RT).[3)] However, the detailed "epitaxial" nitriding mechanism of Ti films during N-implantation have not yet been understood.

The purpose of this study is to elucidate the nitriding mechanism of deposited-Ti films. In this paper, the "epitaxial" growth mechanism of TiN films, especially the changes in the bond strength, by N-implantation were examined by *in-situ* transmission electron microscope (TEM) observations, *in-situ* electron energy loss spectroscopy (EELS), and a self-consistent charge discrete variational (DV)-Xα molecular orbital (MO) calculation.

2.Experimental

Detailed descriptions of the preparation of deposited-Ti films were presented in the earlier paper.[3)] The 100-nm-thick Ti films were deposited by an electron-beam heating method in an ultra-high vacuum onto thermally cleaned NaCl substrates held at RT. The implantations of N_2^+ ions with 62 keV into the deposited Ti films held at RT were performed in the 400 kV analytical and high resolution TEM combined with ion accelerators at JAERI- Takasaki.[4)] According to the Monte Carlo simulation using the SRIM2003 code, the projected range of N_2^+ with 62 keV was 55 nm, and thus most of the implanted ions are thought to be retained inside the Ti films. The N- concentrations in Ti films were able to be estimated from the implantation dose measured by a Faraday cage. The maximum dose in this experiment was 3.66×10^{17} ions/cm^2, which corresponded to the N/Ti ratio of 0.645 (the average atomic concentration of N in the Ti film).

3.Results and discussion

In-situ observations by TEM elucidated that deposited Ti films grown on thermally cleaned NaCl (001) surfaces held at RT consisted of (03•5)-oriented hcp-Ti (lattice constants: a=0.296 nm, c=0.471 nm) and (110)-oriented CaF_2-type TiH_x (lattice constant: a=0.441 nm). The areas where the TiH_x was grown, had the band-like contrast elongated along the <110> direction of TiH_x and NaCl. The N-implantation into the Ti films results in the epitaxial growth of the (001)- and (110)-oriented NaCl-type TiN_y (N/Ti=0.645, lattice constant: a=0.422 nm).

Figures 1 and 2 show electron energy loss spectra taken from the nitriding area of TiH_x and from that of hcp-Ti, respectively. Analysis of EELS spectra has elucidated that the loss energy (about 20 eV, indicated by ▼ in Fig. 1(a)) due to the excitation of a plasma oscillation for TiH_x is different from that (about 17.5 eV, indicated

by ▼ in Fig. 2(a)) for hcp-Ti. The loss peak (about 47 eV) denoted by the line of Ti3p-3d is due to the Ti3p-3d resonant photoemission.

The loss peak indicated by ▼ in Fig. 1 (b) has been shifted to lower loss energy, compared with that in Fig 1 (a). This means the release of H from the TiH_x. On the other hand, there is no shift of the loss peak indicated by ▼ in Fig. 2 (a)-(b). In light of these results, it can be concluded that the release of H from the TiH_x occurs preferentially rather than the occupation of N in O-sites of the H-escaped fcc-Ti sublattice, in the early N-implanting stage.

Now, the loss peak due to the plasma excitation in both Figs. 1(b)-1(e) and 2(b)-2(e) has been gradually shifted to higher loss energy in the subsequent N-implanting stage. This means that the electron density in the hybridised N2p/Ti3d valence band has increased gradually with the dose of N, and that the number of N atoms bonding to Ti atoms has also increased. It can be considered that the increase in the electron density of the hybridised band leads to the reinforcement of covalent bonds. The loss peaks (-16.0 eV) denoted by the dotted lines in Figs. 1 and 2 can be seen at $N/Ti \geq 0.266$. This peak is considered to be due to excitation of N 2s electrons to the conduction band.

To investigate changes in the strength of Ti-Ti and Ti-N bonds of N-implanted Ti films in detail, DV-$X\alpha$ MO calculations have been performed for Ti_{19} cluster and $Ti_{19}N$ cluster models shown in Fig. 3. The Ti_{19} cluster of Fig. 3 corresponds to a part of bulk ideal hcp-Ti structure. The nitrogen atom as indicated by G occupies the O-sites of the octahedron as formed by A-F atoms in the hcp-Ti sublattice.

The Mulliken overlap population (OP) value of each bond between Ti atoms and between Ti and N atoms for Ti_{19} and $Ti_{19}N$ cluster models in Fig. 3 has been inspected in detail, and is shown in Table 1. The values of OP refer to the strength of covalent bonds. Table 1 shows the existence of relatively large differences between the OP value of A-B, A-C, A-D, A-E atoms and that of A-I, A-H atoms, and between the OP

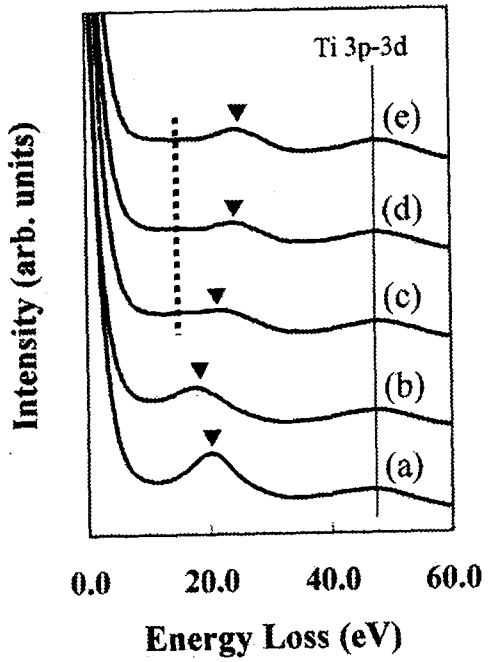

Fig. 1 Variation of EELS spectra for nitriding of TiH_x. N/Ti ratios are (a) 0, (b) 0.077, (c) 0.266, (d) 0.415, (e) 0.645.

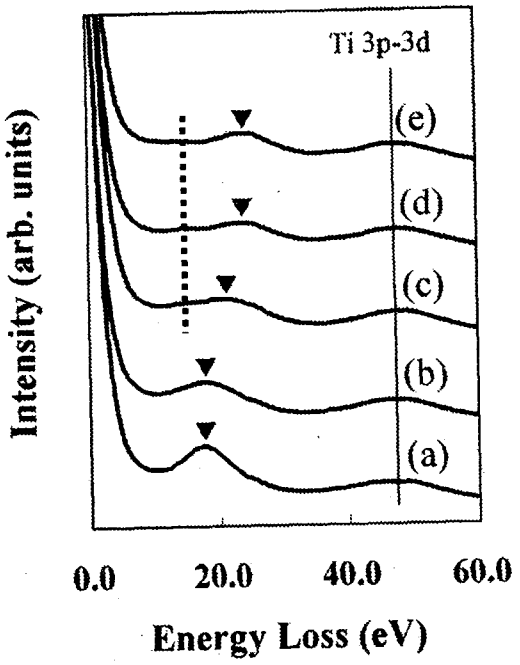

Fig. 2 Variation of EELS spectra for nitriding of hcp-Ti. N/Ti ratios are (a) 0, (b) 0.077, (c) 0.266, (d) 0.415, (e) 0.645.

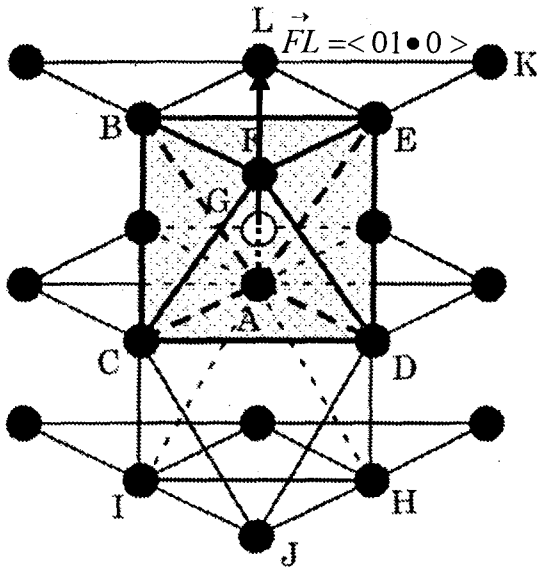

Fig. 3 Schematic illustration of Ti_{19} (without an open circle) and $Ti_{19}N$ cluster models. Solid and open circles represent Ti and N atoms, respectively. An octahedron is indicated by A-F atoms.

value of C-B, D-E atoms and that of C-I, D-H atoms for $Ti_{19}N$, compared with those for Ti_{19}. This indicates that bonds between Ti atoms of the octahedron occupied by N atom at the center, as the octahedron ABCDEF in Fig. 3, weaken, whereas bonds between Ti atoms of the octahedron not occupied by N atoms, as the octahedron ACDHIJ, are not changed, or rather strengthen a little. The weakening of bonds caused by the occupation of the O-sites by N atoms induces expansion of the spacing between (00 · 1)-planes, which results in the lattice expansion of hcp-Ti by N-implantation. On the other hand, the OP of Ti-N bonds as A-G and F-G bonds becomes relatively large compared with the OP of Ti-Ti bonds in the octahedron ABCDEF in Fig. 3. Thus, it can be considered that the strengthening of the A-G and F-G bonds induces the shear in the FL <01•0> direction on

Table 1. Overlap population of each bond between Ti atoms for the Ti_{19} and $Ti_{19}N$ cluster models.

Cluster Model	A-B, A-C, A-D, A-E atoms	A-I, A-H atoms	C-B, D-E atoms	C-I, D-H atoms
Ti_{19}	0.231	0.231	0.319	0.319
$Ti_{19}N$	0.135	0.254	0.200	0.348

the (00·1)-plane including B, E, F atoms in Fig. 3. In order to obtain an fcc sublattice by the hcp-fcc transformation, the atoms on the (00·1)-plane including B, E, F atoms in Fig. 3 have to be shifted. The direction of shift is the FL <01•0> direction. After the shift, the F atom, for example, has to be at the center of gravity of the BEF triangle. The projected line of line FA to the (00·1)-plane including B, E, F atoms in Fig. 3 is on the line FL. Thus, the shift of the F atom to the center of gravity of the triangle BEF induced by the forming of the strong A-G and F-G bonds and the weakening of the C-B and D-E bonds in Fig. 3 can be considered to be the origin for the hcp-fcc transformation of Ti sublattices.

References

1) C.-S. Shin, D. Gall, N. Hellgren, J. Patscheider, I. Petrov and J. E. Greene, J. Appl. Phys. **93** (2003) 6025-6028.

2) J. E. Sundgren, Thin Solid Films **128** (1895) 21-44.

3) Y. Kasukabe, N. Saito, M. Suzuki, Y. Yamada, Y. Fujino, S. Nagata, M. Kishimoto, and S. Yamaguchi, J. Vac. Sci. & Technol. **A16** (1998) 3366-3375.

4) H. Abe, H. Naramoto, K. Hojou, and S. Furuno, JAERI-Research **96-047** (1996) 1-18.

4.10 Blister Formation in Rutile TiO_2 (100) Films by Helium Ion Implantation

S. Yamamoto, A. Takeyama and M. Yoshikawa
Department of Material Development, JAERI

1. Introduction

The implantation of helium into materials can be used to produce specific microstructures on the surface region, such as bubbles, blisters and craters, with unique properties for the application of catalysis. These structures have potential for the increasing effective surface area and the improving photocatalytic activity. The formation of helium bubbles and blisters in materials is a complex phenomenon depending on the helium implantation energy, fluence, temperature and thermal treatments after the implantation.

In the present study, we explore the suitable condition for helium blister formation in epitaxial TiO_2 film by helium implantation at room temperature. The observation of helium blisters in film surface was made with scanning electron microscope (SEM). The optimal implantation conditions for the blister formation are reported.

2. Experimental

TiO_2 films were deposited on α-Al_2O_3 substrates by pulsed laser deposition (PLD) using a KrF excimer laser (wavelength: 248 nm, Lambda Physik). The laser beam was incident on a target with an incident angle of 45°. It was focused to a 2 mm × 3 mm rectangle on a single-crystal TiO_2 (rutile type) target (ϕ 35 mm). Typical laser energy and repetition rate were 150 mJ/cm^2 and 5 Hz. In this study, ~500 nm thick TiO_2 films were deposited at 500°C under the oxygen pressure of 2 Pa.

The deposited TiO_2 films were irradiated at room temperature with 1~4 keV helium ions up to fluence range from 1×10^{16} to 2.3×10^{17} ions/cm^2. Implantation of helium ions was carried out using a 4 kV ion gun. The irradiation chamber was evacuated up to a base pressure of about 3.7×10^{-6} Pa using a turbomolecular pump. Helium gas (purity: 6N) was introduced up to 3.0×10^{-4} Pa during the implantation. The beam current density was 1 μA/cm^2 through a circler slit with 5.5 mm in diameter.

The surface morphology of the deposited films was examined using a high-resolution field emission SEM (JSM6700F, JEOL). Rutherford backscattering spectroscopy with channeling (RBS/C) analysis using a 3 MV single-stage-accelerator at JAERI/Takasaki was employed to characterize crystal quality of the epitaxial thin films. The analyzing 2.0 MeV $^4He^+$ ions were incident and backscattered particles were detected at 165° scattering angle with a surface barrier detector.

3. Results and discussion

The suitable condition for high quality epitaxial TiO_2 (100) films with rutile type was following conditions; laser energy: 150 mJ/cm^2, oxygen gas pressures: 2 Pa, substrate temperature: 500°C, target species: single-crystal TiO_2 (rutile type). The quality of epitaxial TiO_2 (100) films was characterized through the RBS/C analysis. Figure 1 illustrates 2.0 MeV $^4He^+$ RBS spectra for the TiO_2 film on the α-Al_2O_3 (0001) substrate taken under the random and the axial channeling conditions. The aligned spectrum was taken with the incident beam directed along the <100> axis of the TiO_2 film.

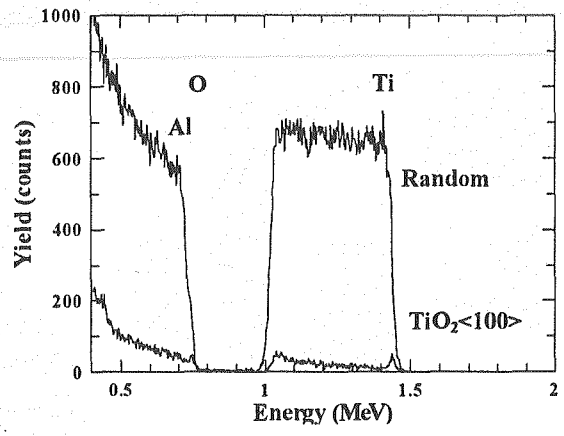

Fig. 1 2.0 MeV $^4He^+$ RBS/C spectra for deposited TiO_2 films on the α-Al_2O_3 (0001) substrate. The thickness of TiO_2 film is 500 nm. The aligned spectrum was taken with the beam directed along the <100> axis of the TiO_2 film.

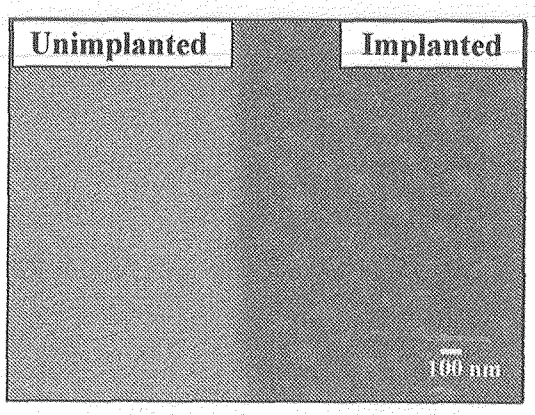

Fig. 2 SEM image of the TiO_2 (100) film, unimplanted and implanted region. The TiO_2 film was irradiated with 3 keV helium ions at room temperature, fluence of 1.0×10^{17} ions/cm^{2}ions.

In the RBS spectra of Fig. 1, one can recognize clearly the separated peaks from the TiO_2 film and α-Al_2O_3 substrate. The peak at 1.45 MeV corresponds to the Ti component in the TiO_2 film. Judging from the peak intensity, the high quality TiO_2 film is grown up from the interface between the film and the substrate. The interface is not mixed with each other within the depth resolution (~10 nm) of this technique. The minimum yield, χ_{min} value, the ratio between the random and the axially aligned yield at the fixed depth near the surface region, gives a measure to evaluate the degree of disorder in crystalline solids. The χ_{min} value in the <100> aligned spectrum is 0.02 at the just area behind the surface peak of the Ti component in the TiO_2 film, which suggests that the crystal quality of the TiO_2 film is high enough as a bulk single-crystal. The planar channeling analysis around the major axes of the TiO_2 film and the α-Al_2O_3 gives the evidence that the TiO_2 <100> crystallographic axis is parallel to the α-Al_2O_3 <0001> axis.

The SEM image of the TiO_2 (100) film unimplanted and implanted region with 3 keV helium ions at room temperature is shown in Fig. 2. The TiO_2 film was irradiated with the helium fluence of 1.0×10^{17} ions/cm^2. It can be seen from Figure 2, smooth surface structure is observed in unimplanted region, and uniform blister formation with about 100 nm sizes is recognized in the implanted region. In general, the size of blisters produced in metal surfaces by helium implantation with a fluence of 10^{18} ions/cm^2 range at room temperature is about several μm. In comparison with helium blister formation in metals, the size of blister produced in TiO_2 films is extremely small.

Figure 3 shows SEM images of the TiO_2 (100) films irradiated with the helium fluences of (a) 1.8×10^{17} ions/cm^2 and (b) 2.3×10^{17} ions/cm^2, respectively. The film samples were irradiated with 3 keV helium ions at room temperature. In Figure 3 (a), one can recognize helium blisters with about 100 nm size were produced without cracks on the blister surface. Further increase of helium implantation fluence up to 2.3×10^{17} ions/cm^2, cracks and holes are formed in the blister surface. These results indicate that exfoliation of flakes of the TiO_2 film occurs

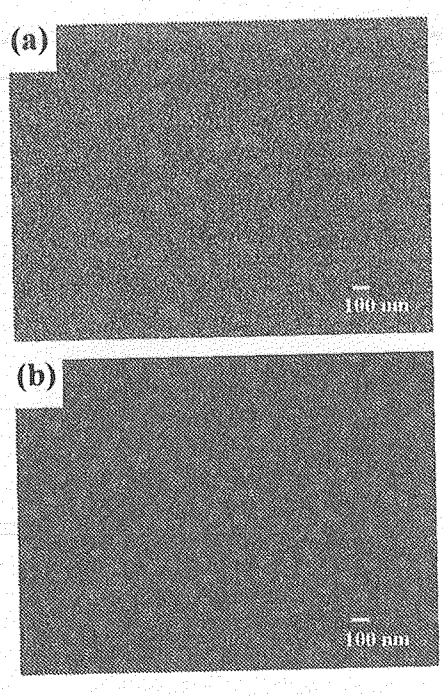

Fig. 3 SEM images of the TiO_2 (100) films irradiated with the helium fluence of (a) 1.8 × 10^{17} ions/cm^2 and (b) 2.3 × 10^{17} ions/cm^2. The film samples were irradiated with 3 keV helium ions at room temperature.

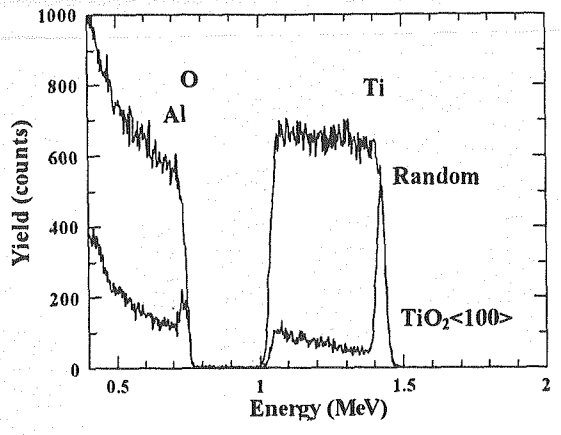

Fig. 4 2.0 MeV $^4He^+$ RBS spectra for the rutile TiO_2 (100) film irradiated with 3 keV helium ions to a fluence of 1.8 × 10^{17} ions/cm^2 at room temperature taken under the random and the TiO_2<100> axial channeling conditions.

with helium ion fluences higher than about 2 × 10^{17} ions/cm^2. In the samples made by helium implantation with 1~4 keV at room temperature, helium blisters with about 100 nm size were formed at 2~4 keV helium ion fluences higher than about 4 × 10^{16} ions/cm^2.

To determine the radiation-induced damage depth profile near surface region, TiO_2 films irradiated with helium ions were examined by RBS/C. Figure 4 illustrates 2.0 MeV $^4He^+$ RBS spectra for the rutile TiO_2 (100) film irradiated with 3 keV helium to a fluence of 1.8 × 10^{17} ions/cm^2 at room temperature taken under the random and the axial channeling conditions. The RBS spectra from unimplanted sample are shown in Fig. 1 for comparison. The RBS spectra taken under TiO_2<100> axial channeling condition in Figure 4, the RBS yield (at 1.45 MeV) from Ti component in the TiO_2 film reaches the random level. In addition, the RBS yield from oxygen component (at 0.74 MeV) in the film is also increase. These increasing of the RBS yields indicate that helium radiation-induced damage exists only near the surface region (~20 nm) of the TiO_2 film.

4. Summary

We have studied the formation of helium blisters in epitaxial rutile TiO_2 (100) films grown on α-Al_2O_3 (0001) substrate as a function of the implantation fluence and energy at room temperature. The surface morphology of TiO_2 films was observed by SEM. The RBS/C was used to determine the radiation-induced damage depth profile near surface region. Helium blisters with ~100 nm in TiO_2 films were observed at 2~4 keV helium ion fluences higher than 2 × 10^{16} ions/cm^2. Further increase of implantation fluences higher than 2 × 10^{17} ions/cm^2, exfoliation of flakes of the TiO_2 film was observed.

JP0650233

4.11 Growth of ZnO Rods on Cu Implanted Substrate

A. Takeyama*, S. Yamamoto*, M. Yoshikawa*, H. Ito* and
H. Naramoto**
Department of Material Development, JAERI*
Advanced Science Research Center, JAERI**

1. Introduction

One dimensional materials have attracted much attention because of its unique physical properties[1]. In particular, ZnO rods have been expected as a promising material for the UV laser. For the growth of ZnO rods, sapphire dispersed with a metal catalysis was often used[2]. Using this substrate, ZnO rods were selectively grown at the location where the catalysis is dispersed. However, sapphire is an insulator and not suitable for processing by the conventional Si processing technology, it is important to develop the technique to grow ZnO rods on Si substrates. However, the lattice parameter and crystal structure of ZnO are quite different from those of Si, it is difficult to grow ZnO rods on Si substrate. So far, although the growth of ZnO on Si was attempted, most of ZnO rods were grown inclined to the substrate[3]. To exploit the application of ZnO rods to novel Si integrated optelectronic devices, the technique is required to grow ZnO rods perpendicularly to Si substrate.

Metal ion implantation into Si substrates has been utilized to produce various metal silicides. The metal silicide including copper silicide has been known that they formed the "mixing" structure on the substrate in which metal silicide island were surrounded by polycrystalline Si grains[4]. Considering the morphology of the "mixing" structure, copper silicide is expected to serve as the catalyst for the growth of ZnO rods perpendicularly to the substrate. In this study, ZnO rods were successfully grown almost perpendicular to the annealed Cu-implanted Si substrate.

2. Experimental

Si (100) wafers were used as substrates. The size of the substrates was 5 mm x 5 mm. Cu ion implantation was carried out at the fluence up to 5×10^{16} atoms/cm^2, with an implantation energy of 200 keV. After the Cu ion implantation, the Cu-implanted substrates were annealed at 773 K for 1 h under Ar atmosphere.

Subsequently ZnO rods were grown on the annealed Cu-implanted substrate using the chemical vapor transport (CVT) technique. Ar was used as the carrier gas and mixed powder of graphite and ZnO was put into the alumina boat then was placed at the upstream of the quartz tube. Annealed Cu-implanted substrate was also placed at the downstream of the tube, then it was heated up to 1223 K for 15 minutes. Surface images of the annealed Cu-implanted substrates and ZnO rods were taken by field emission scanning electron microscopy (FE-SEM, JEOL JSM-6700F). Those crystal structure were characterized using X-ray diffraction (Phillips X'Pert-MRD), and the depth profile of implanted Cu atoms was obtained using Rutherford backscattering spectroscopy (RBS).

3. Results and Discussion

Figure 1 shows the distribution of Cu atoms in the Cu-implanted substrate annealed at 773K for 1h. The Cu fluence was 5×10^{16} atoms/cm^2. In Fig. 1, the Cu concentration at the surface was increased twice as large as that of as-implanted substrate (figure not shown), and this indicates

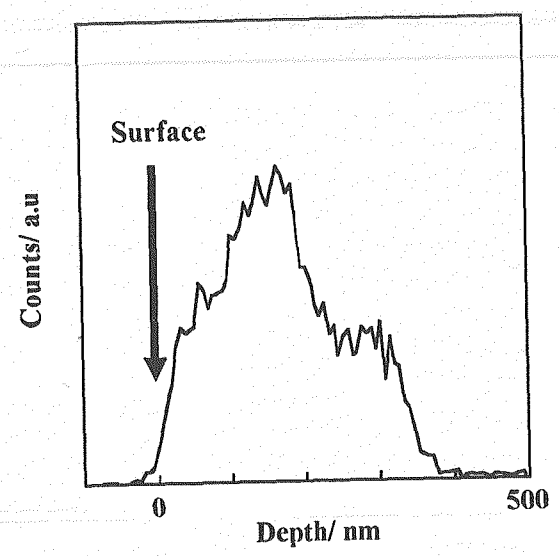

Fig. 1 RBS spectra of Cu-implanted substrate annealed at 773K for 1h.

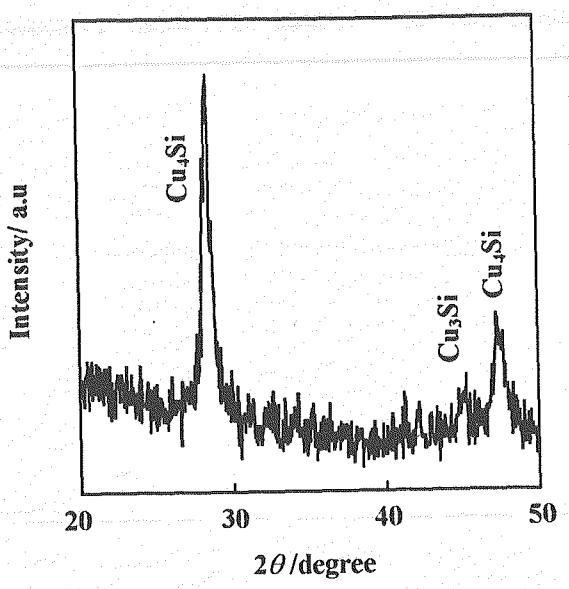

Fig. 2 XRD pattern of Cu-implanted substrate annealed at 773K for 1h.

the implanted Cu atoms diffused to the surface after the annealing.

Figure 2 is an XRD pattern of the annealed Cu-implanted substrate. The peaks are indexed with copper silicide such as Cu_3Si and Cu_4Si. Only a little pure copper is identified with the XRD pattern.

Figure 3 shows the surface morphology of Cu precipitates formed on the annealed Cu-implanted substrate. The Cu fluence was 5 x 10^{16} atoms/cm^2. Light gray colored precipitates with a diameter of approximately 180 nm formed on the surface. When the Cu-implanted substrate was annealed, implanted Cu atoms diffused to the surface of the substrate to form Cu precipitates. The energy dispersive X-ray (EDX) analysis shows the Cu concentration of the precipitates is higher than that of the surface of the substrate, which shows that the precipitate was copper silicide, Cu_4Si.

Figure 4 shows a XRD pattern of ZnO rods grown on the Cu-implanted substrate. The pattern consists of (100) and (002) planes of the wurtzite type crystal structure of ZnO. The latter peak is relatively higher and this shows most of ZnO rods were preferentially grown on the

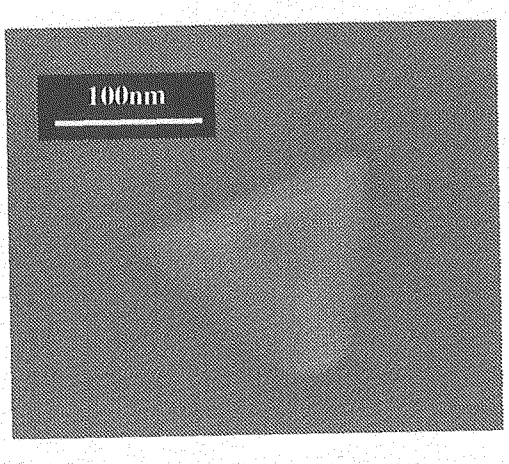

Fig. 3 Cu precipitates formed on the Cu-implanted substrate annealed at 773K for 1h.

annealed Cu-implanted substrate along <0001> direction, in other words, perpendicularly grown on the substrate. The peak of (100) plane appeared in the pattern is derived from some ZnO rods laid on the surface. No Zn peaks in the XRD pattern assures hexagonal shaped rods consisted of pure ZnO.

Figure 5 (a), (b) are the surface images of ZnO rods grown on the annealed Cu-implanted substrate. The Cu fluence was 5 x 10^{16} atoms/cm^2. In Fig.5 (a), hexagonal shaped rods with a diameter ranging from 400 to 1000 nm

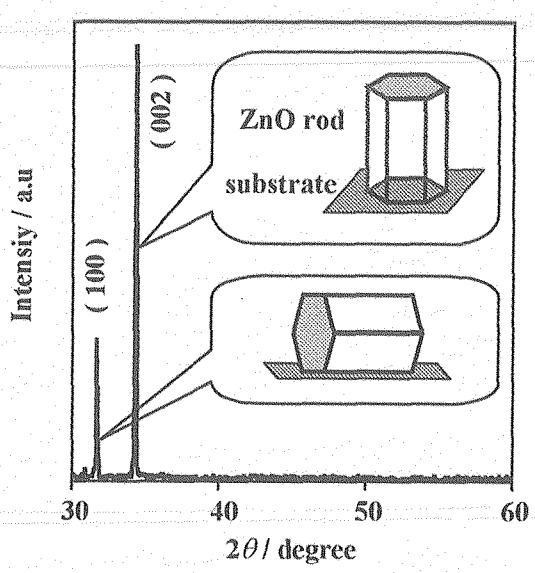

Fig. 4 XRD pattern of ZnO rods grown on the Cu-implanted substrate.

were grown on the substrate. Hexagonal shape of the rods indicates that the rods had the wurtzite type crystal structure and were single crystalline ZnO. In Fig. 5 (b), the ZnO rod (1) with a grayish cap (2) was grown perpendicularly to the substrate. Well faceted side surface of the hexagonal rod in the surface image clearly indicates that the part (1) was the ZnO rods. Such capped rods is the typical shape of one dimentional material via Vapor-Liquid-Solid (VLS) mechanism using metal catalysis[5], and this indicates that the Cu precipitates served as the catalysis for the growth of ZnO rod. It is worth noting that ZnO rods were grown perpendicularly to the substrate, although ZnO has wultzite type crystal strucutre and lattice parameter of a = b = 3.24982 and c = 5.20661 Å and those were quite different from a = b = c = 5.43088 Å of Si which has diamond type crystal structure.

The average density of Cu precipitates and ZnO rods was increased with increasing the Cu fluence. This is an evidence of the Cu precipitates served as the catalysis for the growth of ZnO rods.

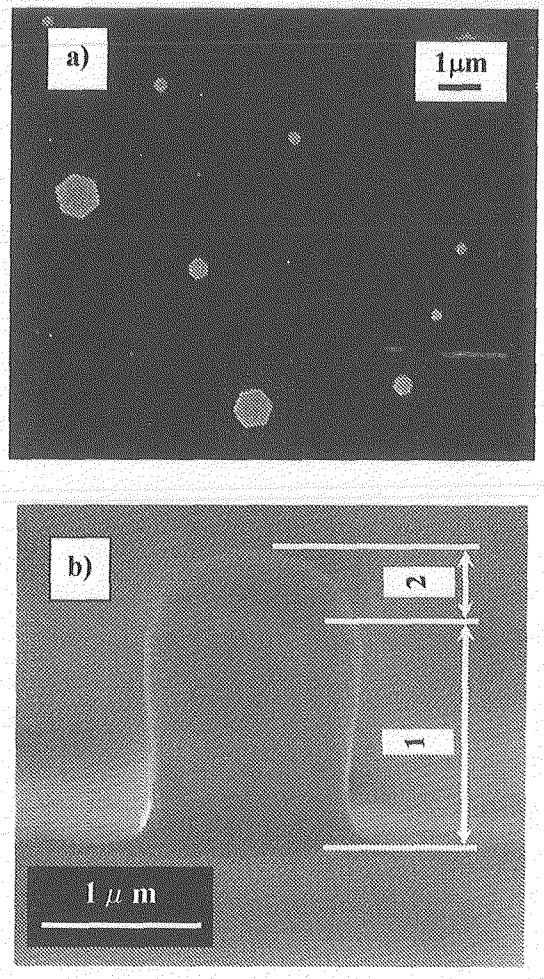

Fig. 5 Surface image of ZnO rods grown on the Cu-implanted substrate.
(a) plane view, (b) enlarged cross sectional view.

References

1) S.Q. Feng, D.P. Yu, H.Z. Zhang, Z.G. Bai and Y. Ding, J. Cryst. Growth, 209 (2000) 513-517.
2) M. H. Huang, S. Mao, H. Feick, H. Yan, Y. Wu, H. Kind, E. Weber, R. Russo and P. Yang, Science 292 (2001) 1897-1899.
3) S. Y. Li, C. Y. Lee and T. Y. Tseng, J. Cryst. Growth 247 (2003) 357-362.
4) E. G. Colgan, J. P. Gambino and Q. Z. Hong, Mater .Sci. Eng. R. 16 (1996) 43-96.
5) Y. Cui, L. J. Lauhon, M. S. Gudiksen, J. Wang and C. M. Lieber, Appl. Phys. Lett., 78 (2001) 2214-2216.

4.12 Application of X-ray Photoelectron Spectroscopy to Characterization of Metallic Nanoclusters Formed by Ion Implantation-II

K. Takahiro*, S. Oizumi*, A. Terai*, K. Kawatsura*, S. Nagata**,
S. Yamamoto***, K. Narumi**** and H. Naramoto****
Department of Chemistry and Materials Technology, Kyoto Institute of Technology*
Institute for Materials Research, Tohoku University**
Department of Material Development, JAERI***
Advanced Science Research Center, JAERI****

1. Introduction

A nanometer-sized cluster, referred to as "nanocluster" hereafter, embedded in a matrix exhibits unusual optical[1], electrical[2], and magnetic[3] properties. A large number of methods, including co-sputtering, sequential evaporation, sol-gel deposition and ion implantation have been applied to preparation of nanoclusters in a matrix. Ion implantation is very promising for the formation of nanoclusters because of its ability to control the type and concentration of the implanted atoms. In addition, ion implantation can be, in principle, applied for any combination of ions and matrices.

Usually implanted atoms as well as defects do not distribute uniformly along depth, resulting in the depth-dependent nucleation and growth of nanoclusters. It is, therefore, necessary to examine the depth-dependent size distribution of nanoclusters. Cross sectional transmission electron microscopy (XTEM) is often used to directly investigate their size. However, much effort and time have to be paid to prepare specimens for XTEM observation.

Alternatively, X-ray photoelectron spectroscopy (XPS) can be used to estimate the size of nanoclusters. It is known that the core level binding energy of nanoclusters shifts toward higher energy from a bulk value, depending on their size. Especially, for Au nanoclusters *supported on* poorly conducting materials such as amorphous carbon and SiO_2, the relationship between Au 4*f* binding energy shift and cluster size has been well studied[4]. In our previous study, XPS core level binding energies were measured for metallic nanoclusters, such as Au, Ag and Cu, embedded in glassy carbon (GC) to estimate their size. A question arises, however, as to whether the relationship is applicable to the nanoclusters *embedded in* GC. The XPS binding energy shifts arise from charging of the cluster during photoemission. The environment around the clusters affects the charging itself. In addition, the interaction of the charged cluster with the outgoing photoelectron depends on the nature of surrounding materials in terms of dielectric constant. The XPS binding energy shifts, therefore, would be sensitive to the surroundings. In contrast, the spin-orbit energy splitting in a valence band level, which is insensitive to the surroundings, can be a measure for the size of nanoclusters. In fact, several groups[5)-8)] showed that the splitting between $5d_{5/2}$ and $5d_{3/2}$ decreased with the size of Au nanoclusters.

In this work, the 5*d* splitting as well as the 4*f* binding energy shift was measured on Au nanoclusters embedded in GC, Al_2O_3 and SiO_2 to estimate the cluster size. The 5*d* splitting is not affected by the sample charging during XPS, and therefore, applicable to estimate the size of Au nanoclusters embedded in dielectrics such as

Al_2O_3 and SiO_2.

2. Experimental procedure

Glassy carbon (Tokai Carbon, Japan; GC-30 grade) was mechanically polished to mirror surface with 1 μm diamond slurry on a cloth lap. A single crystalline sapphire (α-Al_2O_3) and fused silica (SiO_2) were commercially available from Shinkosha and Sendai-Sekiei, respectively. Au^+ ions with an energy of 500 keV were used to implant. The implantation doses are 1×10^{17} cm^{-2} for GC and Al_2O_3 and 4×10^{16} cm^{-2} for SiO_2. Au implantation was performed using a tandem accelerator at Institute for Materials Research, Tohoku University. The depth distributions of implanted atoms were analyzed by using Rutherford backscattering spectrometry (RBS) with 2 MeV He ions from a single-end accelerator at TIARA. The Au depth profile obtained from RBS determined the etching rate by Ar ions in XPS analysis.

XPS analysis using non-monochromatized Mg Kα radiation was performed with JEOL 9010. To obtain depth profile of XPS binding energies for the implanted Au, the surface of implanted samples was etched with 0.8 keV Ar ions from a sputter-etching gun equipped with JEOL 9010. The etching rate was determined to be 0.29, 0.30 and 0.83 nm/sec for GC, Al_2O_3 and SiO_2, respectively.

3. Results and discussion

Figure 1 shows typical Au 5*d* valence band level XPS spectra obtained from Au atoms implanted after sputter etching for 880 sec and 1200 sec, corresponding to the analyzing depths of ~255 nm and ~350 nm, respectively. The spectrum from a bulk Au sample is also shown for comparison. Dashed lines indicate the peak positions of a $5d_{5/2}$ level at ~3.6 eV and a $5d_{3/2}$ level at ~6.3 eV for the bulk sample. The splitting between $5d_{5/2}$ and $5d_{3/2}$ levels significantly reduces for the implanted Au at both depths compared to that for the bulk Au. The decreased splitting of the 5*d* level can be understood to result from the finite size of the Au clusters[5]. Indeed, the 5*d* splitting of a free Au atom is 1.5 eV, relatively smaller that the corresponding value of the bulk Au (2.7 eV). In Fig. 2, the 5*d* splittings together with the depth profile of Au concentration are

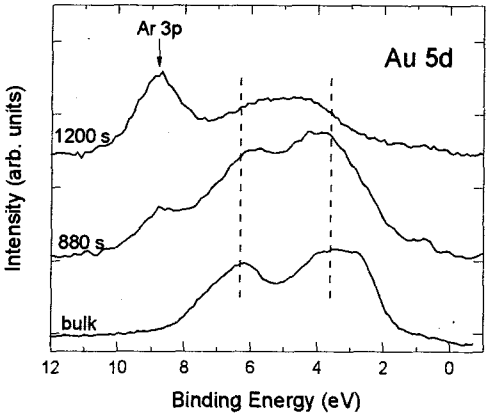

Fig. 1 Au 5*d* valence band level XPS spectra for implanted Au in GC after sputter etching for 880 sec and 1200 sec, corresponding to depths of ~255 nm and ~350 nm, respectively. The XPS spectrum for a bulk Au sample is also shown for a comparison. Dashed lines indicate the peak positions of a $5d_{5/2}$ level at ~3.6 eV and a $5d_{3/2}$ level at ~6.3 eV for the bulk sample.

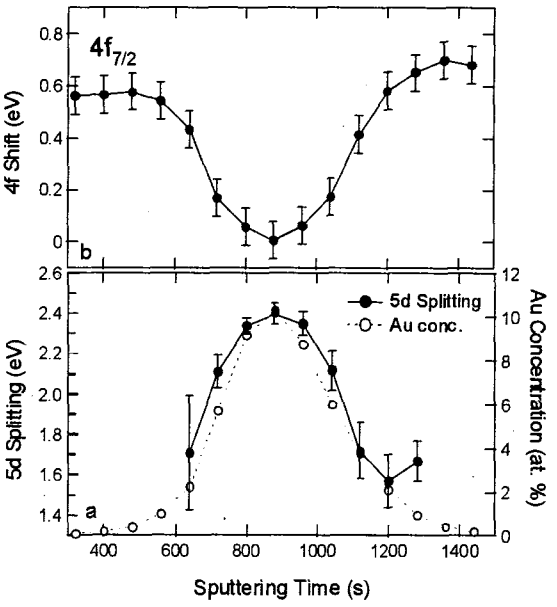

Fig. 2 (a) Au 5*d* line splittings (filled circles) and Au concentrations (open circles), and (b) Au $4f_{7/2}$ binding energy shifts from a bulk value (83.9 eV) as a function of sputtering time.

plotted as a function of sputtering time. The 5*d* splitting correlates well with the Au concentration. As the Au concentration increases, the 5*d* splitting becomes larger, indicating that the Au clusters with the larger size tend to be formed in the vicinity of the projected range of Au ions. According to the relationship between the average coordination number in an Au cluster and the 5*d* splitting derived from the work by DiCenzo *et al.*[7], the average size of Au clusters can be estimated as a function of depth. The average size of Au clusters, for example, is ~2.5 nm for the sputtering time of 880 sec, corresponding to the depth of ~255 nm. On the other hand, the 4*f* core-level shift is close to zero at that depth, as shown in Fig. 2b. Assuming that the relationship between the 4*f* shift and cluster size for Au nanoclusters supported on a substrate[4] is valid for the Au nanoclusters embedded in GC, the 4*f* shift of ~0 eV yields the average size >4 nm[5), 9)], much larger than that estimated from the 5*d* splitting (~2.5 nm). There is a large difference in the estimated average size between the two procedures, 5*d* splitting and 4*f* shift. Figure 3 represents graphs showing the 4*f* shifts versus the 5*d* splittings obtained in this work, along with the previous data for Au nanoclusters onto a carbon substrate[7]. It is quite obvious that the present data differs from the previous one. This discrepancy results from the different environments surrounding Au nanoclusters. In our case, the Au nanoclusters are embedded in GC, resulting in the insensitive size-dependence of 4*f* shifts. It is concluded, therefore, that the 4*f* shift-size relationship derived from the measurements for Au clusters on a carbon substrate is inapplicable to the size estimation for those in a carbon matrix.

Next the measurements of the 5*d* splitting are applied to the estimation of the size of Au nanoclusters formed in Al_2O_3 and SiO_2 matrices. Even for Au nanoclusters in a dielectric matrix, no charge correction is required for the 5*d* splitting analysis. The average sizes of Au nanoclusters are estimated to be 1–4 nm and 1.5–4 nm in Al_2O_3 and SiO_2 matrices, respectively, depending on the Au concentration.

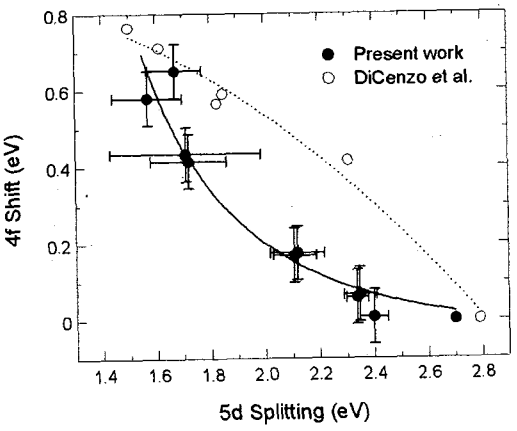

Fig. 3 Au 5*d* line splittings versus $4f_{7/2}$ binding energy shifts obtained from the present work (filled circles) and the previous measurements by DiCenzo *et al.*[7] (open circles). The lines are drawn as guide to the eye.

References

1) R. Ruppin, J. Appl. Phys. 59 (1986) 1355–1359.
2) G. Medeiros-Riberro, D. A. A. Ohlberg, R. S. Williams and J. R. Health, Phys. Rev. B 59 (1999) 1633–1636.
3) G. L. Zhang, W. H. Liu, F. Xu and W. X. Hu, Appl. Phys. Lett. 61 (1992) 2527-2529.
4) H.-G. Boyen *et al.* Phys. Rev. Lett. 94 (2005) 016804-1–016804-4
5) H. Roulet, J.-M. Mariot, G. Dufour and C. F. Hague, J. Phys. F 10 (1980) 1025–1030.
6) S.-T. Lee *et al.*, Phys. Rev. B 23 (1981) 505–508
7) S. B. DiCenzo, S. D. Berry and E. H. Hartford Jr, Phys. Rev. B 38 (1988) 8465–8468.
8) P. Zhang and T. K. Sham, Phys. Rev. Lett. 90 (2003) 245502-1–245502-4.
9) M. G. Mason, Phys. Rev. B 27 (1983) 745–762.

4.13 Improvement of Hydride Characteristics in Hydrogen Absorption Materials by Ion Irradiation

H. Abe*, H. Uchida**, R. Morimoto*** and H. Itoh*
Department of Material Development, JAERI*
Faculty of Engineering, Tokai University**
Graduate school of Engineering, Tokai University***

1. Introduction

Surface modifications are crucial to improve the reactivity of hydrogen with metals because the dissociation of H_2 molecules in gas phase or the dissociation of H_2O molecules in an electrochemical process is the first step of the overall reaction of hydrogen absorption in metals[1]. The dissociation of H_2 or H_2O molecules is markedly influenced by surface conditions of a metal. So far, we have systematically investigated the effects of surface oxide layers on the kinetics of hydrogen absorption in hydrogen absorbing metals[1] and reported several methods of surface modifications such as metallic coating, fluorination treatment, and alkaline treatment[2, 3].

In this study, the surface modifications of Pd have been made by ion irradiation using proton (H^+)[4], argon (Ar^+)[5] and nitrogen (N^+), and the ion irradiation effects on the rate of electrochemical hydrogen absorption in Pd have been investigated.

2. Experimental

Pd sheets (99.99 % purity) with a size of 7.5 mm x 7.5 mm x 0.1 mm were used. Prior to ion irradiation, all samples were annealed for an hour at 1173 K in a flowing pure N_2 gas (99.9998 % purity). Ion irradiation was made onto the surface of Pd samples using H^+, He^+, Ar^+ and N^+ in an energy of 350 keV, and a dose range from 1 x 10^{14} cm^{-2} to 1 x 10^{17} cm^{-2} at room temperature at TIARA, JAERI. Temperature of the samples increased up to 353 K at a beam current of ~10 μA, and almost no annealing effect took place during the irradiation.

For the electrochemical measurements of the hydrogen absorption rate of Pd (cathode), a Pt sheet with a size of 30 mm x 30 mm x 0.3 mm and a purity of 99.98 wt. % was used as an anode. An Hg/HgO electrode was also used as the reference electrode in an open cell[6]. The rate of hydrogen absorption in the Pd samples was evaluated as a change in the current density mA(*g-alloy*)$^{-1}$ in 6 M(*mol/l*)-KOH at room temperature. During the measurements, a constant voltage of -0.93 V was applied to the samples. In all experiments, no gas bubbles were observed during hydrogen absorption. Details of the electrochemical measurements have been reported elsewhere[6].

3. Results and discussion.

Figure 1 shows hydrogen absorption curves of Pd samples before and after H^+ irradiation. The initial rates of irradiated samples become high compared with that of the un-irradiated sample. In comparison with the results of H^+ irradiation, the samples irradiated with He^+ [4] exhibited higher absorption rates. He^+ introduces

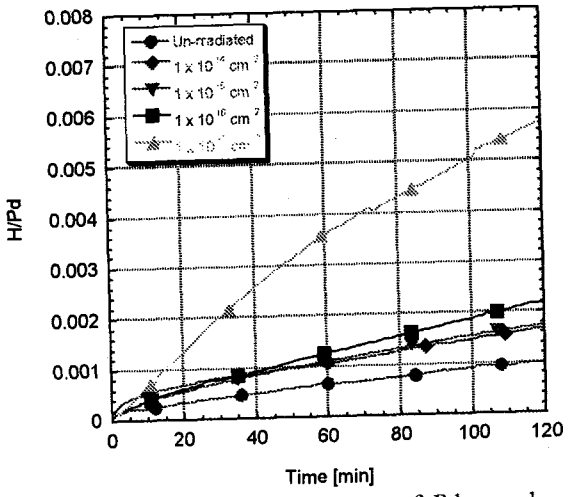

Fig.1 Hydrogen absorption curves of Pd samples irradiated with 350keV H^+ at doses of 1 x 10^{14} cm^{-2}, 1 x 10^{15} cm^{-2}, 1 x 10^{16} cm^{-2} and 1 x $10^{17}cm^{-2}$.

much higher concentrations of vacancies in the surface region than H^+. An increase in the vacancy concentration leads to an increase in the hydrogen trapping sites, resulting in an acceleration of the rates of hydride nucleation and growth in the surface region. It can account for the increase in the hydrogen absorption rate in Pd with increasing of H^+ dose and the higher absorption rates observed in He^+-irradiated Pd samples.

Figure 2 shows the results for 350 keV Ar^+ irradiation. As the Ar^+ dose increased from 1 x 10^{14} cm^{-2} to 1 x 10^{17} cm^{-2}, the hydrogen absorption rate increased. The sample irradiated at a dose of 1 x 10^{17} cm^{-2} exhibited a much higher rate than the others. These results also support the assertion that the initial hydrogen absorption rate of Pd is enhanced by the introduction of vacancies due to ion irradiation.

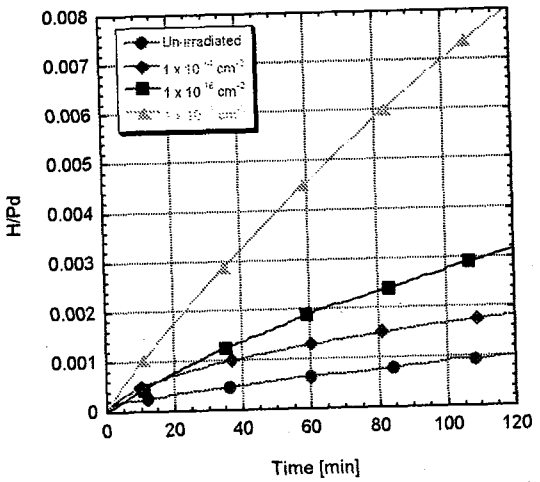

Fig.2 Hydrogen absorption curves of Pd samples irradiated with 350keV Ar^+ at doses of 1 x 10^{14} cm^{-2}, 1 x 10^{16} cm^{-2} and 1 x 10^{17} cm^{-2}.

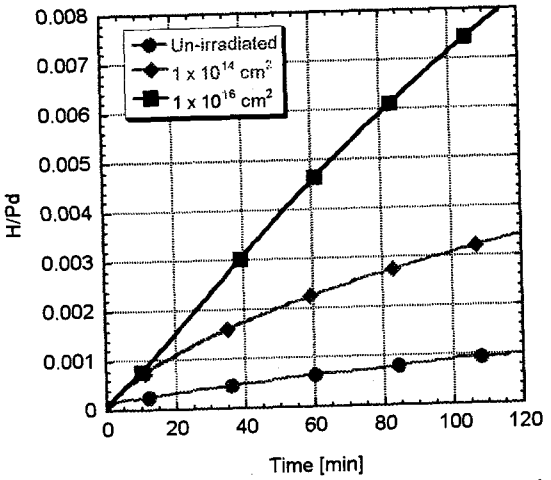

Fig.3 Hydrogen absorption curves of Pd samples irradiated with 350keV N^+ at doses of 1 x 10^{14} cm^{-2} and 1 x 10^{16} cm^{-2}.

Figure 3 shows the N^+ irradiation effects on the hydrogen absorption rate of Pd. Similar to the results obtained for H^+, He^+ and Ar^+ irradiation, the hydrogen absorption rate was found to increase with N^+ dose. At the reaction time of 120 min, the concentration of hydrogen absorbed in the Pd sample irradiated with N^+ at 1 x 10^{16} cm^{-2} was obtained to be [H] / [Pd] > 0.008.

Figure 4 shows the distribution of the hydrogen absorption rate in each ion irradiation, in which the irradiation dose is 1 x 10^{16} cm^{-2}. Data of the un-irradiated sample is also shown for comparison. Among ion species used in this study, N^+ was found most effective for raising the initial hydrogen absorption rate. This result cannot be explained only in terms of the vacancy assisted hydrogen absorption

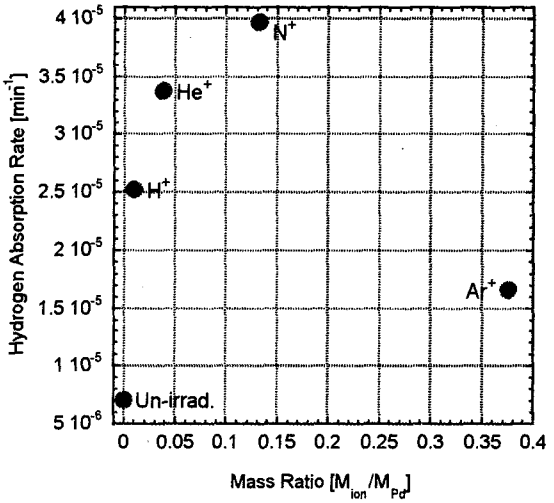

Fig.4 Distribution of the hydrogen absorption rate in each ion irradiation. The abscissa represents the atomic mass ratio of irradiated ion species to Pd.

model described above. Further investigations are necessary to clarify all the implications of ion irradiation effects.

4. Conclusion

The ion irradiation treatment of the surface of Pd using H^+, He^+, Ar^+ and N^+ was found to enhance the initial rate of electrochemical hydrogen absorption in Pd. Among the ion species used in our experiments, N^+ was found most effective for the enhancement of the hydrogen absorption rate. Further studies are required to elucidate the role of each ion in the improvement of the hydrogen absorption in Pd.

References

1) H.Uchida, Int. J. Hydrogen Energy, 24 (1999) pp.861-869.
2) H. Uchida, K. Yamashita and M. Goto, J. Alloys and Comp., 330-332 (2002) pp.622-626.
3) T. B. Flanagan, in "Progress in Hydrogen Treatment of Materials", edited by V. A. Goltsov (Donetsk State Technical Univ., Ukraine, 2001) pp.37-64.
4) H. Abe, H. Uchida, Y. Azuma, A. Uedono, Z. Q. Chen and H. Itoh, Nucl. Inst. and Meth. B, 206 (2003) pp.224-227.
5) H. Abe, A. Uedono, H. Uchida, A. Komatsu, S. Okada and H. Itoh, Mat. Sci. Forum, 363-365 (2001) pp.156-158.
6) H.H. Uchida, Y. Watanabe, Y. Matsumura and H. Uchida, J. Alloys Comp., 231 (1995) pp.679-683.

4.14 Effect of Ion Species on the Production and Thermal Evolution of Implantation Induced Defects in ZnO

Z. Q. Chen, M. Maekawa, A. Kawasuso, S. Sakai and H. Naramoto
Advanced Science Research Center, JAERI

1. Introduction

Zinc oxide (ZnO) is a technologically very important semiconductor for the potential application in short wavelength light emitting devices[1]. It has been revealed that ZnO has high resistance to radiation damage. This is due to the efficient dynamic annealing of the defects occurred during irradiation. It is therefore expected that ZnO is well appropriate for the space application. However, recently an unusual behavior related to the implantation damage in ZnO was also reported. That is the chemical effect of the damage accumulation[2]. The implantation-induced defects can be stabilized by the implanted impurities, and enhance damage buildup or even cause amorphization effects.

In this work, we studied the defects produced by B^+ and O^+-implantation using positron annihilation measurements. Our results show clear difference in the defect recovery process for these two implanted specimens, which might be due to the chemical effects of the impurities.

2. Experiment

The samples are hydrothermally grown ZnO single crystals nominally undoped with n-type conductivity. Ion implantation was carried out at room temperature using a 400 keV implanter. A multi-step implantation process was performed for each ion with seven different energies. The energy range was 50-380 keV and 40-300 keV, and the total doses were 3.9×10^{15} cm^{-2} and 5.2×10^{15} cm^{-2} for O^+ and B^+ ions respectively. A box-shaped implantation profile is obtained after such implantation. The implanted samples were annealed isochronally from 200 to 1000°C for 30 min in nitrogen ambient.

Doppler broadening of positron annihilation radiation was measured using a slow positron beam (0.2-30 keV). The S parameter defined as the ratio of the counts in the central region to the total area of the annihilation peak was used to characterize the Doppler broadening spectrum. Micro-Raman scattering measurements were performed using the NANOFINDER spectrometer in the wave number range of 200-800 cm^{-1}. The 488.0 nm-line of an Ar^+-ion laser was used for excitation and the incident laser power was ~1 mW.

3. Results and discussion

Figure 1 shows the S parameter as a function of incident positron energy (S-E curve) for the as-grown and implanted samples by B^+ and O^+ ions. After ion implantation, an increase of the S parameter can be observed, which shows introduction of vacancy defects. The S parameter in the positron energy range of 5-13 keV is nearly constant, which corresponds to the box-shaped implantation layer. The S value of 1.05-1.06 suggests that implantation produces mostly vacancy clusters. Some monovacancies may also have been produced and coexist with vacancy clusters.

Figure 2 shows the average S parameter in the implanted layer as a function of annealing temperature for the implanted samples. For the O^+-implanted ZnO, the S parameter first shows

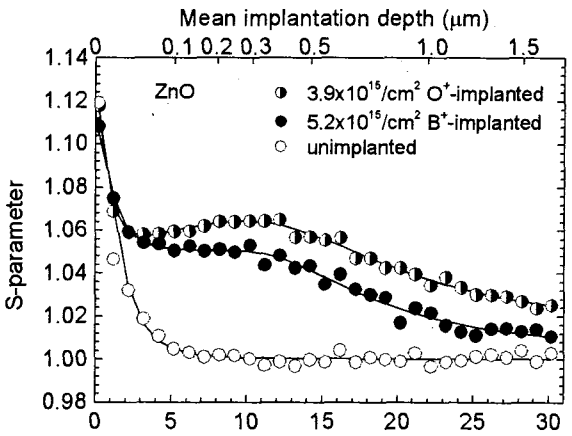

Fig.1 S-E curves measured for ZnO samples before and after implantation. The solid lines are drawn as guidance to the eye.

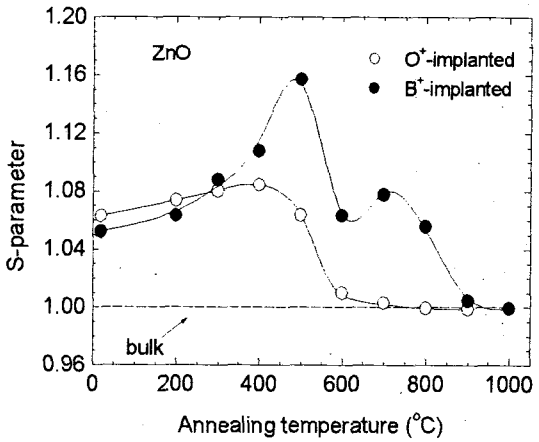

Fig.2 Average S parameter in the implanted layer as a function of annealing temperature for the O^+ and B^+-implanted samples.

increase up to about 1.08 at 400°C, and then decreases rapidly with increasing annealing temperature. The increase of S parameter suggests mostly increase of the vacancy cluster size during annealing. This is due to the migration and agglomeration of vacancies into larger size. After further annealing at high temperatures, these vacancy clusters are no longer stable, and they gradually recover. At 700-800°C, the S parameter decreases to the bulk value, suggesting full recovery of these vacancies.

For the B^+-implanted sample, the annealing behavior of the vacancies is similar. However, the S parameter increases to a high value of nearly 1.16 after annealing at 500°C. This means that much larger vacancy clusters or microvoids are formed. After annealing at 600°C, the S parameter begins to decrease. However, it shows a small increase again at 700°C, and after that, it decreases gradually to the bulk value at 900-1000°C, which indicates annealing out of the vacancy defects introduced by implantation.

The TRIM simulation shows that the average vacancy concentration produced by O^+-implantation in the box-layer is about 7×10^{22} cm^{-3}, while it is 4×10^{22} cm^{-3} for B^+-implantation. Therefore, it is expected that larger size or higher concentration of vacancy clusters will be formed in the O^+-implanted sample. This has been reflected by a higher S parameter in the O^+ as-implanted ZnO. Nevertheless, after annealing, the S parameter shows very slight increase in this sample, suggesting that further agglomeration of the vacancy clusters is very weak. On the contrary, for the B^+-implanted sample, the vacancy clusters grow into very large during annealing. This suggests that boron might have a special chemical effect that favors the agglomeration of vacancy clusters.

Figure 3 shows the Raman spectra measured for the implanted samples before and after annealing. In the as-grown ZnO, there are three phonon modes: E_2 at 437 cm^{-1}, A_1 (LO) at 575 cm^{-1}, and a multi-phonon mode at 331 cm^{-1}. After implantation, the peak at 575 cm^{-1} becomes strong and broad. This is apparently due to the implantation-induced damage. It has been attributed to the oxygen vacancy (V_O) since it also appears in the ZnO grown under oxygen deficient condition.

With increasing annealing temperature, the broad peak in both O^+ and B^+-implanted samples decreases gradually. However, their annealing processes show differences. As shown in Fig. 4, in the O^+-implanted sample, the relative intensity of the 575 cm^{-1} peak decreases rapidly

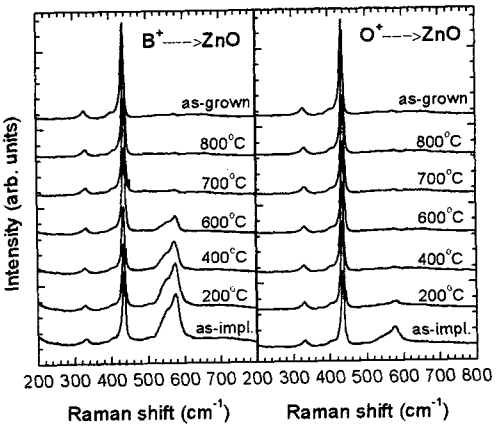

Fig.3 Raman spectra measured for the O^+ and B^+-implanted ZnO samples after annealing.

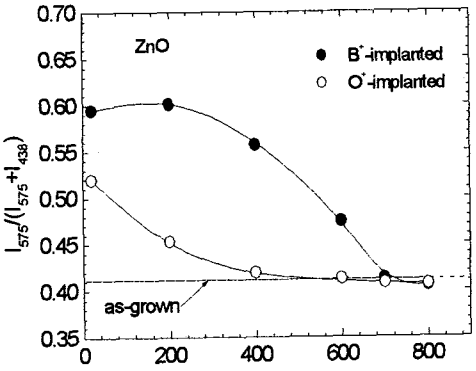

Fig.4 Relative ratio of the integrated 575 cm^{-1} peak intensity to the sum of the 437 cm^{-1} and 575 cm^{-1} peaks as a function of annealing temperature for the O^+ and B^+-implanted ZnO.

and reaches the same level as the unimplanted state after annealing at 400°C. This means that V_O disappears early at 400°C. While for the B^+-implanted sample, the broad peak remains high intensity until annealing at 700°C, indicating that V_O has much higher thermal stability.

The agglomeration of vacancy clusters involves combining small vacancies like monovacancies (V_{Zn} and V_O), so that the size of the vacancy cluster increases. This means that V_O has a contribution to the vacancy cluster agglomeration. In the O^+-implanted sample, the number of V_O is much smaller as compared with that in the B^+-implanted sample, and they disappear rapidly after annealing, therefore their contribution to the vacancy cluster growth is also small. This might be the reason for the slight increase of S parameter after annealing. For the B^+-implanted sample, it introduces much higher concentration of V_O, and they are stable up to 700°C, thus the vacancy cluster can grow into a sufficiently large size. This may well explain the positron annihilation results.

The chemical effect of boron is thus due to the stabilization of V_O. The boron impurity might trap O_i produced by implantation, and form oxide complexes like B_2O_3. Since the B_2O_3 compound has a much lower enthalpy of formation (-1273.5 kJ/mol) than ZnO (-350.5 kJ/mol), the formation of such complex is very likely. Due to this complex formation, the recombination of V_O with O_i is suppressed, so the oxygen vacancies are stabilized, and they are likely to contribute to the formation of large vacancy clusters or microvoids through agglomeration. While for O^+-implantation, as it is a self-atom in ZnO, there is no complex formation with O_i. On the contrary, the O^+-implantation produces large amounts of oxygen interstitials, which expedite the recombination of V_O with them. Therefore, we can observe a fast recovery of the oxygen vacancies. The agglomeration of the vacancy clusters is therefore suppressed.

References

1) D. C. Look, D. C. Reynolds, C. W. Litton, R. L. Jones, D. B. Eason, and G. Cantwell, Appl. Phys. Lett. **81**(2002) 1830-1832.

2) R. Krause-Rehberg and H. S. Leipner, *Positron Annihilation in Semiconductors, Defect Studies*, Springer Series in Solid-State Sciences **127** (Springer, Berlin,1999)

4.15 Positron Annihilation Spectroscopy to Getter Sites for Cu in Si

M. Fujinami*, K. Watanabe*, K. Oguma*, T. Akahane**,
A. Kawasuso***, M. Maekawa*** and Z.Q. Chen***
Department of Applied Chemistry and Biotechnology, Chiba University*
National Institute for Materials Science**
Advanced Science Research Center, JAERI***

1. Introduction

Copper and other transition metals are known to deteriorate the device properties if they are located in active device layers. Much attention has been paid regarding their distribution during thermal processes. Impurity gettering method is one of the most important techniques to remove them from active device areas. Defects in Si effectively trap impurities after annealing at relatively high temperature. It is known that implantation-induced defects are promising trap sites and that metals are accumulated at about half of the mean projected ion range, R_p[1-2]. However, the interaction between defects and metals has been still unknown.

Positron annihilation spectroscopy (PAS) is one of the most powerful tools for open-volume type defects. The positron lifetime stands for the size of defects and the Doppler broadening gives us elemental information of them[3]. Especially using a positron beam, information of a very thin layer can be obtained. When metals are trapped at defects in the implanted layer, PAS shows the location and the structure of trap sites. In this study, we present the use of positrons for clarification of getter sites for Cu atoms in Si.

2. Experimental procedure

2.1 Sample preparation

Cz-Si wafers were implanted with 3 MeV Si^+ ions at a dose of 1 x 10^{15} cm^{-2}, followed by a Cu^+ ion implantation (200 keV, 1 x 10^{14} cm^{-2}) into the backside of the wafer. The mean projected range and straggling of the implanted Si^+ are calculated to be 2.39 μm and 0.25 μm, respectively. The samples were annealed at various temperatures for 1 hour in N_2 atmosphere.

2.2 Positron annihilation spectroscopy

Monoenergetic positrons in the energy range 0.1 – 30 keV were implanted into the samples. The Doppler broadening S parameter of γ-ray spectra was analyzed using one Ge detector and defined as the ratio of the counts in a central region of the annihilation peak (510.25 – 511.75 keV) to the total counts in the annihilation line. A spectrum with total counts of 10^6 was measured at each positron energy. Generally speaking, the annihilation peak of positrons trapped by vacancy-type defects becomes narrow and results in a large S parameter due to fewer annihilations with high-momentum core electrons. However, much attention should be paid in S parameter analysis, because the shape of annihilation peaks is greatly influenced by the electronic shell structures of impurities coupled with vacancies.

Coincidence Doppler broadening (CDB) measurements were made using two high purity Ge detectors with energy resolutions of 1.6 keV and 2.0 keV for 1.17 MeV γ-ray of ^{60}Co with the shaping time of the spectroscopy amplifier as 3 μs. More than 10^7 counts were accumulated for each CDB spectrum, which was the diagonal cross section of the two-dimensional spectrum with a width of ($2m_0c^2$ −1.2 keV < $E_1 + E_2$ < $2m_0c^2$ +1.2 keV). The peak to background ratio was improved to 10^5. The CDB ratio curve was calculated by normalizing the momentum distribution of each spectrum to that of a reference material of the bulk Si. The ratio curves for defects in Si have a peak around 10×10^{-3} m_0c. The momentum density around this region is caused by the rapid decrease at the Jones zone boundary due to the valence electrons, and dangling bond electrons with a localized wave function are likely to smear out this kink. As a result, all of the defects in Si including the top surface itself give the peak around 10×10^{-3} m_0c in the ratio CDB curve.

3. Results and Discussion

Ion implantation at a dose of 1 x 10^{15} cm^{-2} induces open-volume type defects and results in large S. Figure 1 shows the S-E curve for the sample annealed at 400°C. The S parameter for the bulk Si is 0.516. Comparing an additional implantation of Cu^+ with non-additional implantation, no differences can be observed.

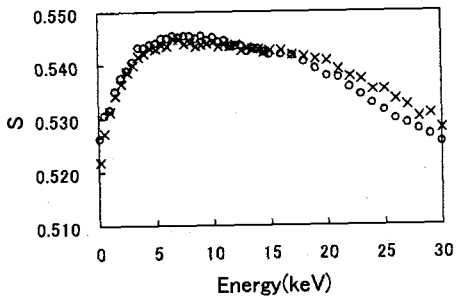

Fig. 1 S-E curves for self-ion implanted Si (3 MeV, 1x10^{15} /cm^2) annealed at 400°C. ○: No additional implantation, ×: Cu^+ implantation into backside.

Further annealing at 600°C gives rise to small difference in S-E curves, as shown in Fig. 2. In the additional Cu^+ implantation, a small decrease of S is observed. On the other hand, the CDB ratio curve shows a big difference (Fig. 3). In the additional Cu^+ implantation, high intensity profile at high momentum region is observed. This profile is characteristic to that due to pure Cu. Large S means that positrons annihilated at open-volume type defects in

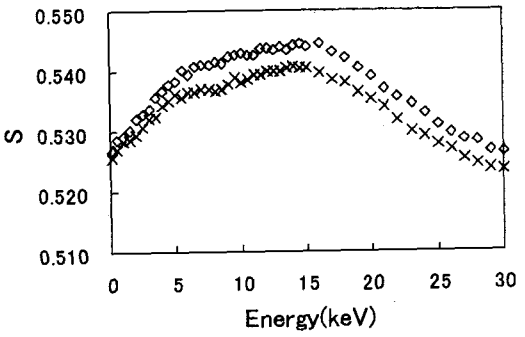

Fig. 2 S-E curves for self-ion implanted Si (3 MeV, 1x10^{15} /cm^2) annealed at 600°C. ◇: No additional implantation, × : Cu^+ implantation into backside.

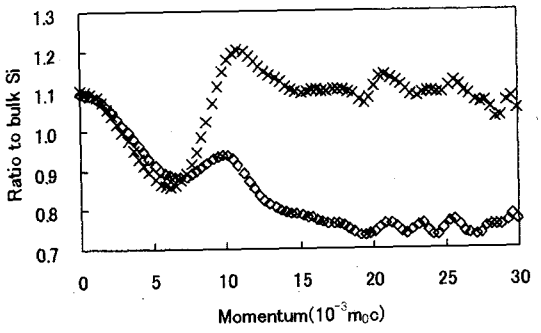

Fig. 3 CDB ratio curves for self-ion implanted Si (3 MeV, 1x10^{15} /cm^2) annealed at 600°C. The positron energy is 15 keV. ◇: No additional implantation, × : Cu^+ implantation into backside.

Si. The CDB curve shows that positrons partially annihilated electrons due to Cu. It is, therefore, concluded that the wall of defects is partially covered with Cu atoms and that the open-volume type defects become gettering sites for Cu atoms.

The positron energy which gives the largest intensity at high momentum region is 15 keV. The mean positron projected range at 15 keV is estimated to be 1.3 μm and corresponds to $R_p/2$.

After annealing at 700°C, both of the samples show the same S-E curves and CDB ratio curves, as shown in Figs. 4 and 5, respectively. S value becomes lower than that for the bulk Si. The ratio curves have a characteristic shape of that for oxygen-related defects[4]. It is considered that the Cu-decorated defects formed at 600 °C collapse and are transformed into extended defects such as stacking faults and dislocations, which are shallow traps of positrons in Si. On the contrary, oxygen

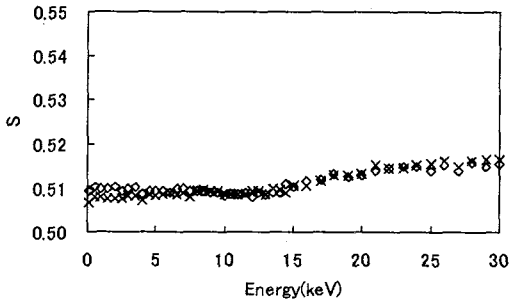

Fig. 4 S-E curves for self-ion implanted Si (3 MeV, $1x10^{15}$ /cm^2) annealed at 700°C. ◇: No additional implantation, × : Cu^+ implantation into backside.

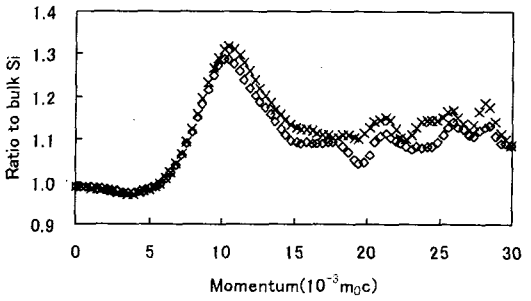

Fig. 5 CDB ratio curves for self-ion implanted Si (3 MeV, $1x10^{15}$ /cm^2) annealed at 700°C. The positron energy is 15 keV. ◇: No additional implantation, × : Cu^+ implantation into backside.

atoms involved in Cz-Si are coupled with vacancies and O-related defects become positron trap sites.

Further studies on the distribution of Cu and the vacancy size are planed and similar measurement on Fe and Ni are in progress.

References

1) R. Krause-Rehberg, F. Börner, F. Redmann, J. Gebauer, R. Kögler, R. Kliemann, W. Skorupa, W. Egger, G. Kögel, W. Triftshäuser, Physica B 308-310 (2001) 442-445.

2) R. Krause-Rehberg, F. Börner, F. Redmann, J. Gebauer, R. Kögler, R. Kliemann, W. Skorupa, W. Egger, G. Kögel, W. Triftshäuser, Physica B 308-310 (2001) 442-445.

3) P. Asoka-Kumar, M. Alatalo, V.J. Ghosh, A.C. Kruseman, B. Nielsen, K.G. Lynn, Phys. Rev. Lett. 77 (1996) 2097-2100.

4) M. Fujinami, T. Miyagoe, T. Sawada, R. Suzuki, T. Ohdaira, T. Akahane, J. Appl. Phys. 95 (2004) 3404-3410.

4.16 Polymerization of C_{60} Thin Films by Ion Irradiation

K. Narumi*, S. Sakai*, H. Naramoto* and K. Takanashi*, **
Advanced Science Research Center, JAERI*
Institute for Materials Research, Tohoku University**

1. Introduction

Since the first report on photoinduced polymerization in thin solid C_{60} films[1], C_{60} polymers produced by several methods have been studied extensively. It has been proposed that C_{60} molecules are linked by a four-membered ring structure via a "2 + 2" cycloaddition. This bonding distorts a C_{60} molecule and the crystal structure of a pristine C_{60} solid where van der Waals interaction bonds the molecules; the symmetry reductions of the molecule and the crystal structure are reflected in a variety of vibrational spectra such as Infrared and Raman spectroscopies and of X-ray-diffraction patterns, respectively[2-4]. There have been published some reports on ion-irradiation-induced polymerization of C_{60} thin films[5]; Electronic excitation by a fast ion is considered to induce the polymerization. However, no report on detailed characterization of the C_{60} solid polymerized by ion irradiation has been published yet. In the present study, polymerization of C_{60} films by 7-MeV C^{2+} ion irradiation has been investigated with X-ray diffraction (XRD) and Raman spectroscopy.

2. Experimental

The details of sample preparation and ion irradiation were described elsewhere[6]; brief outline is summarized here. Thin films of C_{60} were prepared on α-Al_2O_3(0001) substrates by sublimation of C_{60}. The temperature of the substrates was kept around 80 °C and the vacuum level of a deposition chamber was better than 4×10^{-6} Pa during the deposition. The thickness of the films was approximately 350 nm. XRD analysis indicated that (111) layers in a C_{60} fcc crystal grew with its <111> axis along the <0001> axis of α-Al_2O_3. The films were irradiated with 7-MeV C^{2+} ions at room temperature. The energy of the incident ions was high enough for the ion to penetrate through the film, so that the effect of implanted C ions can be neglected. After the irradiation, the films were characterized with XRD and Raman spectroscopy: Raman

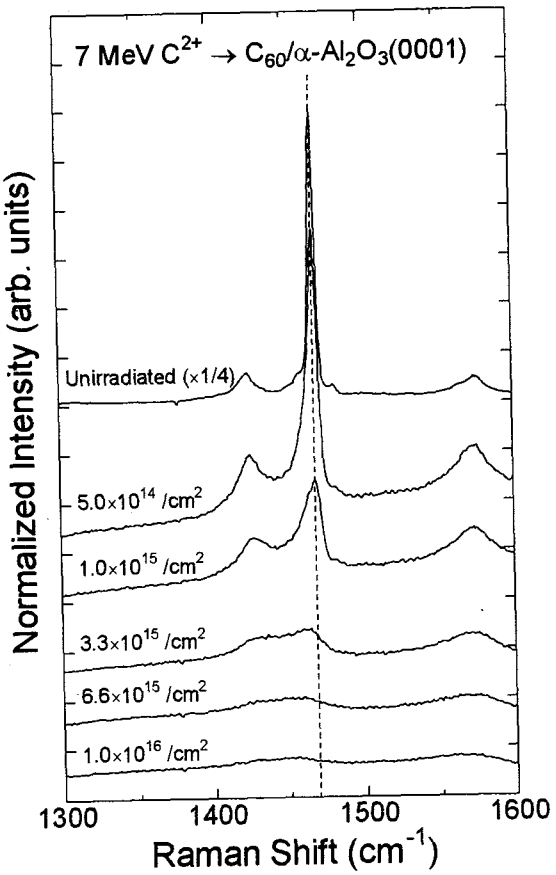

Fig. 1 Fluence dependence of the Raman spectrum around the $A_g(2)$ mode for the C_{60} films irradiated with 7-MeV C^{2+} ions. The broken line shows the position of the $A_g(2)$ mode for the unirradiated film, 1469 cm^{-1}.

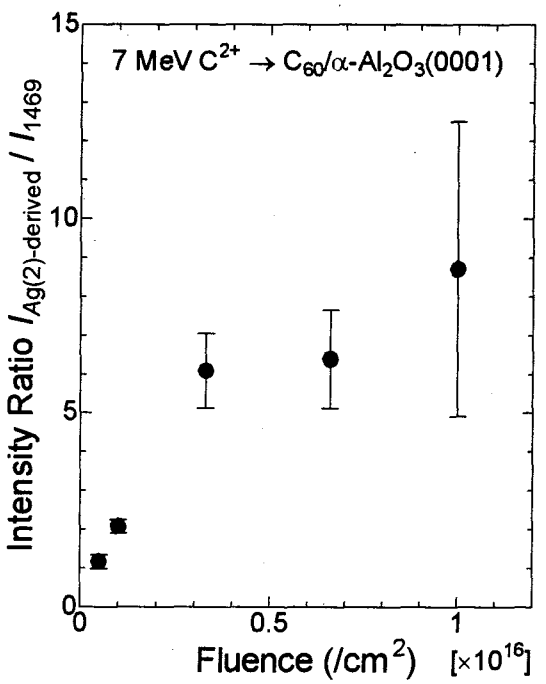

Fig. 2 Fluence dependence of the Raman-intensity ratio of the sum of the $A_g(2)$-derived lines to the 1469-cm^{-1} line for the C_{60} films irradiated with 7-MeV C^{2+} ions.

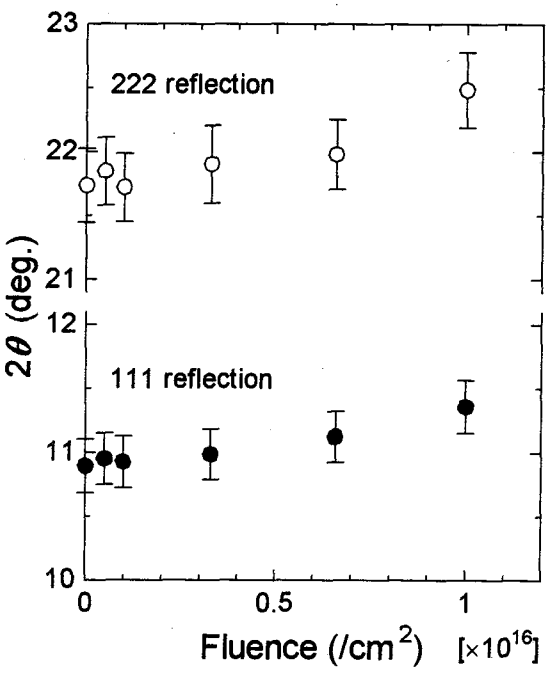

Fig. 3 Fluence dependence of the 111- and 222-reflection angles for the C_{60} films irradiated with 7-MeV C^{2+} ions. Error bars indicate the full width at half maximum of the reflected peak.

measurement was performed in air with a Nanofinder Raman microscopy system (Tokyo Instruments, Inc.) using the 488 nm spectral line of an Ar^+ laser. 2θ-θ scans of XRD were performed in air with an X'Pert X-ray diffraction system (Philips) using the Cu Kα line.

3. Results and discussion

The fluence dependence of the Raman spectrum around the $A_g(2)$ mode is shown in Fig. 1. It is observed that a sharp and intense peak at 1469 cm^{-1} gradually changes into broader and weaker one, which is finally combined with the $H_g(7)$ mode, as the ion fluence increases. This variation of the spectrum around the $A_g(2)$ mode is characteristic for ion-irradiated C_{60} thin films and considered to be attributed to polymerization and disintegration of C_{60} molecules by ion bombardment[5]: The broadening of the line is due to the polymerization and the reduction of the line intensity is mainly due to the disintegration. In order to evaluate the development of the polymerization, we have resolved the peaks in the region of the $A_g(2)$ mode with Voight-line-fit analysis using the lines assigned for the photopolymer and pressure-induced polymer, 1464, 1460, 1454, 1447 and 1434 cm^{-1} [4, 7]. Figure 2 shows the fluence dependence of the Raman-intensity ratio of the sum of the $A_g(2)$-derived lines to the 1469-cm^{-1} line. The intensity ratio of the $A_g(2)$-derived lines to the 1469-cm^{-1} line obviously increases with the increasing ion fluence and becomes almost constant after the fluence of 3.3×10^{15} /cm^2. This indicates that the ratio of the polymerized C_{60} molecule increases as the ion fluence increases and that the polymerization has almost reached saturation after the irradiation with 3.3×10^{15} /cm^2.

In the XRD measurement, we observed that peak positions of the reflection from the (111)

plane in an fcc crystal of C_{60} shifted to higher angles gradually with the increasing ion fluence: The fluence dependence of the 111- and 222-reflection angles is shown in Fig. 3. This result indicates that the spacing of the (111) plane in the fcc crystal of C_{60} has been reduced: The reduction amounts to ~4 % after irradiation with 1×10^{16} /cm^2. It has been predicted theoretically that the centers of mass of the two C_{60}'s in a C_{60} dimer are separated by 0.9022 nm, which is shorter than the intermolecular distance 1.002 nm between the individual molecules in pristine C_{60} solid[8]. The present Raman analysis shows that most of the C_{60} molecules that survived the ion bombardment with 1×10^{16} /cm^2 have been polymerized. Therefore it is concluded that the observed reduction of the spacing of the (111) plane is induced by the polymerization of the C_{60} molecule by the ion irradiation. If it is assumed that the crystal structure of the polymerized C_{60} thin film is fcc, the intermolecular distance is estimated to be 0.955 nm after the irradiation with 1×10^{16} /cm^2. This value is close to 0.962 nm for a contracted fcc phase obtained by high-pressure and high-temperature treatment[2].

References

1) A.M. Rao, P. Zhou, K.-A. Wang, G.T. Hager, J.M. Holden, Y. Wang, W.-T. Lee, X.-X. Bi, P.C. Eklund, D.S. Cornett, M.A. Duncan, I.J. Amster, Science **259** (1993) 955-957.
2) Y. Iwasa, T. Arima, R.M. Fleming, T. Siegrist, O. Zhou, R.C. Haddon, L.J. Rothberg, K.B. Lyons, H.L. Carter Jr, A.F. Hebard, R. Tycko, G. Dabbagh, J.J. Krajewski, G.A. Thomas, T. Yagi, Science **264** (1994) 1570-1572.
3) M. Núñez-Regueiro, L. Marques, J-L. Hodeau, O. Béthoux, M. Perroux, Phys. Rev. Let. **74** (1995) 278-281.
4) A.M. Rao, P.C. Eklund, J-L. Hodeau, L. Marques, M. Núñez-Regueiro, Phys. Rev. B **55** (1997) 4766-4773.
5) For example, J. Kastner, H. Kuzmany, L. Palmetshofer, Appl. Phys. Lett. **65** (1994) 543-545.
6) K. Narumi, Y. Xu, K. Miyashita, H. Naramoto, Euro. Phys. J. D **24** (2003) 385-388.
7) T. Wågberg, P. Jacobsson, B. Sundqvist, Phys. Rev. B **60** (1999) 4535-4538.
8) G.B. Adams, J.B. Page, O.F. Sankey, M. O'Keefe, Phys. Rev. B **50** (1994) 17471-17479.

4.17 Cluster Effects Observed for X-ray Diffraction Pattern of Oxides Irradiated with Cluster Beam

A. Iwase[*], N. Ishikawa[**], Y. Chimi[**], Y. Ohta[***], T. Hashimoto[***], O. Michikami[***], M. Fukuzumi[*], F. Hori[*], Y. Saitoh[****] and A. Chiba[****]
Department of Materials Science, Osaka Prefecture University[*]
Department of Materials Science, JAERI[**]
Faculty of Engineering, Iwate University[***]
Advanced Radiation Technology Center, JAERI[****]

1.Introduction

Our previous study shows that irradiation of oxide superconductors with 0.5MeV C monoatomic ion beam causes atomic displacements via elastic collision and it results in lattice expansion[1]. We have recently reported that the cluster effect is absent in lattice expansion for oxide superconductors $EuBa_2Cu_3O_7$ irradiated with 4MeV C_8 cluster ions, indicating the absence of cluster effect in terms of defect density[2]. However, in the present report we report a new insight on the cluster effect observed for some aspects of XRD(X-ray diffraction) pattern of $EuBa_2Cu_3O_7$ irradiated with cluster ions.

2.Experimental Procedure

Thin films of c-axis oriented $EuBa_2Cu_3O_y$ (y=7) were prepared on MgO substrates by a sputtering method. [0.5 × n]MeV C_n (n=1,4,8) ions, all having the same velocity, were irradiated at room temperature using the tandem accelerator at JAERI-Takasaki. The projected range of those ions is about 0.6μm, but for the cluster ions they become dissociated during the passage in the sample and have no more spatial correlation as the clusters proceed deeper into the sample. In order to observe the cluster effect, the sample thickness was determined to be 0.1μm, which we believe is enough to assure the spatial correlation of clusters during their passage through the sample. The fluence dependence of c-axis lattice parameter was examined by measuring the positions of XRD peaks. The fluence dependence of XRD peak intensity and FWHM(Full Width at Half Maximum) of those peaks was also measured.

3.Results and Discussion

As reported in the previous report[2], the XRD peak position corresponding to c-axis lattice spacing shifts to lower angle side in the same manner for the irradiation with 0.5MeV C, 2.0MeV C_4 and 4MeV C_8 when the effects are compared in the unit of carbons/cm^2. Since the lattice expansion by 0.5MeV C irradiation has already been known to be attributed to the elastic displacements[1], the lattice expansion for the irradiation with 2.0MeV C_4 and 4MeV C_8 can be understood in the framework of the elastic displacements. From the above results, no sign of the cluster effects is detected. However, as demonstrated in Figs.1 and 2, the cluster effect is observed for some aspects of an XRD peak; the fluence dependence of XRD peak intensity, and that of FWHM of XRD peaks.

These cluster effects can be understood in the framework of elastic displacements, and the key parameter for the interpretation for

the present result is the energy of PKA (primay knock-on atoms). The irradiation with larger cluster is expected to cause higher maximum PKA energy, since larger cluster has higher mass (with same velocity in this case). Higher maximum PKA energy can create larger defect agglomerates rather than simple defects. The larger decrease in intensity of XRD peak and larger increase in FWHM for irradiation with larger cluster may be related to the higher energy of PKA.

References

1) N. Ishikawa et al., Nucl. Instr. Meth. B 135 (1998) 184.
2) A. Iwase et al., TIARA annual report 2003 (2004) 217.

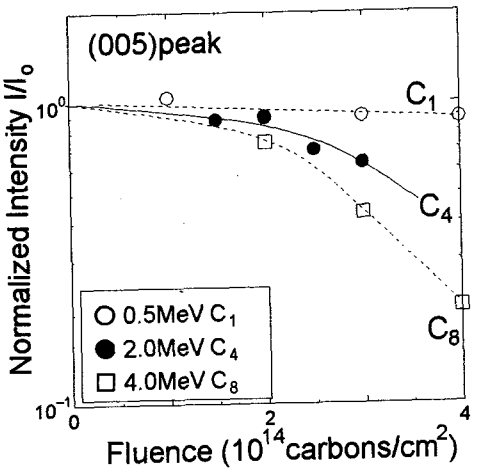

Fig.1 Fluence dependence of the intensity of (005) peak for 0.5MeV C, 2.0MeV C_4 and 4MeV C_8 irradiation. The fluence is indicated in the unit of carbons/cm^2 in order to facilitate detection of the cluster effect.

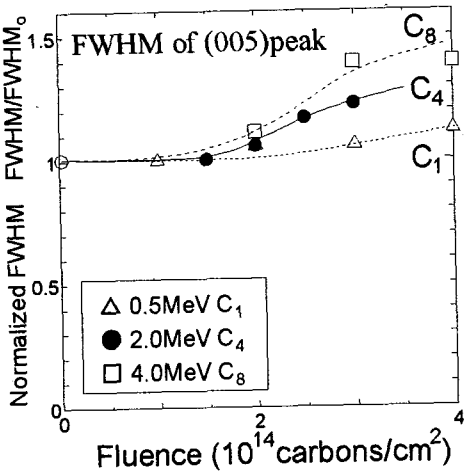

Fig.2 Fluence dependence of FWHM of (005) peak for 0.5MeV C, 2.0MeV C_4 and 4MeV C_8 irradiation. The fluence is indicated in the unit of carbons/cm^2 in order to facilitate detection of the cluster effect.

4.18 In-Situ Measurement of Defect Concentration in Metals Irradiated with Energetic Electrons

N. Ishikawa and Y. Chimi
Department of Materials Science, JAERI

1.Introduction

So far we have systematically investigated the ion-irradiation effect in metals and other inorganic materials irradiated with high-energy ions. In the case of metals effect of elastic displacements occupies most of the irradiation effect. This means that, in order to extract the effect of electronic energy loss hidden in the total irradiation effect, precise quantification of the effect of elastic displacements is absolutely necessary. In metals the atomic displacements caused by electron irradiation are expected to be dominated only by elastic displacements. In this respect the data of (low-temperature) electron irradiation experiments plays an important role for defining the process of elastic displacements[1,2].

In recent years intriguing phenomenon induced by high-energy ion irradiation, that is irradiation-induced crystallographic phase transition by high electronic energy loss, has been found for a titanium metal[3,4]. In order to evaluate this effect quantitatively, a precise measurement of elastic displacement is necessary as mentioned above. Under this recognition, in this study a Ti foil is irradiated with energetic electrons and a Zr foil is irradiated at the same time. The reason for this simultaneous irradiation of both Ti and Zr is as follows.

Both Ti and Zr has almost the same temperature-pressure phase diagram, but the irradiation-induced phase transition is observed only for Ti irradiated with high-energy heavy ions. Comparative study of Ti and Zr is thus important for clarifying the phase transition process observed only for Ti. In this study, we have performed low-temperature electron irradiation and subsequent in-situ measurement of electrical resistivity in order to evaluate the effect of elastic displacements.

2.Experimental procedure

Commercial metal foils of Ti and Zr, both having 25μm thickness, were cooled down to 19K, and were irradiated with 2.0MeV electrons using a single-ended accelerator at TIARA facility. The unique characteristic of this irradiation chamber installed in this facility is that the sample temperature during irradiation is variable and at the same time in-situ measurement of electrical resistivity is possible.

The temperature was controlled to low temperature below 30K during the irradiation, and the electrical resistivity was always measured at 19K. The fluence dependence of electrical resistivity was measured both for Ti and for Zr. In metals it has already been established that the concentration of irradiation-induced defects is proportional to increase in electrical resistivity, therefore the result can be directly converted to fluence dependence of defect concentration.

3.Results and discussion

In Fig.1 fluence dependence of defect concentration for Ti and Zr which is estimated by electrical resistivity measurement is shown. For estimating the defect concentration, Frenkel pair resistivity, which is the coefficient for converting electrical resistivity increase to defect concentration, is assumed to be reasonable value of ρ_F=1.8x10^{3}μΩcm for Ti and 3.5 x10^{3}μΩcm for Zr. The figure shows that for both metals defect concentration linearly increases as a function of the fluence. From the present result cross section for defect creation is estimated to be σ_d=1.1x10^{-22}cm^2 for Ti and 7.3 x10^{-22}cm^2 for Zr. It is found that defect accumulation is greater for Ti than for Zr for about 33%, and there is no significant difference in defect accumulation between the two metals which can lead to presence/absence of phase transition.

The cross section for defect creation estimated experimentally is compared with the calculated one assuming only elastic displacements are dominant, and as was expected the experimentally obtained cross section almost agrees with the calculated one for both Ti and Zr. In conclusion the electron irradiation results in normal Frenkel pair creation, and no sign of phase transition is detected as expected from the framework of elastic displacement process.

As the mass of the incident particles becomes bigger than electrons, the cross section for defect creation is expected to become smaller than the calculated one because of the increase in average energy of PKA(Primary knock-on Atoms). If high-energy heavy ions are irradiated, then the sign of phase transition may be detected. The irradiation experiment using heavier particles and the comparison with the present result is therefore necessary to quantify and clarify the effect of electronic energy loss, namely phase transition.

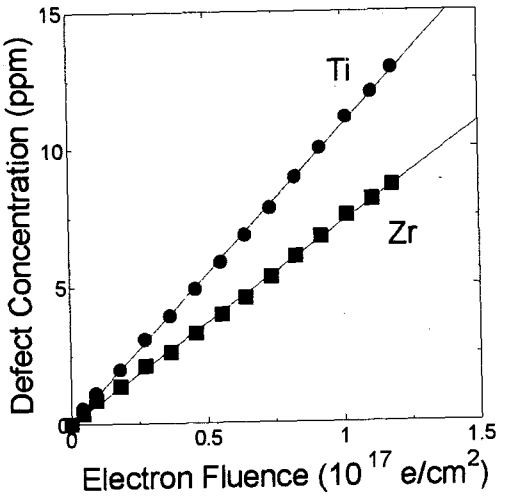

Fig.1 Fluence dependence of defect concentration for Ti and Zr irradiated with 2.0MeV electrons.

References

1) N. Ishikawa, A. Iwase, Y. Chimi, O,Michikami, H. Wakana, T. Kambara, J.of Phys. Soc. Jap. 69 (2000) 3563.
2) Y. Chimi, A. Iwase, and N. Ishikawa,J. Nucl. Mater. 271&272 (1999) 236.
3) H. Dammak, A. Barbu, A. Dunlop, D.Lesueur and N. Lorenzelli, Phil. Mag.Lett. 67 (1993) 253.
4) H. Dammak, A. Dunlop and D. Lesueur, Nucl. Instr. and Meth. B 107 (1996) 204.

4.19 Reaction Kinetics Calculation of Electron Irradiation Effect in Fe Based Model Alloy

T. Tobita*, Y. Chimi**, N. Ishikawa**, Y. Nishiyama*, M. Suzuki*
and A. Iwase***
Department of Reactor Safety Research, JAERI*
Department of Materials Science, JAERI**
Department of Materials Science, Osaka Prefecture University***

1. INTRODUCTION

To provide for long term operation of light water reactors, improvements on the irradiation embrittlement prediction method are necessary. Therefore, it is an important subject in recent years to investigate the mechanisms of irradiation embrittlement in reactor pressure vessel steel (RPVs). The irradiation rate effect is one of the significant factors of the irradiation embrittlement of RPVs materials; however, the exact mechanism has not been understood yet. The impurities in RPVs materials have been known to have a storing effect on the irradiation embrittlement. The Cu precipitates which grow during irradiation cause irradiation hardening. It has been assumed that the irradiation enhanced diffusion based on the vacancy mechanism can explain the Cu clustering during irradiation.

In the present paper, we tried to make a comparative study of calculation and experiment of irradiation effect on the electrical resistivity of Fe-Cu model alloys. We developed a numerical calculation code based on the reaction kinetics, which gives the time-varying concentration of the various defects by calculating the interaction among an interstitial, a vacancy and a Cu atom. In the present experiment, we measured the electrical resistivity of Fe-Cu model alloys as an index of irradiation effect during electron irradiations. The electrical resistivity measurements provide an excellent means to obtain information on irradiation effects, because it is very sensitive to defect concentration and the obtained information is the average over the measured region of a specimen. The high energy electron induces the Frenkel pair consisting of a vacancy and an interstitial, which is a suitable defect for calculation.

2. EXPERIMENTS

The materials were four kinds of Fe-Cu model alloys with different Cu contents. The chemical composition of these materials is shown in Table 1. The Fe-Cu model alloys were fabricated as pure as possible to eliminate the effects of impurities. After the heat treatment at 850°C for 10 min, the materials were gas-quenched to keep the Cu atoms in supersaturated solid solution at room temperature. The specimen geometry and the test procedure are shown in Fig.1. The specimens were cut into ribbons of 1mm width, and the four electrodes were spot-welded.

Table 2 shows a test matrix. We measured the electrical resistance under three conditions, i.e. low temperature and room temperature under electron irradiation, and room temperature without irradiation. To investigate the relationship between the Frenkel pair concentration and the electrical resistivity, 2 MeV electron irradiation at low temperature (11K) was performed. In the case of the electron irradiation at low temperature, an interstitial and a vacancy accumulate simply without thermal diffusion. Consequently, the displacement per

atom (dpa) means the Frenkel pair concentration. To investigate the relationship between the solid-soluted Cu atom concentration and the electrical resistivity, we measured the electrical resistivity of the various Fe-Cu materials at room temperature (300K). To compare with the calculation, 2MeV electron irradiation at room temperature was performed. In this condition, the production of a Frenkel pair and the interaction of defects occur simultaneously during irradiation. In order to investigate dose rate effects, irradiation at room temperature was performed at two dose rate, 2.7×10^{-9} and 3×10^{-10}dpa/s.

Table 1 Chemical composition of materials

Material	Fe	Cu	C	Si	O	N
Fe-0.02wt%Cu	Bal.	0.022	0.003	0.003	0.015	0.0006
Fe-0.1wt%Cu	Bal.	0.1	0.002	0.003	0.014	0.0005
Fe-0.6wt%Cu	Bal.	0.61	0.002	0.002	0.015	0.0006
Fe-1.2wt%Cu	Bal.	1.19	0.002	0.001	0.013	0.0006

Table 2 Test matrix

Measuring condition	Material	Experimental purpose
Low Temp.(11K) Irrad. 2.7×10^{-9}dpa/s	Fe-0.02wt%Cu	The resistivity change per Frenkel pair concentration
Room Temp.(300K) without Irrad.	Fe-0.02, Fe-0.1, Fe-0.6, Fe-1.2wt%Cu	The resistivity change per Cu atom concentration
Room Temp.(300K) Irrad. 2.7×10^{-9}, 3×10^{-10}dpa/s	Fe-0.6wt%Cu	Comparison of Calculation and Experiment

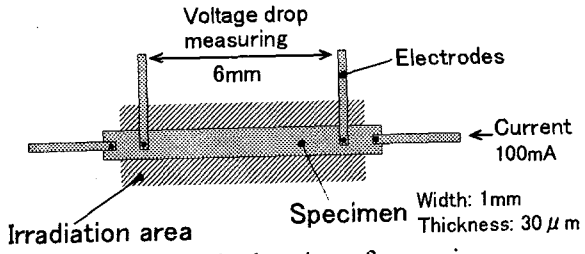

Fig. 1 Schematic drawing of a specimen

3. CALCULATION PROCEDURE

In order to simplify the calculation, we assumed three defect types, a vacancy (V_N), an interstitial (I_N) and a Cu atom (Cu_N), and four defect cluster scales, $N=1, 2, 3$ and C (≥4). We assumed that V_1 and I_1 could jump, while Cu_1 could move via interaction with V_1. The calculation model consists of twelve simultaneous equations. The basic model for the calculation of the defect concentration is expressed by the following equation:

$$dC_{VI}/dt = P_{VI} - C_S M_{VI} C_{VI} \pm Z_{VI+VI} C_{VI} \times M_{VI} C_{VI}, \quad \text{----(1)}$$

where C denotes a concentration, t denotes time, P denotes a Frenkel pair generation frequency, Cs denotes a sink concentration, M denotes a jump frequency and Z is the number of a reaction site. There are many combinations of reactions: for example,

$V_N + V_1 \rightarrow V_{N+1}$, $V_N + I_1 \rightarrow V_{N-1}$, $V_N \rightarrow V_1 + V_{N-1}$.

In this case of electron irradiation, P_{VI} is equivalent to the dpa rate. The parameters we used, such as migration energy, binding energy, reaction site number, etc. were quoted from the literature [1].

4. RESULTS AND DISCUSSION

We have obtained a relationship between the Frenkel pair concentration and the electrical resistivity from the electron irradiation at low temperature. The relationship has been obtained as the following equation:

$$\Delta\rho = 1.15 \times 10^{-5} \times (\textit{Frenkel pair concentration}), \quad \text{---(2)}$$

where $\Delta\rho$ is the electrical resistivity change. We assumed that this *Frenkel pair concentration* was equivalent to average of the vacancy concentration and the interstitial concentration.

We can obtain a relationship between the solid-soluted Cu atom concentration and the electrical resistivity from the electrical resistivity measurement of the various Fe-Cu alloys at room temperature. The effect of the solid-soluted Cu (Cu_1) concentration on the electrical resistivity is given by the following equation:

$$\Delta\rho = 4.15 \times 10^{-6} \times (Cu_1 \textit{ concentration}). \quad \text{---(3)}$$

We assumed that Cu_2, Cu_3 and Cu_C didn't

contribute to the electrical resistivity.

From equations (2) and (3), we derive the following equation:

$$\Delta\rho = 1.15 \times 10^{-5} \times (C_{Vtotal} + C_{Itotal}) / 2 - 4.15 \times 10^{-6} \times (\Delta C_{Cu1}), \quad \text{----(4)}$$

where C_{Vtotal} denotes a vacancy concentration, i.e. the ratio of the total vacancy number to the Fe atom number, C_{Itotal} denotes an interstitial concentration and ΔC_{Cu1} denotes decrease of the solid-soluted Cu concentration. This decrease is due to the irradiation-induced Cu clustering. Using equation (4), we can convert a calculated defect concentration into the electrical resistivity change. Figure 2 shows the dose dependence of calculated value and measured the electrical resistivity change for the dose rates, 2.7×10^{-9} and 3×10^{-10}dpa/s. Regarding the reaction kinetics calculation, the vacancy migration energy is the most effective parameter in resistivity change. We assumed the vacancy migration energy was 0.65eV in the present calculation.

Both the calculated and measured resistivity decreases steadily with dose. There is a transient peak in the measured values at 2.7×10^{-9} dpa/s, but we can not explain this phenomenon yet. For effect of the dose rate on the resistivity change, the same trend is observed in both the calculated and measured values: a low dose rate induces electron resistivity change effectively. It is suggested that the present reaction kinetics calculation is qualitatively adequate to simulate defect behavior.

References

1) S. Yanagita, et al., Mat. Trans., 43(2002) 1663-1669.

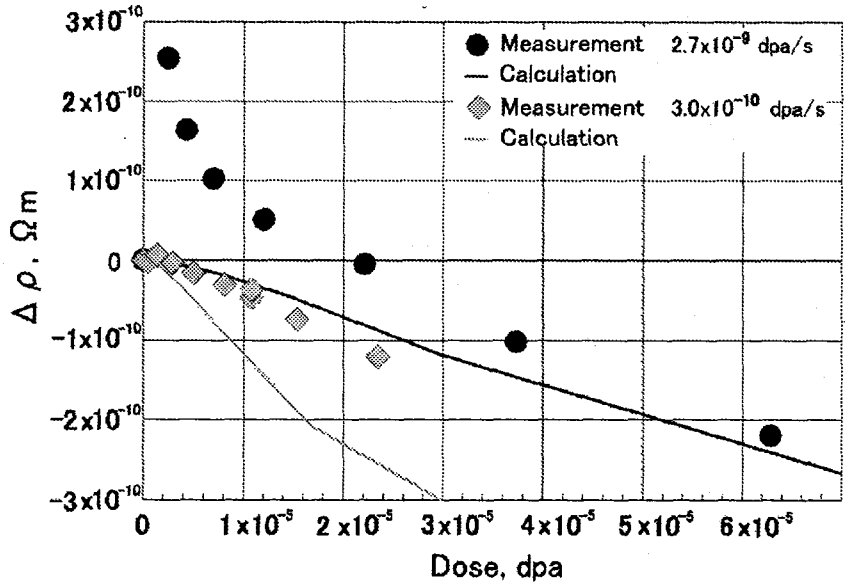

Fig. 2 Dose dependence of the electrical resistivity change

JP0650242

4.20 Change in Electrical Resistivity of FeRh by Energetic Electron Irradiation

M. Fukuzumi*, N. Ishikawa**, Y. Chimi**, F. Ono*** and A. Iwase*
Department of Materials Science, Osaka Prefecture University*
Department of Materials Science, JAERI**
Department of Physics, Okayama University***

1. Introduction

One of the interesting properties of ordered Fe-Rh alloys is the magnetic phase transition at about 310 K from a low temperature antiferromagnetic (AF) state to a high temperature ferromagnetic state (FM). At the phase transition temperature, value of electrical resistivity decreases by about 50 %. In the previous study, we performed 8 MeV electron irradiation of Fe-50at.%Rh alloy, leading to the result that the lattice parameter increased by about 0.1 - 0.3 % and that, resulting from SQUID measurement, the AF-FM transition temperature decreased by 3-18 deg., without any crystal structure changes [1]. The change in magnetic properties by electron irradiation has also been studied by using X-ray magnetic circular dichroism (XMCD) measurement, which provides site-specific information on electronic states of constituent elements of magnetic materials. In the present experiment, we confirm the irradiation-induced change in magnetic transition temperature by using an electrical resistivity measurement.

2. Experimental Procedure

An Fe-50at.%Rh alloy was prepared by induction melting in a vacuum. This specimen was cut into 10 mm x 1 mm x 0.2 mm pieces and they were sealed in evacuated silica capsule, annealed at 1373 K for 173 ksec for homogenization and quenched into ice water. Pure-Fe films as current and voltage terminals were spot-welded on each specimen for a four-probe electrical resistance measurement. Then a specimen was mounted on an aluminum substrate by using epoxy resin (Araldite) in to insulate the specimen from the substrate. The specimen was irradiated with 2.0 MeV electrons from a 3 MV single-ended accelerator in TIARA, JAERI-Takasaki to the fluence up to 3.0 x 10^{18} e^-/cm^2 below 50 K. The change in electrical resistance of the specimen was measured as a function of temperature up to 310 K at the rate of 2 K/min.

3. Results and Discussion

Figure 1 shows the change in electrical resistivity of an Fe-50at.%Rh alloy as a function of specimen temperature before and after irradiation. The figure shows that the value of electrical resistivity of the unirradiated specimen decreases around 300 K, corresponding to the magnetic transition from AF to FM. In addition, the profile of electrical resistivity with increasing

the specimen temperature differs from that with decreasing the specimen temperature. It is attributed to the fact that AF-FM magnetic transition is a first order phase transition. After the irradiation, the temperature where the value of electrical resistivity changes clearly shifts to a lower temperature. It represents that AF-FM magnetic transition temperature shifts to the lower temperature by electron irradiation. The present result confirms the change in AF-FM transition temperature by electron irradiation which has been found by SQUID measurements.

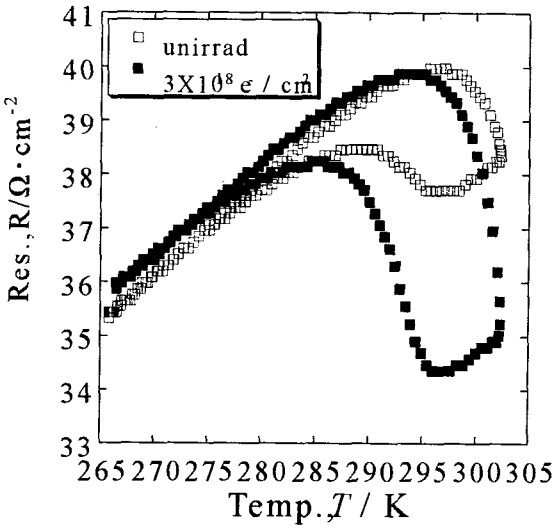

Fig.1 Relationship between electrical resistance and temperature of an Fe-50at.%Rh alloy before and after 2 MeV

References

1) M. Fukuzumi, R. Taniguchi, S. Komatsu, F. Ono, A. Iwase, Mat. Res. Soc. Symp. Proc., vol.792 (2004) 393.

4.21 Reversible Deformation of Au Foils Induced by Electron and Proton Irradiation

H. Tsuchida*, A. Itoh*, I. Katayama**, S. C. Jeong**, M. Awano***, H. Ogawa***, N. Sakamoto***, A. Iwase****, N. Ishikawa***** and Y. Chimi*****
Quantum Science and Engineering Center, Kyoto University*
Particle and Nuclear Studies, KEK**
Department of Physics, Nara Women's University***
Department of Materials Science, Osaka Prefecture University****
Department of Materials Science, JAERI*****

1. Introduction

Recently, we have investigated reversible deformation of metallic foils induced by ion irradiation [1]. The deformation during irradiation was measured by using a laser displacement meter. We have studied beam flux dependence of the deformation of Al foils and time-response of the deformation. It was found that the foil is deformed reversibly under beam-on and beam-off conditions, and the magnitude of deformation depends on a grain size of a target foil. Interestingly, anomalously large deformation was observed for the fine-grained foil with mean grain size of about three hundreds nm. This deformation is larger than that resulting from thermal expansion.

In order to understand the mechanism of the deformation, in this work we examined projectile dependence of the deformation of Au foils by using two types of projectile beams of electrons and protons. Preliminary results are reported.

2. Experimental

Electron irradiation experiments were carried out by using a 3 MV single-ended accelerator at Japan Atomic Energy Research Institute (JAERI), Takasaki Establishment. The experimental setup is schematically shown in Fig. 1. A self-supported target foil was irradiated with 2 MeV electron beams. The target size was 7 mm in diameter. The beams were carefully collimated with a cylindrical-shaped slit to achieve a uniform intensity distribution. The beam spot size was 3 mm in diameter and the beam flux was between 4×10^{13} and 4×10^{14} particles/(cm^2 s).

Two kinds of Au foils of 1 μm in thickness, made by rolling and evaporation, were used as a target. To characterize materials properties of the foil used, an electrical resistivity of the foils before irradiation was measured at the temperature of below 300 K by a conventional four-probe method. Results are shown in Fig. 2, indicating that the electrical resistivity for the evaporation is about two

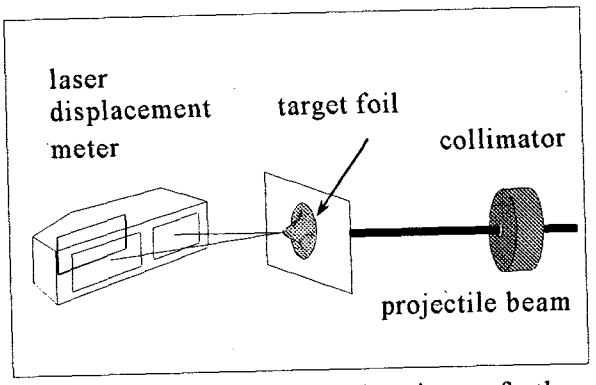

Fig. 1 A schematic drawing of the experimental setup.

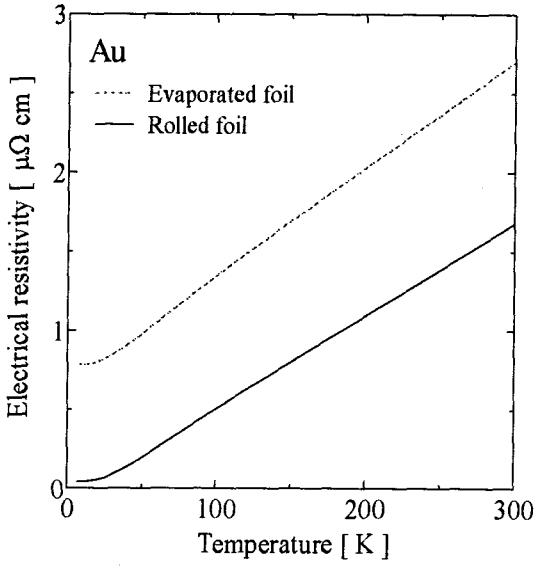

Fig. 2 Electrical resistivity of the Au foils made by evaporation and rolling as a function of the temperature.

times as large as that for the rolling.

Foil-deformation induced by irradiation was measured with a laser reflection technique[2]. When projectile beam is turned on, bell-shaped deformation appears in an irradiated area, as schematically shown in Fig.1. The magnitude of deformation was measured at the center of projectile beam spot.

We also made an irradiation experiment with a proton beam obtained from a 1.7 MV Pelletron accelerator of Nara Women's University. The experimental procedure is essentially the same as that for the electron irradiation experiments described above. An energy of proton was 2.5 MeV and the beam flux was between 9×10^{10} and 9×10^{12} particles/(cm^2 s).

3. Results and Discussion

Figure 3 shows spectra of the magnitude of deformation of the evaporated foil for irradiation with electrons and protons as a function of time. Note that in both irradiation parameters the energy flux is almost the same value of about 0.05 [W/cm^2], where energy deposition was calculated from SRIM code[3]. Results indicate that the magnitude of deformation for proton-irradiation is about two times as large as that for electron-irradiation. This means that the magnitude of deformation does not correlate with the energy flux deposited into the foil.

In order to see this correlation in more detail, results for the magnitude of deformation as a function of energy flux is shown in Fig. 4. Open symbols are the data for the rolled foil and closed symbols are the data for the evaporated foil. Main results include that (1) the magnitude of deformation depends on type of foil and deformation of the evaporated foil is larger than that of the rolled foil, (2) for the rolled

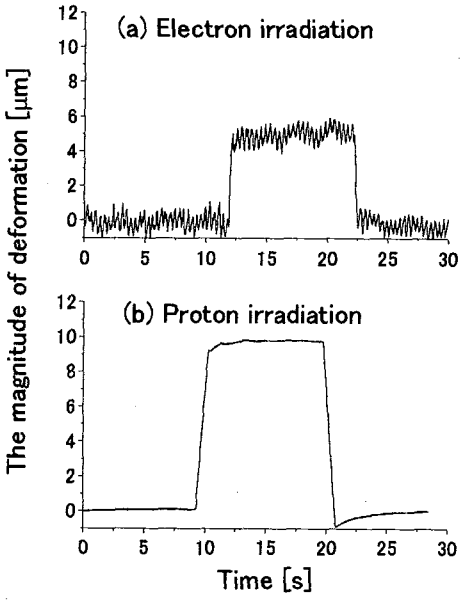

Fig. 3 Time spectra of the magnitude of deformation of an evaporated Au foil of 1 m in thickness: (a) 2.0 MeV electron irradiation at energy flux of 0.05 W/cm^2, and (b) 2.5 MeV proton irradiation at 0.045 W/cm^2.

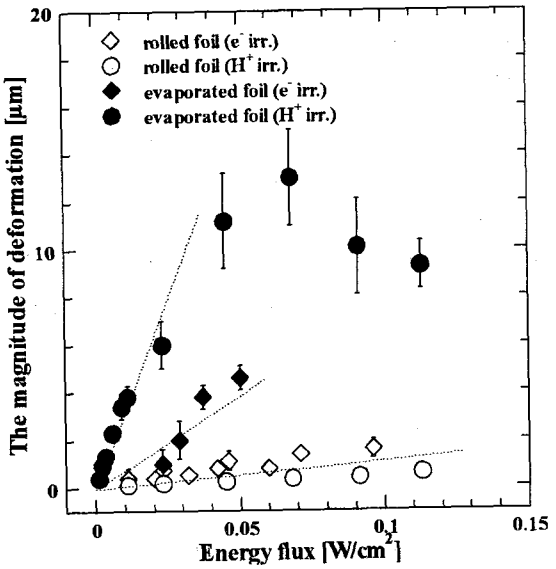

Fig. 4 Energy flux dependence of the magnitude of deformation of evaporated and rolled Au foils by 2.0 MeV electrons and 2.5 MeV protons.

foil, the results for proton and electron irradiation are the same, suggesting that the deformation correlates with the energy flux, and (3) for evaporated foil, the deformation by proton is larger than electron at the same energy flux, indicating that deformation depends on projectile type. The second result may be interpreted as that the deformation is due to beam heating. On the other hand, the third result can not be explained by beam heating effects, and the deformation may be caused by other effect.

In order to interpret the projectile dependence of deformation we estimated a cross section for the production of primary displaced atoms (the damage cross section). For electron impacts, we used the formalism by Lucasson and Walker[4], and the damage cross section is estimated as about 2×10^{-23} cm^2. For proton impacts we estimated the cross section by using a number of vacancies calculated from TRIM[3]. The calculated cross section was about 2×10^{-21} cm^2, which is two order of magnitude larger than that for electron impacts.

As descried above, the deformation depends on type of foils (which are made by evaporation and rolling). The foils used in this work may be different in grain size. If the evaporated foil is likely to accumulate the vacancies produced by irradiation, the vacancy accumulation may lead to volume expansion of foil. If this speculation is correct, we reach the preliminary conclusion that the deformation observed for irradiation of evaporated Au foil by proton was caused by both heating and the formation of defects. Further experiments will be needed to understand this mechanism.

References

1) H. Tsuchida, I. Katayama, S. C. Jeong, M. Haba, H. Ogawa, N. Sakamoto, H. Mori, J. G. Lee and A. Itoh, Phys. Rev. B 70 (2004) 054112.

2) H. Tsuchida, I. Katayama, S. C. Jeong, H. Ogawa, N. Sakamoto, and A. Itoh, AIP Conf. Proc. 576 (2001) 931-934.

3) J. F. Ziegler, J. P. Biersack, and U. Littmark, *The Stopping and Range of Ions in Solids* (Pergamon, New York, 1985).

4) P. G. Lucasson and R. M. Walker, Phys. Rev. 127 (1962) 485-500.

JP0650244

4.22 Phosphorous Donors in Semiconductors for Quantum Computing

J. Isoya*, M. Katagiri*, N. Mizuochi*, T. Umeda*, T. Ohshima**, N. Morishita** and H. Itoh**
Graduate School of Library, Information, and Media studies, University of Tsukuba*
Department of Material Development, JAERI**

1. Introduction

Donors in semiconductors are the possible candidate for a qubit (quantum bit) of quantum computer [1]. A donor has an electron spin of 1/2 or a nuclear spin of 1/2 which generate a simple two-level quantum system, and can therefore realize an ideal qubit. So far, the most well-studied donor was phosphorus (P) in Si. However, this donor may not be suitable to the quantum computing, because the fabrication and operation of the quantum computer was practically very difficult even using the state-of-the-art Si technology [2]. Thus, other semiconductors such as Ge-based compounds were explored as alternatives [2]. Last year, we found [3] that silicon carbide (SiC) has a good characteristic for quantum computing, as is demonstrated in Fig. 1. The P and N donor electron spins in SiC exhibited much longer spin coherence time (T_1) as compared to P in Si. Thus, in this work, we tried to clarify why the donors in SiC have such a longer T_1 or what are the necessary conditions to make the donors being suitable to the quantum computing.

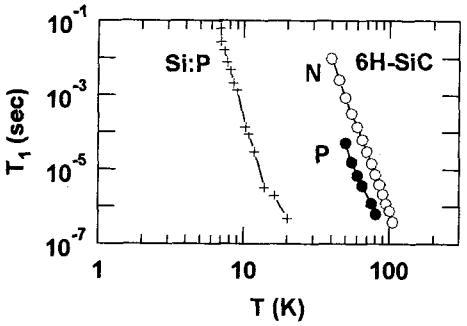

Fig. 1 T_1 (spin-lattice relaxation time) of P and N donors in SiC are much longer than P in Si [3].

2. Experimental

The P donors in SiC were created by P ion implantation to SiC substrates in TIARA. Starting substrates were commercial *n*-type (N-doped) 4*H*- or 6*H*-SiC wafers (room-temperature carrier concentration = 1×10^{17} cm^{-3}). P ions were implanted at 800°C with a total dose of 4.5×10^{14} cm^{-2} at 9 ~ 21 MeV by the TIARA tandem accelerator. This process produced a box-like profile (2-μm in depth) of P dopants with a concentration of 1×10^{18} cm^{-3}. After the implantation, the activation anneal of 1650°C (in Ar ambient) was subjected to the samples.

The characteristics of the P donors were measured by a pulsed electron paramagnetic resonance (pulsed EPR) spectrometer (Bruker E580 model). We characterized the spin-lattice relaxation time T_1 which indicates how long time an electron spin maintains its spin state.

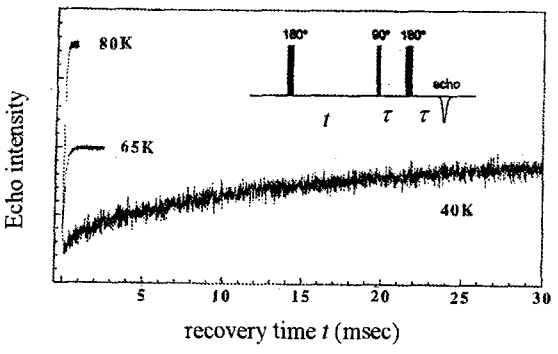

Fig. 2 Three-pulse inversion recovery experiment of pulsed EPR. T_1 is determined from the recovery curve, because echo intensity $\propto [1 - \exp(-t/T_1)]$ [4].

This coherence time should be longer as possible for the quantum computing, because T_1 sets a limit of the computation time. The determination of T_1 is explained in Fig. 2 [4].

3. Results and Discussion

3.1 The C-site P donors in SiC

We have reported [5] that our ion implantation to 6*H*-SiC creates the P donors labeled P_a and P_b, as shown in the EPR spectrum of Fig. 3. Recently, our P_a and P_b donors were identified as the carbon (C)-site P donors by means of the first-principles calculation[6]. Table 1 summarizes the hyperfine (HF) parameters of P donors between experiment and theory. Clearly P_a and P_b are in good agreement with the calculated C-site P donors at h and $k_{1,2}$ sites of 6*H*-SiC, respectively.

The C-site P donors (6*H*-SiC:P) and the N donor (6*H*-SiC:N) showed a thermally activated behavior in T_1, as shown in Fig. 4. T_1 was in proportion to $\exp(\Delta/kT)$, which is known as the Orbach relaxation process [3]. Its physical meaning is that a spin state is perturbed when an electron is excited between the two electronic levels (energy difference = Δ) as illustrated in the inset of Fig. 4. The Δ values were determined to be 44 or 77 meV for 6*H*-SiC:N, 52 meV for 6*H*-SiC:P, and 11 meV for Si:P (not shown here). Therefore, the main reason why the donors in SiC have much longer spin coherence times as compared to those in Si is the larger Δ values. The Δ of 44meV for 6*H*-SiC:N was known as the valley-orbit splitting between the 1s(E) and 1s(A_1) states of N donor [3]. Therefore, we speculate that the valley-orbit splitting is the key to the longer T_1 for donors in semiconductors. This point will be also supported by the next experiment.

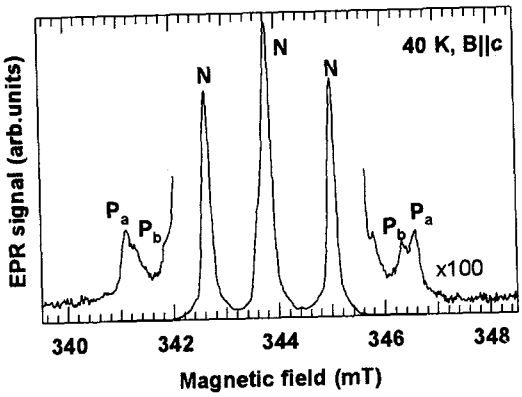

Fig. 3 EPR spectrum of P-implanted 6*H*-SiC. "N" denotes the signal of ^{14}N donors (nuclear spin I = 1, natural abundance = 99.6 %), while "P_a" and "P_b" denote that of ^{31}P donors (I = 1/2, natural abundance = 100 %).

Table 1 Hyperfine (HF) constants of P donors between experiment [5] and theory [6]. Units for A_{iso} and b are MHz.

Exp.	A_{iso}	b	Theory	A_{iso}	b
P_a	152.7	0.8	C-site P(h)	156.1	0.0
P_b	142.6	0	C-site P($k_{1,2}$)	147.2	5.0

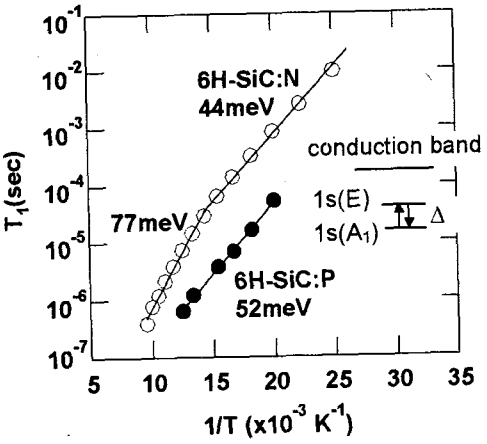

Fig. 4 Thermally activated behavior of T_1.

3.2 The Si-site P donors in SiC

In general, P atoms should be favorably introduced into Si sites rather than C sites, because of similar atomic sizes between P and Si. Therefore, the Si-site P donor should also exist in P-implanted SiC. This donor could be found when we performed P-implantation to 4*H*-SiC, which is shown in Fig. 5. The signal labeled "P" is due to P donors, although a ^{31}P HF splitting is too small to be detected. Recently, the same P signal was observed for CVD

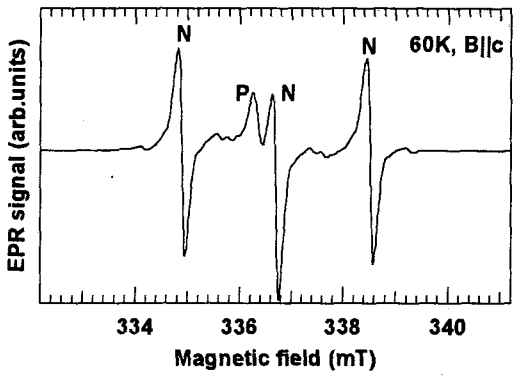

Fig. 5 EPR spectrum of P donors (Si-site) in P-implanted 4H-SiC.

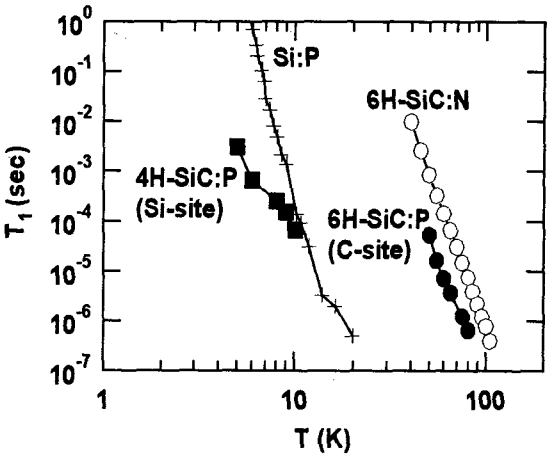

Fig. 6 Temperature dependence of T_1.

Table 2 The Δ values for P donors

types	Δ (meV)	sites
Si:P	11	Si-site
6H-SiC:P(P-implant)	52	C-site
4H-SiC:P(P-implant)	6	Si-site
6H-SiC:P(CVD)	4	Si-site

(chemical vapor deposition) P-doped SiC [7]. In contrast to our P-implanted SiC (Fig. 5), the CVD P-doped SiC achieved a very low concentration of N, so that ^{31}P HF splitting as well as ^{13}C super HF structure was successfully detected in the CVD sample [7]. The presence of the ^{13}C super HF structure ensured that this P donor signal originates from the Si-site P donors.

To compare between the two types of P donors (C-site or Si-site), we also studied T_1 of the Si-site P donors (4H-SiC:P). The result is shown in Fig. 6 and Table 2. The 4*H*-SiC:P has even shorter T_1 than Si:P (Fig. 6). The Δ value was only 6 meV (Table 2). Therefore, there was a significant difference between the C-site and Si-site P donors in SiC. This difference is not due to the difference between 4*H*- and 6*H*-SiC. Because we also examined 6*H*-SiC:P that was created by CVD P-doping [7], and then obtained a similar small Δ value (4 meV) for 6*H*-SiC:P. Therefore, we conclude that the longer T_1 does relate to the larger Δ value rather than the host material.

One of the physical factors to determine the Δ value is probably the degree of the lattice strain around a donor. Because of the large atomic radius of P atom, the C-site P donor should involve a larger strain as compared to the Si-site one, which can induce the larger valley-orbit splitting. Namely, we will have to explore such a "strained" donor system for gaining longer spin coherence times.

References

1) B. E. Kane, Nature 393, 133 (1998).

2) R. Vrijen, E. Yablonovitch, K. Wang, H.-W. Jiang, A. Balandin, V. Roychowdhury, T. Mor, D. DiVincenzo, Phys. Rev. A 62, 012306 (2000).

3) J. Isoya, T. Ohshima, N. Morishita, T. Kamiya, H. Itoh, S. Yamasaki, Physica B 340-342 (2003) 903.

4) J. Isoya, S. Yamasaki, H. Okushi, A. Matsuda, K. Tanaka, Phys. Rev. B 47, 7013 (1993).

5) J. Isoya, T. Ohshima, A. Ohi, N. Morishita, H. Itoh, Nuclear Instruments and Methods in Phys. Res. B 206 (2003) 965.

6) E. Rauls, M. V. B. Pinheiro, S. Greulich-Weber, U. Gerstmann, Phys. Rev. B 70, 085202 (2004).

7) N. T. Son, A. Henry, J. Isoya, E. Janzén, Mat. Sci. Forum 483-485, 515 (2005).

4.23 Effects of Hydrogen and Hydroxyl on Ion-beam Induced Luminescence of Ceramics

S. Nagata*, S. Yamamoto**, K. Toh*, B. Tsuchiya* and T. Shikama*
Institute for Materials Research, Tohoku University*
Department of Material Development, JAERI**

1. Introduction

Fundamental defects such as the E'centers, the peroxy radical and non-bridging oxygen hole center (NBOHC) in silica glasses, have been extensively studied by electron paramagnetic resonance (EPR). Besides these defects having un-paired electron, neutral oxygen-deficiency centers (ODCs) affect optical absorption for practical application[1]. Additionally, the ODCs interact with atomic hydrogen, which is one of the major impurities in silica glasses as a form of hydroxyl (OH)[2]. The incorporation of hydrogen improves optical transmission property of optical fibers under neutron and gamma irradiation[3]. Our knowledge about ODCs, however, is still limited owing to their diamagnetic characteristics. The ion beam is one of the powerful probes to detect non-paramagnetic ODCs, which emit blue luminescence at around 2.7 and 3.1 eV by ionizing radiation. The luminescence measurements during ion bombardment also allow us to measure dynamic process involving damage creation and relaxation in the glass network[4]. Besides nuclear collision, electronic energy deposition can create Frenkel type defects in silica glasses[5], and can simultaneously stimulate rearrangement of damaged structure. Because the observed phenomena composed of these complex processes are affected by a small amount of impurities, ion beam induced luminescence from silica glasses is not fully understood. In the present experiments, we studied luminescence increase at the beginning of the irradiation and on the OH content to clarify responsible process of defect formation during the light ion irradiation for silica glasses.

2. Experimental procedure

Samples of SiO_2 glasses used in the present experiments were commercially available fused and synthesized silica glasses, produced by Toshiba Ceramics, Co. Ltd., with a size of 10 mm x 10 mm with a thickness of 0.5 mm. The ion-beam induced luminescence was measured at room temperature using a scattering chamber with base pressure of 2×10^{-6} Pa, connected to an accelerator. A proton or helium ion beam of about 1mm diameter was incident on the specimen at an angle of 40 degrees at energies between 0.01 and 2.0 MeV with a flux density of about 10 nA/mm^2, corresponding to 6×10^{12} ions/cm^2. For irradiation with 10 keV, a low energy ion gun with a mass filter was used in the same chamber. The ion induced luminescence was transmitted through optical fibers inserted in the vacuum chamber or by an optical window, and was detected with a multi-channel spectrum analyzer (Hamamatsu C5967, 5098, Roper Scientific PIXE100, Acton300). Photo Luminescence (PL) measurements for 3.1 eV centers were also carried out using a Xe lamp with a 5 eV interference filter. Hydrogen concentration in the near surface layer was determined by Elastic Recoil Detection Analysis (ERDA). An ion beam of 2.8 MeV He^{2+} was incident on

the specimen at an angle of 75 degree to the surface normal and the recoiled hydrogen atoms were detected using Al foil of 12 μ m thickness an at an angle of 30 degrees with respect to the analyzing beam. OH content in the samples was measured using Fourier Transform Infrared Spectroscopy (FTIR).

3. Results and Discussion

Figure 1 shows typical fluence dependence of the proton induced luminescence intensity at 2.7 eV from samples containing different OH concentration. The luminescence intensity was normalized with the incident current. The higher intensity was observed from silica glasses with the lower concentration of OH. The fluence dependence curve for T-2030 was nearly identical to the curve for T-2630. In both samples, the nominal OH concentration was 1 ppm , and almost no absorption due to OH was found in the FTIR spectrum, while a small difference of other impurities existed between them. Therefore, production of ODCs and/or luminescence efficiency can be attributed to the OH. Enhanced photo-generation of E' center was observed for H_2 treated oxygen deficient silica[6], in which an oxygen vacancy traps an atomic hydrogen and finally transforms to E' center. In case of the ion irradiation, formation of NBOHC appeared as 1.9 eV luminescence corresponds to the dissociation of OH. The lower intensity of 2.7 eV luminescence from silica with higher OH can be explained by the formation of atomic hydrogen by the ion induced dissociation of OH. Although a considerable amount of excess hydrogen about several hundreds ppm were detected in silica by the ERDA, these hydrogen, probably because of molecular form, did not directly interact with ODCs.

From a slope of the growth curve of the luminescence intensity at the beginning of the

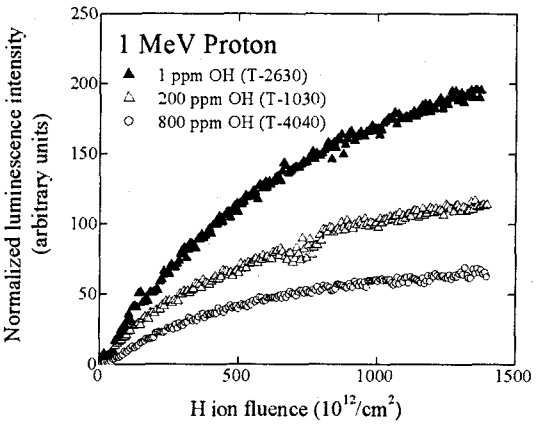

Fig. 1 Typical fluence dependence of the proton induced luminescence intensity at 2.7 eV from silica glasses containing various OH concentration.

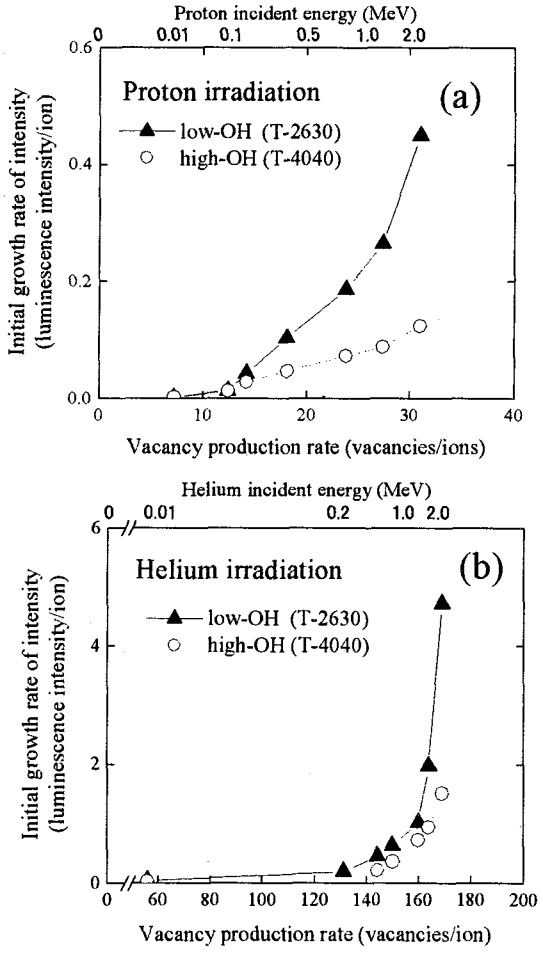

Fig. 2 Initial increase rate of 2.7 eV luminescence from silica with low-OH (▲) and high-OH (○) plotted against rate of vacancy production based on Kinchin-Pease model, for proton and helium irradiation, (a) and (b), respectively.

irradiation, growth rates of 2.7 eV luminescence were estimated and plotted against the rate of vacancy production calculated by SRIM2003 code based on Kinchin-Pease model, in Fig. 2(a) and (b), for proton and helium irradiation, respectively. The initial growth rate of luminescence did not linearly increase with increasing displacement rate. For example, the intensity of luminescence from low-OH silica by 2.0 MeV helium ion irradiation was about five times larger than that for 1 MeV, while the increase of vacancy production rate was less than 10 %. The prominent enhancement of the growth rate was observed for the higher energy, indicting significant defect production due to electronic energy deposition. For incident energies below 30 keV, luminescence induced by both deuteron and helium was related with the displacement production by nuclear collision[7].

Because the observed luminescence intensity is integrated along the entire trajectory of the incident ion, a growth rate of luminescence intensity at a mean energy can be evaluated from the successive data for energy dependence of the net raise rate. Figure 3 shows initial growth rates per unit length, plotted against the ion energy. If the luminescence is caused by electronic energy deposition Ee on the oxygen deficient defects created by nuclear energy deposition En, the growth of the luminescence intensity is related to the Ee x En. But in an opposite extreme case, if the luminescence centers are created significantly by electronic energy deposition, the increase of the intensity is attributed to Ee x Ee. The calculated curve of Ee x Ee fairly agrees with the shape of experimentally obtained growth rate in the lower energy region below 1 MeV. Above 1 MeV, on the contrary to the calculated curves, the experimental initial growth rate increased with increasing the ion

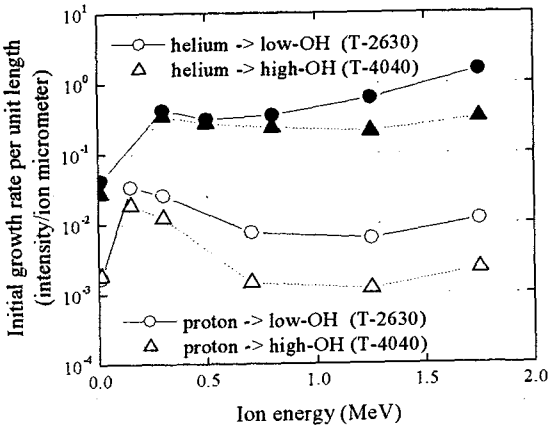

Fig. 3 Initial increase rate of 2.7 eV luminescence intensity per unit length evaluated from data in fig. 2, and plotted against the ion energy of proton and helium ion.

energy. The disagreement between experimental and calculated curves at the higher ion energy can be explained by annealing effects[8] for the lower energy where the electronic stopping is relatively high. Differences of the intensity growth between silica glasses with various OH contents appeared when the electronic stopping is relatively small, for proton with higher energy. This fact also might be support the annealing effects by electronic excitation.

References

1) L. Skuja, J. Non-Cryst. Solids 239 (1998) 16-48
2) B.C. Schmidt, F.M. Holtz, J.-M. Beny, J. Non-Cryst. Solids 240 (1998) 91-98.
3) D.L. Griscom, J. Appl. Phys. 80 (1996) 2142-2155.
4) H. Hosono, H. Kawazoe, N. Matsunami, Phys. Rev. Lett. 80 (1988) .317-320.
5) P.J. Chandler, F. Jaque, P.D. Townsend, Radiation Effects, 42 (1979) 45-53.
6) H. Nishioka, R. Nakamura, Y. Ohki, Y. Hama, Phys. Rev. B 48 (1993) 2968-2973.
7) T. Tanabe, A. Omori, M. Fujiwara, J. Nucl. Mater. 258-263 (1998) 1914-1918.
8) F.J. Jaque, P.D.Townsend, Nucl. Instr. and Meth. 182/183 (1981) 781-786.

JP0650246

4.24 Evaluation of Three Dimensional Microstructures on Silica Glass Fabricated by Ion Microbeam

T. Nakamura*, Y. Ohki*, K. Fukagawa**, M. Murai**, H. Nishikawa**, M. Oikawa***, T. Satoh*** and K. Arakawa***

Department of Electrical Engineering and Bioscience, Waseda University*

Department of Electrical Engineering, Shibaura Institute of Technology**

Advanced Radiation Technology Center, JAERI***

1. Introduction

It is well known that high energy ion-beam irradiation of silica glass (amorphous SiO_2) can induce refractive index changes and defects creation[1]. The first phenomenon is attributed to internal compaction in silica depending on the increase of smaller planar rings than the regular planar 6 or 5-fold rings of silica structure[1]. The structural changes in silica induced by ion implantation are different according to the differences of ion species, fluence, and acceleration energy.

We studied ion microbeam irradiation effects in micro-and nano-scales on silica glass by various conditions.

We also discussed possible application of the microbeam irradiation effects aiming at the fabrication of micrometer scale optical elements on silica[2), 3)].

2.Experimental Procedures

Ion microbeam irradiation was carried out using a 3-MV single-ended accelerator (for light ions) or 3-MV tandem accelerator (for heavy ions) both equipped with microbeam systems (TIARA, JAERI Takasaki, beam diameter is ~1 μm). Implanted ion species were H^+ (1.7 MeV), He^+ (1.7 MeV), B^{3+} (12 MeV), C^{4+} (15 MeV), N^{4+} (13.6 MeV), O^{4+} (15 MeV) and Si^{5+} (18 MeV) with a fluence of 1×10^{13} to 5×10^{18} cm^{-2}. Detailed conditions are shown in Table 1.

Also, Table 1 shows projected ranges, energy loss by electronic collision, and the one by atomic collision predicted by SRIM 2003 simulation.

Samples are high purity silica substrates ([OH]: 1300 ppm) with dimensions of 3 × 3 × 10 mm^3, and each sample surface was optically polished for microscopic observations.

The shapes of microbeam scanned areas are shown in Fig. 1. One is rectangular with a dimension of 10 μm × 50 μm scanned over on the surface across the sample edge for observation of defects along the direction of depth from the side surface by means of micro-photoluminescence (PL). The second is square on the surface of 5 μm × 5 μm for investigation of the surface deformation (Δh_s), and for studying the relation between the surface deformation and ion energies by atomic force microscopy (AFM).

3.Results and discussion

Figure 2 shows phase microscope images of the side surface of silica, where the refractive index changed area can be visible as bright regions from the surface to the projected range (7 to 33 μm). The refractive index changes can be attributed to the compaction, as we already reported[1].

Figure 3 shows the intensity of the PL band at 540 nm as a function of ion fluences

Table 1 Conditions of microbeam irradiation on silica and results of calculation by SRIM2003.

ION	ENERGY [MeV]	FLUENCE [ions/cm^2]	PROJECTED RANGE [μm]	ELECTRONIC STOPPING POWER [keV/ion]	NUCLEAR STOPPING POWER [keV/ion]
H^+	1.7	3E15-5E18	33	1.61E3	0.394
He^+	1.7	3E15-3E16	5.9	1.69E3	1.04
B^{3+}	12	1E14-5E15	14	11.9E3	3.11
C^{4+}	15	1E13-3E16	14	14.9E3	3.55
N^{4+}	13.6	1E13-5E14	11	13.5E3	3.81
O^{4+}	15	1E13-5E16	10	14.9E3	4.41
Si^{5+}	18	1E13-5E16	7.3	17.6E3	6.60

for various ion species. The PL intensities induced by impacts of heavy ions such as He^+, B^{3+}, C^{4+}, N^{4+}, O^{4+} and Si^{5+}, become saturated at smaller fluences, when compared with H^+. This can be attributed to the fact that much higher energy was deposited at the regions of the smaller projected ranges, compared with the protons, as shown in Table 1.

Figure 4 (a) shows the depth of surface grooves as a function of the ion fluence.

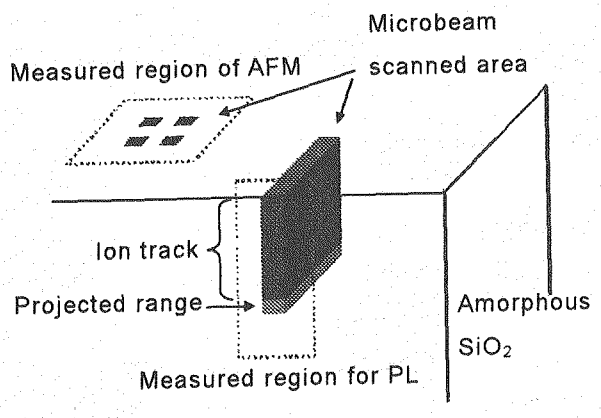

Fig. 1 Schematic illustration of the shapes of microbeam scanned areas. One is rectangular with a dimension of 10 μm × 50 μm scanned over on the surface across the sample edge, and the second is square on the surface of 5 μm × 5 μm.

Similar trend was observed for the surface grooves as a function of the ion fluence, as already observed for PL. Taking into account of the effects of both nuclear (E_n) and electronic (E_e) stopping powers, and the projected range (R_p) on the depth of grooves, we have plotted the data as a function of the value proportional to $E_n \times E_e/R_p$, as shown in Fig. 4 (b), where the data can be drawn on a single curve.

This suggests that the induced surface groove or internal compaction was affected not only by electronic stopping powers dominating the energy loss process, but also by nuclear stopping power at the projected range.

4.References

1) H. Nishikawa et al., The 8th IUMRS International Conference on Advanced Materials, Innovative Nanomaterials Using Ion Technology, A9-09-O09, pp.96(2003).
2) M. Hattori et al., 8th ICNMTA, P1-29,p.57 (2002)
3) T. Souno et al., 8th ICNMTA, P2-19, p.101 (2002)

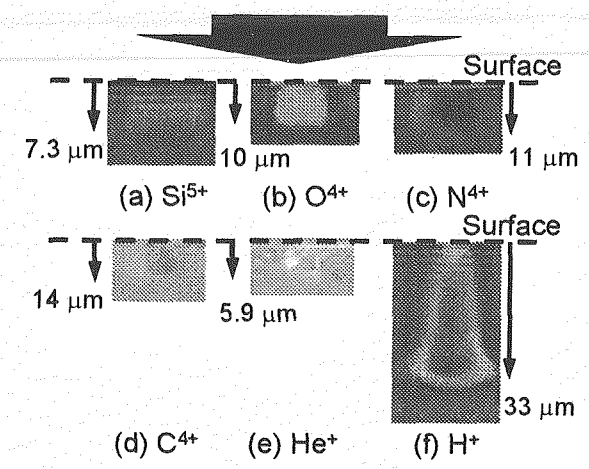

Fig. 2 Phase microscopic images obtained from the side surface of silica irradiated with various ions and accelerated energy from 1.7 MeV to 18 MeV. (Fluence: (a)1 × 10^{14} cm^{-2}, (b)1 × 10^{16} cm^{-2}, (c)1 × 10^{14} cm^{-2}, (d)1 × 10^{14} cm^{-2}, (e)3 × 10^{15} cm^{-2}, (f)3 × 10^{16} cm^{-2}).

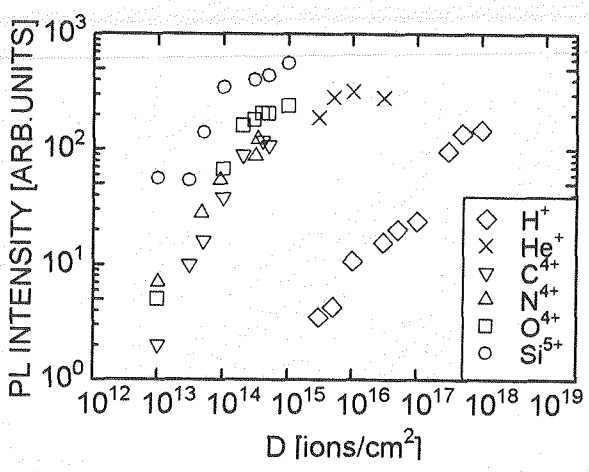

Fig. 3 The PL intensity at 540 nm as a function of ion fluence.

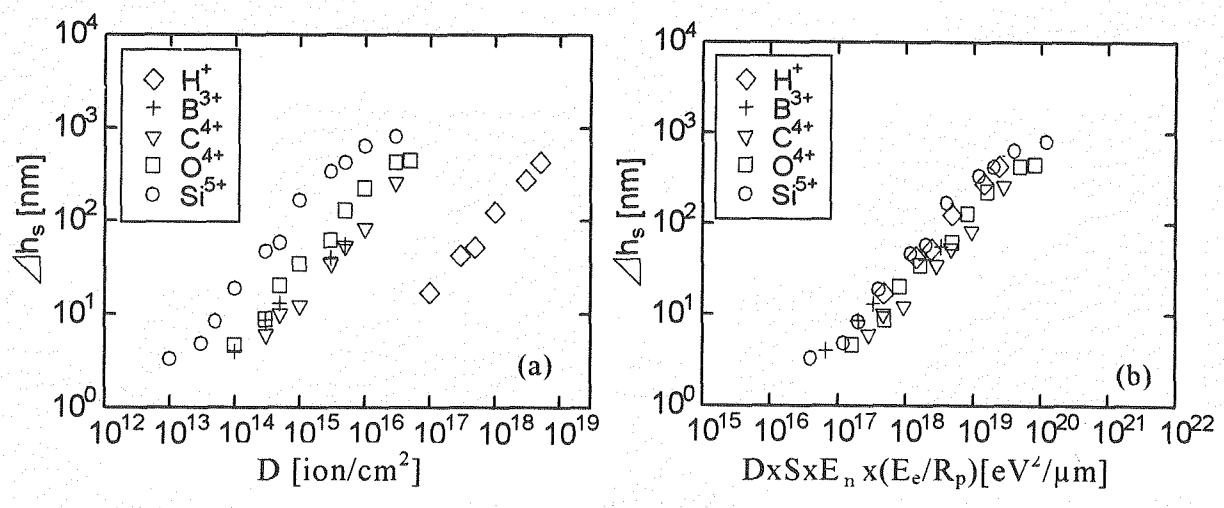

Fig.4 (a) Depth of the surface groove (Δh_s) as a function of fluence. Irradiated area is 5 μm × 5 μm, and (b) the plot of Δh_s as a function of the value proportional to $E_n \times E_e/R_p$. (D: fluence [ions/cm^2], S: irradiated area [μm^2], E_e: Electronic Stopping Power [eV], E_n: Nuclear Stopping Power [eV], R_p: projected range [μm], Δh_s: deformation depth [μm]).

This is a blank page.

5. Material Analysis

This is a blank page.

5.1 Characterization of Sulfur-doped TiO_2 Films by RBS

S. Yamamoto, A. Takeyama, A. Miyashita and M. Yoshikawa
Department of Material Development, JAERI

1. Introduction

Titanium dioxide (TiO_2), an extensively studied and widely used photocatalyst, has attracted many interests from the viewpoints of basic science and applications. TiO_2 doped with several kinds of elements has been studied for the improving photocatalysis, the modification of optical, electrical and magnetic properties. TiO_2 doped with a few atomic percent sulfur prepared by heating titanium disulfide (TiS_2) powders in air has showed extending their optical absorption edge into the visible light region. But the influence of sulfur doping on the photocatalytic properties of TiO_2 films has not been clarified. Therefore, the synthesis of sulfur-doped TiO_2 films is necessary. In the present study, we explore the preparation processes of polycrystalline and epitaixal TiO_2 films doped with sulfur by pulsed laser deposition (PLD) technique. The crystal structure of the deposited films and the concentration of doped sulfur were evaluated by x-ray diffraction (XRD) and Rutherford backscattering spectroscopy with channeling (RBS/C). The effects of the substrate temperature during the deposition on the crystallinity and on the composition of TiO_2 films are reported.

2. Experimental

Sulfur-doped TiO_2 films were prepared by PLD using a KrF excimer laser (wavelength: 248 nm, repetition rate: 5 Hz). To fabricate polycrystalline sulfur-doped TiO_2 films, the films were deposited on Si (100) substrates at ambient temperature using a TiS_2 (purity, 99.9%) target under pressure of 10^{-4} Pa range and then heat-treated up to 500°C in air. In this experiment, TiS_2 was used for the sulfur source for the deposition of polycrystalline TiO_2 films. Since TiS_2 is oxidized by heating in air and then transformed to TiO_2. On the other hand, epitaxial sulfur-doped TiO_2 films were grown on α-Al_2O_3 (0001) substrates using titanium oxide targets, which included various concentrations of sulfur, prepared by heat treatment of compression molding of TiS_2 powders in air up to 400°C. During the deposition for epitaxial growth, the substrate temperature was kept at 400°C and 500°C under pressure of 10^{-4} Pa range. The composition of evaporation targets and deposited films was determined by energy dispersive X-ray spectroscopy (EDS). The RBS/C analysis using a 3 MV single-stage-accelerator at JAERI/Takasaki was employed to characterize the epitaxial films. The analyzing 2.0 MeV $^4He^+$ beam were incident and backscattered particles were detected at the scattering angle of 165°. The crystallographic relationships between the TiO_2 films and the substrates were determined by XRD.

3. Results and discussion

Figure 1 shows the 2.0 MeV $^4He^+$ RBS/C spectra for (a) the as-deposited titanium disulfide film, (b) the film annealed at 300°C in air for 1 h, and (c) the film annealed at 500°C in air for 1 h. The thickness of deposited films was about 150

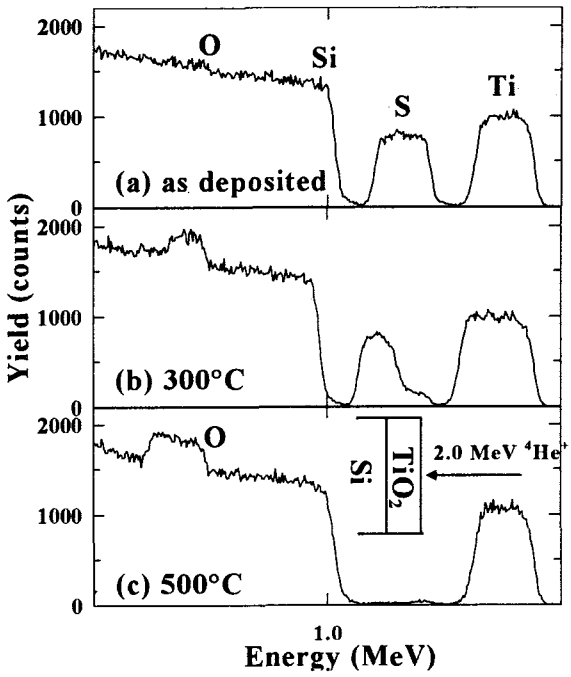

Fig. 1 2.0 MeV $^4He^+$ RBS/C spectra for the sulfur-doped titanium oxide films on Si (100) substrates, as deposited and annealed at different temperatures.

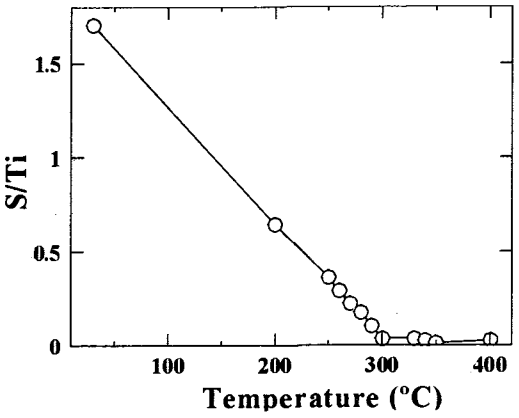

Fig. 2 The influence of the heat treatment temperatures on the composition of titanium disulfide targets.

nm. As can be seen in Fig. 1 (b), the reduction of the peak from sulfur and the increase of the peak from oxygen at the surface region of the deposited film are observed. Furthermore, the film heat-treated at 500°C in Fig. 1 (c), the whole region of the film was oxidized and the concentration of sulfur reaches about 1 at. %. It is recognized that the TiS_2 film is oxidized by heating in air and transformed to TiO_2. The results of XRD analysis showed that the films annealed at 500°C have a polycrystalline anatase TiO_2 structure. It indicates that the concentration of sulfur-doped polycrystalline TiO_2 films is controllable by using heat treatment temperatures ranging between 300 and 500°C.

In order to fabricate sulfur-doped epitaxial TiO_2 films with a desirable sulfur concentration, the control of target's composition is necessary. The effect of the heat treatment temperature on the composition of titanium disulfide is shown in Fig. 2. It can be seen that the heat treatment below 300°C induces a proportional decrease of the sulfur component of targets. For the heat treatment temperatures higher than 300°C, the sulfur component is saturated. For the epitaxial growth of TiO_2 films doped with sulfur, films were deposited on the α-Al_2O_3 (0001) substrates at 400 and 500°C under pressure of 10^{-4} Pa. Fig. 3 shows the XRD pattern for the film deposited on the α-Al_2O_3 (0001) substrate at 400°C using a titanium disulfide target annealed at 200°C. As can be seen in Figure 3, only the reflection from the rutile TiO_2 (200) is observed without any reflection from the substrate. It is confirmed that the sulfur-doped rutile TiO_2 (100) film is grown on the α-Al_2O_3 (0001) substrate. Fig. 4 illustrates the 2.0 MeV $^4He^+$ RBS/C spectra for the same sample in Fig. 3 under the axial channeling and random conditions. The thickness of this

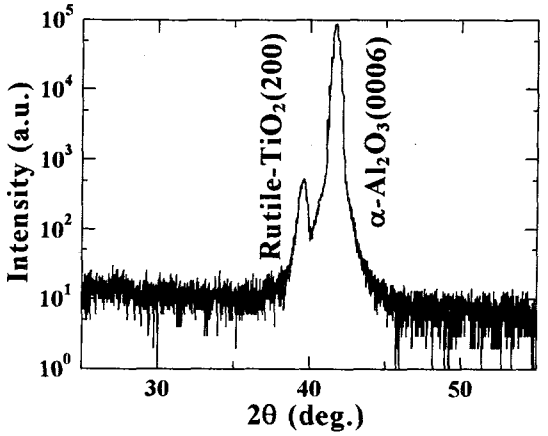

Fig. 3 X-ray diffraction pattern for the sulfur-doped TiO_2 film on the α-Al_2O_3 (0001) substrate.

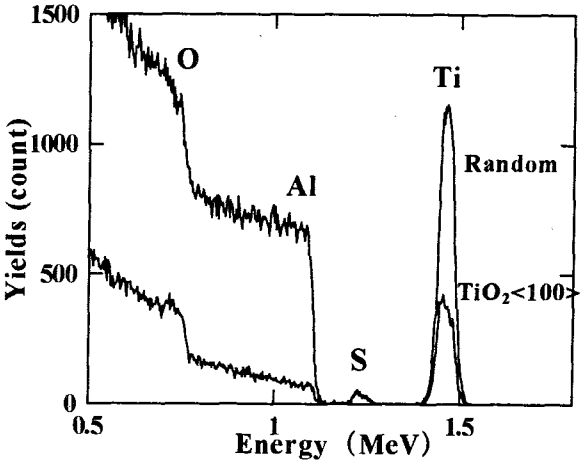

Fig. 4 2.0 MeV $^4He^+$ RBS/C spectra for the sulfur-doped rutile TiO_2 (100) film (thickness: 52 nm) on the α-Al_2O_3 (0001) substrate. The concentration of sulfur in the film is 2.1 at. %.

film is 52 nm and the concentration of sulfur in the film is 2.1 at. %. In Fig. 4, the reduction of the peak from Ti component of the TiO_2 film in the aligned spectrum is observed compared with the random one. It indicates that the deposited film was epitaxially grown on the α-Al_2O_3 (0001) substrate. But the doped sulfur atoms in the rutrile TiO_2 (100) film is distributed randomly. Rutile TiO_2 (100) films with various sulfur concentrations were prepared be controlling the sulfur concentration of targets. The TiO_2 (100) films with high sulfur concentrations deposited on α-Al_2O_3 (0001) substrates showed poor crystallinity. Furthermore, for the RBS/C spectra for the films deposited at 500°C, the peak from sulfur was not observed. The concentration of sulfur in TiO_2 (100) films was mainly influenced by α-Al_2O_3 (0001) substrate temperature during the deposition. It can be seen that thermal oxidation is an essential process for the growth of the sulfur-doped epitaxial TiO_2 (100) film.

4. Summary

Sulfur-doped TiO_2 films were prepared by PLD. Polycrystalline sulfur-doped TiO_2 films were obtained by depositing at ambient temperature using a TiS_2 targets and then annealing in air up to 500°C. Furthermore, sulfur-doped tile TiO_2 (100) films were obtained on α-Al_2O_3 (0001) heated at 400°C using an annealed titanium disulfide target. It was found that the concentration of sulfur in rutile TiO_2 films was mainly influenced by α-Al_2O_3 (0001) substrate temperature.